

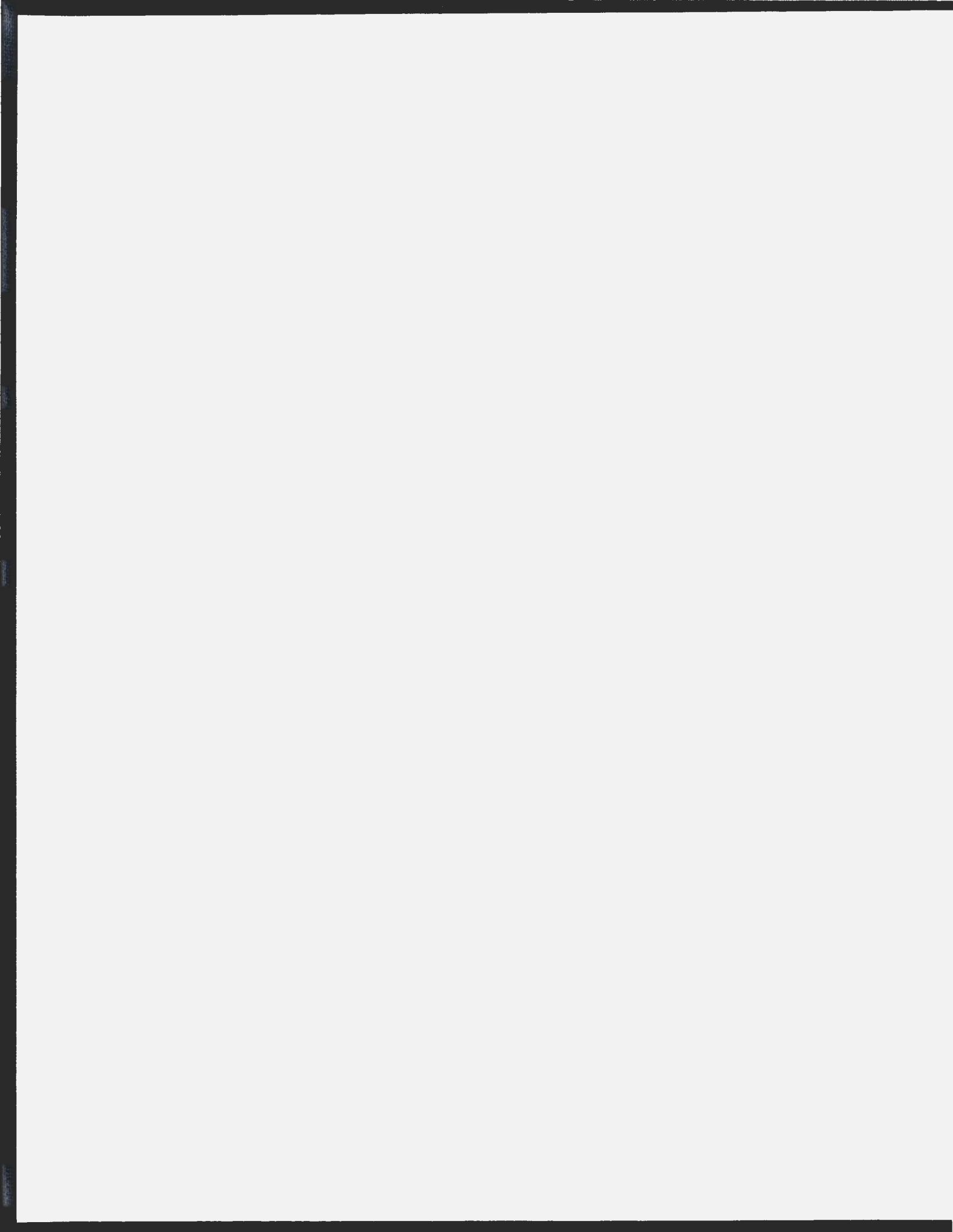
IDENTIFICATION OF LINEAR AND NON-LINEAR
MULTI-MODAL VIV RESPONSES FOR FLEXIBLE
DEEPWATER RISERS

CENTRE FOR NEWFOUNDLAND STUDIES

**TOTAL OF 10 PAGES ONLY
MAY BE XEROXED**

(Without Author's Permission)

XIANGQUN LI



Identification of Linear and Non-linear Multi-Modal VIV Responses for Flexible Deepwater Risers

by

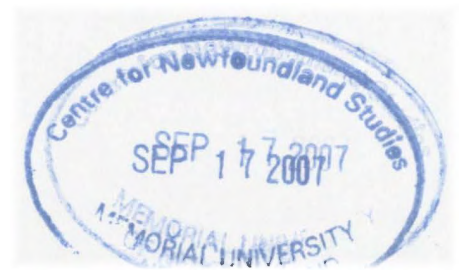
Xiangqun Li, B. Eng., M. Eng.

A Thesis Submitted to the School of Graduate Studies
in Partial Fulfillment of the Requirements for the Degree of
Doctor of Philosophy in Engineering

Faculty of Engineering and Applied Science
Memorial University of Newfoundland

November 2005

St. John's, Newfoundland, Canada



Acknowledgements

I would like to thank my supervisors Dr. Neil Bose, Dr. Emile Baddour, Dr. Pengfei Liu and Dr. Bruce Colbourne for their valuable advice and consultation throughout the tenure of this degree program.

I would also like to thank Dr. Wayne Raman-Nair, Mr. Don Spencer, Dr. Owen H. Oakley, Andy Wallace, Peter Hackett, Brian Hill and Austin Bugden for their valuable contributions or consultations during the tenure of this degree program.

I would like to give special thanks to Mrs. Lin Zhu, my wife, for her valuable support in the design and construction of the experimental equipment and in the performance of the experiments.

I am grateful for the financial support provided by the Institute for Ocean Technology (IOT), National Research Council, Canada; Memorial University of Newfoundland (MUN); Petroleum Research Atlantic Canada (PRAC); the National Sciences and Engineering Research Council, Canada (NSERC); and the National Research Council, Canada (NRCC).

Abstract

Offshore energy exploration has been moving into ever increasing water depths. For floating offshore drilling structures, the riser system is a crucial element. Vortex-induced vibration (VIV) is a major concern for deepwater riser developments, as vortex-induced vibration is a major cause of riser fatigue damage. For deepwater risers, current is the dominant factor causing VIV responses. Due to the increased water depth, deep-water risers have long and flexible structures, so that they have the potential to be subject to very high modes of vibration, i.e. multi-modal VIV. The frequencies, amplitudes and modes of VIV responses are usually the focus of deepwater riser design, as they, along with riser material properties, directly determine the riser fatigue life. In recent years, much effort has been devoted into the investigation of riser VIV response, but there are still many uncertainties, especially for the risers with multi-mode VIV responses in currents. For example, frequency lock-in phenomena and modal resonances are still not fully understood for multi-modal VIV responses; the vibration shapes over riser length and the motion trajectories in the cross-sectional plane for a flexible riser with multi-modal VIV can not be found in the literature. The frequency and mode components contained in the multi-modal VIV responses in both in-line and cross-flow directions have not been published in previous work.

This research aims to improve the understanding of multi-modal VIV in currents. The research objectives include i) frequency characteristics for multi-modal VIV responses, such as frequency versus current velocity and frequency lock-in phenomenon; ii) amplitude characteristics for multi-modal VIV responses, such as amplitude versus

current velocity, amplitude range and amplitude resonance; iii) spectral characteristics for multi-modal VIV responses, such as dominant frequencies, power spectrum versus current velocity and power spectrum versus location on the riser; iv) modal characteristics for multi-modal VIV responses, such as modal distribution, dominant mode and mode versus current velocity; v) modal system parameters for a flexible riser in calm water, including modal mass, modal damping, modal stiffness and non-linear damping; and vi) the correlation between the modal parameters and the VIV responses.

After a review of the state-of-the-art literature involving VIV investigation, an experimental method was proposed for this research. Based on a prototype riser, a length-distorted model riser was designed with similarity of the mass, the bending stiffness and the frequency ratio. Two model riser tests were designed and conducted. The first one was a shaker-excitation test, which was designed to investigate the modal system parameters. A shaker was used to generate an excitation to the riser, and the riser responses were measured. The modal system parameters were estimated from the frequency response functions based on a simplified governing equation for the shaker/riser system. Modal analysis was used to estimate the linear modal system parameters, and Bendat's technique was used to estimate the non-linear damping for the flexible riser.

Another model riser test was a current-excitation test. This test was designed to investigate the VIV responses in currents. The uniform currents were generated by towing carriage. Sixteen pairs of accelerometers were used to measure the VIV responses at sixteen locations on the riser. Spectral analysis and modal analysis are two major tools to analyze the measured data.

It was found that the frequencies of the multi-modal VIV responses in both the cross-flow and in-line directions follow the Strouhal frequencies for a flexible riser. The measured Strouhal number was about 0.12. The frequency lock-in phenomena occurred in both the in-line and cross-flow directions at some modal natural frequencies. The vibration amplitudes fluctuate from 0.3 to $0.9D$ (D denotes the riser diameter) in both the in-line and cross-flow directions for the flexible riser tested, and no increasing trend existed as the current velocity increases. The resonances are not strong as the vibration energy is shared by several modes. The VIV responses for a flexible riser contained a number of modal components, but one or two were the dominant modes.

It was also found that flexible risers have a variety of natural frequencies, which correspond to a variety of mode shapes. The modal natural frequencies depend on the tension. The estimated added mass coefficients C_a depend on the tensions and mode shapes for a flexible riser, ranging from 1.0 to 3.7, and the estimated damping coefficients C_d have a relatively big scatter, ranging from 0.5 to 2.5. There is a degree of correlation between the estimated modal parameters and the VIV responses.

TABLE OF CONTENTS

Acknowledgements

Abstract

Table of Contents

List of Figures

List of Tables

| | |
|---|-----------|
| 1. Introduction..... | 1 |
| 1.1 Marine Risers..... | 2 |
| 1.2 Single-Modal Vortex-Induced Vibrations..... | 4 |
| 1.3 Currents in Deep Waters..... | 12 |
| 1.4 Multi-Modal Vortex-Induced Vibrations..... | 14 |
| 1.5 System Identification Technique..... | 16 |
| 1.6 Experimental Techniques for Risers..... | 18 |
| 1.7 Problem Discussion..... | 22 |
| 1.8 Objectives and Methodology..... | 22 |
| 1.9 Outline of the Thesis..... | 24 |
| 1.10 Contributions of the Thesis..... | 27 |
| 2. Test Apparatus..... | 29 |
| 2.1 Model Riser..... | 30 |
| 2.1.1 Analytical Model for Design of Model Riser..... | 30 |
| 2.1.2 Design of Modal Riser..... | 33 |
| 2.1.3 Construction of Model Riser..... | 37 |
| 2.2 Supporting Steel Frame..... | 39 |
| 2.3 Shaker System..... | 41 |
| 2.4 Instrumentation..... | 43 |
| 2.4.1 Sensors..... | 43 |
| 2.4.2 Calibration of Accelerometers..... | 44 |
| 2.4.3 Accelerations in the In-line and the Cross-flow Directions..... | 47 |
| 2.4.4 Vibration Velocities and Displacements..... | 49 |
| 3. Shaker-Excitation Tests..... | 51 |
| 3.1 Experimental Design..... | 52 |
| 3.2 Excitation Design..... | 53 |
| 3.3 Data Analysis..... | 58 |
| 3.3.1 Modal Governing Equation for Shaker/Riser System..... | 58 |
| 3.3.2 Relationship between Shaker Displacement and Shaker Force..... | 61 |

| | | |
|-----------|---|------------|
| 3.3.3 | Frequency Response Function for Shaker/Riser System..... | 61 |
| 3.3.4 | Estimate of Modal Parameters..... | 63 |
| 3.4 | Test Results..... | 64 |
| 3.4.1 | Test results at Pretension of 500N..... | 65 |
| 3.4.1.1 | Frequency Responses Functions..... | 65 |
| 3.4.1.2 | Vibration Modes..... | 71 |
| 3.4.1.3 | Modal Parameters..... | 79 |
| 3.4.2 | Test Results for Pretension of 700N..... | 87 |
| 3.4.2.1 | Frequency Response Functions..... | 87 |
| 3.4.2.2 | Vibration Modes..... | 88 |
| 3.4.2.3 | Modal Parameters..... | 93 |
| 3.4.3 | Test Results at Pretension of 900N..... | 96 |
| 3.4.3.1 | Frequency Response Functions..... | 96 |
| 3.4.3.2 | Vibration Modes..... | 100 |
| 3.4.3.3 | Modal Parameters..... | 105 |
| 3.4.4 | Non-linear Component Analysis..... | 110 |
| 3.4.5 | Summary of Shaker-Excitation Test Results..... | 115 |
| 4. | Vortex-Induced Vibration Tests..... | 121 |
| 4.1 | Experimental Design and Performance..... | 121 |
| 4.2 | Test Results..... | 126 |
| 4.2.1 | Tensions and Modal Natural Frequencies at Different Currents..... | 126 |
| 4.2.2 | Test Results at Low Pretension of 200N..... | 130 |
| 4.2.2.1 | Amplitude and Frequency versus Current Velocity..... | 130 |
| 4.2.2.2 | Vibration Power Spectra..... | 136 |
| 4.2.2.3 | Modal Components of VIV Response..... | 157 |
| 4.2.2.4 | Vibration Time Histories..... | 165 |
| 4.2.2.5 | Vibration Shapes..... | 177 |
| 4.2.2.6 | Vibration Trajectories..... | 180 |
| 4.2.3 | Test Results at High Pretension of 600N..... | 185 |
| 4.2.3.1 | Amplitude and Frequency versus Current Velocity..... | 185 |
| 4.2.3.2 | Vibration Power Spectra..... | 189 |
| 4.2.3.3 | Modal Components of VIV Response..... | 208 |
| 4.2.3.4 | Vibration Time Histories..... | 215 |
| 4.2.3.5 | Vibration Shapes..... | 224 |
| 4.2.3.6 | Vibration Trajectories..... | 227 |
| 4.3 | Summary of VIV Test Results..... | 231 |
| 5. | Correlation between Modal Parameter and VIV Response | 234 |
| 5.1 | Correlation between Modal Natural Frequencies and Frequency Lock-in of VIV Response..... | 235 |
| 5.2 | Correlation between Modal Added Mass Coefficient and Upper Limit Values.... | 236 |
| 5.3 | Correlation between Modal Natural Frequencies and Resonance of VIV Responses | 237 |
| 6. | Conclusions..... | 239 |

| | |
|--|------------|
| 6.1 Modal Parameters in Calm Water..... | 241 |
| 6.2 Multi-Modal Vortex-Induced Vibration in Currents..... | 242 |
| 6.3 Correlation between Modal Parameters and VIV Responses | 245 |
| 6.4 Recommendations for Future Work..... | 246 |
| References..... | 248 |
| Appendix A Governing equation for riser motions..... | 252 |
| Appendix B Validation of the program to estimate of spectral density functions..... | 261 |
| Method of Estimation..... | 261 |
| Case Studies..... | 263 |
| Case study 1 Auto-spectral density function of single sine wave..... | 263 |
| Case study 2 Auto-spectral density functions of sum of two sine waves..... | 266 |
| Case study 3 Cross-spectral density function of two sine waves..... | 268 |
| Case study 4 Auto-spectral density function of single random wave..... | 270 |
| Case study 5 Cross-spectral density function of two random waves..... | 272 |
| Conclusions..... | 274 |
| Appendix C Validation of the program to estimate of system parameters for a linear system..... | 278 |
| Method of Estimation..... | 278 |
| Case Studies..... | 280 |
| Case study C-1 System parameters of large-damping system..... | 280 |
| Case study C-2 System parameters of moderate-damping system..... | 283 |
| Case study C-3 System parameters of small-damping system..... | 289 |
| Conclusions..... | 297 |
| Appendix D Validation of the program to estimate of system parameters for a nonlinear system..... | 299 |
| Method of Estimation..... | 299 |
| Case Study..... | 300 |

LIST OF FIGURES

| | | |
|------------|---|----|
| Figure 1-1 | Strouhal number versus Reynolds number for a circular cylinder | 7 |
| Figure 1-2 | Lift coefficient versus Reynolds number for a circular cylinder | 8 |
| Figure 1-3 | Frequency “lock-in” phenomena for an elastically mounted cylinder | 9 |
| Figure 1-4 | General behavior of VIV for an elastically mounted cylinder..... | 10 |
| Figure 1-5 | Two vortex wake patterns (left: 2S mode and right: 2P mode)..... | 11 |
| Figure 1-6 | Current velocity distribution over water depth on three waters..... | 14 |
| Figure 1-7 | Two distorted deep-water riser models due to limited basin depth..... | 19 |
| Figure 1-8 | The investigation overview..... | 23 |
| Figure 2-1 | Sketch of the test apparatus..... | 29 |
| Figure 2-2 | Sketch of model riser..... | 38 |
| Figure 2-3 | The length-distorted model riser and the supporting frame..... | 40 |
| Figure 2-4 | Pretension adjust vertical lever mechanism..... | 41 |
| Figure 2-5 | The shaker and connection rod..... | 42 |
| Figure 2-6 | Calibration of accelerometers..... | 45 |
| Figure 2-7 | Relationship between the total riser accelerations and the accelerations measured by the accelerometers..... | 47 |
| Figure 3-1 | Shaker-excitation test..... | 54 |
| Figure 3-2 | Amplitudes and frequencies for harmonic excitations..... | 56 |
| Figure 3-3 | Amplitudes of harmonic components for random excitation..... | 57 |
| Figure 3-4 | Time series of the random excitation used for the tests..... | 57 |
| Figure 3-5 | The measured shaker force and shaker motion at a pretension of 500N | 66 |
| Figure 3-6 | The estimated auto-spectral density function of the shaker motion at a pretension of 500N..... | 67 |
| Figure 3-7 | The estimated cross-spectral density function of the shaker motion and the shaker force at a pretension of 500N..... | 68 |

| | | |
|--------------------|--|-----------|
| Figure 3-8 | Amplitude of frequency response function of the riser in calm water at a pretension of 500N..... | 69 |
| Figure 3-9 | Vibration shape at an excitation frequency of 0.88Hz..... | 73 |
| Figure 3-10 | Vibration shape at an excitation frequency of 1.48Hz..... | 73 |
| Figure 3-11 | Vibration shape at an excitation frequency of 2.20Hz..... | 74 |
| Figure 3-12 | Vibration shape at an excitation frequency of 3.04Hz..... | 74 |
| Figure 3-13 | Vibration shape at an excitation frequency of 4.00Hz..... | 75 |
| Figure 3-14 | Vibration shape at an excitation frequency of 4.72Hz..... | 75 |
| Figure 3-15 | Vibration shape at an excitation frequency of 5.68Hz..... | 76 |
| Figure 3-16 | Vibration shape at an excitation frequency of 6.16Hz..... | 76 |
| Figure 3-17 | Vibration shape at an excitation frequency of 7.60Hz..... | 77 |
| Figure 3-18 | Vibration shape at an excitation frequency of 8.20Hz..... | 77 |
| Figure 3-19 | Real part of DS estimated from the harmonic excitation tests at a pretension of 500N..... | 80 |
| Figure 3-20 | Real part of DS estimated from the random excitation tests at a pretension of 500N..... | 81 |
| Figure 3-21 | Imaginary part of DS function between the excitation force and the displacement at the middle of the riser..... | 86 |
| Figure 3-22 | Amplitude of frequency response function of the riser in calm water at a pretension of 700N..... | 87 |
| Figure 3-23 | Vibration shape at an excitation frequency of 0.88Hz..... | 88 |
| Figure 3-24 | Vibration shape at an excitation frequency of 1.96Hz..... | 89 |
| Figure 3-25 | Vibration shape at an excitation frequency of 2.80Hz..... | 89 |
| Figure 3-26 | Vibration shape at an excitation frequency of 4.00Hz..... | 90 |
| Figure 3-27 | Vibration shape at an excitation frequency of 4.60Hz..... | 90 |
| Figure 3-28 | Vibration shape at an excitation frequency of 5.44Hz..... | 91 |
| Figure 3-29 | Vibration shape at an excitation frequency of 6.28Hz..... | 91 |

| | | |
|--------------------|---|------------|
| Figure 3-30 | Vibration shape at an excitation frequency of 7.48Hz..... | 92 |
| Figure 3-31 | Vibration shape at an excitation frequency of 8.44Hz..... | 92 |
| Figure 3-32 | Real part of DS function estimated from the harmonic excitations at a pretension of 700N..... | 94 |
| Figure 3-33 | Imaginary part of DS function between the excitation force and the displacement at the middle of the riser..... | 95 |
| Figure 3-34 | The measured shaker force and shaker motion at a pretension of 900N..... | 98 |
| Figure 3-35 | The estimated auto-spectral density function of the shaker motion at a pretension of 900N..... | 98 |
| Figure 3-36 | The estimated cross-spectral density function of the shaker motion and the shaker force at a pretension of 900N..... | 99 |
| Figure 3-37 | Amplitude of frequency response function of the riser in calm water at a pretension of 900N..... | 100 |
| Figure 3-38 | Vibration shape at an excitation frequency of 0.40Hz..... | 101 |
| Figure 3-39 | Vibration shape at an excitation frequency of 2.20Hz..... | 102 |
| Figure 3-40 | Vibration shape at an excitation frequency of 3.16Hz..... | 102 |
| Figure 3-41 | Vibration shape at an excitation frequency of 4.48Hz..... | 103 |
| Figure 3-42 | Vibration shape at an excitation frequency of 5.44Hz..... | 103 |
| Figure 3-43 | Vibration shape at an excitation frequency of 6.88Hz..... | 104 |
| Figure 3-44 | Vibration shape at an excitation frequency of 7.48Hz..... | 104 |
| Figure 3-45 | Vibration shape at an excitation frequency of 8.56Hz..... | 105 |
| Figure 3-46 | Real part of DS function between the excitation force and the displacement at the middle of the riser using the random excitation..... | 106 |
| Figure 3-47 | Real part of DS function between the excitation force and the displacement at the middle of the riser using the random excitation..... | 107 |
| Figure 3-48 | Imaginary part of DS function between the excitation force and the displacement at the middle of the riser..... | 109 |
| Figure 3-49 | Auto-spectral density function of random shaker displacement..... | 112 |

| | |
|--|-----|
| Figure 3-50 Auto-spectral density function of random shaker velocity-squared..... | 113 |
| Figure 3-51 Cross-spectral density function of random shaker displacement and velocity-squared..... | 113 |
| Figure 3-52 Cross-spectral density function of random shaker displacement and force..... | 113 |
| Figure 3-53 Cross-spectral density function of random shaker force and velocity-squared..... | 114 |
| Figure 3-54 Non-linear component versus frequency..... | 114 |
| Figure 3-55 Linear fit for estimation of nonlinear damping..... | 114 |
| Figure 3-56 Tension effects on the frequency response functions..... | 115 |
| Figure 4-1 Current-excitation tests..... | 124 |
| Figure 4-2 Modal natural frequency versus tension..... | 126 |
| Figure 4-3 The relationship between the tension and the current velocity at a pretension of 600N..... | 129 |
| Figure 4-4 The relationship between the modal natural frequency and the current velocity at a pretension of 600N..... | 129 |
| Figure 4-5 The relationship between the modal natural frequency and the current velocity at a pretension of 200N..... | 130 |
| Figure 4-6 The average peak-pick-up amplitude and frequency of in-line and cross-flow VIV at a pretension of 200N..... | 131 |
| Figure 4-7 Power spectrum of cross-flow VIV at the middle of riser at a current velocity of 0.2m/s and a pretension of 200N..... | 137 |
| Figure 4-8 Power spectrum of in-line VIV at the middle of riser at a current velocity of 0.2m/s and a pretension of 200N..... | 137 |
| Figure 4-9 Power spectrum of cross-flow VIV at the middle of riser at a current velocity of 0.8m/s and a pretension of 200N..... | 138 |
| Figure 4-10 Power spectrum of in-line VIV at the middle of riser at a current velocity of 0.8m/s and a pretension of 200N..... | 139 |
| Figure 4-11 Power spectrum of cross-flow VIV at the middle of riser at a current velocity of 1.1m/s and a pretension of 200N..... | 140 |

| | |
|---|------------|
| Figure 4-12 Power spectrum of in-line VIV at the middle of riser at a current velocity of 1.1m/s and a pretension of 200N..... | 140 |
| <u>Figure 4-13</u> Power spectrum of cross-flow VIV at the middle of riser at a current velocity of 1.3m/s and a pretension of 200N..... | 141 |
| Figure 4-14 Power spectrum of in-line VIV at the middle of riser at a current velocity of 1.3m/s and a pretension of 200N..... | 141 |
| Figure 4-15 Power spectrum of cross-flow VIV at the middle of riser at a current velocity of 0.4m/s and a pretension of 200N..... | 143 |
| Figure 4-16 Power spectrum of in-line VIV at the middle of riser at a current velocity of 0.4m/s and a pretension of 200N..... | 143 |
| Figure 4-17 Power spectrum of cross-flow VIV at the middle of riser at a current velocity of 0.6m/s and a pretension of 200N..... | 145 |
| Figure 4-18 Power spectrum of in-line VIV at the middle of riser at a current velocity of 0.6m/s and a pretension of 200N..... | 145 |
| Figure 4-19 Power spectra of in-line VIV at different location on riser at a current velocity of 0.4m/s and a pretension of 200N..... | 147 |
| Figure 4-20 Power spectra of in-line VIV at different location on riser at a current velocity of 0.6m/s and a pretension of 200N..... | 148 |
| Figure 4-21 Power spectra of in-line VIV at different location on riser at a current velocity of 0.9m/s and a pretension of 200N..... | 149 |
| Figure 4-22 Power spectra of in-line VIV at different location on riser at a current velocity of 1.3m/s and a pretension of 200N..... | 150 |
| Figure 4-23 Power spectra of cross-flow VIV at different location on riser at a current velocity of 0.4m/s and a pretension of 200N..... | 152 |
| Figure 4-24 Power spectra of cross-flow VIV at different location on riser at a current velocity of 0.9m/s and a pretension of 200N..... | 153 |
| Figure 4-25 Power spectra of cross-flow VIV at different location on riser at a current velocity of 1.3m/s and a pretension of 200N..... | 154 |
| Figure 4-26 Power spectra of cross-flow VIV at different location on riser at a current velocity of 1.5m/s and a pretension of 200N..... | 155 |
| Figure 4-27 The modal component distribution of the in-line and cross-flow VIV responses at a pretension of 200N..... | 159 |

| | |
|---|-----|
| Figure 4-28 The component of mode 1 in VIV responses at a pretension of 200N..... | 160 |
| Figure 4-29 The component of mode 2 in VIV responses at a pretension of 200N..... | 161 |
| Figure 4-30 The component of mode 3 in VIV responses at a pretension of 200N..... | 162 |
| Figure 4-31 The component of mode 4 in VIV responses at a pretension of 200N..... | 163 |
| Figure 4-32 The component of mode 5 in VIV responses at a pretension of 200N..... | 164 |
| Figure 4-33 The component of mode 6 in VIV responses at a pretension of 200N..... | 164 |
| Figure 4-34 The component of mode 7 in VIV responses at a pretension of 200N..... | 164 |
| Figure 4-35 The component of mode 8 in VIV responses at a pretension of 200N..... | 165 |
| Figure 4-36 The component of mode 9 in VIV responses at a pretension of 200N..... | 165 |
| Figure 4-37 Time history of cross-flow VIV at a current velocity of 0.4m/s and a pretension of 200N..... | 167 |
| Figure 4-38 Time history of cross-flow VIV at a current velocity of 0.6m/s and a pretension of 200N..... | 167 |
| Figure 4-39 Time history of cross-flow VIV at a current velocity of 0.8m/s and a pretension of 200N..... | 168 |
| Figure 4-40 Time history of cross-flow VIV at a current velocity of 1.3m/s and a pretension of 200N..... | 168 |
| Figure 4-41 Time history of cross-flow VIV at a current velocity of 1.5m/s and a pretension of 200N..... | 168 |
| Figure 4-42 Time history of in-line VIV at a current velocity of 0.4m/s and a pretension of 200N..... | 170 |
| Figure 4-43 Time history of in-line VIV at a current velocity of 0.6m/s and a pretension of 200N..... | 170 |
| Figure 4-44 Time history of in-line VIV at a current velocity of 0.8m/s | |

| | |
|--|------------|
| and a pretension of 200N..... | 170 |
| Figure 4-45 Time history of in-line VIV at a current velocity of 1.3m/s and a pretension of 200N..... | 171 |
| Figure 4-46 Time history of in-line VIV at a current velocity of 1.5m/s and a pretension of 200N..... | 171 |
| Figure 4-47 Time history of cross-flow VIV at different locations at a current velocity of 0.4m/s and a pretension of 200N..... | 173 |
| Figure 4-48 Time history of in-line VIV at different locations at a current velocity of 0.4m/s and a pretension of 200N..... | 174 |
| Figure 4-49 Time history of cross-flow VIV at different locations at a current velocity of 1.5m/s and a pretension of 200N..... | 175 |
| Figure 4-50 Time history of in-line VIV at different locations at a current velocity of 1.3m/s and a pretension of 200N..... | 176 |
| Figure 4-51 Vibration shapes at a current velocity of 0.4m/s and a pretension of 200N..... | 178 |
| Figure 4-52 Vibration shapes at a current velocity of 0.6m/s and a pretension of 200N..... | 179 |
| Figure 4-53 Vibration shapes at a current velocity of 0.8m/s and a pretension of 200N..... | 179 |
| Figure 4-54 Vibration shapes at a current velocity of 1.3m/s and a pretension of 200N..... | 179 |
| Figure 4-55 Vibration shapes at a current velocity of 1.5m/s and a pretension of 200N..... | 180 |
| Figure 4-56 Trajectory of VIV at a current velocity of 0.4m/s and a pretension of 200N..... | 182 |
| Figure 4-57 Trajectory of VIV at a current velocity of 0.6m/s and a pretension of 200N..... | 183 |
| Figure 4-58 Trajectory of VIV at a current velocity of 1.00m/s and a pretension of 200N..... | 183 |
| Figure 4-59 Trajectory of VIV at a current velocity of 1.20m/s and a pretension of 200N..... | 184 |
| Figure 4-60 Trajectory of VIV at a current velocity of 1.50m/s and a pretension of 200N..... | 184 |

| | | |
|--------------------|--|------------|
| Figure 4-61 | The average peak-pick-up amplitude and frequency of in-line and cross-flow VIV at a pretension of 600N..... | 186 |
| Figure 4-62 | Power spectrum of cross-flow VIV at the middle of riser at a current velocity of 0.2m/s and a pretension of 600N..... | 190 |
| Figure 4-63 | Power spectrum of in-line VIV at the middle of riser at a current velocity of 0.2m/s and a pretension of 600N..... | 190 |
| Figure 4-64 | Power spectrum of cross-flow VIV at the middle of riser at a current velocity of 0.4m/s and a pretension of 600N..... | 191 |
| Figure 4-65 | Power spectrum of in-line VIV at the middle of riser at a current velocity of 0.4m/s and a pretension of 600N..... | 192 |
| Figure 4-66 | Power spectrum of cross-flow VIV at the middle of riser at a current velocity of 0.6m/s and a pretension of 600N..... | 193 |
| Figure 4-67 | Power spectrum of in-line VIV at the middle of riser at a current velocity of 0.6m/s and a pretension of 600N..... | 193 |
| Figure 4-68 | Power spectrum of cross-flow VIV at the middle of riser at a current velocity of 0.8m/s and a pretension of 600N..... | 194 |
| Figure 4-69 | Power spectrum of in-line VIV at the middle of riser at a current velocity of 0.8m/s and a pretension of 600N..... | 195 |
| Figure 4-70 | Power spectrum of cross-flow VIV at the middle of riser at a current velocity of 1.2m/s and a pretension of 600N..... | 196 |
| Figure 4-71 | Power spectrum of in-line VIV at the middle of riser at a current velocity of 1.2m/s and a pretension of 600N..... | 196 |
| Figure 4-72 | Power spectrum of cross-flow VIV at the middle of riser at a current velocity of 1.5m/s and a pretension of 600N..... | 197 |
| Figure 4-73 | Power spectrum of in-line VIV at the middle of riser at a current velocity of 1.5m/s and a pretension of 600N..... | 198 |
| Figure 4-74 | Power spectra of in-line VIV at different location on riser at a current velocity of 0.4m/s and a pretension of 600N..... | 200 |
| Figure 4-75 | Power spectra of in-line VIV at different location on riser at a current velocity of 0.8m/s and a pretension of 600N..... | 201 |
| Figure 4-76 | Power spectra of in-line VIV at different location on riser at a current velocity of 1.5m/s and a pretension of 600N..... | 202 |

| | | |
|--------------------|---|------------|
| Figure 4-77 | Power spectra of cross-flow VIV at different location on riser at a current velocity of 0.4m/s and a pretension of 600N..... | 204 |
| Figure 4-78 | Power spectra of cross-flow VIV at different location on riser at a current velocity of 0.8m/s and a pretension of 600N..... | 205 |
| Figure 4-79 | Power spectra of cross-flow VIV at different location on riser at a current velocity of 1.5m/s and a pretension of 600N..... | 206 |
| Figure 4-80 | Modal component distributions of the in-line VIV and cross-flow VIV at a pretension of 600N..... | 209 |
| Figure 4-81 | The component of mode 1 in VIV responses at a pretension of 600N..... | 212 |
| Figure 4-82 | The component of mode 2 in VIV responses at a pretension of 600N..... | 212 |
| Figure 4-83 | The component of mode 3 in VIV responses at a pretension of 600N..... | 212 |
| Figure 4-84 | The component of mode 4 in VIV responses at a pretension of 600N..... | 213 |
| Figure 4-85 | The component of mode 5 in VIV responses at a pretension of 600N..... | 213 |
| Figure 4-86 | The component of mode 6 in VIV responses at a pretension of 600N..... | 213 |
| Figure 4-87 | The component of mode 7 in VIV responses at a pretension of 600N..... | 214 |
| Figure 4-88 | The component of mode 8 in VIV responses at a pretension of 600N..... | 214 |
| Figure 4-89 | The component of mode 9 in VIV responses at a pretension of 600N..... | 214 |
| Figure 4-90 | Time history of in-line VIV at a current velocity of 0.4m/s and a pretension of 600N..... | 216 |
| Figure 4-91 | Time history of in-line VIV at a current velocity of 0.6m/s and a pretension of 600N..... | 216 |
| Figure 4-92 | Time history of in-line VIV at a current velocity of 0.8m/s and a pretension of 600N..... | 216 |
| Figure 4-93 | Time history of in-line VIV at a current velocity of 1.2m/s | |

| | | |
|---------------------|--|------------|
| | and a pretension of 600N..... | 217 |
| Figure 4-94 | Time history of in-line VIV at a current velocity of 1.5m/s and a pretension of 600N..... | 217 |
| Figure 4-95 | Time history of cross-flow VIV at a current velocity of 0.6m/s and a pretension of 600N..... | 217 |
| Figure 4-96 | Time history of cross-flow VIV at a current velocity of 0.8m/s and a pretension of 600N..... | 218 |
| Figure 4-97 | Time history of cross-flow VIV at a current velocity of 1.2m/s and a pretension of 600N..... | 218 |
| Figure 4-98 | Time history of cross-flow VIV at a current velocity of 1.5m/s and a pretension of 600N..... | 219 |
| Figure 4-99 | Time history of in-line VIV at different locations at a current velocity of 0.4m/s and a pretension of 600N..... | 220 |
| Figure 4-100 | Time history of in-line VIV at different locations at a current velocity of 1.2m/s and a pretension of 600N..... | 221 |
| Figure 4-101 | Time history of cross-flow VIV at different locations at a current velocity of 0.4m/s and a pretension of 600N..... | 222 |
| Figure 4-102 | Time history of cross-flow VIV at different locations at a current velocity of 1.2m/s and a pretension of 600N..... | 223 |
| Figure 4-103 | Vibration shapes at a current velocity of 0.2m/s and a pretension of 600N..... | 225 |
| Figure 4-104 | Vibration shapes at a current velocity of 0.6m/s and a pretension of 600N..... | 226 |
| Figure 4-105 | Vibration shapes at a current velocity of 0.8m/s and a pretension of 600N..... | 226 |
| Figure 4-106 | Vibration shapes at a current velocity of 1.0m/s and a pretension of 600N..... | 226 |
| Figure 4-107 | Vibration shapes at a current velocity of 1.2m/s and a pretension of 600N..... | 227 |
| Figure 4-108 | Trajectory of VIV at a current velocity of 0.4m/s and a pretension of 600N..... | 229 |
| Figure 4-109 | Trajectory of VIV at a current velocity of 0.6m/s | |

| | |
|---|------------|
| and a pretension of 600N..... | 229 |
| Figure 4-110 Trajectory of VIV at a current velocity of 0.8m/s and a pretension of 600N..... | 230 |
| Figure 4-111 Trajectory of VIV at a current velocity of 1.2m/s and a pretension of 600N..... | 230 |
| Figure 4-112 Trajectory of VIV at a current velocity of 1.5m/s and a pretension of 600N..... | 231 |
| Figure A-1 Forces acting on a differential riser element..... | 253 |
| Figure A-2 Pressure integration variables..... | 255 |
| Figure B-1 Estimated auto-spectral density function of a single sine wave using Parzen window function..... | 264 |
| Figure B-2 Estimated auto-spectral density functions using different window functions..... | 265 |
| Figure B-3 Estimated auto-spectral density function of the sum of two sine waves with far frequencies..... | 267 |
| Figure B-4 Estimated auto-spectral density functions of sum of two sine waves with close frequencies..... | 268 |
| Figure B-5 Estimated cross-spectral density functions of the sum of two sine waves..... | 269 |
| Figure B-6 Estimated cross-spectral density function for the sum of two sine waves using different window functions..... | 270 |
| Figure B-7 A random wave generated by Matlab using a seed of 123..... | 271 |
| Figure B-8 Estimated auto-spectral density function of random wave | 272 |
| Figure B-9 Another random wave generated by an assumed mass-damping-spring system..... | 273 |
| Figure B-10 Estimated cross-spectral density function of two random waves..... | 274 |
| Figure C-1 The actual and estimated FRF amplitude for a large-damping s..... | 282 |
| Figure C-2 Linear fit for mass and stiffness for a large-damping system..... | 282 |

| | | |
|--------------------|--|------------|
| Figure C-3 | Imaginary part of dynamic stiffness function for a large-damping system..... | 283 |
| Figure C-4 | The actual and estimated FRFs for a moderate-damping system..... | 284 |
| Figure C-5 | Linear fit for mass and stiffness for a moderate-damping system..... | 285 |
| Figure C-6 | Imaginary part of dynamic stiffness function for a moderate-damping system..... | 285 |
| Figure C-7 | The actual and estimated FRFs for a moderate-damping system..... | 286 |
| Figure C-8 | Linear fit for mass and stiffness for a moderate-damping system..... | 286 |
| Figure C-9 | Imaginary part of dynamic stiffness function for a moderate-damping syste..... | 287 |
| Figure C-10 | The actual and estimated FRFs for a moderate-damping system..... | 288 |
| Figure C-11 | Linear fit for mass and stiffness for a moderate-damping system..... | 288 |
| Figure C-12 | Imaginary part of dynamic stiffness function for a moderate-damping system..... | 289 |
| Figure C-13 | The actual and estimated FRFs for a small-damping system..... | 290 |
| Figure C-14 | Linear fit for mass and stiffness for a small-damping system..... | 290 |
| Figure C-15 | Imaginary part of dynamic stiffness function for small-damping system..... | 291 |
| Figure C-16 | The actual and estimated FRFs for a small-damping system..... | 292 |
| Figure C-17 | Linear fit for mass and stiffness for a small-damping system..... | 292 |
| Figure C-18 | Imaginary part of dynamic stiffness function for a small-damping system..... | 293 |
| Figure C-19 | The actual and estimated FRFs for a small-damping system..... | 294 |
| Figure C-20 | Linear fit for mass and stiffness for a small-damping system..... | 294 |
| Figure C-21 | Imaginary part of dynamic stiffness function for a small-damping system..... | 295 |

| | | |
|-------------|---|-----|
| Figure C-22 | The actual and estimated FRFs for a small-damping system..... | 296 |
| Figure C-23 | Linear fit for mass and stiffness for a small-damping system..... | 296 |
| Figure C-24 | Imaginary part of dynamic stiffness function for a small-damping system..... | 297 |
| Figure D-1 | The linear input generated by equation (D-9)..... | 302 |
| Figure D-2 | The nonlinear input generated by equation (D-9)..... | 302 |
| Figure D-3 | The output generated by equation (D-11)..... | 303 |
| Figure D-4 | The auto-spectral density function $S_{xx}(\omega)$ of linear input $x(t)$ | 304 |
| Figure D-5 | The auto-spectral density function $S_{qq}(\omega)$ of nonlinear input $q(t)$ | 304 |
| Figure D-6 | The cross-spectral density function $S_{xq}(\omega)$ of linear input $x(t)$ and nonlinear input $q(t)$ | 305 |
| Figure D-7 | The cross-spectral density function $S_{xp}(\omega)$ of linear input $x(t)$ and output $p(t)$ | 305 |
| Figure D-8 | The cross-spectral density function $S_{qp}(\omega)$ of nonlinear input $q(t)$ and output $p(t)$ | 306 |
| Figure D-9 | Linear fit for mass and linear stiffness..... | 306 |
| Figure D-10 | Linear fit for mass and linear stiffness..... | 307 |
| Figure D-11 | Linear fit for nonlinear stiffness..... | 307 |

LIST OF TABLES

| | | |
|-------------------|--|------------|
| Table 1-1 | Wake pattern versus Reynolds number for a fixed cylinder | 6 |
| Table 2-1 | Prototype riser properties..... | 34 |
| Table 2-2 | Model riser properties..... | 39 |
| Table 2-3 | Accelerometer pair locations on the model riser..... | 43 |
| Table 2-4 | Calibration factors of accelerometer..... | 46 |
| Table 2-5 | Orientation angles of accelerometer..... | 46 |
| Table 2-6 | Comparison of the results measured from two independent measurement systems..... | 50 |
| Table 3-1 | Modal parameters estimated from the harmonic and random excitation tests at a pretension of 500N..... | 82 |
| Table 3-2 | Added mass coefficients estimated from the harmonic and random excitation tests..... | 83 |
| Table 3-3 | Modal damping estimated from the harmonic and random excitation tests(N.s/m)..... | 86 |
| Table 3-4 | Damping coefficients estimated from the harmonic and random excitation tests..... | 86 |
| Table 3-5 | Modal parameters estimated from the harmonic and random excitation tests at a pretension of 700N..... | 94 |
| Table 3-6 | Added mass coefficients estimated from the harmonic excitation tests at a pretension of 700N..... | 95 |
| Table 3-7 | Modal damping estimated from the harmonic and random excitation tests(N.s/m)..... | 96 |
| Table 3-8 | Damping coefficients estimated from the harmonic and random excitation tests(N.s/m)..... | 96 |
| Table 3-9 | Modal parameters estimated from the harmonic and random excitation tests at a pretension of 900N..... | 107 |
| Table 3-10 | Added mass coefficients estimated from the harmonic and random excitation tests..... | 108 |

Table 3-11 Modal damping estimated from the harmonic and random excitation tests(N.s/m).....109

Table 3-12 Damping coefficients estimated from the harmonic and random excitation tests.....109

Table 3-13 Summary of the modal stiffness (N/m).....116

Table 3-14 Summary of the modal mass (kg).....116

Table 3-15 Summary of added mass coefficients.....117

Table 3-16 Summary of the modal natural frequency (Hz).....118

Table 3-17 Modal natural frequency (Hz) estimated from equation (3-8).....118

Table 3-18 Modal natural frequency (Hz) estimated from Vandiver’s equation.....118

Table 3-19 Summary of the modal damping (N.s/m).....119

Table 3-20 Summary of damping coefficients.....119

Table B-1.....275

Table C-1 The comparison of the actual and estimated values.....297

CHAPTER 1

INTRODUCTION

1. Introduction

The development of the offshore oil industry commenced with the use of fixed structures. In 1887, the first offshore structure appeared off the California coast, which was a wooden wharf used to aid in oil drilling (Wilson, 1984). The offshore operations then made a gradual move from the swamps and marsh lands of Louisiana into the Gulf of Mexico in the United States (Patel and Witz, 1991), and the first oil platform was built in Louisiana in 1947 (Chakrabarti, 1987). The water depth capability of drilling equipment was gradually increased by the use of jack up rigs, which can operate in severe weather at water depth of up to 107m (Morgan, 1990). For water depths of more than 800m, fixed structures lose their technological and economic advantages and a floating facility may be the only technological and economic alternative (Olson, 1985).

For a floating platform, the maximum drilling water depth is usually governed by three factors: i) its mooring system; ii) the amount of drill pipe and riser pipe that it can carry

and iii) heave compensator limits imposed by the vessel's motion responses. A catenary line mooring system is impractical above water depths of about 457m. For deeper waters, a dynamically positioned platform may be required (Wilson, 1984). The maximum water depth to which a dynamically positioned platform can work is theoretically unlimited, but in practice there are two limitations: i) the length of the marine riser and ii) tensioner and heave compensator performance.

Presently, offshore energy exploration has been moving into ever increasing water depths. Some studies have considered water depths approaching more than 3,000m (e.g. Ward *et al.* 1999). In fact, deepwater offshore activity commands a growing share of the global offshore exploration and development industry, with work in the deep-water zones of 56 countries, adjacent to every continent. The principal deep-water areas worldwide include: a) Brazil, b) US Gulf of Mexico, c) West of Shetland, d) Northern Norway, e) West Africa, f) Asia-Pacific and g) Australia's Northwest.

1.1 Marine Risers

For floating offshore drilling structures, the riser system is a crucial element. Marine risers are used to transport oil, gas, water and mud from producing field to a surface platform and back down for export through a subsea pipeline or a tanker loading system. Some risers may also be used to re-inject water or gas into the field. In terms of function, marine risers can be classified into three types of drilling riser, production riser and export riser (Olson, 1985).

a) **Drilling riser:** The drilling riser usually has a diameter of about 20 inches, which is used only on a temporary basis for well drilling. A drilling riser is often used: i) to protect

the drilling pipe from environmental loads, such as wave and current loads; ii) to provide a return path for drilling mud and cuttings; iii) to give a path to the well bore for control of formation pressure and iv) to support the control lines to the blow out preventer.

b) **Production riser:** The production riser usually has a diameter of from 4 to 10 inches, which is used to transport the gas, oil or water produced by the wells to the surface vessel for processing. Production risers are usually designed as a structure with a long lifetime experiencing higher pressures.

c) **Export riser:** The export riser usually has a diameter of from 6 to 15 inches, which is used to ship the produced oil and gas to market, or re-inject produced water and gas back into the formation. Export risers are also designed as a structure with long lifetime experiencing fairly high pressures.

Usually, for a fixed platform, marine risers can be clamped at intervals to structural members of the platform along their vertical run up to the surface, while for a floating platform, marine risers can be freely strung from the surface platform to seabed with a sufficiently high tension at their top to prevent buckling resulting from their self weight. As these marine risers are connected vertically from the surface platform to seabed, they are called vertical risers (Morgan, 1990). A rigid steel marine riser can be used for a vertical riser. In recent years, the pipes of composite steel and elastomer construction have been used as marine risers. These risers are strung in non-vertical catenary shapes from surface platform to seabed and they are, therefore, called flexible risers (Morgan, 1990). In deep or ultra-deep waters, it is popular to use the flexible risers. Serta *et al.* (2001) reviewed two types of the most often used flexible riser systems for deep and ultra-deep waters. The first is the catenary riser system. The riser in a catenary riser

system is directly connected to the seabed with a riser anchor and there is, therefore, a “touch-down” between the riser and seabed near the lower end of the riser. The “touch-down” often complicates the structural performance of the riser. Another is the so-called hybrid riser system. The hybrid riser system can avoid the “touch-down” from the riser, as the riser in a hybrid riser system is connected to seabed through a structure standing on seabed. This structure may be a riser tower or a subsurface buoy. Also, some special devices may be attached to risers. For example, the distributed buoyancy may be mounted on the riser to withstand the over-weight of the riser, which often appears for a deepwater riser due to its long structure. Another device may be the “helical strakes”, which are employed to suppress the responses of vortex-induced vibrations (VIV) for a riser (Williamson and Govardhan, 2004).

1.2 Single-Modal Vortex-Induced Vibrations

The dynamic responses of risers to environmental loads are major concerns in deep-water riser development. These responses mainly include deformations, tension forces and vortex-induced vibrations, and directly dominate some dangerous riser behaviors, such as stress damage, fatigue damage and clashing between two risers.

One of the causes of fatigue damage is vortex-induced vibrations. The vortex-induced vibrations result from the vortex shedding from the surface of the risers due to a flow past the structure. When a flow with enough high velocity passes a cylinder, vortices will be generated at the boundaries and transported in the fluid, and a vortex wake is formed behind the cylinder. The wake is defined as a low-pressure region near the boundary of a submerged body (Chakrabarti, 2002). The vortices in the wake will finally separate from

the surface of the cylinder, and this separation process is referred to as vortex-shedding. The vortex formation–shedding process behind the cylinder causes a varying hydrodynamic force on the cylinder in the flow direction (in-line direction). As the vortex formation and shedding behind a cylinder do not occur at the same time and the vortex-shedding are not symmetric with respect to the direction of flow, this leads to an alternating hydrodynamic force transverse to the flow (cross-flow direction) acting on the cylinder. The varying in-line and cross-flow hydrodynamic forces are referred to as vortex-shedding forces.

The vortex formation and shedding behind a cylinder is a most complicated problem in fluid dynamics. This process is influenced by many factors. For a fixed rigid cylinder, the Reynolds number, defined as $R_e=UD/\nu$, where: ν is the kinematic viscosity of water, D is the riser diameter and U is the current velocity, is a major factor affecting the vortex formation-shedding process. Table 1-1 summarizes the major regimes of vortex shedding across a fixed cylinder versus the Reynolds number (Morgan, 1990).

Another parameter affecting the vortex shedding is the roughness on the surface of the cylinder. The flow on a rough surface separates from the surface earlier than the flow around a smooth surface, namely the vortices and turbulence behind a cylinder with rough surface appear at a lower current velocity than behind a cylinder with smooth surface.

For a fixed cylinder, the frequency of vortex shedding force is a function of flow velocity, cylinder diameter and the Strouhal number S_t , namely $f_v=S_tU/D$. This frequency is referred to as the Strouhal frequency. The amplitude of vortex-shedding force in the cross-flow direction can be represented by a lift force coefficient C_L , namely

$$F_L = \frac{1}{2} \rho C_L D U^2$$

where: ρ is the water density.

Table 1-1 Wake pattern versus Reynolds number for a fixed cylinder

| Reynolds number | Wake pattern |
|--|---|
| $Re < 5$ | Regime of un-separated flow |
| $5 < Re < 40$ | A fixed pair of vortices in wake |
| $40 < Re < 150$ | Laminar vortex street |
| $150 < Re < 300$ | Transition range to turbulent vortex |
| $300 < Re < 3 \times 10^5$ | Fully turbulent vortex |
| $3 \times 10^5 < Re < 3.5 \times 10^6$ | Wake is narrower and disorganized |
| $3.5 \times 10^6 < Re$ | Re-establishment of turbulent vortex street |

Both the Strouhal number and lift force coefficient are a function of the Reynolds number. Figure 1-1 gives a general picture of the Strouhal number versus Reynolds number for a stationary circular cylinder. As seen in Figure 1-1, the Strouhal number is approximately a constant of 0.18 over a wide range of Re varying from 2×10^2 to 2×10^5 for a rigid cylinder. In the region of Re ranging from 3×10^5 to 3.5×10^6 , which is called the critical region where laminar boundary layer undergoes turbulent transition, the Strouhal number demonstrates a big scatter varying from 0.16 to 0.42.

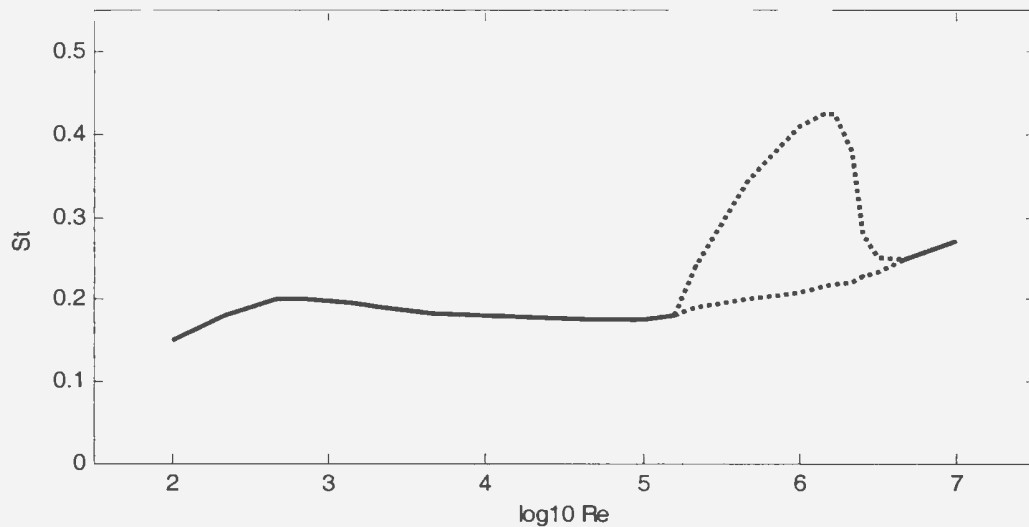


Figure 1-1 Strouhal number versus Reynolds number for a stationary rigid circular cylinder

The lift force coefficients have been measured by numerous experiments from circular cylinders transverse to steady flow. Figure 1-2 gives the general behavior of the lift force coefficients versus Reynolds number for a smooth elastically-mounted rigid cylinder under 2D flow conditions. The low and high curves in Figure 1-2 cover all the values from different experiments. Obviously, the measured lift force coefficients have a considerable scatter, and most of this scatter may be attributed to the free stream turbulence in the flow, flow over the ends of the cylinder, lack of rigidity in the mounting system and other physical sources (Chakrabarti, 2002). The highest values appear in the Reynolds number range of 2×10^4 to 8×10^4 .

For an elastically mounted rigid cylinder, the vortex-shedding forces will result in cylinder vibrations in both the in-line and cross-flow directions. The cross-flow VIV frequencies of an elastically mounted cylinder also follow the Strouhal frequencies except in the frequency region close to the natural frequency of the cylinder. In the frequency region close to the natural frequency, a frequency “lock-in” may occur. The

frequency “lock-in” is a phenomenon that the VIV response frequencies almost remain a constant, which is usually equal to or close to the natural frequency of the cylinder, so that the linear relation between the response frequency and the flow velocity is violated. Figure 1-3 shows the typical experimental results for an elastically mounted cylinder (Khalak and Williamson, 1997 & 1999). In this figure, U^* is the reduced velocity, defined as $U^* = U/f_n D$, where: U is the current velocity, f_n is the natural frequency of the cylinder, and D is the diameter of the riser; and f^* is the frequency ratio, defined as $f^* = f/f_n$, where: f is the vibration frequency. As seen in Figure 1-3, the frequency “lock-in” ranges over a region from $U^* \approx 3$ to 13.

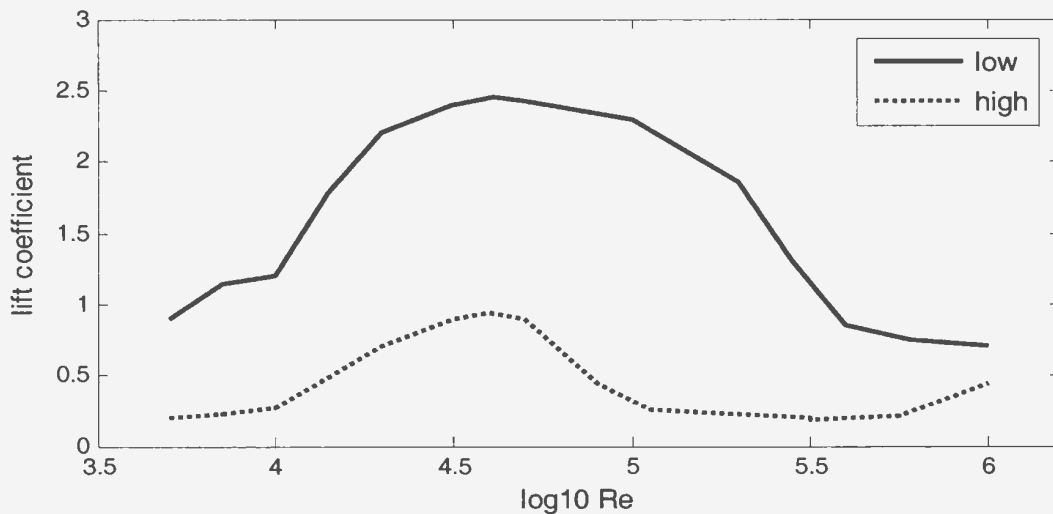


Figure 1-2 Lift coefficient versus Reynolds number for a stationary rigid circular cylinder under 2D flow conditions

The mass ratio m^* , defined as $m^* = 4m/\pi\rho D^2$, where: m is the mass per unit length of the riser and ρ is the water density, is an important parameter affecting the “lock-in” behavior. A cylinder with small mass ratio will experience a wider reduced velocity region of “lock-in” than a cylinder with large mass ratio. There is a “critical mass” of

$m^* = 0.54 \pm 0.02$, and the width of reduced velocity region of “lock-in” will become infinite as the mass ratio becomes equal to or less than this “critical mass” (Williamson and Govardhan, 2004). The previous experiments showed that the cylinders with very small mass ratios have a “lock-in” frequency equal to its natural frequency, while the cylinders with relatively big mass ratios have a “lock-in” frequency slightly larger than its natural frequency.

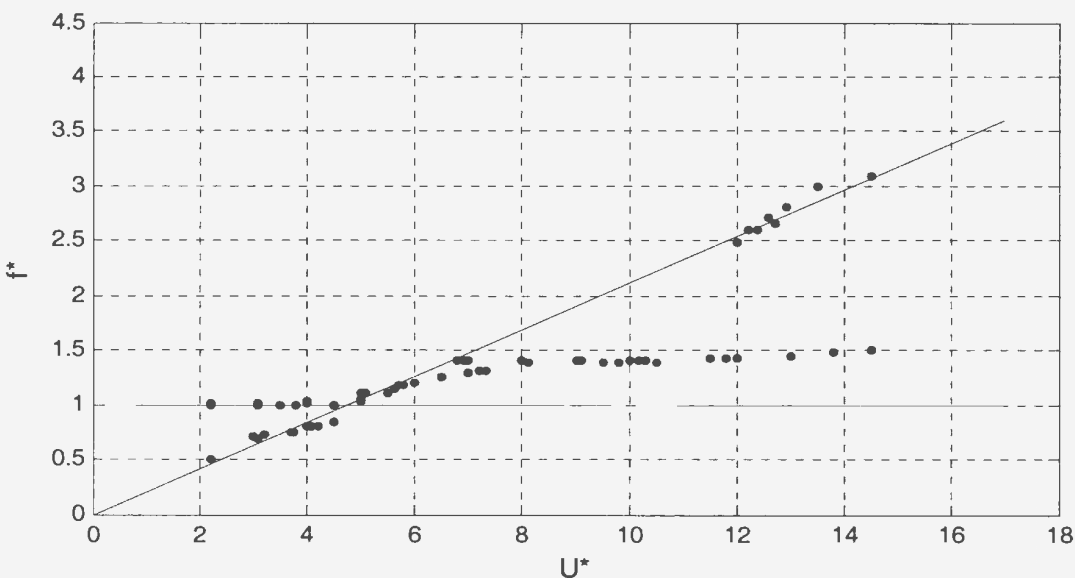


Figure 1-3 Frequency “lock-in” phenomena for an elastically mounted cylinder under 2D flow conditions

Figure 1-4 shows the general behavior of the cross-flow VIV response amplitudes of an elastically mounted cylinder for two different mass-ratios. A^* is the amplitude ratio, defined as $A^* = z_0/D$, where: z_0 is the vibration amplitude. As seen in Figure 1-4, three different regions can be found. The first covers the relatively low current velocities, which is called the initial excitation region. At the higher current velocity boundary of the initial excitation region, a “jump” of vibration amplitude occurs, and then the vibration

responses come to the second region, which is called the upper branch region. In the upper branch region the cylinder vibrations reach to a maximum. As the current velocity increases further, the response amplitude decreases, and the cylinder vibrations come to the third region, which is called the lower branch region. It is noted that increased mass ratio results in shrunk size of upper branch region. The upper branch region may completely disappear if the mass ratio becomes big enough.

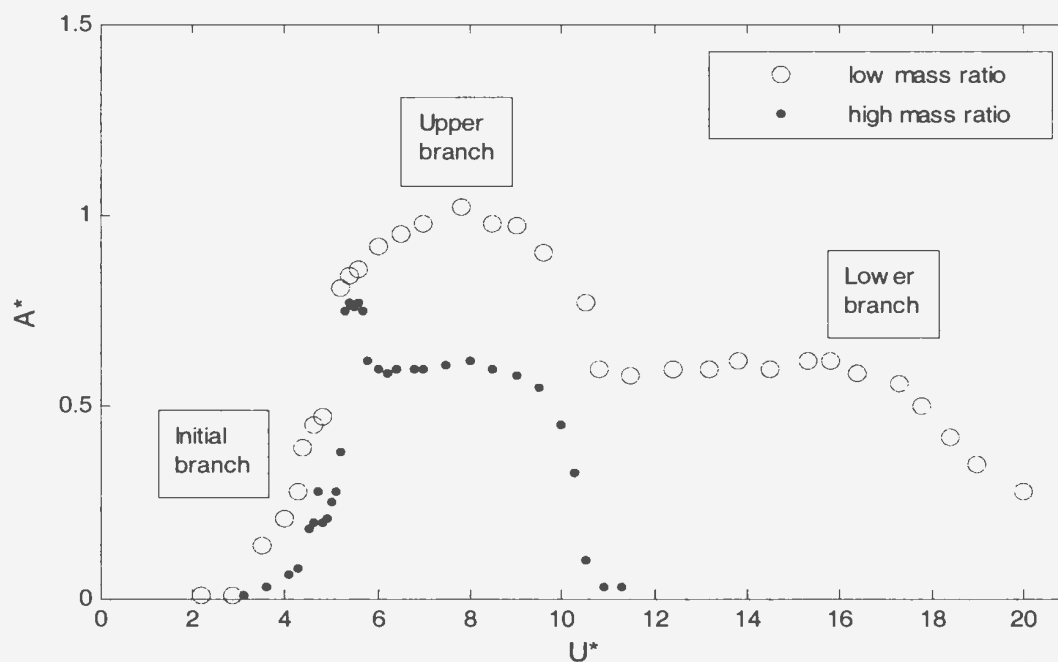


Figure 1-4 General behavior of VIV for an elastically mounted cylinder under 2D flow conditions

In recent years, the highly effective Particle-Image Velocimetry (PIV) technique has been employed to observe the vortex wake modes behind freely vibrating or forced oscillating cylinders, and it is found that the different characteristics of cylinder vibration responses in the three regions result from different vortex wake modes. These observations showed that the vortex wake pattern behind a freely vibrating or a forced oscillating cylinder may comprise single vortices (S) and vortex pairs (P), giving patterns

such as the 2S, 2P, P+S and 2P+2S modes (Williamson and Govardhan, 2004). The 2S mode means two single vortices exist per half cycle, the 2P mode means two vortex pairs exist per half cycle, and so on. Figure 1-5 presents two vortex wake patterns of 2S and 2P modes. The previous experiments showed that a freely vibrating cylinder only encounters the 2S and 2P modes. The 2S mode always appears in the initial branch region, while the 2P mode always appears in the upper branch region and the lower branch regions, but in the upper branch region the second vortex of each pair is much weaker than the first one (Govardhan and Williamson, 2000). For a forced oscillating cylinder, more complicated modes may appear. At a low current velocity, a P+S mode may be caused by the cylinder, while at a high current velocity a 2P+2S mode may be found behind the cylinder.



Figure 1-5 Two vortex wake patterns (left: 2S mode and right: 2P mode)

Most of previous work was dedicated to the investigation of cross-flow vibrations for a cylinder which was not allowed to vibrate in the in-line direction, but in the last decade some effort was devoted to the coupled vibrations in the cross-flow and in-line directions. These studies demonstrated a broad region of “lock-in” in the in-line VIV, but no new response branches were found. An interesting finding is that the in-line vibrations have little effect on the transverse responses and the vortex wake dynamics (Jauvtis and Williamson, 2003).

The VIV behavior for a long and rigid cylinder may have significant differences from those for a short and rigid cylinder. It is well known that for a long and rigid cylinder, vortex shedding in the turbulent wake regime ($Re > 200$) occurs in cells along the cylinder length (Sumer and Fredsoe, 1997), and this means that the vortex shedding characteristics behind a long and rigid cylinder may have significant variations over its length. The average length of these cells may be termed the correlation length, and the correlation between the VIV responses on different cells may be measured by the correlation coefficient. For a long cylinder, the correlation length is usually not equal to the cylinder length while the correlation coefficient is usually not equal to 1. Another cause of the vortex shedding variation in span is the flexibility of the cylinder. A flexible cylinder often has vibrations that vary over its length, and this will lead to the vortex shedding variation over span. Presently, the VIV behavior for a long and flexible cylinder is still not fully understood due to insufficient effort devoted into research in this area.

1.3 Currents in Deep Waters

A deep-water riser will face more technological challenges than a shallow-water riser. The first challenge is the complex environment for deep-water risers. In addition to waves, currents become a significant factor causing VIV responses in deep waters. The flow of water in the ocean is very complicated and is often highly variable both in time and space. Surface currents, deep-ocean currents and tidal currents are three major types of currents in the ocean. Surface currents are created by the winds. The patterns of surface currents are similar in all of the major ocean basins, and the velocities depend on the patterns of surface winds, the influences of the land masses and the Coriolis effect of

the earth's rotation. The maximum surface current speed can reach up to 1.4m/s (Clayton and Bishop, 1982). Deep-ocean currents are driven by temperature and density differences between waters at different latitudes. The horizontal currents in the deep ocean are driven by large scale sinking of dense water masses formed primarily in high latitudes and flow with a relatively small speed of 1-2cm/s (Morgan, 1990) along the continental shelf, down the continental slope and on to the bottom of the ocean basins. Tidal currents are caused by the gravitational forces of the sun and the moon. The normal tidal movement is usually between 0.5 and 2m/s (Morgan, 1990), but local geographical features can often produce larger variations. For example, the tidal currents in the Bristol Channel in the UK are up to 15m/s, and in the Bay of Fundy in Canada are up to 21m/s. In contrast, almost land locked seas, such as the Mediterranean, have little or no tidal movement.

Figure 1-6 presents three examples of current profile in three waters. The first is the current profile in the deepwater Gulf of Mexico (DiMarco *et al.* 2001). The currents decrease rapidly with depth from 1.8m/s near the surface to 0.6m/s at the depth of 1,000m and then again increase to another peak (1.3m/s) at the depth of 2,000m. After this peak the currents again decline rapidly to 0.3m/s at the depth of 2,500m, and then this speed remains relatively steady from this depth to the seabed of 3,500m. The second example is the current profile in the Faroes Gap (Robinson, 2002). In the Faroes Gap, the water depth approaches 1,000m. The maximum current speed of 1.5m/s appears near the surface, and the currents then decrease with depth to 0.4m/s at the half water depth. At depths larger than the half water depth, the currents remain relatively steady at values of about 0.4m/s. The third example is the current profile in the West of Africa (Robinson,

2002). In offshore Angola (West of Africa), the water depths approach 1,500 to 2,500m. The currents in this water also have the features similar to those in the Faroes Gap, but the largest current speed is 1.0m/s, and the current speed has declined to 0.4m/s at one-tenth of water depth.

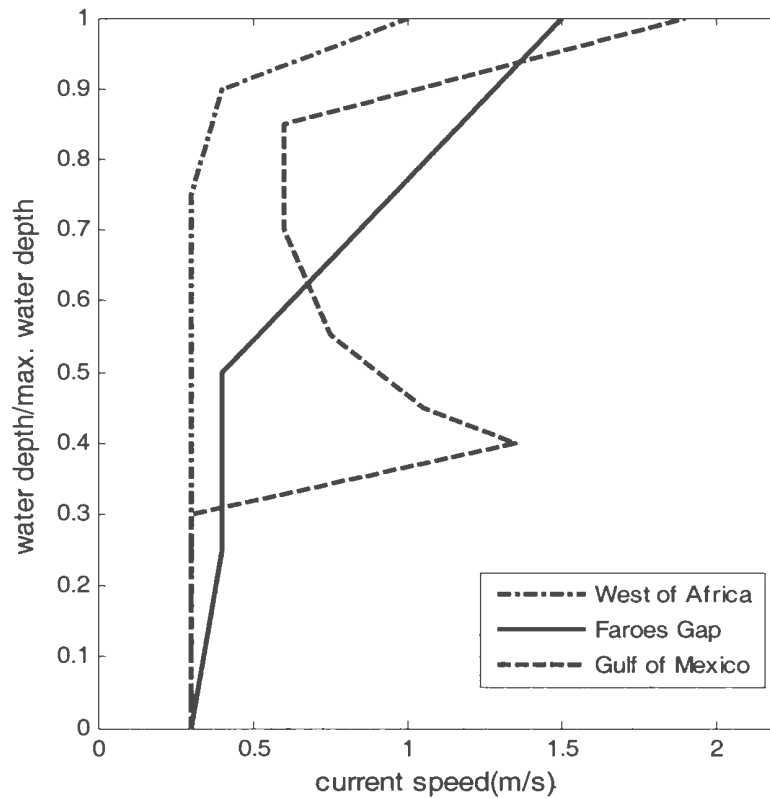


Figure 1-6 Current velocity distribution over water depth on three waters

1.4 Multi-Modal Vortex-Induced Vibrations

Due to the increased water depth, deep-water risers become very long and highly flexible, and this means that they have the potential to be subject to very high modes of vibration. Usually while only the first mode of vibration is excited on shallow-water risers, more than one mode of vibration is excited on deep-water risers (Allen and

Henning, 2001), and normally several modes are excited simultaneously, i.e. multi-modal VIV. The multi-modal VIV responses depend on the modal parameters of the riser vibration system, such as modal natural frequencies, modal mass, modal damping and modal stiffness. A flexible riser has a number of modal natural frequencies, modal mass, modal damping and modal stiffness values, which respectively correspond to a number of modal shapes. The natural frequencies mainly depend on three factors: i) the structural and hydrodynamic masses (added mass) of the riser; ii) the stiffness of the riser and iii) the tensions acting on the riser. The modal mass is influenced by the structural and hydrodynamic mass, and the modal damping is influenced by the structural damping and hydrodynamic damping. The modal stiffness is affected by both the structural stiffness and the tensions acting on the riser. The tensions depend on the pretensions, the structural weight of the riser, the hydrostatic forces and the drag forces acting on the riser.

The multi-modal VIV responses depend also on the characteristics of vortex-shedding forces. The amplitudes, frequencies and span-wise distributions of vortex-shedding forces are three major factors affecting the multi-modal VIV responses. In fact, there is an obvious interaction between modal parameters and vortex-shedding forces. For example, vibrations resulting from vortex-shedding forces may increase the drag forces acting on the riser, and the increased drag force will change the modal parameters, such as modal stiffness and modal natural frequencies. On the other hand, the change of modal stiffness and natural frequencies may influence the vibration responses of the riser and the wake patterns behind the riser, and finally leads to the change of the characteristics of the vortex-shedding forces.

In recent years, much effort has been devoted into the investigation of riser VIV responses and many valuable results have been obtained. However, due to the complexity of multi-modal VIV responses, multi-modal VIV responses are still not fully understood and many uncertainties still exist, especially for highly flexible deep-water risers. For example, modal parameters such as modal natural frequencies, modal mass, modal damping and modal stiffness play an important role in understanding the multi-modal VIV responses for highly flexible deep-water risers in currents, but so far little effort has been devoted to this field, and this obviously hinders the understanding of the multi-modal VIV phenomenon.

1.5 System Identification Technique

System identification techniques can be used to determine the modal parameters of risers. The aim of system identification is to identify the coefficients in an assumed governing equation for the analyzed system. These coefficients are usually called system parameters. For a mass-spring vibration system, such as a riser vibration system, the system parameters are usually the mass, damping and stiffness. The assumed governing equation is either a linear equation or a non-linear equation.

For riser vibration systems, several types of governing equations have been suggested. According to different arrangements of the riser structural dynamics, these governing equations can be classified into two categories: i) the discrete models and ii) the continuous models. The finite element method (FEM) (Bai, 2001) and the lumped mass model (Thomas and Hearn, 1994; Raman-Nair and Baddour 2001) are two well-known discrete models for the dynamic analysis of riser structures. As risers have the relatively

simple structure of a cylinder, it is possible to directly employ a continuous model for the dynamic analysis of risers. An often used continuous model is beam theory combined with corresponding hydrodynamic loads acting on the riser, and then a modal analysis is applied to the continuous model (Vandiver and Chung, 1988; Furnes, 2000). Since the continuous model followed by a modal analysis can explicitly reveal the modal characteristics of riser vibrations, the continuous models are more effective to analyze the multi-modal VIV responses for a flexible riser than the discrete models. Usually, the hydrodynamic loads acting on risers are determined in two ways: numerical methods and empirical methods. In the numerical methods, the hydrodynamic loads acting on risers are obtained through solving the basic equations in two dimensions. These basic equations include the flow continuity equation and the momentum equation, which are written in the vorticity and stream function form (Sarpkaya and Dalton 1992; Sampaio and Coutinho, 2000). In the empirical models, the hydrodynamic loads are determined from an extensive database of hydrodynamic data on sectional force coefficients and correlation length (Triantafyllou *et al.*, 1999).

The analytical models can also be classified into two categories: linear models and non-linear models. In essence, all physical and engineering systems including riser vibration systems are nonlinear systems, as no system can completely follow the linear assumptions without any conditions, but it is possible to regard a system as a linear system, or to linearize a non-linear system to a linear system, under some special conditions. For example, a beam vibrating in air with small amplitude can be considered as a linear system because the damping loads and elastic loads approximately follow the linear assumptions. However, if its vibration amplitude is large, the beam vibration

system must be regarded as a non-linear system, as the damping loads and elastic loads may no longer follow the linear assumptions. For a riser vibrating in currents, strong nonlinear effects mainly exist in its damping loads and tension forces. In the linear models, these nonlinear loads are often linearized, so that the riser vibration system can be handled as a linear system.

The system identification technique is used to determine the system parameters based on the inputs and outputs of an identified system. The inputs and outputs can be obtained by experimental methods. An often used experiment is the so-called excitation test. In such a test, one or more excitations (inputs) are given to the tested system, and then the responses (outputs) from the system are measured. The system identification technique is used to extract system parameters from the relationship between the inputs and outputs. Recently, the system identification technique has been applied to a variety of physical and engineering systems (Bendat, 1998), including ocean engineering structure systems (Liagre and Niedzwecki, 2003). This technique was also used to analyze the nonlinear responses of marine risers in waves (Niedzwecki and Liagre, 2003).

1.6 Experimental Techniques for Risers

Due to their long and thin structures, the experiments in a laboratory for deep-water risers will experience many challenges. The first challenge is the modeling of riser length. Usually, the dimensions of current tanks are too small to model the lengths of deep-water risers, and this often results in difficulty when we design a realistic model riser. Models used for deep-water risers are therefore normally only partially similar to prototype risers, and these models are called distorted models. Figure 1-7 shows two

typical distorted riser models. The first is the truncated riser model. In such a model, the model riser only represents a segment of its prototype riser, and the dynamic and static characteristics of other segments are modeled by additional springs. Another one is the length-distorted riser model. In such a model, the scale for riser length takes a smaller value than the scale for riser diameter, so that the model riser can be placed in a basin with a limited dimension. As the length-distorted models can more realistically model the full span-wise characteristics of riser responses, which are important for a multi-modal VIV test, these models are more suitable for multi-modal VIV tests than truncated riser models.

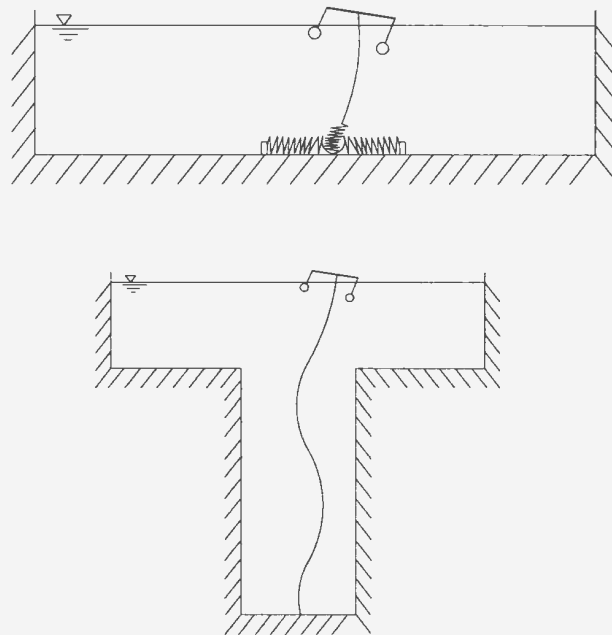


Figure 1-7 Two distorted deep-water riser models due to limited basin depth

The second difficulty for the tests of a deep-water riser in a laboratory is the instrumentation. As discussed earlier, deep-water risers have long and thin structures and this means that the diameter of a model riser may be too small to provide enough space

inside the model riser to mount instrumentation. This is especially true for cases involving the measurement of high-modal VIV responses, as high-modal vibrations normally require more measurement points over the riser length than low-modal vibrations, so that the vibration components with high modes can be analyzed from the measurement. Accelerometers and strain gauges are the sensors often used to measure VIV responses for model risers (e.g. Allen and Henning, 2001; Vandiver *et al.*, 1996; Lie *et al.*, 1998; Hong *et al.*, 2002). Riser vibration displacements can be obtained by double-integration of the accelerations measured by accelerometers, or by analyzing the strain measured by strain gauges based on beam theory.

So far much effort has been devoted into experimental investigations of VIV responses, and some have involved the VIV responses containing multi-modal components. Lie *et al.* (1998) conducted a model test to investigate cross-flow multi-modal VIVs using a rotating rig, and the vibration amplitudes, frequencies and power spectra were obtained. Their work showed that the Strouhal number for multi-modal cross-flow VIV is about 0.15, and the riser shifted between a lock-in behavior and a non-lock-in behavior. In both uniform and shear currents, mainly one peak was observed in the cross-flow displacement spectra. However, their work did not analyze the modal components, as a small number of accelerometers (9 accelerometers) were used.

Allen and Henning (2001) performed a test to investigate both cross-flow and in-line VIV responses using two 100 ft long flexible cylinders. In their tests, the rotating arm could potentially excite mode numbers as high as 15 and 25, but the span-wise characteristics of the multi-modal VIV could hardly be analyzed as only four biaxial accelerometers were used to measure the VIV responses over cylinder length.

Vandiver and Chung (1987) conducted a shear flow experiment in a mill canal using a cable. A dam diverts the water from a river into the canal, and the flow is controlled by four submerged gates on the dam. By controlling the various gate openings a shear flow was created. The cable is 58ft in length and 1.125in in diameter. Six biaxial pairs of accelerometers were used to measure the VIV responses, and the acceleration spectra were analyzed.

Vandiver (1993) reviewed the case studies involving the lock-in phenomenon for flexible cylinders. He pointed out that there are three reasons causing non-lock-in phenomenon for a flexible cylinder: i) the damping is sufficiently large; ii) the vortex-shedding frequency does not correspond to any natural frequency; and iii) the vortex-shedding excitation bandwidth includes the natural frequencies of more than one mode, resulting in a multi-moded responses with random vibration characteristics.

Vandiver and Marcollo (2003) further explained the lock-in phenomenon. They found that added mass also plays an important role in lock-in phenomena. In uniform currents, added mass of a cylinder decreases dramatically as the reduced velocity is increased through the lock-in range, and this causes an increase in the natural frequency of the cylinder. They pointed out that the natural frequency change is responsible for the lock-in phenomenon, namely the bigger the natural frequency change is, the wider the lock-in region is. Their findings explain why a low mass ratio cylinder has a wider lock-in range than a high mass ratio cylinder. The added mass of a high mass ratio cylinder is a lower percentage of the total mass per unit length than that of a low mass ratio cylinder; a high mass ratio cylinders is, therefore, less affected by change in the added mass than a low mass ratio cylinder and, as a result, the total mass change of the high mass ratio cylinder

is smaller than that of the low mass ratio cylinder. This means that a low mass ratio cylinder has a wider lock-in range than a high mass ratio cylinder.

1.7 Problem Discussion

As addressed earlier, the multi-mode VIV behavior for a flexible riser is still not fully understood. In particular: i) a direct observation of the multi-modal vibration shape over riser length has still not been made in previous work; ii) the motion trajectories of the multi-modal vibration in the cross-section plane of risers are still unclear; iii) the modal components in multi-modal VIV responses were still not presented in the literature; iv) the investigation of frequency lock-in for flexible risers is still insufficient; v) the modal parameters, such as modal natural frequencies, modal mass, modal damping and modal stiffness, have not been directly measured in previous studies; and vi) the correlation between the modal parameters and VIV responses is still unclear. These problems are the objectives of this research.

1.8 Objectives and Methodology

This research aims to improve the understanding of multi-modal VIV responses of deepwater risers in currents based on model tests. The objectives of this research also include the development of an applicable model test method and corresponding data analysis procedure. In this research, a length-distorted model riser is designed and two model tests are conducted. The first is a shaker-excitation test, which is designed to investigate the modal parameters of the model riser. The other is a current-excitation test (VIV test), which is designed to investigate the multi-modal VIV responses of the model

riser. A data analysis procedure is developed based on three techniques: i) the spectral analysis technique; ii) the modal analysis technique and iii) Bendat's nonlinear analysis technique (Bendat, 1998).

Figure 1-8 gives an overview of the research. As seen in Figure 1-8, the research mainly contains three activities:

- i) the design of the test apparatus, including a length-distorted model riser, a supporting steel frame and a shaker system;
- ii) the performance of the model tests, including a shaker-excitation test in calm water and a VIV test in uniform currents;
- iii) the analysis of the measured data, including analysis in the time-domain, analysis in the space-domain, analysis in the frequency-domain and non-linear analysis.

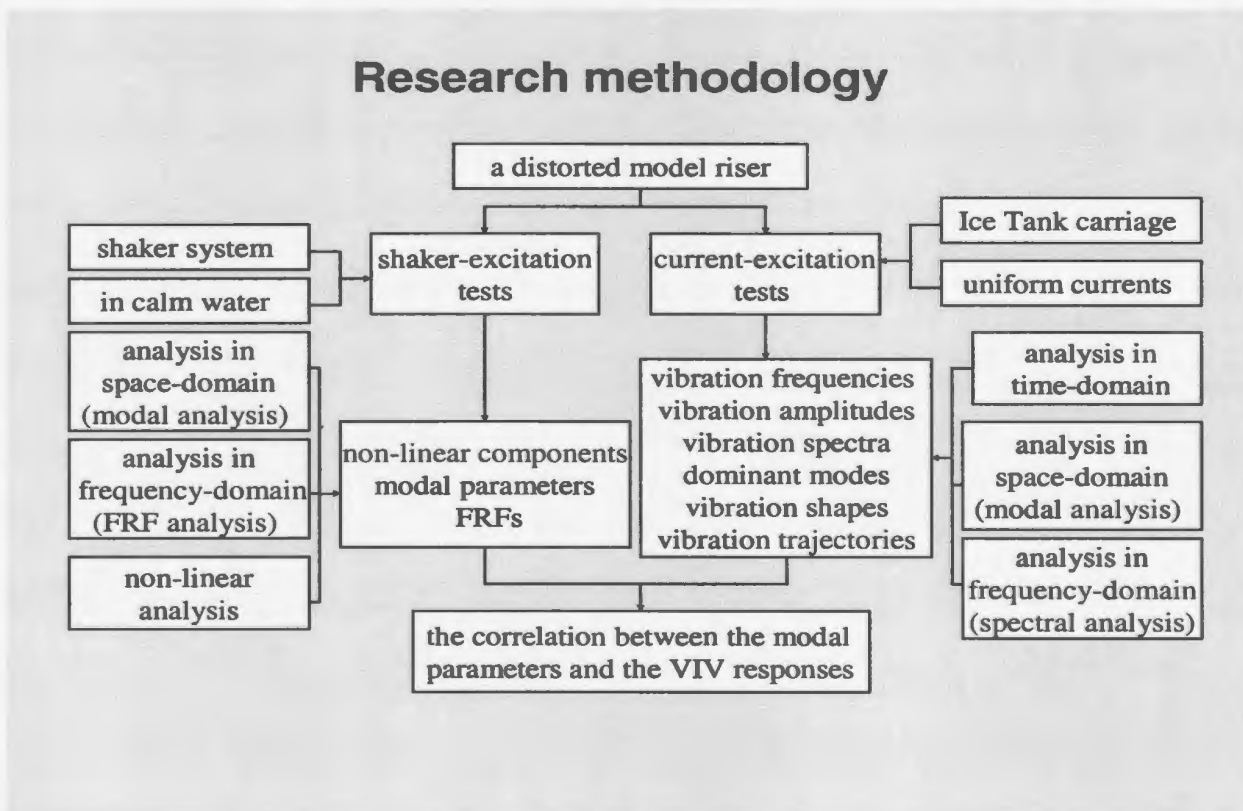


Figure 1-8 The investigation overview

1.9 Outline of the Thesis

This thesis consists of six chapters and four appendices. Chapter one provides an introduction to the research. Some background knowledge on currents on deep waters, marine risers, vortex-induced vibrations and experimental methods for model risers is reviewed, and an overview of this research is presented.

Chapter two exhibits the test apparatus for both the shaker-excitation test and current-excitation test, including the model riser, the supporting steel frame, the shaker system and the instrumentation. In this chapter, a design approach for length-distorted model risers is developed based on similarity theory and the modal governing equations for risers vibrating in currents. The governing differential equations for risers vibrating in water are obtained by applying beam theory to a hollow pipe submerged in water. The external loads acting on the hollow pipe include hydrostatic pressure, hydrodynamic forces and shaker-excitation forces. This chapter also discusses the fundamental principles for the design and calibration of the instrumentation used for the research.

Chapter three presents the research methods used for the shaker-excitation tests and the research results from these tests. An analysis procedure to extract linear and nonlinear modal parameters, such as modal masses, modal damping, modal stiffness, modal natural frequencies and nonlinear damping, from the shaker-excitation test data is developed. This procedure is based on the modal governing equations for risers, frequency response functions and Bendat's nonlinear system parameter identification technique (1998). This procedure was applied to analyze the modal parameters of the model riser in calm water, but it can also be used to analyze the modal parameters of the model riser in currents in

future work. In this chapter, the test results are discussed, and some of these results are compared with the values estimated from the formulas presented by other researchers.

Chapter four involves the methods used for the current-excitation tests and the results from these tests. For the first time, multi-modal vibration shapes over riser length and motion trajectories on the cross-section plane are presented. The results from the time-domain analysis show that the frequency lock-in phenomenon may occur in the cross-flow or in-line direction for multi-modal VIV responses. The number and values of dominant frequencies in multi-modal VIV responses are investigated, and the modal components in multi-modal VIV responses are analyzed based on space-domain analysis.

Chapter five discusses the correlation between the estimated modal parameters and the measured VIV responses. The modal parameters were estimated from the shaker-excitation tests in calm water, and these estimated modal parameters only correspond to modal parameters in calm water. Although in theory the VIV responses only have correlations with the modal parameters in currents, the discussions presented in chapter five still find a degree of correlation between the VIV responses and the modal parameters in calm water, such as the correlation between the modal natural frequencies and the frequency lock-in of the VIV responses, the correlation between the modal added mass coefficients and the upper limit values, and the correlation between the modal natural frequencies and the resonance of VIV responses.

Chapter six extracts the conclusions from the research work. The main conclusions include that:

i) flexible risers have a variety of natural frequencies, which correspond to a variety of mode shapes, and these modal natural frequencies depend strongly on tensions;

- ii) modal mass for a flexible riser depends weakly on tensions and mode shapes, and the estimated added mass coefficient C_a ranges from 1.0 to 3.7 for the model riser tested in calm water;
- iii) modal damping depends on mode shapes, and the estimated damping coefficient C_d ranges from 0.5 to 2.5 for the model riser tested in calm water;
- iv) non-linear effects are relatively large in the low frequency and modal resonance regions;
- v) the frequencies of multi-modal VIV responses in both cross-flow and in-line directions follow the Strouhal frequencies for a flexible riser in the frequency un-lock-in regions and the measured Strouhal number is about 0.12 for the model riser tested. Frequency lock-in may take place in both in-line and cross-flow directions at some modal natural frequencies;
- vi) the vibration amplitudes fluctuate from 0.3 to 0.9 D , where D is the riser diameter, in both the in-line and cross-flow directions for the flexible riser tested, and no increasing trend exists as the current velocity increases;
- vii) there are three types of power spectra in multi-modal VIV responses for a flexible riser: vibrations with single dominant frequency, vibrations with double dominant frequencies and vibrations with multi-dominant frequencies;
- viii) the dominant modes for in-line VIV and cross-flow VIV are usually different, and modal responses may experience a resonance region;
- ix) at lower current velocities, the vibration shapes over riser length often exhibit a clear dominant mode with clear nodes, while at higher current velocities, there are several dominant modes in multi-modal VIV responses and the dominant modes become vague;

- x) the motion trajectories on the cross-section plane contain two fundamental motions. The first motion is a basic figure of 8-, L- and O-shaped or other complicated vibration motion, and another is a shifted motion of the basic figure motion. The basic figures of 8- and L-shaped correspond to the vibrations at lower current velocities, while other basic figures correspond to the vibrations at higher current velocities; and
- xi) there is a degree of correlation between the VIV responses and the modal parameters in calm water, although in theory the VIV responses only have correlations with the modal parameters in currents.

1.10 Contributions of the Thesis

This thesis presents new contributions to the understanding of multi-modal VIV responses. The following results are presented for the first time:

- i) the multi-modal vibration shapes over riser length and motion trajectories in the cross-sectional plane are measured for a flexible riser;
- ii) the frequency lock-in in both in-line and cross-flow directions are directly observed for a flexible riser with multi-modal vibrations;
- iii) the modal components of multi-modal VIV responses are analyzed in both in-line and cross-flow directions;
- iv) the modal parameters of a flexible riser are measured, and the correlations between the multi-modal VIV responses and modal parameters are analyzed.

The new contributions to the test technique for deepwater risers include that:

- i) a method to design a length-distorted model riser is presented. For the first time, the theoretical correlation between a short model riser and a long deepwater riser is established;
- ii) a shaker-excitation test is presented to measure the modal parameters of a flexible riser, and an applicable data analysis procedure is developed.

CHAPTER 2

TEST APPARATUS

2. Test Apparatus

The test apparatus includes a model riser, a supporting steel frame, a shaker system and the instrumentation. A sketch of the apparatus is shown in Figure 2-1.

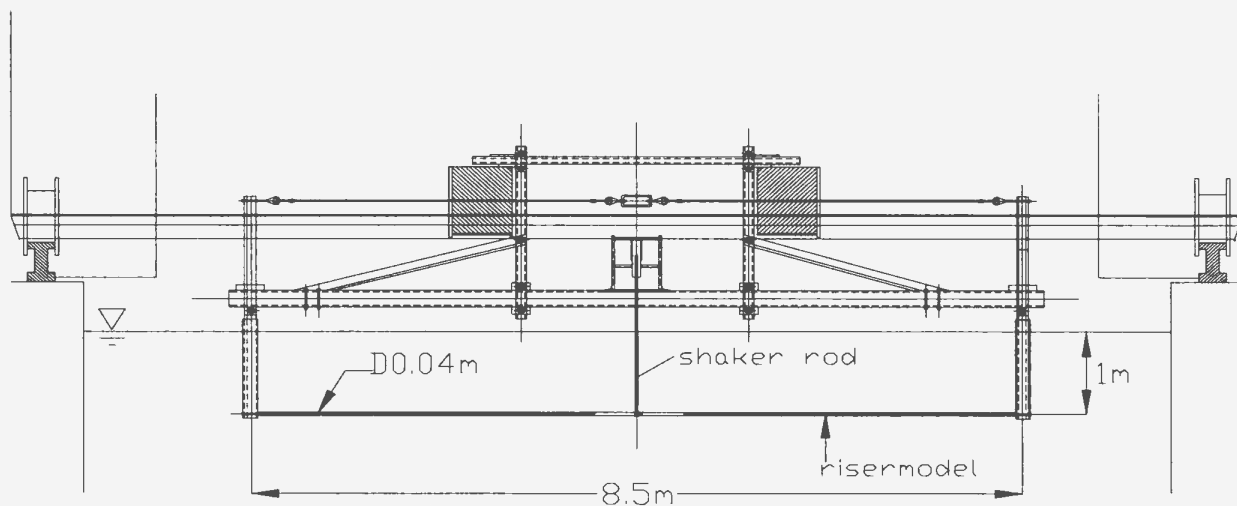


Figure 2-1 Sketch of the test apparatus

2.1 Model Riser

2.1.1 Analytical Model for Design of Model Riser

A length-distorted model riser with uniform geometrical and structural properties was designed based on a linear analytical model and similarity theory. An analytical model for the structural dynamics of a riser in water is shown in Appendix A, which assumes that the vibrations in the in-line and the cross-flow directions are uncoupled. If different patterns of hydrodynamic loads are assumed, this analytical model can be used respectively for the model riser design, linear modal parameter determination and nonlinear system parameter determination.

In order to design the length-distorted model riser, it was assumed that: i) the hydrodynamic loads acting on the riser are frequency-independent; ii) the hydrodynamic and structural loads acting on the riser are location-independent; and iii) the hydrodynamic damping can be linearized.

The hydrodynamic loads acting on the riser include the following components: i) the hydrodynamic inertial force, which is represented by an added mass coefficient C_a ; ii) the hydrodynamic damping force, which is represented by a damping coefficient C_d ; and the vortex shedding force, which is represented by a lift coefficient C_l . Usually, the added mass m_a , the linearized damping c_a and the vortex-shedding force f_v can be respectively written as

$$\left. \begin{aligned} m_a &= \frac{\pi}{4} \rho C_a D^2 \\ c_a &= \frac{1}{\pi} \rho C_d \omega z_0 \\ f_v &= f_0 \sin(\omega t) \end{aligned} \right\} \quad (2-1)$$

where ρ is the water density; D is the riser diameter; C_a is the added mass coefficient; C_d is the drag coefficient; z_0 is the amplitude of riser vibration. The terms f_0 and ω are respectively the amplitude and frequency of the vortex-shedding force, and they can be written as

$$\left. \begin{aligned} f_0 &= \frac{1}{2} \rho C_l D U^2 \\ \omega &= 2\pi S_t \frac{U}{D} \end{aligned} \right\} \quad (2-2)$$

where C_l is the lift coefficient; S_t is the Strouhal number; and U is the current velocity.

Substituting equation (2-1) into equation (A-18) in Appendix A and considering the boundary condition represented by equation (A-20), a simplified governing equation for the dynamics of the model riser in the cross-flow direction can be described as

$$\left. \begin{aligned} [m_s + \frac{\pi}{4} \rho C_a D^2] \frac{\partial^2 z}{\partial t^2} + (c_s + \frac{1}{\pi} \rho C_d D \omega z_0) \frac{\partial z}{\partial t} - T \frac{\partial^2 z}{\partial x^2} + k_b \frac{\partial^4 z}{\partial x^4} &= f_0 \sin(\omega t) \\ z(t, 0) &= 0 \\ \frac{\partial^2 z(t, 0)}{\partial x^2} &= 0 \\ z(t, L) &= 0 \\ \frac{\partial^2 z(t, L)}{\partial x^2} &= 0 \end{aligned} \right\} \quad (2-3)$$

where z denotes the vibration displacement in the cross-flow direction; m_s is the riser structural mass per unit length; c_s is the riser structural damping per unit length; T is the riser tension; k_b is the bending stiffness of the riser; and L is the riser length.

The solutions to equation (2-3) can be written in modal form as:

$$z(t, x) = \sum_{k=1}^{\infty} z_k(t) \sin\left(\frac{k\pi}{L} x\right) \quad (2-4)$$

where z_k denotes the modal vibration responses, which are defined as:

$$z_k(t) = \frac{2}{L} \int_0^L z(t, x) \sin\left(\frac{k\pi}{L}x\right) dx \quad (2-5)$$

Substitution of equation (2-4) into equation (2-3) and integration of both sides of equation (2-3), which are multiplied by $\sin(k\pi x/L)$, over riser length gives the following modal governing equations:

$$\begin{aligned} A_k \ddot{z}_k(t) + B_k \dot{z}_k(t) + C_k z_k(t) &= f_{k0} \sin(\omega t) \\ k &= 1, 2, 3, \dots \end{aligned} \quad (2-6)$$

where A_k , B_k and C_k respectively denotes the modal mass, damping and stiffness of the riser, and f_{k0} is the amplitude of modal vortex shedding force. These parameters can be calculated by

$$\left. \begin{aligned} A_k &= \frac{L}{2} \left(m_s + \frac{\pi}{4} \rho C_d D^2 \right) \\ B_k &= \frac{L}{2} \left(c_s + \frac{1}{\pi} \rho C_d D \omega z_0 \right) \\ C_k &= \frac{L}{2} \left[k_b \left(\frac{k\pi}{L} \right)^4 + T \left(\frac{k\pi}{L} \right)^2 \right] \\ f_{k0} &= \frac{2L}{k\pi} f_0 \end{aligned} \right\} \quad (2-7)$$

The modal responses are the solutions to equation (2-6). The time-domain solutions have the following forms:

$$z_k = a_k \sin(\omega t - \alpha_k)$$

where

$$\left. \begin{aligned} a_k &= \frac{f_{k0}}{\sqrt{(\omega_{nk}^2 - \omega^2)^2 A_k^2 + \omega^2 B_k^2}} \\ \alpha_k &= \tan^{-1} \left(\frac{-\omega B_k}{(\omega_{nk}^2 - \omega^2) A_k} \right) \end{aligned} \right\} \quad (2-8)$$

The modal natural frequencies ω_{nk} can be estimated based on modal mass A_k and modal stiffness C_k . From equation (2-7), a formula for the estimation of modal natural frequencies can be obtained as:

$$\omega_{nk} = \sqrt{\frac{C_k}{A_k}} = \sqrt{\frac{k_b \left(\frac{k\pi}{L} \right)^4 + T \left(\frac{k\pi}{L} \right)^2}{m_s + \frac{\pi}{4} \rho C_a D^2}} \quad (2-9)$$

Vandiver and Marcollo (2003) also suggested a formula to estimate modal natural frequencies for a long flexible cylinder as follows:

$$f_{nk} = \frac{k}{2L} \sqrt{\frac{T}{m_T}}$$

where f_{nk} is the natural frequencies with the unit of Hz, and m_T is the total mass per unit length including structural mass and added mass. Obviously, this formula is a simplification of equation (2-9) under an assumption of a zero bending stiffness k_b .

2. 1. 2 Design of Model Riser

Equations (2-7), (2-8) and (2-9) were used to design the distorted model riser through similarity theory. In order to design the distorted model riser, a nominal prototype marine riser was chosen as a basis for the design. The geometric and physical properties of the riser are shown in Table 2-1.

Table 2-1 Nominal prototype riser properties

| item | unit | value |
|-------------------|-------------------|--------|
| length | m | 1000.0 |
| outside diameter | m | 0.292 |
| air weight, empty | kN/m | 0.895 |
| wet weight, empty | kN/m | 0.238 |
| bending stiffness | kN.m ² | 36.3 |

From equation (2-8), it is known that the riser modal responses depend on five parameters: i) the amplitudes of modal vortex-shedding force, f_{k0} ; ii) the frequency of vortex-shedding, ω ; iii) the modal natural frequencies, ω_{nk} ; iv) the modal mass, A_k , and v) the modal damping B_k . The dimensional analysis (Sharp *et al.* 1992) can produce five non-dimensional parameter groups related to the modal response amplitudes, and the relationship between these non-dimensional parameter groups can be written as

$$\frac{a_k}{D} = \phi \left(\frac{f_{k0}}{\rho g L D^2}, \frac{\omega}{\omega_{nk}}, \frac{A_k}{\rho L D^2}, \frac{B_k}{\rho L D \omega x_0} \right)$$

where g is the gravitational acceleration. According to similarity theory, the model riser will be completely similar to the prototype riser if all non-dimensional parameter groups are equal between the two systems; thus, from equations (2-7) and (2-9), the conditions for complete similarity can be established as:

$$\left[\frac{m_s}{\rho D^2} + \frac{\pi}{4} C_a \right]^{(m)} = \left[\frac{m_s}{\rho D^2} + \frac{\pi}{4} C_a \right]^{(p)} \quad (2-10)$$

$$\left[\frac{S_t U L^2}{\sqrt{k_b (k\pi)^2 + T L^2}} \right]^{(m)} = \left[\frac{S_t U L^2}{\sqrt{k_b (k\pi)^2 + T L^2}} \right]^{(p)} \quad (2-11)$$

$$\left[\frac{c_s}{2\rho S_t U z_0} + C_d \right]^{(m)} = \left[\frac{c_s}{2\rho S_t U z_0} + C_d \right]^{(p)} \quad (2-12)$$

$$\left[\frac{C_l U^2}{D} \right]^{(m)} = \left[\frac{C_l U^2}{D} \right]^{(p)} \quad (2-13)$$

where the superscripts (m) and (p) respectively indicate the values of the model riser system and the prototype riser system.

Note that only equation (2-11) contains the parameter of riser length. This implies that a distorted riser length only influences the modeling of the frequency ratio, and not the modeling of other parameters. Equations (2-10), (2-11), (2-12) and (2-13) contain the hydrodynamic coefficients, such as C_a , C_d , C_l and S_t . These hydrodynamic coefficients usually depend on the Reynolds numbers, R_e , and they can be approximately considered as the same values if the Reynolds number R_e is similar between the model riser system and the prototype riser system. In other words, as the similarity of the Reynolds number R_e is the prerequisite for the similarity of the hydrodynamic coefficients C_a , C_d , C_l and S_t , the requirement of the Reynolds number R_e similarity is implicitly contained in the similarity of the hydrodynamic coefficients C_a , C_d , C_l and S_t . Based on the similarity of the hydrodynamic coefficients C_a , C_d , C_l and S_t , equations (2-10), (2-11), (2-12) and (2-13) can be simplified to:

$$\left[\frac{m_s}{D^2} \right]^{(m)} = \left[\frac{m_s}{D^2} \right]^{(p)} \quad (2-14)$$

$$\left[\frac{UL^2}{\sqrt{k_b(k\pi)^2 + TL^2}} \right]^{(m)} = \left[\frac{UL^2}{\sqrt{k_b(k\pi)^2 + TL^2}} \right]^{(p)} \quad (2-15)$$

$$\left[\frac{c_s}{Uz_0} \right]^{(m)} = \left[\frac{c_s}{Uz_0} \right]^{(p)} \quad (2-16)$$

$$\left[\frac{U^2}{D} \right]^{(m)} = \left[\frac{U^2}{D} \right]^{(p)} \quad (2-17)$$

For a small scale factor the R_e similarity requires a bigger model current velocity than the prototype current velocity, while equation (2-17) requires a smaller model current velocity, and this makes it impossible to design a model riser with complete similarity. An option is to remove the similarity condition of equation (2-17) so that a model riser with partial similarity is designed. Obviously, the elimination of the similarity condition represented by equation (2-17) will cause the model riser to experience a bigger lift force than the lift force required by similarity theory, and this means that the lift force and lift coefficient are no longer similar between the designed model riser and the prototype riser.

The process of the model riser design in this research is described as follows: first two different scale factors were used to determine the length and diameter of the model riser such that the model riser can be placed in the tank used and the instrumentation can be placed inside the model riser. The structural mass of the model riser was designed based on equation (2-14). Equation (2-15) provides a way to determine the equivalent tension T of the model riser if the bending stiffness k_b is determined by other means. The dimensional analysis can also produce a non-dimensional parameter group about k_b , and

the required value of k_b can be determined based on the equality of this non-dimensional parameter group as follows:

$$\left[\frac{k_b}{\rho g D^5} \right]^{(m)} = \left[\frac{k_b}{\rho g D^5} \right]^{(p)}$$

The structural damping of the model riser can be designed through equation (2-16). Assume that the ratio of the riser vibration amplitude z_0 to the riser diameter D is the same between the model riser system and the prototype riser system, and from equation (2-16) the required structural damping of the model riser can be calculated by

$$\left[\frac{c_s}{UD} \right]^{(m)} = \left[\frac{c_s}{UD} \right]^{(p)} \quad (2-18)$$

Although equation (2-18) provides a way to design the structural damping of the model riser, it is often difficult to achieve the required structural damping in construction of model riser, as so far no appropriate methods have been found to model the designed structural damping for model risers. Fortunately, the structural damping is usually much smaller than the hydrodynamic damping and, as a result, it is taken to be acceptable that the modeling of the structural damping is ignored, as we did in the present work.

2.1.3 Construction of Model Riser

The model riser was made of two continuous rubber hoses with different diameters. The designed riser bending stiffness k_b was satisfied through selecting the appropriate hose materials and wall thickness, and the designed riser structural mass, m_s , through placing an appropriate amount of lead weights into the hoses. The outer hose was split along its length and the instrumented inner hose was then placed into it. Silicone sealant

in the space between the inner and outer hoses made the model riser waterproof. A steel cable was placed inside the inner hose to withstand the riser tensions. The cable was connected to two aluminum connection ends, and the outer hose was clamped onto the two aluminum ends. There was a hole in one of the aluminum connection ends, and the signal and power wires went out through this hole. The model riser was wrapped in latex tape to make the riser surface smooth.

Figure 2-2 demonstrates a sketch of the model riser. In the figure, 1 indicates the power and signal wires; 2 the aluminum connection end; 3 the steel cable end bolt; 4 the inner hose; 5 the steel cable; 6 the supporting wood block; 7 the connecting bolt; 8 the clamp; 9 the outer hose; and 10 the lead weight. The actual model riser is shown in Figure 2-3, and the actually measured properties of the model riser are listed in Table 2-2.

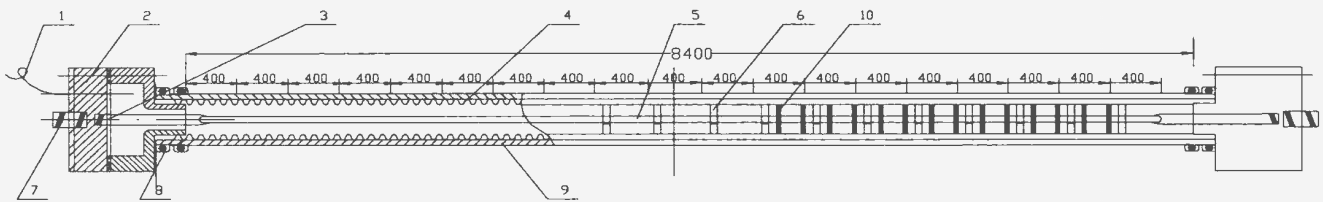


Figure 2-2 Sketch of model riser

Table 2-2 Model riser properties

| item | unit | model riser |
|-------------------------------|-------------------|-------------|
| length | m | 8.5 |
| outside diameter | m | 0.040 |
| weight per unit length in air | N/m | 16.8 |
| bending stiffness | N. m ² | 1.52 |

2.2 Supporting Steel Frame

The model riser was mounted horizontally on a supporting steel frame which was fixed on the tank carriage. The requirements for the frame included that: i) it had enough strength to withstand the static and dynamic loads acting on it, including the drag load acting on the model riser and the inertial load of the frame structure when the frame moves with an acceleration of the carriage, and this was ensured through a stress check and a deflection check; ii) it had a mechanism to adjust the pre-tensions acting on the model riser, and this was achieved through a vertical lever mechanism; and iii) it had a structure symmetrical with respect to its middle point, and this ensured the identical deflections at the connection points for two ends of the model riser when the carriage moved.

Figure 2-3 is a picture of the supporting steel frame with the model riser, and Figure 2-4 is a sketch of the pre-tension adjustment vertical lever mechanism. In Figure 2-4, 1- denotes the horizontal beam; 2- the vertical supporting rod; 3- the vertical bar; 4- the enforcing rod; 5- the pre-tension adjustment steel cable with turn-buckle. The pre-

tensions acting on the riser were changed when the turn-buckle was adjusted; and 6- the vertical lever.

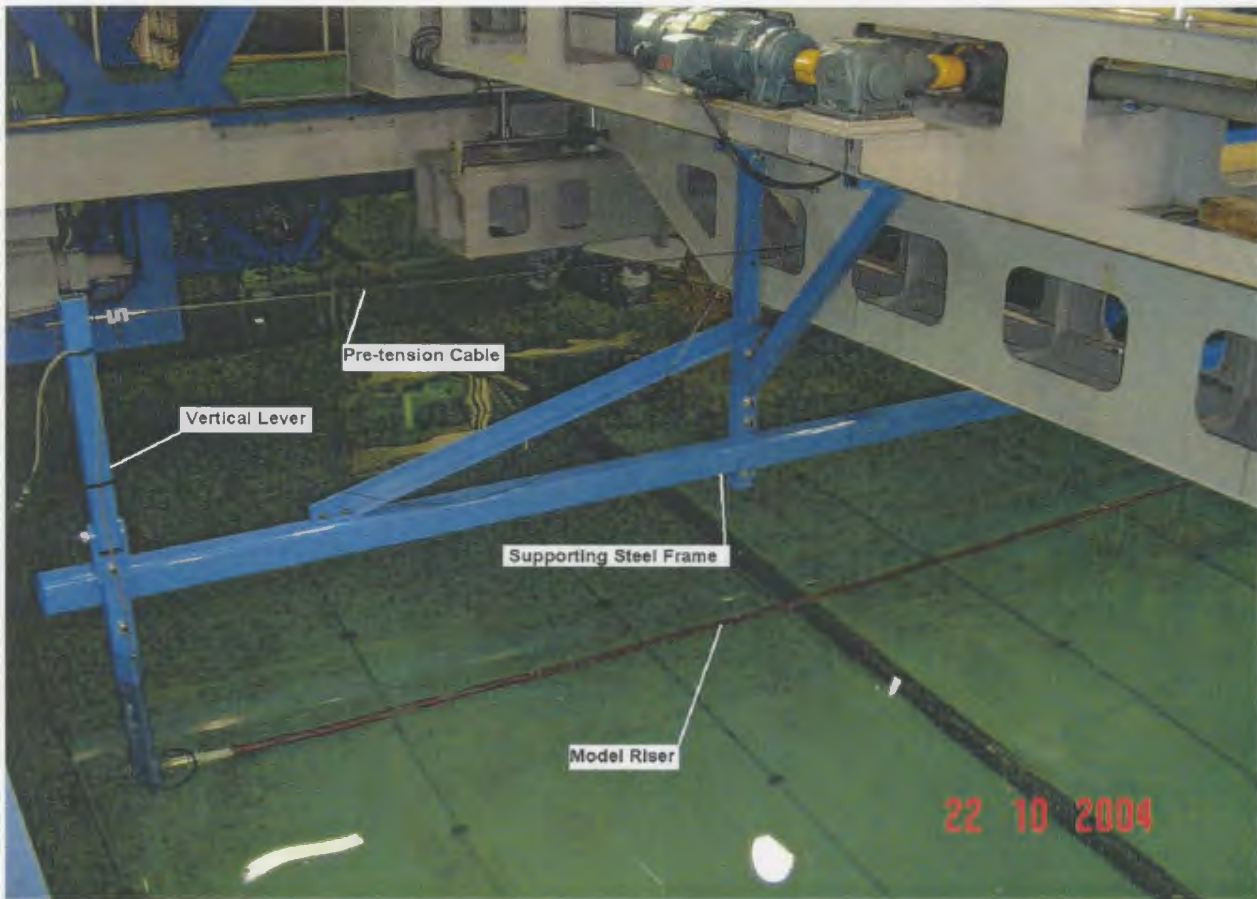


Figure 2-3 The length-distorted model riser and the supporting frame

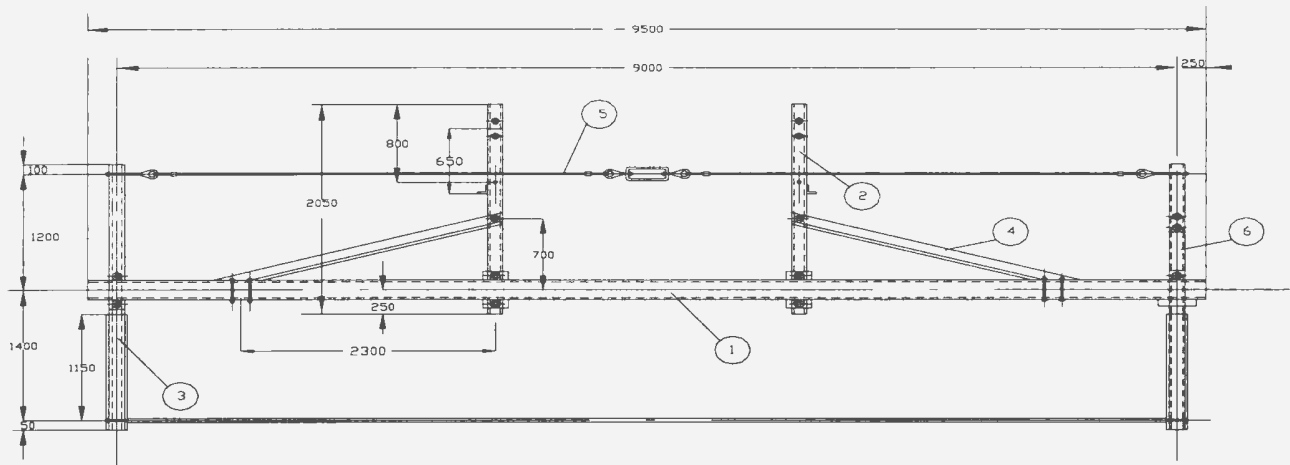


Figure 2-4 Pretension adjust vertical lever mechanism

2.3 Shaker System

A shaker system was used to conduct the shaker excitation tests. This system consists of three major parts: a control computer, a shaker and a shaker motion transmission rod.

Control computer: The control computer was provided by NRC Institute for Ocean Technology. The computer generated the voltage control signals based on the digital control signals previously stored in the data files on the computer;

Shaker: The shaker was provided by Oceanic Consultant Corporation. It was driven by an electrical motor. The motor moved based on the voltage control signals from the control computer. The shaker could generate two patterns of shaker motion, namely the harmonic vibration and the random vibration. The limit of frequency and amplitude of the shaker motion was 10Hz and 10cm.

Shaker motion transmission rod: This rod was used to transmit the shaker motion to the model riser. The rod was connected onto the middle of the riser through a clamp. The

Test Apparatus

requirements for the transmission rod included that: i) the rod had enough strength to withstand the excitation forces acting on it; ii) it could remain stable when a compression force of 100N was experienced; and iii) the rod was as light as possible so that its inertial force did not severely influence the shaker motion. In order to reduce the mass, aluminum was selected as the material of the rod. Figure 2-5 shows a picture of the shaker and the connection rod.

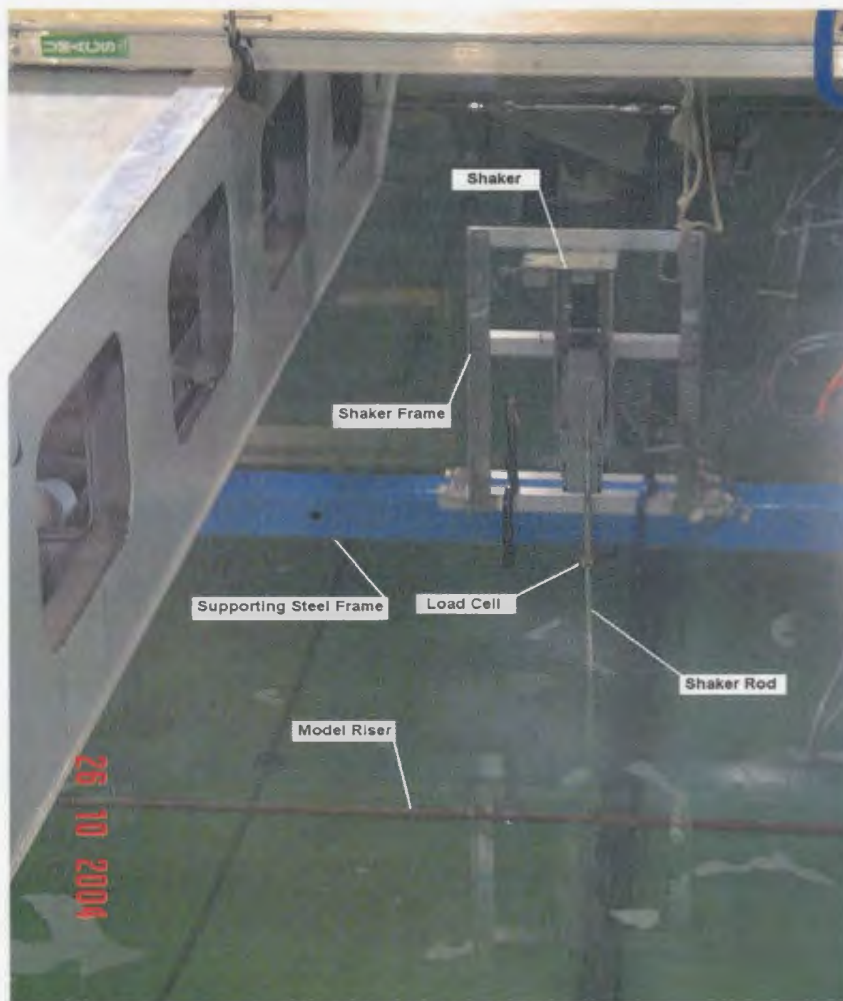


Figure 2-5 The shaker and connection rod

2. 4 Instrumentation

2. 4. 1 Sensors

The sensors used were forty uniaxial ADXL150JQC accelerometers, two load cells and a displacement transducer. These accelerometers were mounted inside the model riser to measure the vibration accelerations over the riser length. One of two load cells was mounted on the tensioned steel cable to measure the pretensions, and another was mounted on the shaker motion transmission rod to measure the shaker-excitation forces. The displacement transducer was mounted on the shaker motion transmission rod to measure the shaker motion displacement.

Forty accelerometers were glued into twenty pairs. The directions of two accelerometers in each pair were approximately equal to 90° . The twenty pairs of accelerometers were evenly distributed over the riser length, but only sixteen pairs could work. The locations of the sixteen pairs of accelerometers which worked are shown in Table 2-3.

Table 2-3 Accelerometer pair locations on the model riser

| | | | | | | | | |
|-------------|-------|-------|-------|-------|-------|-------|-------|-------|
| pair No. | 1 | 2 | 3 | 4 | 5 | 6 | 7 | 8 |
| location(m) | 0.810 | 1.214 | 1.619 | 2.024 | 2.429 | 2.833 | 3.238 | 3.643 |
| pair No. | 9 | 10 | 11 | 12 | 13 | 14 | 15 | 16 |
| location(m) | 4.048 | 4.452 | 4.857 | 5.262 | 6.476 | 6.881 | 7.286 | 7.691 |

2.4.2 Calibration of Accelerometers

The accelerometers were calibrated by a rotating test. In the rotating test, the model riser was horizontally mounted on the supporting steel frame, and then turned around its longitudinal axis with thirteen rotating angles ranging from zero to 360°. Thirty-two records of the accelerometer voltage output versus the rotating angle were obtained. The fits with sinusoidal curve were then applied to the records of voltage output versus rotating angle for each accelerometer. The calibration factors and the orientation of the accelerometers inside the model riser were estimated from the amplitudes and phases of the fitted sinusoidal curves based on the following relationships:

$$\begin{aligned}\lambda_j &= A_j g \\ \beta_j &= \alpha_j\end{aligned}$$

where λ_j is the calibration factor of the j th accelerometer, β_j is the orientation angle of the j th accelerometer, g is the gravitational acceleration, and A_j and α_j are respectively the amplitude and phase of the fitted sinusoidal curve for the j th accelerometer.

Figure 2-6 shows six examples of the data measured in the rotating tests and the corresponding fitted sinusoidal curves. Table 2-4 and Table 2-5 give the calibration factors and the orientation angles of the thirty-two accelerometers based on the fitted sinusoidal curves.

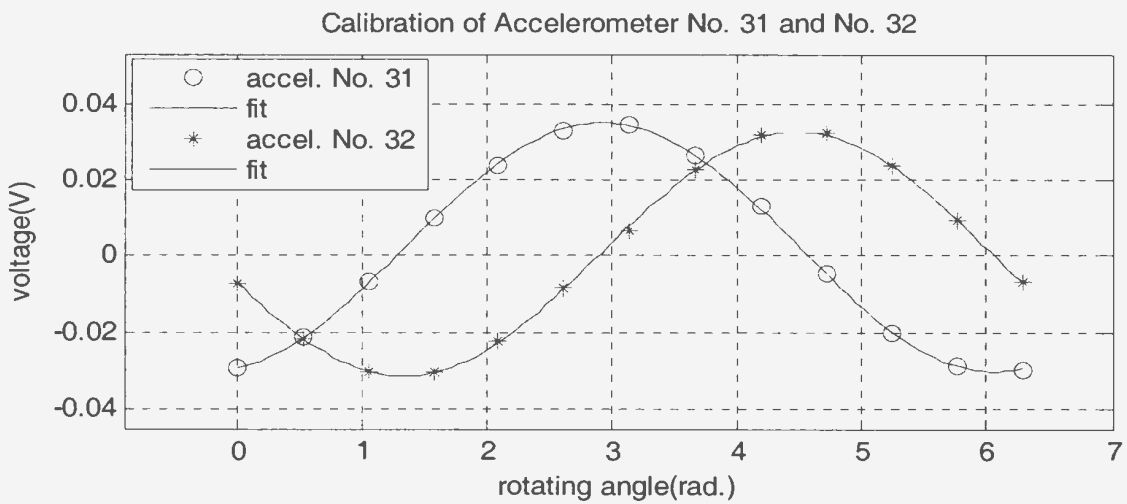
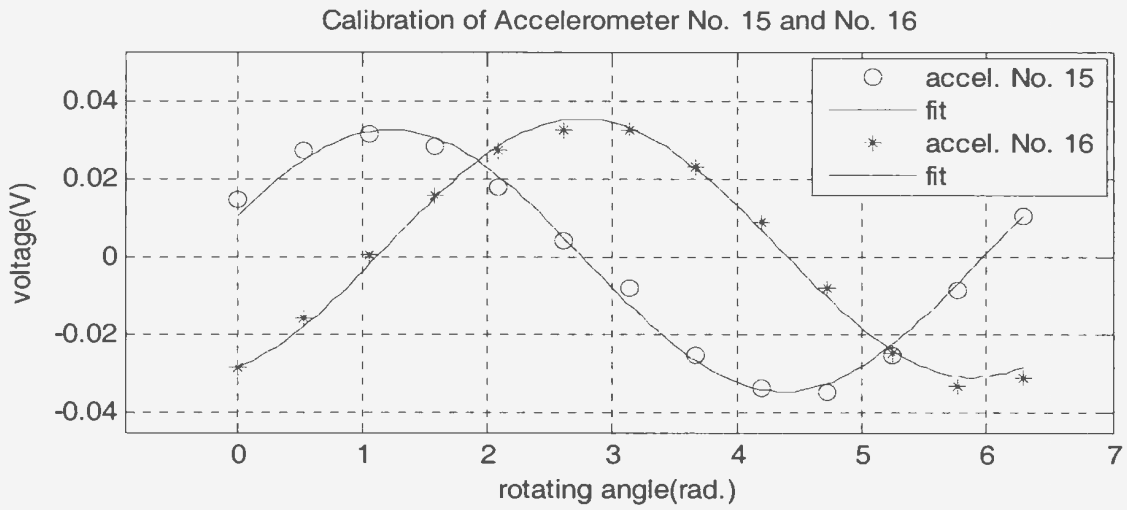
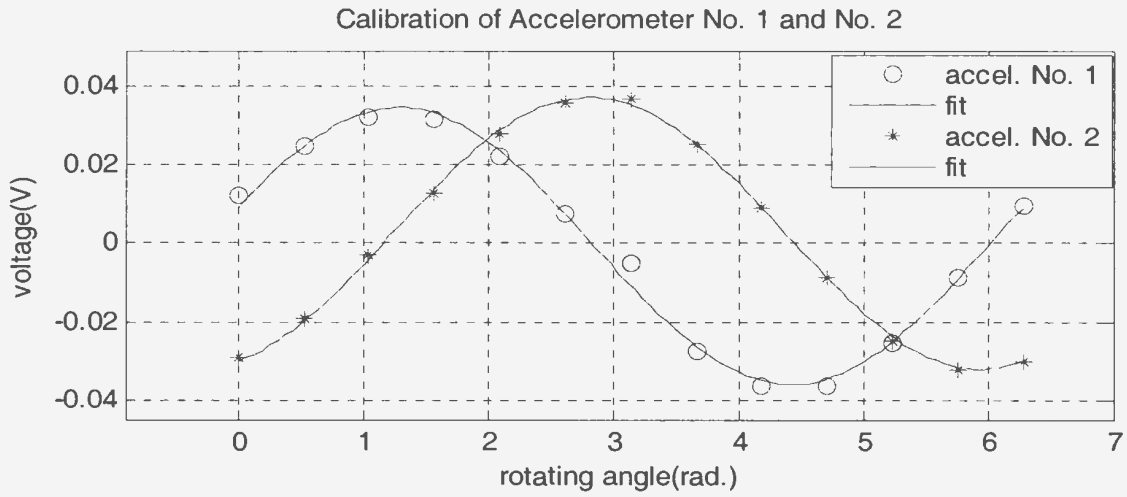


Figure 2-6 Calibration of accelerometers

Table 2-4 Calibration factors of accelerometer

| | | | | | | | | |
|-------------|--------|--------|--------|--------|--------|--------|--------|--------|
| accel. No. | 1 | 2 | 3 | 4 | 5 | 6 | 7 | 8 |
| factor(V/g) | 0.0352 | 0.0345 | 0.0385 | 0.0342 | 0.0344 | 0.0336 | 0.0340 | 0.0334 |
| accel. No. | 9 | 10 | 11 | 12 | 13 | 14 | 15 | 16 |
| factor(V/g) | 0.0335 | 0.0330 | 0.0339 | 0.0332 | 0.0331 | 0.0333 | 0.0337 | 0.0332 |
| accel. No. | 17 | 18 | 19 | 20 | 21 | 22 | 23 | 24 |
| factor(V/g) | 0.0336 | 0.0327 | 0.0330 | 0.0327 | 0.0330 | 0.0326 | 0.0331 | 0.0333 |
| accel. No. | 25 | 26 | 27 | 28 | 29 | 30 | 31 | 32 |
| factor(V/g) | 0.0329 | 0.0323 | 0.0326 | 0.0325 | 0.0326 | 0.0324 | 0.0326 | 0.0320 |

Table 2-5 Orientation angles of accelerometer

| | | | | | | | | |
|-------------|--------|--------|--------|--------|--------|--------|--------|--------|
| accel. No. | 1 | 2 | 3 | 4 | 5 | 6 | 7 | 8 |
| angle(rad.) | 1.6834 | 6.4446 | 1.7904 | 6.2320 | 1.5699 | 6.2918 | 1.2321 | 6.0335 |
| accel. No. | 9 | 10 | 11 | 12 | 13 | 14 | 15 | 16 |
| angle(rad.) | 1.0238 | 5.7549 | 0.5077 | 5.4232 | 1.3050 | 6.0893 | 1.7432 | 6.4945 |
| accel. No. | 17 | 18 | 19 | 20 | 21 | 22 | 23 | 24 |
| angle(rad.) | 0.8895 | 5.6228 | 1.0940 | 5.7338 | 0.6078 | 5.4336 | 1.3050 | 6.0893 |
| accel. No. | 25 | 26 | 27 | 28 | 29 | 30 | 31 | 32 |
| angle(rad.) | 6.1857 | 4.7241 | 6.1905 | 4.7213 | 6.2292 | 4.8244 | 0.0461 | 4.7737 |

2. 4. 3 Accelerations in the In-line and the Cross-flow Directions

As each pair of accelerometers was not placed in the exact in-line and cross-flow directions, the accelerations measured by each pair of accelerometers were a little different from the accelerations in the in-line and cross-flow directions. The riser vibration accelerations in the in-line and cross-flow directions could be obtained through combining the accelerations measured by each pair of accelerometers based on the orientation angles. Figure 2-7 demonstrates the relationship between the acceleration A of the riser vibration and the accelerations A_1 and A_2 measured by the accelerometers.

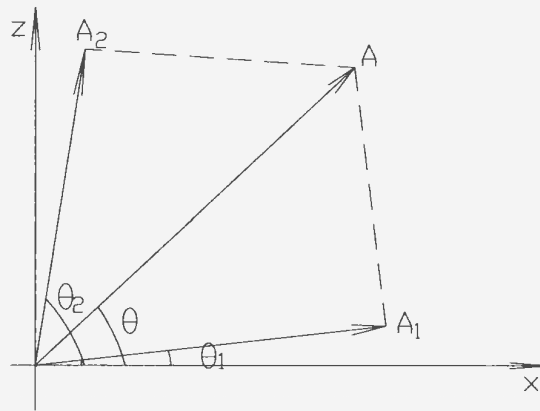


Figure 2-7 Relationship between the total riser accelerations and the accelerations measured by the accelerometers

Obviously, the magnitudes of A_1 and A_2 are equal to the projection values of the total riser acceleration A in the directions of the accelerometers, namely

$$\left. \begin{aligned} |A_1| &= |A| \cos(\theta - \theta_1) \\ |A_2| &= |A| \cos(\theta_2 - \theta) \end{aligned} \right\} \quad (2-19)$$

Equation (2-19) leads to

$$\left. \begin{aligned} |A|(\cos \theta \cos \theta_1 + \sin \theta \sin \theta_1) &= |A_1| \\ |A|(\cos \theta_2 \cos \theta + \sin \theta_2 \sin \theta) &= |A_2| \end{aligned} \right\} \quad (2-20)$$

From equation (2-20), we have:

$$\frac{\cos \theta_1 + \tan \theta \sin \theta_1}{\cos \theta_1 + \tan \theta \sin \theta_1} = \frac{|A_1|}{|A_2|} \quad (2-21)$$

Equations (2-19) and (2-21) give the magnitude and angle of the riser acceleration vector **A** as follows:

$$\left. \begin{aligned} \tan \theta &= \frac{|A_2| \cos \theta_1 - |A_1| \cos \theta_2}{|A_1| \sin \theta_2 - |A_2| \sin \theta_1} \\ |A| &= \frac{|A_1|}{\cos(\theta - \theta_1)} \end{aligned} \right\} \quad (2-22)$$

where $|A_1|$ and $|A_2|$ are the magnitudes of the accelerations measured by the accelerometers, and θ_1 and θ_2 are the orientation angles of the accelerometers.

The magnitudes of the in-line and cross-flow components of the riser vibration acceleration are equal to the projection values of the total acceleration in the directions of y-axis and z-axis, namely the in-line and cross-flow accelerations can be written as follows:

$$\left. \begin{aligned} a_y &= |A| \cos \theta \\ a_z &= |A| \sin \theta \end{aligned} \right\} \quad (2-23)$$

where $|A|$ and θ are respectively the magnitude and angle of the riser acceleration vector **A**, which can be obtained from equation (2-22).

2. 4. 4 Vibration Velocities and Displacements

Equation (2-23) gives the in-line and cross-flow vibration accelerations of the riser, and the in-line and cross-flow riser vibration velocities and displacements can then be obtained through single- and double-integration of these accelerations. The equations used for these integration processes are presented here:

$$\left. \begin{aligned}
 v_y(t_{n+1}) &= v_y(t_n) + \frac{1}{2} [a_y(t_n) + a_y(t_{n+1})] \Delta t \\
 v_z(t_{n+1}) &= v_z(t_n) + \frac{1}{2} [a_z(t_n) + a_z(t_{n+1})] \Delta t \\
 y(t_{n+1}) &= y(t_n) + \frac{1}{2} [v_y(t_n) + v_y(t_{n+1})] \Delta t \\
 z(t_{n+1}) &= z(t_n) + \frac{1}{2} [v_z(t_n) + v_z(t_{n+1})] \Delta t
 \end{aligned} \right\} \quad (2-24)$$

$$n = 1, 2, 3, \dots, N$$

where Δt is the sampling time interval, N is the sampling size, t_n is the time instant of sampling, and a_y , a_z , v_y , v_z , y and z are respectively the riser vibration accelerations, velocities and displacements in the in-line and the cross-flow directions.

In order to check the accuracy of the displacements measured by the sensors, a comparison test was conducted. As addressed earlier, there was a displacement transducer on the shaker motion transmission rod. In the comparison test, the shaker provided a displacement time series to the middle of the model riser, which was measured by the displacement transducer. At the same time, the accelerations near the middle of the riser were measured by four pairs of accelerometers at those locations, and then the displacements at the middle of the riser were estimated based on these measured accelerations through equation (2-24); thus, two groups of displacement values were obtained, which respectively come from two independent measurement systems. If the

two groups of results have almost the same values, it can be said that the two independent measurement systems are reliable. Table 2-6 presents the two groups of data at seven shaker frequencies. As seen in Table 2-6, the values of the two groups are close, and this means that the accelerometers and the integration processes are applicable.

Table 2-6 Comparison of the results measured from two independent measurement systems

| test No. | 1 | 2 | 3 | 4 | 5 | 6 | 7 |
|-------------------------------|--------|--------|--------|--------|--------|--------|--------|
| shaker freq. (Hz) | 0.4 | 1.6 | 2.32 | 3.04 | 5.44 | 6.64 | 9.28 |
| by displacement transducer(m) | 0.0393 | 0.0194 | 0.0145 | 0.0091 | 0.0038 | 0.0029 | 0.0014 |
| by accelerometer (m) | 0.0382 | 0.0193 | 0.0143 | 0.0101 | 0.0027 | 0.0031 | 0.0012 |

CHAPTER 3

SHAKER-EXCITATION TESTS

3. Shaker-Excitation Tests

The model tests started with the current-excitation tests and ended with the shaker-excitation tests. However, in this thesis, the results of the shaker-excitation tests will be discussed first. The shaker-excitation tests were designed to determine the properties of the model riser, such as the added mass, the linear and nonlinear hydrodynamic damping, the structural stiffness and the natural frequencies, and these properties can help understand the complicated multi-modal VIV responses for the flexible model riser.

The shaker-excitation tests were performed in the Ice Tank at the Institute for Ocean Technology, the National Research Council of Canada. This tank is 90m in length, 12m in width and 4m in depth, which is the longest ice-towing tank in the world. The model riser was mounted horizontally on the steel frame, and then was placed at a water depth of 1.0m. The shaker was placed on a horizontal beam of the supporting steel frame and gave the excitations to the riser.

3. 1 Experimental Design

As discussed earlier, multi-modal VIV responses depend on the modal parameters of a riser vibration system, such as modal natural frequencies, modal mass, modal damping and modal stiffness, and the modal parameters are influenced by both the structural and hydrodynamic properties of the riser vibration system. For a riser with uniform geometrical and physical properties over its length, the structural and hydrodynamic properties may be thought of as space-independent parameters, namely they do not vary over riser length, so that the continuous governing equations over riser length for riser vibrations, which are shown in Appendix A, can be simplified to an infinite number of uncoupled modal governing equations.

An excitation test can be used to determine the modal parameters of a riser. In such a test, a known excitation (input) is applied to the tested riser, and the riser response (output) is measured by a sensor. Similar to the systems described by Bendat (1998), the frequency response functions (FRF) of the riser vibration system may be obtained based on the relationship between the input and the output, which contain the characteristics of the riser vibration system. The relationship between these FRFs and the modal parameters of the riser can be established through the modal governing equations, and the modal parameters were then estimated based on this relationship. Usually, both of harmonic and random excitations can be used to obtain FRFs for a linear or weakly non-linear system, but the two different excitations may lead to a significant difference in the estimated FRF results if the system is a strongly non-linear system.

In this research, a shaker-excitation test was designed to investigate the modal parameters for the highly flexible model riser. A shaker system was used to generate the

excitation at the middle of the riser. The shaker displacements were regarded as the inputs to the riser vibration system, which were measured by a displacement transducer on the shaker, and the shaker forces were regarded as the outputs from the riser vibration system, which were measured by a load cell mounted on the shaker. The shaker was placed on a horizontal steel beam on the steel frame. Both harmonic and random excitations were applied to the riser, and then the results respectively from the two types of excitations were compared. Three different pretensions were designed for the tests, and the effects of pretension on the modal parameters were investigated. Sixteen pairs of accelerometers inside the riser were used to measure the vibration shapes over riser length. A picture of the apparatus used for the shaker-excitation tests is shown in Figure 3-1.

3. 2 Excitation Design

Harmonic excitation is the most traditional method for a vibration excitation test. The excitation contains one single frequency at a time and the excitation sweeps from one frequency to another with a given step. This excitation is effective for exciting vibration modes, although it may be very time-consuming. When the excitation frequency is tuned to near a modal natural frequency, the response is dominated by that vibration mode, so that the direct modal parameter identification can be made. Random excitation is a stationary random signal, and it contains all frequencies within a frequency range. The random excitation is usually time-saving, but this type of excitation has two major disadvantages: i) as the riser vibration system is actually a nonlinear system with nonlinear hydrodynamic loads, the random excitation has the tendency to linearize the behavior from the measurement data, namely the frequency response function derived

Shaker-excitation tests

from random excitation measurement is the linearized FRF and it is best only for the particular random excitation used (He and Fu, 2001). In other words, we may have a series of linearized FRFs for varying excitation levels; and ii) the fact that either the excitations or the responses are periodic within an infinite time history gives rise to an leakage error, although this error can be reduced through the application of time window functions in digital signal processing (Heylen *et al.* 1998).

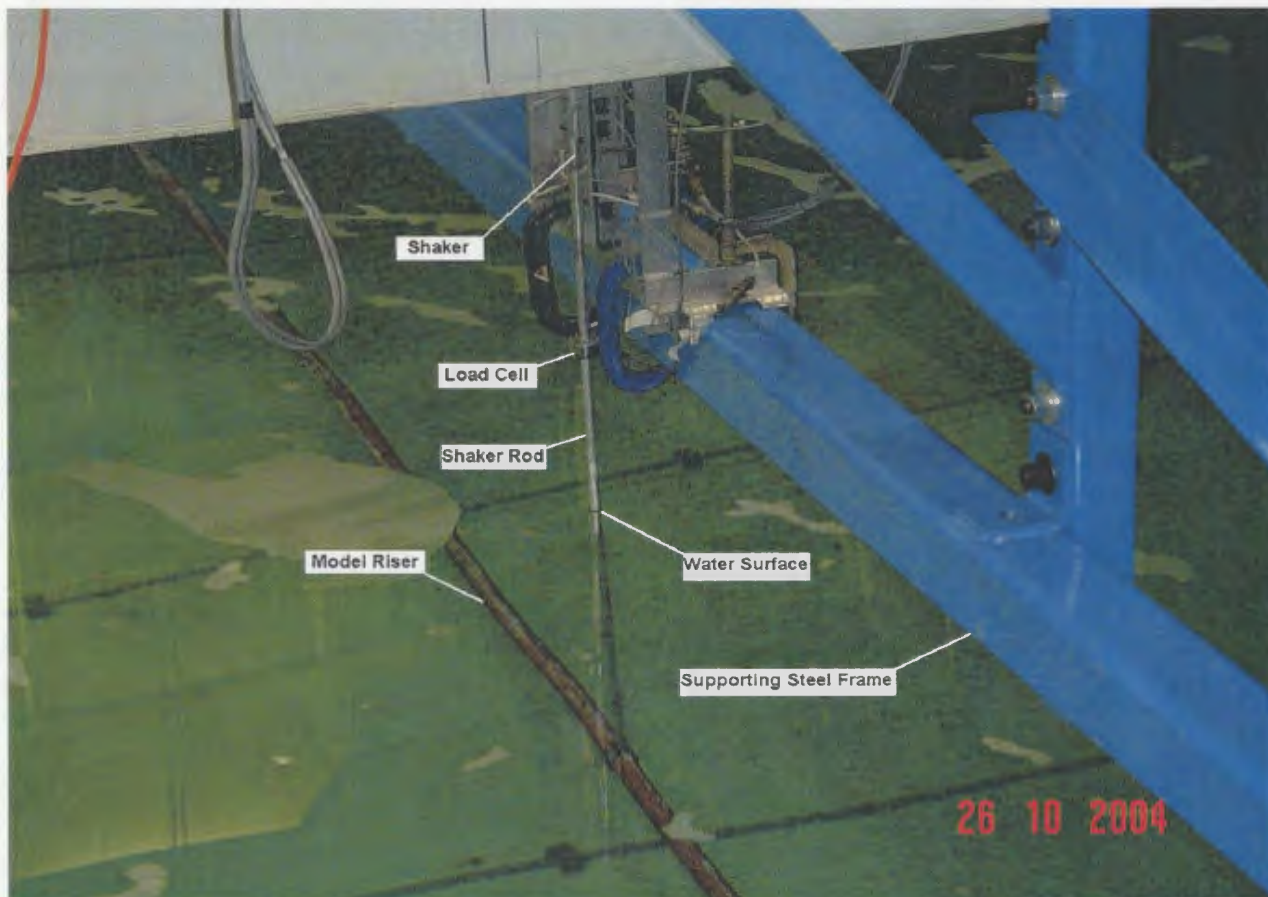


Figure 3-1 Shaker-excitation test

In this research, shaker displacements were considered as the excitation applied to the riser vibration system. The excitation frequencies and amplitudes were designed based on three considerations: i) the resulting riser vibrations must contain the expected modes, namely the excitation frequencies must cover all modal natural frequencies corresponding to all modes of interest; ii) the resulting riser vibrations have amplitudes close to the most often encountered VIV amplitude, i. e. 0.25 to $1.0D$, where: D is the riser diameter; and iii) the shaker motions do not exceed the capacity of the existing shaker provided by Oceanic Consulting Corporation. The reason for the second consideration is that the characteristics of the riser vibration system may depend on the vibration amplitudes, and the use of the shake motion amplitudes close to the most often encountered VIV amplitude may produce more applicable test results than the use of other shaker motion amplitudes.

Eighty harmonic time histories of shaker motion were generated for the harmonic excitation tests. The amplitude versus frequency for these harmonic time histories is shown in Figure 3-2. As shown in Figure 3-2, due to the limit of acceleration of the existing shaker, the time histories with low frequencies were designed to have the amplitudes larger than those with high frequencies.

The time series of the random displacement excitation was obtained from composition of a large amount of harmonic components with random phases, namely the time series was obtained by the following equation:

$$y_s(t) = \sum_{j=1}^n a_j \sin(\omega_j t + \alpha_j)$$

where n is the total amount of the harmonic components, and a_j , ω_j and α_j are respectively the amplitudes, frequencies and phases of these harmonic components. In the

present tests, n took a value of 1601, ω_j ranged from 1.0 to 63 rad/s, α_j took random values ranging from 0 to 2π . The total amount of the harmonic components, n , was selected based on consideration of un-repeatability of the time series of the random displacement excitation during the sampling period. An actual random signal does not repeat itself forever, but the random signal generated by composition of a large amount of harmonic components is a periodic function. The period can be calculated from

$$T = \frac{2\pi}{\Delta\omega}$$

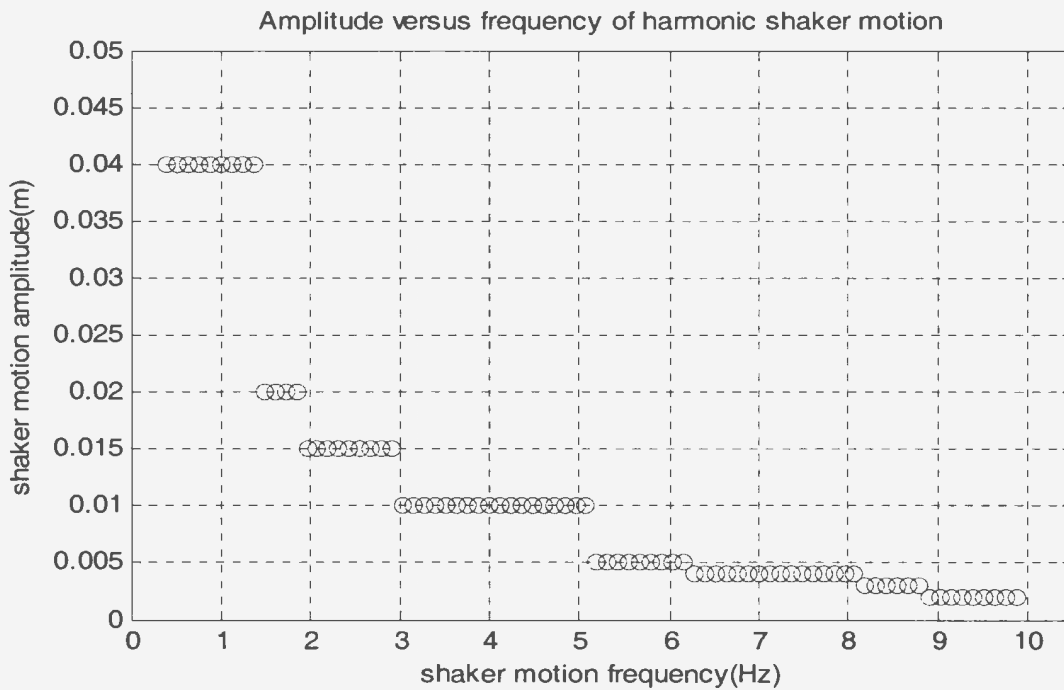


Figure 3-2 Amplitudes and frequencies for harmonic excitations

For a frequency increment of 0.03875(rad/s), which was used in the present tests, the maximum sampling time is 162s, which is longer than actual sampling time of 100s, and this means that an unrepeated time series can be obtained. Figure 3-3 shows the a_j values

used to generate the random excitation, and Figure 3-4 is the time series of random excitation used for the shaker-excitation tests.

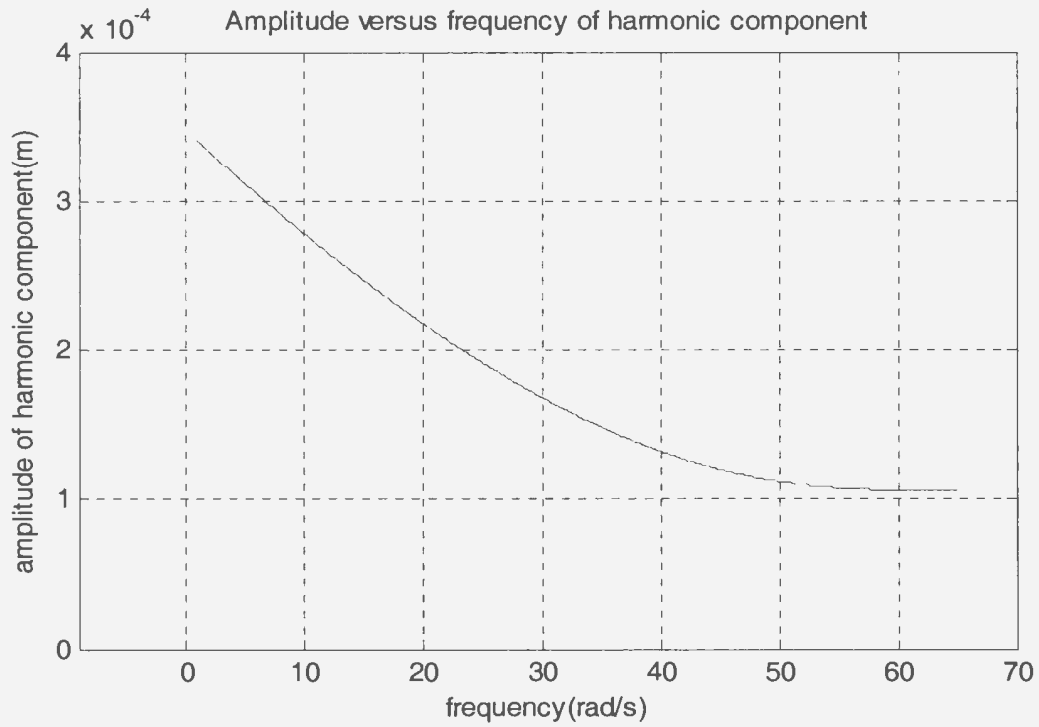


Figure 3-3 Amplitudes of harmonic components for random excitation

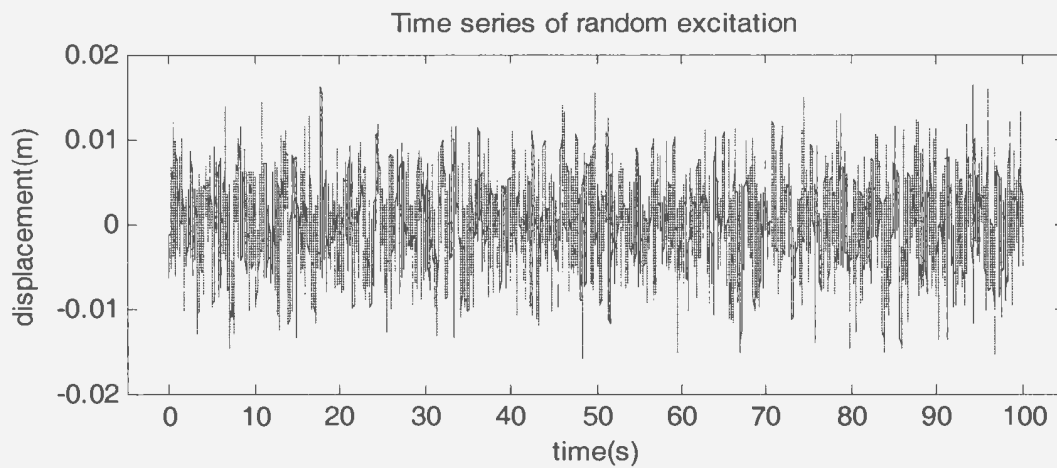


Figure 3-4 Time series of the random excitation used for the tests

3.3 Data Analysis

3.3.1 Modal Governing Equation for Shaker/Riser System

The continuous governing equations over riser length for the structural dynamics of risers are shown in Appendix A. These equations can be employed to describe the shaker excitation/riser response system in calm water. In this case, only the forces and motion in the vertical direction are considered, namely only equations (A-18) and (A-21) will be used for analysis of the data measured from the shaker-excitation tests. As the shaker-excitation tests conducted in calm water, it can be assumed that the vortex-shedding forces do not exist, and the shaker excitation forces can be written as

$$f_s(t, x) = p(t)\delta(x_s)$$

where $p(t)$ is the time series of shaker excitation force, x_s is the shaker position, and the symbol $\delta(\)$ denotes a unit impulse function. Substitute this equation into equation (A-18), and a simplified linear governing equation for the riser vibration response to the shaker excitation can be established as

$$\begin{aligned} [m_s + m_a(x)] \frac{\partial^2 z(t, x)}{\partial t^2} + [c_s + c_a(x)] \frac{\partial z(t, x)}{\partial t} + k_b \frac{\partial^4 z(t, x)}{\partial x^4} - T \frac{\partial^2 z(t, x)}{\partial x^2} \\ = p(t)\delta(x_s) \end{aligned} \quad (3-1)$$

where $z(t, x)$ is the riser vibration displacement, m_s the structural mass, m_a the added mass, c_s the structural damping, c_a the linear hydrodynamic damping, k_b the bending stiffness of the riser, and T the tension acting on the riser.

The added mass and hydrodynamic damping in equation (3-1) is space-dependent, and they can be written in the Fourier series form as

$$\left. \begin{aligned} m_a(x) &= m_{a0} + \sum_{j=1}^{\infty} m_{aj} \cos\left(\frac{j\pi x}{L}\right) \\ c_a(x) &= c_{a0} + \sum_{j=1}^{\infty} c_{aj} \cos\left(\frac{j\pi x}{L}\right) \end{aligned} \right\} \quad (3-2)$$

where L is the riser length, and m_{aj} and c_{aj} are defined by

$$\begin{aligned} m_{aj} &= \frac{2}{L} \int_0^L m_a(x) \cos\left(\frac{j\pi x}{L}\right) dx \\ c_{aj} &= \frac{2}{L} \int_0^L c_a(x) \cos\left(\frac{j\pi x}{L}\right) dx \end{aligned}$$

Consider the boundary conditions represented by equation (A-21) in Appendix A, and the vibration displacement can be written in the Fourier series form as

$$z(t, x) = \sum_{k=1}^{\infty} z_k(t) \sin\left(\frac{k\pi x}{L}\right) \quad (3-3)$$

where $z_k(t)$ are the modal components of the riser vibration responses, which are defined by

$$z_k(t) = \frac{2}{L} \int_0^L z(t, x) \sin\left(\frac{j\pi x}{L}\right) dx \quad (3-4)$$

Substituting equations (3-2) and (3-3) into equation (3-1) leads to

$$\begin{aligned} &(m_s + m_{a0}) \sum_{k=1}^{\infty} \ddot{z}_k(t) \sin\left(\frac{k\pi x}{L}\right) + (c_s + c_{a0}) \sum_{k=1}^{\infty} \dot{z}_k(t) \sin\left(\frac{k\pi x}{L}\right) + \\ &\sum_{k=1}^{\infty} \left[k_b \left(\frac{k\pi}{L}\right)^4 + T \left(\frac{k\pi}{L}\right)^2 \right] z_k(t) \sin\left(\frac{k\pi x}{L}\right) + \sum_{j=1}^{\infty} m_{aj} \cos\left(\frac{j\pi x}{L}\right) \sum_{k=1}^{\infty} \ddot{z}_k(t) \sin\left(\frac{k\pi x}{L}\right) + \\ &\sum_{j=1}^{\infty} c_{aj} \cos\left(\frac{j\pi x}{L}\right) \sum_{k=1}^{\infty} \dot{z}_k(t) \sin\left(\frac{k\pi x}{L}\right) = p(t) \delta(x_s) \end{aligned}$$

Multiplying the two sides of the equation above with the expression $\sin(n\pi x/L)$, $n=1,2,3,\dots$, and integrating over the riser length yields the modal governing equations in the time-domain as

$$\begin{aligned} & \frac{(m_s + m_{a0})L}{2} \ddot{z}_n(t) + \frac{(c_s + c_{a0})L}{2} \dot{z}_n(t) + \frac{L}{2} \left[k_b \left(\frac{n\pi}{L} \right)^4 + T \left(\frac{n\pi}{L} \right)^2 \right] z_n(t) + \\ & \sum_{k=1}^{\infty} \sum_{j=1}^{\infty} I_{nj k} m_{aj} \ddot{z}_k(t) + \sum_{k=1}^{\infty} \sum_{j=1}^{\infty} I_{nj k} c_{aj} \dot{z}_k(t) = p(t) \sin\left(\frac{n\pi x_s}{L}\right) \end{aligned} \quad (3-5)$$

where

$$I_{nj k} = \int_0^L \sin\left(\frac{n\pi x}{L}\right) \cos\left(\frac{j\pi x}{L}\right) \sin\left(\frac{k\pi x}{L}\right) dx$$

Letting n and k be equal to $1, 2, 3, \dots, r$, and taking Fourier transform of two sides of equation (3-5) leads to the modal governing equations in the frequency domain in matrix form as

$$(-\omega^2 [A] + [C] + i\omega [B]) \{Z(\omega)\} = \{S\} P(\omega) \quad (3-6)$$

where i is the imaginary unit, $\{Z(\omega)\}$ is the vector of Fourier transform of the modal response components $z_k(t)$, $P(\omega)$ is Fourier transform of the shaker force, and $[A]$, $[B]$ and $[C]$ are respectively the matrices of the modal mass, modal damping and modal stiffness.

The vector $\{S\}$ and the elements of these matrices have the forms as follows:

$$\begin{aligned} \{S\} &= \left[\sin\left(\frac{\pi x_s}{L}\right) \quad \sin\left(\frac{2\pi x_s}{L}\right) \quad \sin\left(\frac{3\pi x_s}{L}\right) \quad \dots \quad \sin\left(\frac{r\pi x_s}{L}\right) \right]^T \\ A_{nk} &= \frac{(m_s + m_{a0})L}{2} \delta_{nk} + \sum_{j=1}^{\infty} m_{aj} I_{nj k} \\ B_{nk} &= \frac{(c_s + c_{a0})L}{2} \delta_{nk} + \sum_{j=1}^{\infty} c_{aj} I_{nj k} \\ C_{nk} &= \frac{L}{2} \left[k_b \left(\frac{n\pi}{L} \right)^4 + T \left(\frac{n\pi}{L} \right)^2 \right] \delta_{nk} \\ n, k &= 1, 2, 3, \dots, r \end{aligned}$$

where the symbol δ_{nk} denotes an impulse function, which is equal to 1 when n is equal to k and is equal to 0 when n is not equal to k , and A_{nk} , B_{nk} and C_{nk} are the elements of matrices $[A]$, $[B]$ and $[C]$.

3. 3. 2 Relationship between Shaker Displacement and Shaker Force

The modal governing equations give the relationship between the shaker force and the modal responses. In fact, the shaker displacement $z_s(t)$ is equal to the riser vibration displacement at the shaker location. Equation (3-3) gives the riser vibration displacement at the shaker location x_s in the form as

$$z_s(t) = \sum_{k=1}^{\infty} z_k(t) \sin\left(\frac{k\pi x_s}{L}\right)$$

Letting $k=1,2,3,\dots, r$, Fourier transform of this equation leads to

$$Z_s(\omega) = \{S\}^T \{Z(\omega)\} \quad (3-7)$$

where $Z_s(\omega)$ is Fourier transform of the shaker displacement $z_s(t)$, and $\{Z(\omega)\}$ is the vector of Fourier transform of the modal response components $z_k(t)$.

From equations (3-6) and (3-7), we have the relationship between the shaker force and the shaker displacement as follows:

$$Z_s(\omega) = \{S\}^T [G] \{S\} P(\omega) \quad (3-8)$$

where $[G]$ is a matrix with the form:

$$[G] = \left(-\omega^2 [A] + [C] + i\omega [B] \right)^{-1}$$

3. 3. 3 Frequency Response Function for Shaker/Riser System

Frequency response functions (FRF) reveal the fundamental characteristics of a linear input/output system in the frequency-domain. The inverse of FRF is called dynamic stiffness (DS) (He and Fu, 2001). The FRF or DS can be obtained by the relationship between inputs and outputs. For the shaker excitation/riser response system used for this research, the input is the shaker motion displacement, or the riser vibration displacement

at the middle of the riser, and the output is the shaker force. For harmonic excitations, the FRF can be conveniently calculated from the amplitudes and phases of the harmonic input and output. Specifically, the DS function can be estimated based on the following equation:

$$H(\omega) = \frac{a_q(\omega)}{a_v(\omega)} [\cos \chi(\omega) + i \sin \chi(\omega)]$$

where $a_q(\omega)$ is the amplitude of the harmonic output, $a_v(\omega)$ is the amplitude of the harmonic input and $\chi(\omega)$ is the phase difference between the input and the output.

For random excitations, the DS function can be estimated based on the auto- and cross-spectral functions of the random input and the random output. Generally, the dynamic characteristics of a linear input $v(t)$ /output $q(t)$ system can be described by a weighting function $h(\tau)$, and the time-domain relationship between the input $v(t)$ and the output $q(t)$ can be established as

$$q(t) = \int_{-\infty}^{\infty} h(\tau)v(t - \tau)d\tau \quad (3-9)$$

From equation (3-9), two expressions of DS function can be obtained. Fourier transform of equation (3-9) gives the first expression as follows:

$$Q(\omega) = H(\omega)V(\omega) \quad (3-10)$$

where $H(\omega)$, $Q(\omega)$ and $V(\omega)$ respectively denote Fourier transforms of $h(\tau)$, $q(t)$ and $v(t)$.

According to equation (3-9), the product $v(t)q(t+\tau)$ is given by

$$v(t)q(t + \tau) = \int_{-\infty}^{+\infty} h(\xi)v(t)v(t + \tau - \xi)d\xi \quad (3-11)$$

Fourier transform of two sides of equation (3-11) yields the second expression of the DS function as follows:

$$S_{vv}(\omega)H(\omega) = S_{vq}(\omega) \quad (3-12)$$

where the symbols $S_{vv}(\omega)$ and $S_{vq}(\omega)$ respectively denote Fourier transforms of the auto-correlation function of $v(t)$ and the cross-correlation function of $v(t)$ and $q(t)$, namely the auto-spectral density function of $v(t)$ and the cross-spectral density function of $v(t)$ and $q(t)$.

For the shaker excitation/riser response system used for the present tests, equations (3-10) and (3-12) can be written as

$$\begin{cases} P(\omega) = H(\omega)Z_s(\omega) \\ S_{zp}(\omega) = H(\omega)S_{zz}(\omega) \end{cases} \quad (3-13)$$

where $H(\omega)$ is the DS function of the riser, $P(\omega)$ and $Z_s(\omega)$ are respectively Fourier transforms of the shaker force and the shaker displacement $z_s(t)$, and $S_{zz}(\omega)$ and $S_{zp}(\omega)$ are respectively the auto-correlation function of $z_s(t)$ and the cross-correlation functions of $z_s(t)$ and $p(t)$.

3. 3. 4 Estimate of Modal Parameters

Assume that the structural and hydrodynamic properties are constant in space, and the matrices $[A]$, $[B]$ and $[C]$ in equation (3-6) become diagonal matrices. This means that the modal responses $z_k(t)$ are no longer coupled to each other. In this case, as the shaker was placed at the middle of the riser, i. e. $x_s=0.5L$, equation (3-6) can be written as

$$Z_n(\omega) = \frac{(-1)^{n+1} P(\omega)}{-\omega^2 A_{nn} + C_{nn} + i\omega B_{nn}} \quad (3-14)$$

$n = 1, 2, 3, \dots, r$

where $Z_n(\omega)$ is Fourier transform of the modal response $z_n(t)$.

Consider the resonance region for the n -th mode. In this region, we assume that the responses of the n -th mode are much bigger than the responses of other modes (this

assumption can be verified by the test results of the vibration modes addressed later in this thesis), so that the responses of other modes can be ignored, namely equation (3-7) becomes

$$Z_s(\omega) \approx (-1)^{n+1} Z_n(\omega) \quad (3-15)$$

Thus, from equations (3-13), (3-14) and (3-15), we have the relationship between the modal parameters and the DS function as

$$-\omega^2 A_{nn} + C_{nn} + i\omega B_{nn} \approx \frac{P(\omega)}{Z_s(\omega)} = \frac{S_{zp}(\omega)}{S_{zz}(\omega)} = H(\omega) \quad (3-16)$$

Note that there is a linear relationship between the real part of $H(\omega)$ and ω^2 in equation (3-16), namely

$$R_e[H(\omega)] = R_e\left[\frac{S_{zp}(\omega)}{S_{zz}(\omega)}\right] \approx -\omega^2 A_{nn} + C_{nn}$$

Obviously, the slope is related to the modal mass A_{nn} , and the intercept is related to the modal stiffness C_{nn} . This linear relationship provides a way to estimate the modal parameters A_{nn} and C_{nn} using a linear fit based on $H(\omega)$. The modal natural frequency ω_n and the modal damping can then be estimated using the following formulae:

$$\omega_n = \sqrt{\frac{C_{nn}}{A_{nn}}}$$

$$B_{nn} = \frac{1}{\omega_n} I_m \left[\frac{S_{zp}(\omega_n)}{S_{zz}(\omega_n)} \right]$$

3.4 Test Results

Three pretensions of 500, 700 and 900N were designed for the shaker-excitation tests, and the vibration shapes at different excitation frequencies, the frequency response

functions, and the modal parameters were investigated. The results at the three pretensions can be used to determine a function between the modal parameters and the tensions acting on the riser, and this function, along with the function between the tension and the current velocity, is expected to provide a picture of the modal parameters over a wide current velocity region.

3. 4. 1 Test Results at Pretension of 500N

The first pretension was 500N. It was the lowest pretension for the shaker-excitation tests. Fifty three harmonic excitations with different frequencies and a random excitation were used. The shaker control signals were created prior to the tests using a Matlab program based on the methods described in Section 3. 2. These excitations were given to the mid-point of the model riser.

3. 4. 1. 1 Frequency Response Functions

A magnitude plot of the frequency response function clearly exhibits the resonances with peaks and the anti-resonances with minima. In this research, both harmonic and random excitations were used to obtain the frequency response functions. Fifty three frequencies ranging from 0.5 to 10Hz, which are shown in Figure 3-2, were used for the harmonic excitation tests, while the time series of random excitations, which is shown in Figure 3-4, was used for the random excitation tests.

The measured time histories of the random shaker force and displacement are shown in Figure 3-5. It is noted that the measured shaker displacements are a little smaller than the expected shaker displacements shown in Figure 3-4.

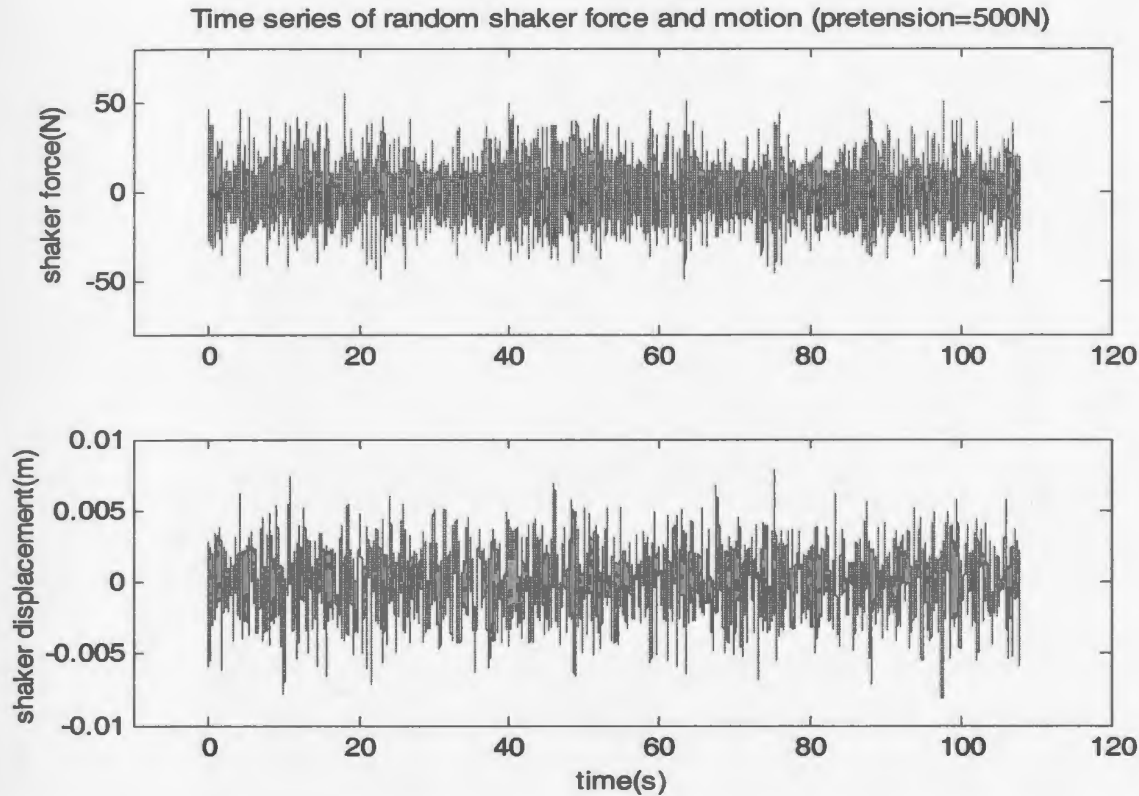


Figure 3-5 The measured shaker force and shaker motion at a pretension of 500N

The auto-spectral density functions of the shaker displacement and the cross-spectral density function of the shaker displacement and shaker excitation force were estimated based on the methods shown in Appendix B. Figure 3-6 shows the estimated auto-spectral density function of the shaker displacement, and Figure 3-7 shows the estimated cross-spectral density function of the shaker displacement and shaker force. The Parzen window function was used to reduce the leakage errors. As seen in Figure 3-6, the values of auto-spectral function of the shaker displacement are close to zero at the frequencies higher than 7.8Hz, and this indicates that these frequencies may exceed the capability of the shaker, so that the shaker could not generate the components with these frequencies, even though the digital signals contain these components.

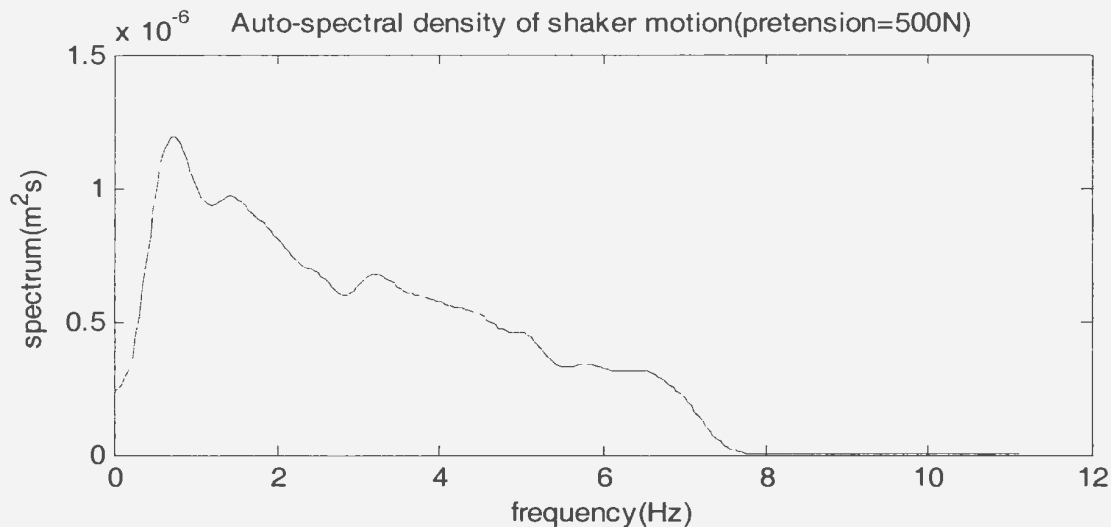


Figure 3-6 The estimated auto-spectral density function of the shaker motion at a pretension of 500N

There are several peaks and minima in Figure 3-7. The peaks correspond to the resonances and the minima to the anti-resonances. It is noted that, in similarity to Figure 3-6, the values of cross-spectral function of the shaker displacement and shaker force are close to zero at the frequency higher than 7.8Hz. Figure 3-8 presents the results of frequency response function between the shaker force and the shaker displacement using fifty three harmonic excitations and a random excitation. A major feature for the dynamic characteristics of a flexible riser is that there are a number of modal natural frequencies, which corresponding to a number of mode shapes, and these modal natural frequencies are represented by the peaks in the frequency response function, as seen in Figure 3-8.

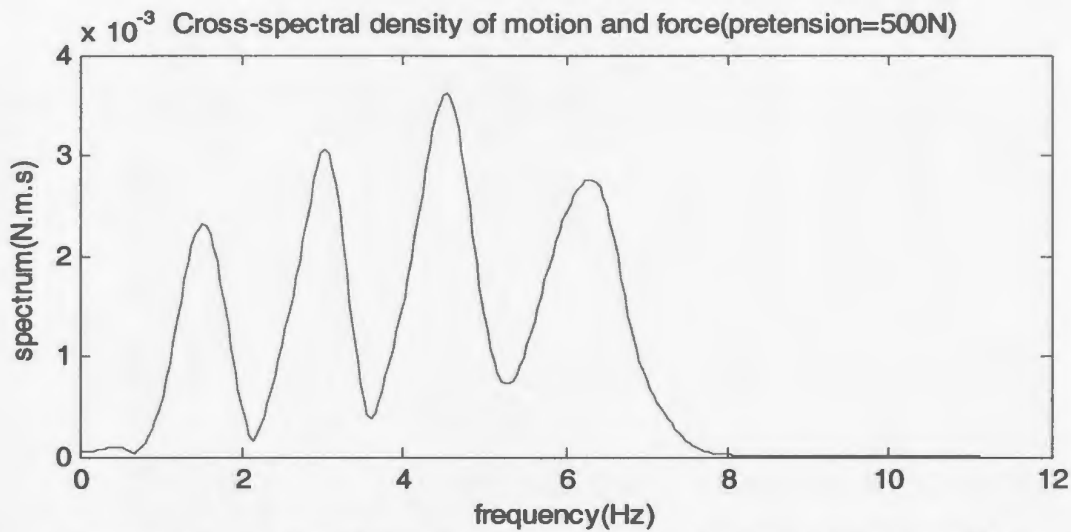


Figure 3-7 The estimated cross-spectral density function of the shaker motion and the shaker force at a pretension of 500N

According to the basic theory of vibration, the maximum displacement responses occur when the excitation frequencies are equal to the damped natural frequencies ω_{dn} (Chakrabarti, 2002), defined as

$$\omega_{dn} = \omega_n \sqrt{1 - \zeta_n^2}$$

where ζ_n is the damping factor. For a flexible riser, the damping factor ζ_n is defined as

$$\zeta_n = \frac{B_{nn}}{2A_{nn}\omega_n}$$

where ω_n , A_{nn} and B_{nn} are respectively the modal natural frequency, modal mass and modal damping for the n -th mode. Obviously, the damped natural frequencies are approximately equal to the undamped natural frequencies for a small-damping system, while the damped natural frequencies may have considerable difference from the undamped natural frequency for a big-damping system. This means that the frequencies at the peaks of FRF are approximately equal to the natural frequencies for a riser with small-damping.

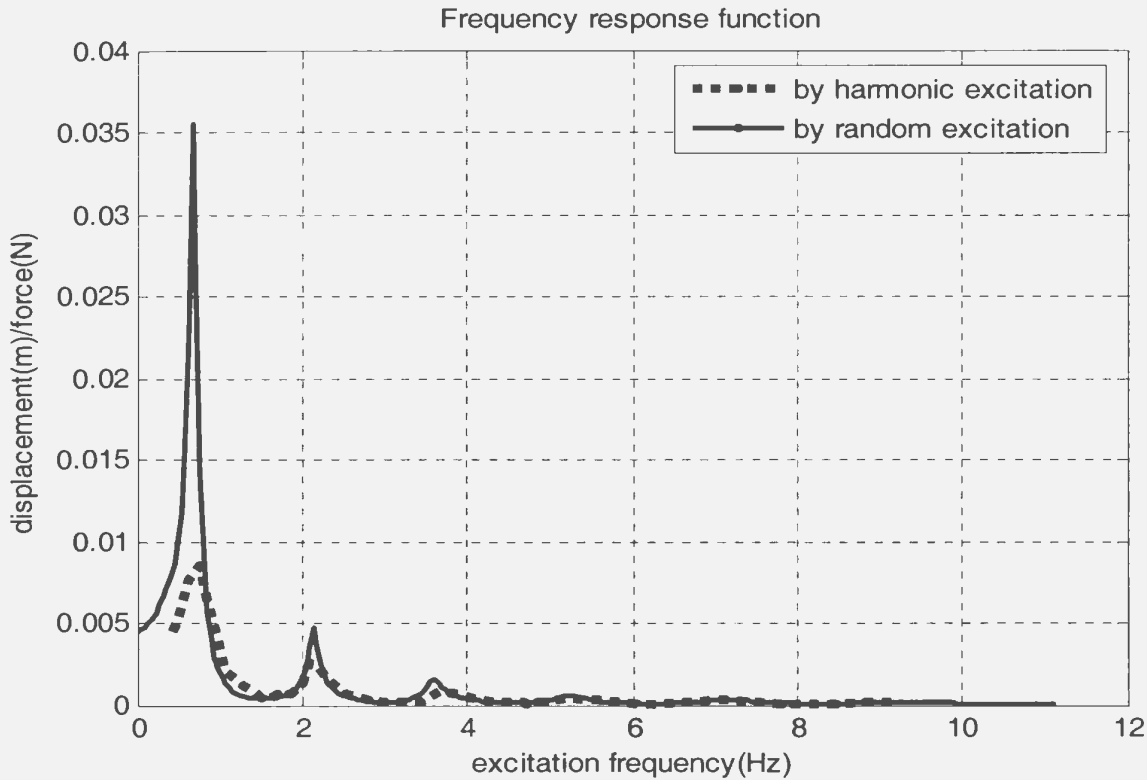


Figure 3-8 Amplitude of frequency response function of the riser in calm water at a pretension of 500N

In this research, as the riser had a symmetric structure over its length and the shaker was placed at the middle of the model riser, the riser vibration had a shape approximately symmetrical with respect to the mid-point of the riser. This causes the even vibration modes, such as mode 2, 4, 6 and so on, not to appear and the peaks only correspond to the natural frequencies for the odd vibration modes. In other words, the first peak in the FRF function corresponds to the natural frequency for the first mode; the second peak corresponds to the natural frequency for the third mode; the third peak corresponds to the natural frequency for the fifth mode; and so on.

The test results exhibit, as expected, that the lower mode shapes have lower natural frequencies, while the higher mode shapes have higher natural frequencies. It is noted

that the peaks corresponding to the low mode shapes are greater than those corresponding to the high mode shapes.

Figure 3-8 also gives a comparison of the frequency response functions respectively obtained from the harmonic and random excitation tests. As seen in Figure 3-8, there are considerable differences between the results from the two types of excitations in the peak regions and in the low frequency region from 0.25 to 0.8Hz. In these regions, the values of the frequency response function estimated from the random excitation tests are much larger than those estimated from the harmonic excitation tests. A possible explanation for these differences is that the vibration amplitudes in the resonance regions and the low frequency region were relatively large, and the relatively large amplitudes may cause the relatively large non-linear effects. It is well known that the damping force acting on a cylinder vibrating in water is proportional to the square of vibration velocity, and this induces a nonlinear effect on the vibration of the cylinder. For a relatively strong non-linear system, the different excitation patterns would result in a big difference in the estimated frequency response functions. The fact that relatively large nonlinear effects exist in the low frequency region and the resonance regions will also be verified by the nonlinear analysis results later.

It is noted that the difference between the two estimated frequency response functions demonstrates a decreasing trend as the excitation frequencies become higher, and this means that the non-linear effects decreased as the excitation frequencies become higher. This resulted from the excitation amplitudes which were designed to decrease with the frequency, as shown in Figures 3-2 and 3-3.

A sharp peak implies small damping. The peaks in the frequency response function estimated from the random excitation tests are sharper than those in the frequency response function estimated from the harmonic excitation tests, and this implies that the modal damping in the random excitation tests may be smaller than that in the harmonic excitation tests. It is also noted that the difference in sharpness of the peaks exhibits a decreased trend as the excitation frequency increases. In fact, it is easy to understand these results. In the low frequency region, the shaker vibration amplitudes for the harmonic excitation tests were designed to be greater than those for the random excitation tests, and the damping forces in the harmonic excitation tests were of course greater than those in the random excitation tests. In high frequency region, the amplitudes of the harmonic shaker vibration were designed to be close to the average amplitude of the random shaker vibration and, as a result, the difference in sharpness of the peaks becomes small.

The peak frequencies in the FRFs, however, seem to be less dependent on the excitation patterns than the peak magnitude values, and this means that different excitation patterns have smaller effects on the estimated modal natural frequencies than on the estimated modal damping.

3.4.1.2 Vibration Modes

Through the use of the accelerometers at sixteen locations inside the model riser, a clear vibration shape over the riser length can be observed. The vibration shapes depend on the shaker excitation frequencies, and it is expected that the vibration shapes with single dominant mode are excited at the frequencies close to the modal natural

frequencies, while the vibration shapes with mixed dominant modes are excited at the frequencies far away from the modal natural frequencies. The indication of a vibration shape with single dominant mode is relatively clear nodes of vibration over riser length.

Ten excitation frequencies of 0.88, 1.48, 2.20, 3.04, 4.00, 4.72, 5.68, 6.16, 7.60 and 8.20Hz were chosen to check the vibration shapes. From Figure 3-8, it is known that the frequencies of 0.88, 2.20, 4.00, 5.68 and 7.60Hz are close to the modal natural frequencies of mode 1, 3, 5, 7 and 9, and the frequencies of 0.48, 3.04, 4.72, 6.16 and 8.20Hz are far away from these modal natural frequencies. Figures 3-9 to 3-18 show the vibration shapes at the ten excitation frequencies. Note that the vibration shape at the locations from $x=5.27\text{m}$ to $x=6.47\text{m}$ may have been skewed due to the lack of the measurement at these locations. Also, as these vibration shapes are snapshots over a short time period, they are only representatives of the vibrations during the whole vibration period. The corresponding time series of the harmonic displacement excitation are also shown in these figures, but the cut-offs (unsmooth at the peaks) in the plots of these time series are not true. The actual sampling frequency was 50Hz in the model tests, but smaller than 50Hz sampling frequencies were chosen to plot these figures so that the clear snapshots could be obtained. These smaller sampling frequencies produced the cut-offs; these cut-offs are, therefore, not true.

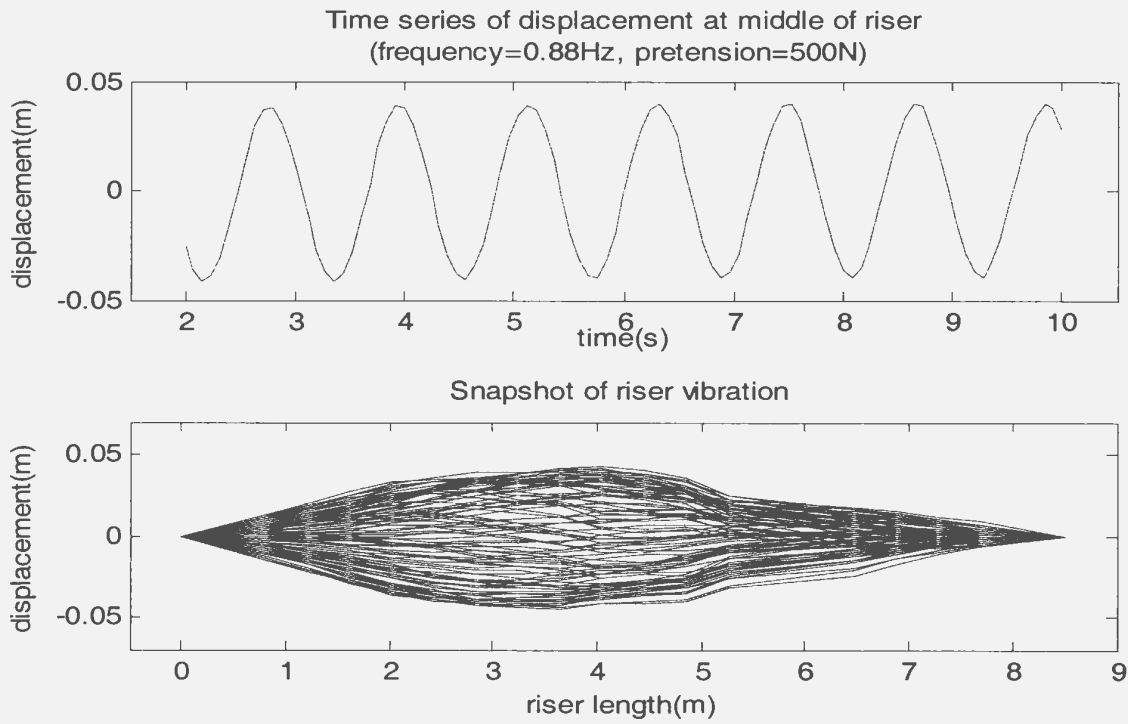


Figure 3-9 Vibration shape at an excitation frequency of 0.88Hz

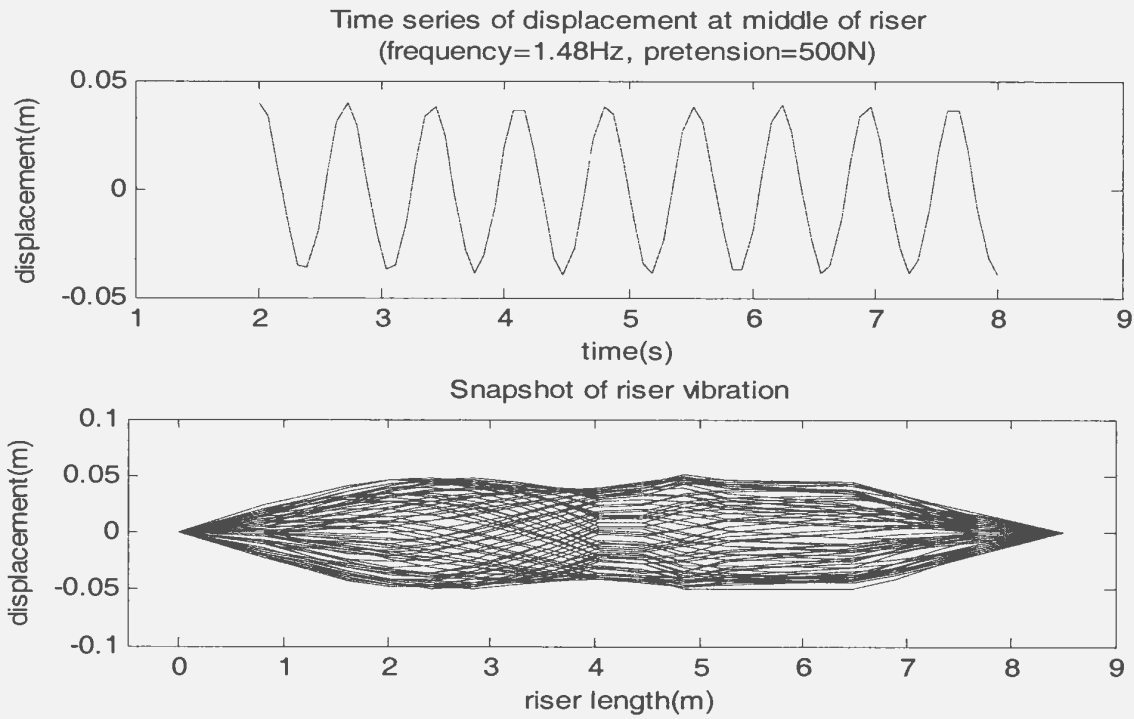


Figure 3-10 Vibration shape at an excitation frequency of 1.48Hz

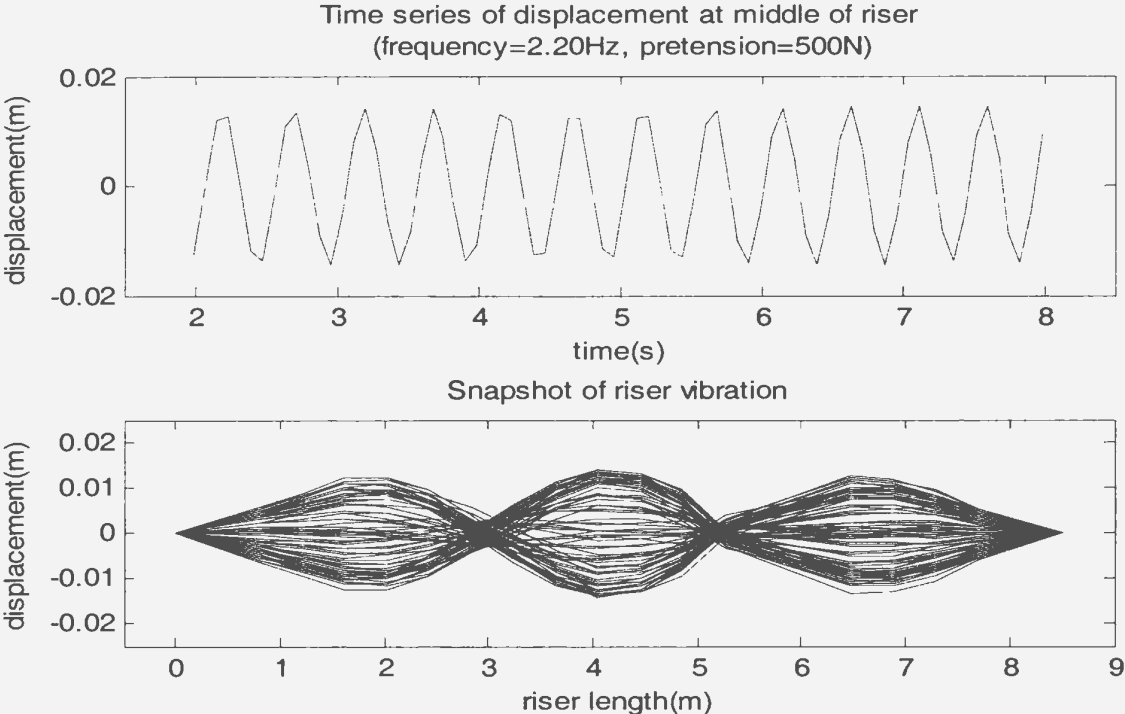


Figure 3-11 Vibration shape at an excitation frequency of 2.20Hz

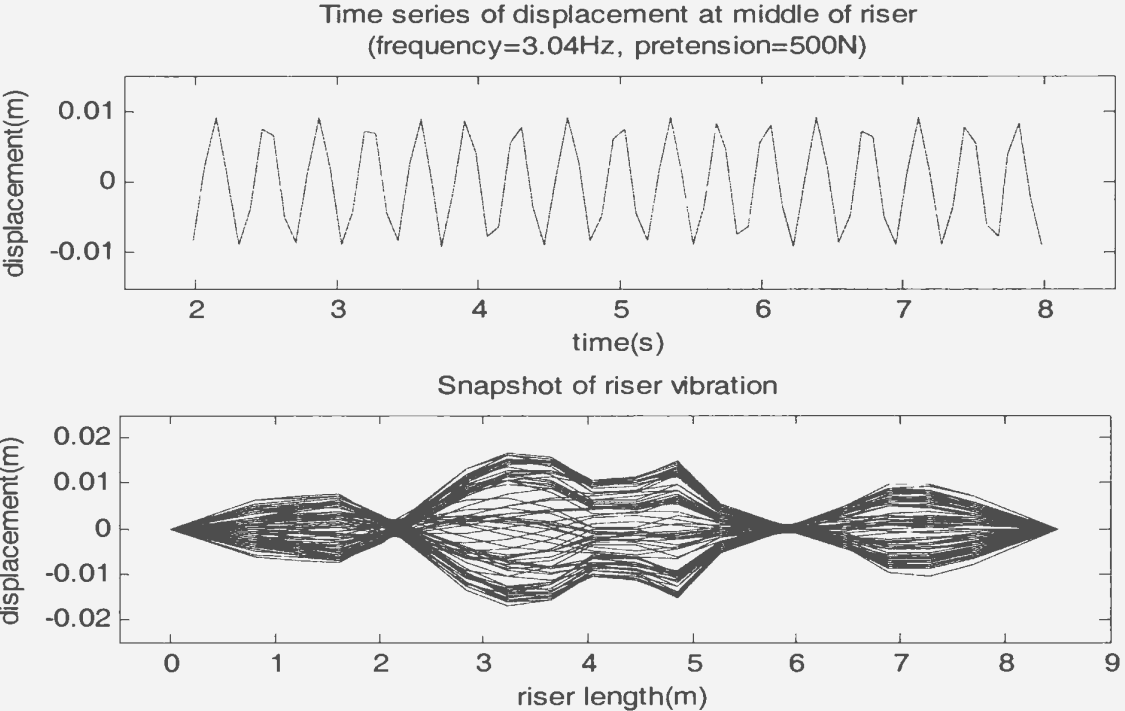


Figure 3-12 Vibration shape at an excitation frequency of 3.04Hz

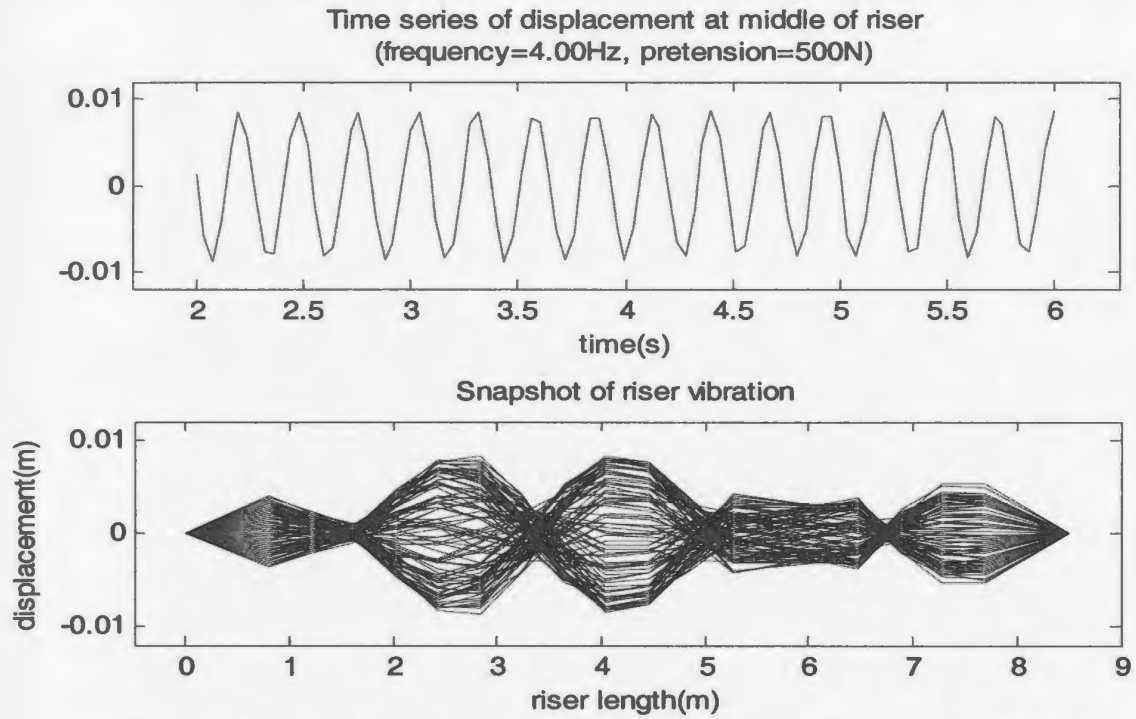


Figure 3-13 Vibration shape at an excitation frequency of 4.00Hz

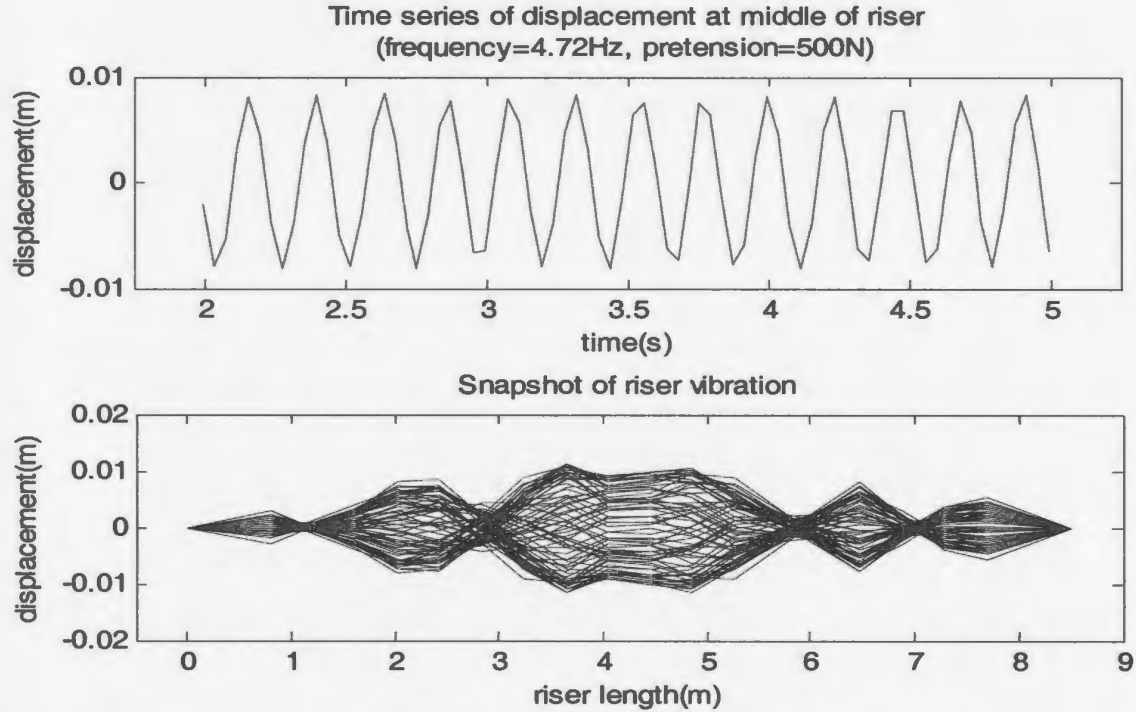


Figure 3-14 Vibration shape at an excitation frequency of 4.72Hz

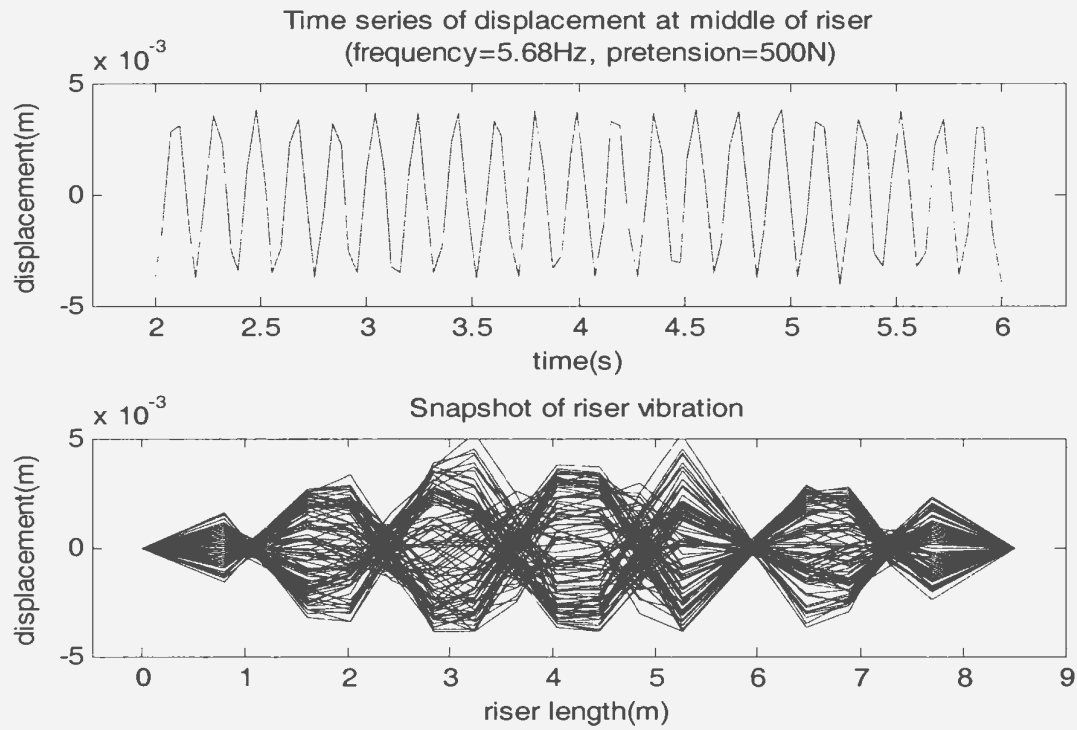


Figure 3-15 Vibration shape at an excitation frequency of 5.68Hz

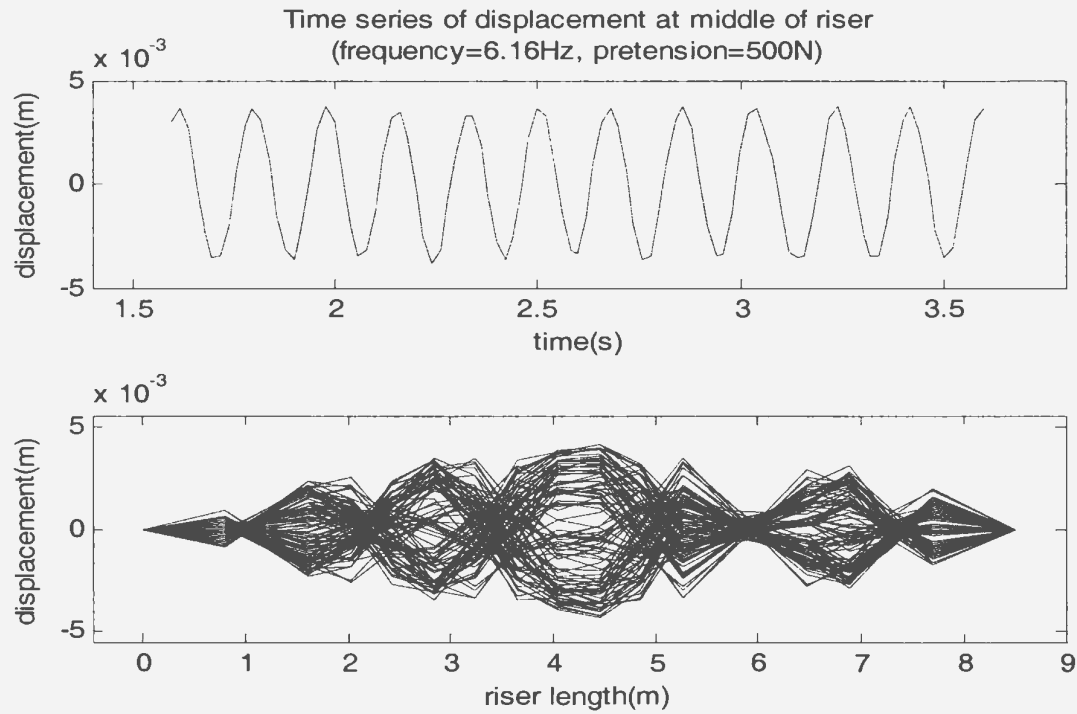


Figure 3-16 Vibration shape at an excitation frequency of 6.16Hz

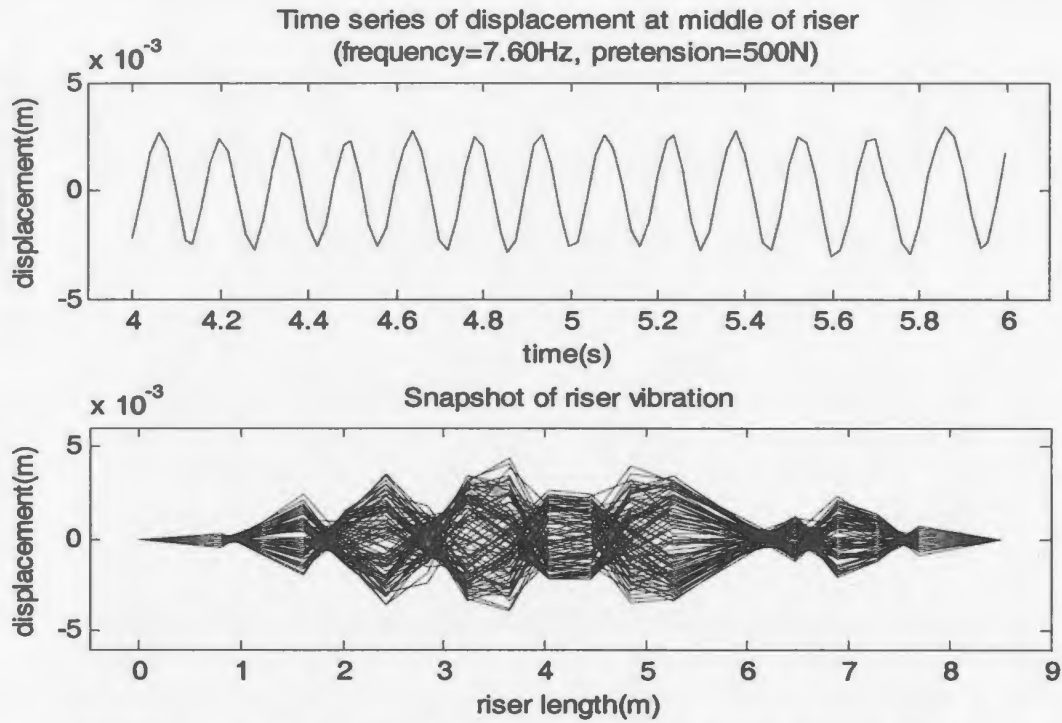


Figure 3-17 Vibration shape at an excitation frequency of 7.60Hz

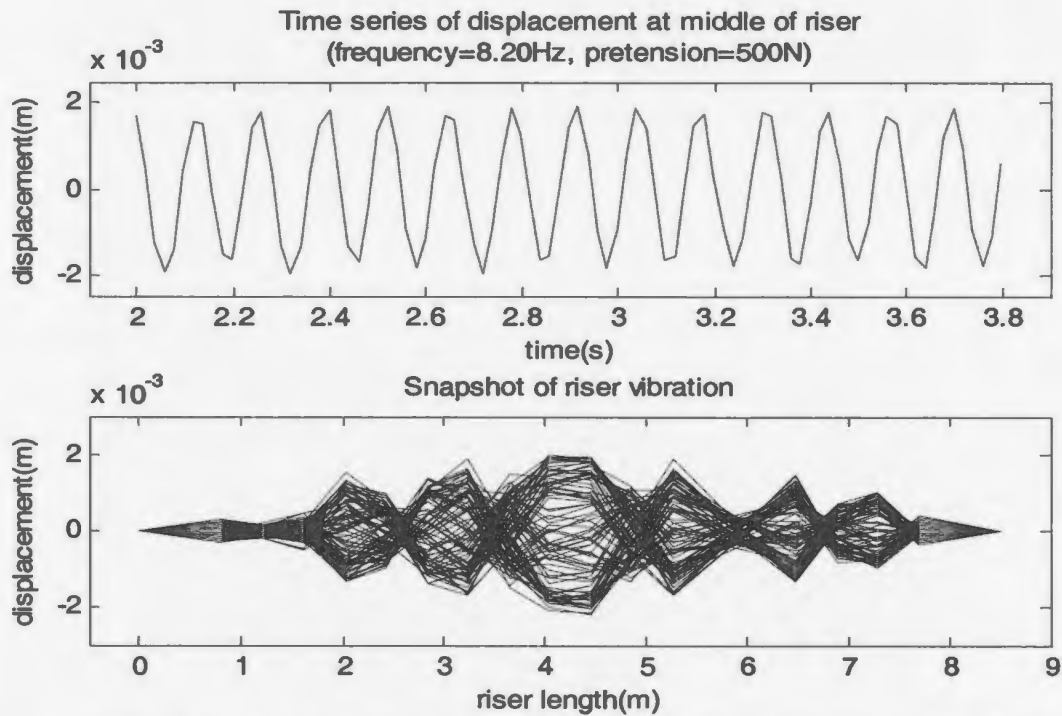


Figure 3-18 Vibration shape at an excitation frequency of 8.20Hz

As seen in Figures 3-9, 3-11, 3-13, 3-15 and 3-17, the excitation frequencies close to the modal natural frequencies excite the nearly single dominant mode vibrations with relatively clear nodes. These dominant modes are respectively mode 1, 3, 5, 7 and 9, and they are close to the sinusoidal mode shapes, especially for the low modes. These results endorse the assumption that in the resonance regions the modal responses corresponding to the resonance mode is much larger than the modal responses corresponding to other modes, which was addressed earlier to establish the method to estimate the modal parameters based on FRFs.

It is also noted that these vibration shapes are not exact sinusoidal mode shapes, especially for the higher modes. The vibration amplitudes at the locations close to the riser ends are smaller than those at the locations near the middle of the riser, and this resulted from the damping of the riser (Vandiver and Chung, 1988). Vandiver and Chung analyzed the Green's function of a finite cable with tension and uniformly distributed mass. The vibration shape of the cable is called the Green's function when a unit harmonic force acts at a single point on the cable. For the special case that a unit harmonic force acts at the mid-point of the cable, the Green's function is an exact sinusoidal shape if the value of $n\zeta_n$ is equal to zero, while the values of the Green's function at the locations near the ends of the cable trend to zeros if the value of $n\zeta_n$ is much larger than 1, where n is the mode number and ζ_n is the damping factor, meaning that the waves are damped out traveling from the middle to the ends of the riser. For other values of $n\zeta_n$, the vibration amplitudes at the locations close to the cable ends are smaller than those at the locations near the middle of the cable, as observed in this research.

As seen in Figures 3-5, 3-7, 3-9, 3-11 and 3-13, the mixed dominant mode vibration shapes appeared as the excitation frequencies were far away from the modal natural frequencies.

3.4.1.3 Modal Parameters

As discussed earlier, the modal parameters including modal mass, modal damping, modal stiffness and modal natural frequency can be estimated by dynamic stiffness (DS) functions. Over resonance regions, the real part of DS function is approximately a linear function of the square of excitation frequency, if the modal mass is weakly dependent on the excitation frequency. The modal mass can be estimated from the slope of the linear function, and the modal stiffness can be estimated from the intercept of the linear function. In this research, in order to estimate the modal mass and the modal stiffness, a plot of the real part of DS function versus frequency-squared was first made, and the linear fits were then conducted in the resonance regions.

Figure 3-19 shows the real part of the DS function versus the frequency-squared at a pretension of 500N, which was obtained from the harmonic excitation tests. As seen in Figure 3-19, the real part of the dynamic stiffness starts with a positive value at the lowest frequency, and then it decreases with the excitation frequency. It changes its sign in the resonance region for the first mode. In the resonance region, the value of the real part of the dynamic stiffness function exhibits a relatively good linear relationship with the excitation frequency-squared. At the excitation frequency of 1.8Hz, the value of the real part of the dynamic stiffness function jumps from the first mode-dominant region to the third mode-dominant region and its sign becomes positive again. These phenomena

repeat in the third mode-dominant region and other mode-dominant regions. The good linearity in the resonance regions verifies that the added mass of the riser is weakly dependent of the excitation frequency, so that the assumption that the hydrodynamic properties do not depend on the frequency is applicable over a small frequency range, such as a modal resonance region. The good linear characteristics of the real part of DS function also ensure that a good linear fit can be achieved.

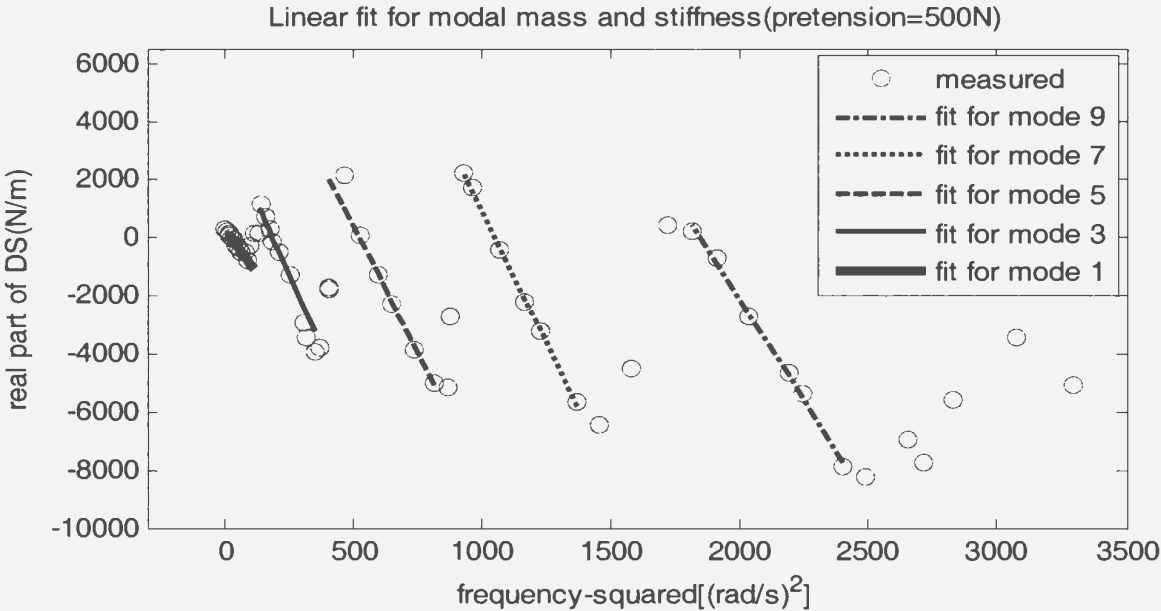


Figure 3-19 Real part of DS estimated from the harmonic excitation tests at a pretension of 500N

Figure 3-20 presents the real part of the dynamic stiffness function versus the frequency-squared at a pretension of 500N, which were obtained from the random excitation tests. The results estimated from the random excitation tests have characteristics similar to the results estimated from the harmonic excitation tests shown in Figure 3-19, but the linearity in the modal resonance regions seems to become worse

compared to the results from the harmonic excitation tests, especially in the resonance regions of the first mode and the ninth mode.

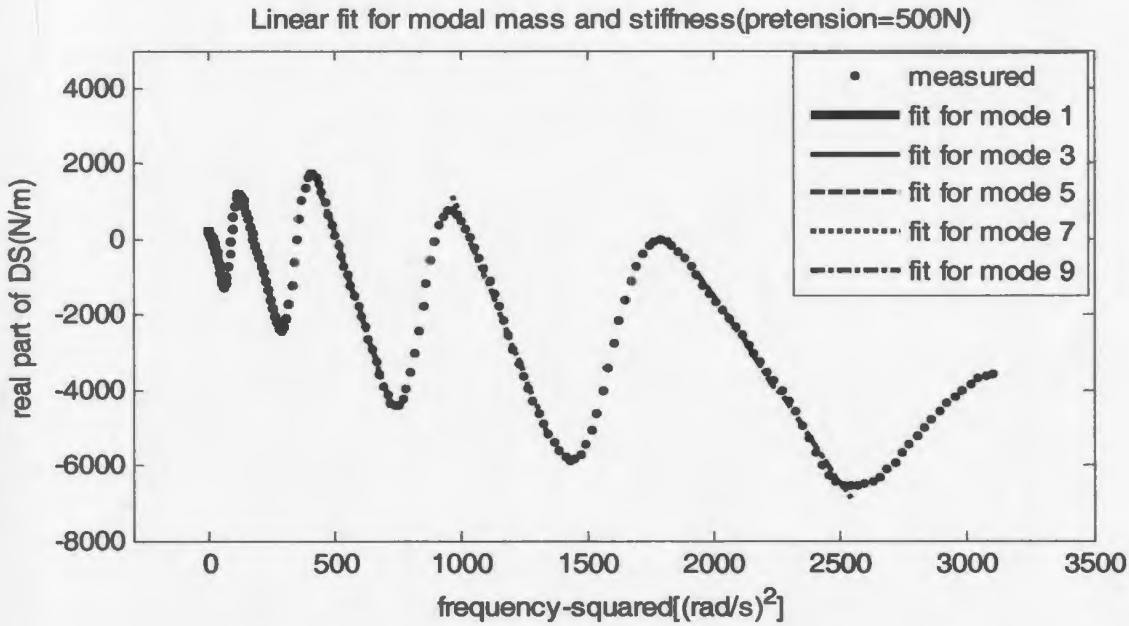


Figure 3-20 Real part of DS estimated from the random excitation tests at a pretension of 500N

The estimated modal parameters are listed in Table 3-1. As seen in Table 3-1, the modal masses depend on the mode number and the tension. From equation (3-6), we know that for a riser with uniform structural and hydrodynamic properties over its length, if assume that the mode shapes are exact sinusoidal shapes, the modal mass is independent of mode number, and there is a relation between the modal masses, the structural mass and the hydrodynamic masses (added masses) as follows:

$$m_j = \frac{L}{2}(m_a + m_s) \quad (3-17)$$

where m_j is the modal mass, m_a is the added mass, m_s is the structural mass per unit length, and L is the riser length. It is noted that the estimated modal mass is dependent of

mode numbers, and this may have resulted from the fact that the vibration shapes in the modal resonance regions are not exact sinusoidal shapes due to the existence of damping for the riser.

Table 3-1 Modal parameters estimated from the harmonic and random excitation tests at a pretension of 500N

| Pattern | Item | Mode 1 | Mode 3 | Mode 5 | Mode 7 | Mode 9 |
|----------|-----------------------|--------|--------|--------|--------|--------|
| Harmonic | Modal mass(kg) | 12.6 | 19.2 | 17.2 | 18.4 | 13.7 |
| | Modal stiffness(N/m) | 317 | 3519 | 8948 | 19350 | 25264 |
| | Natural frequency(Hz) | 0.80 | 2.16 | 3.63 | 5.16 | 6.83 |
| Random | Modal mass(kg) | 21.0 | 23.9 | 20.9 | 16.7 | 9.9 |
| | Modal stiffness(N/m) | 288 | 4308 | 10601 | 17271 | 18163 |
| | Natural frequency(Hz) | 0.59 | 2.14 | 3.59 | 5.12 | 6.83 |

The added mass coefficient C_a for a cylinder is usually defined as

$$C_a = \frac{m_a}{\frac{1}{4}\pi\rho D^2} \quad (3-18)$$

where ρ is the water density and D is the cylinder diameter. Equations (3-17) and (3-18) provides an approximate method to estimate the added mass coefficient C_a based on the estimated modal masses, although equation (3-17) requires the assumption that the structural and hydrodynamic properties over riser length are uniform and the mode shapes are exact sinusoidal shapes, namely we have

$$C_a = \frac{4}{\pi\rho D^2} \left(\frac{2A_{nn}}{L} - m_s \right) \quad (3-19)$$

The estimated added mass coefficients of the tested model riser at a pretension of 500N are shown in Table 3-2. As seen in Table 3-2, the estimated added mass coefficients have a big scatter ranging from 1.0 to 2.6. Chakrabarti (2005) provided the experimental results for a pivoted rigid cylinder of diameter D oscillating harmonically in calm water. It was found that the added mass coefficients depended on Keulegan-Carpenter number KC , defined as $KC=u_0/fD$, where: u_0 is the cylinder oscillating velocity amplitude; f is the cylinder oscillating frequency, or defined as $KC=2\pi z_0/D$, where: z_0 is the oscillating displacement amplitude of a cylinder of diameter D (Chaplin & Subbiah, 1998). These added mass coefficient values ranged from 1.0 to 1.5 in the KC number region from 0 to 7. For a flexible riser, KC number values are different over riser length, due to the variation of vibration amplitude over riser length. In this research, the KC number value at the mid-point of the riser was chosen as a representative of the KC number values over the riser length, which ranged from 0.32 to 6.28 for the harmonic excitations and from 0 to 4.40 for the random excitations. The added mass coefficients found in the above references for a rigid cylinder are smaller than the values estimated from the flexible cylinder used for this research over the same KC value region.

Table 3-2 Added mass coefficients estimated from the harmonic and random excitation tests

| Pretension | Excitation pattern | Mode 1 | Mode 3 | Mode 5 | Mode 7 | Mode 9 |
|------------|--------------------|--------|--------|--------|--------|--------|
| 500(N) | Harmonic | 1.00 | 2.23 | 1.86 | 2.08 | 1.20 |
| | Random | 2.56 | 3.11 | 2.55 | 1.76 | 0.49 |

As expected, the high modes produce larger modal stiffness and natural frequencies than the low modes, as seen in Table 3-1. For a flexible riser vibration system, both of the

tension and the bending stiffness provides the spring force to the vibration system, i.e. both of the tension and the bending stiffness has contribution to the modal stiffness, but usually the bending stiffness has less contribution to the modal stiffness than the tension, especially for low modes.

Comparing modal parameter values respectively estimated from the harmonic and the random excitation tests, two points are found: i) the different excitation patterns produce significant differences in the estimated modal mass and stiffness, i.e. the estimated modal mass and stiffness are sensitive to the excitation patterns used; and ii) although the different excitation patterns produce significant differences in the estimated modal mass and stiffness, the different excitation patterns do not produce significant differences in the estimated modal natural frequencies, or the ratio of the estimated modal stiffness to the estimated modal mass, except for the estimated modal natural frequencies for the first mode. The relatively large differences in the estimated modal natural frequencies for the first mode may result from the poor linear fits in the real part of the DS functions. As seen in Figure 3-19 and 3-20, the first mode shows poor linearity in the real part of DS functions, and this causes a relatively big error in the result of a linear fit.

Figure 3-21 shows the imaginary part of the dynamic stiffness functions versus frequency at a pretension of 500N, which were obtained from the harmonic and the random excitations. The minimum values appear in the modal resonance regions, while the maximum values appear in the regions where the dominant modes transit. It is noted that there are significant differences between the results respectively from the harmonic and the random excitations, but fortunately the values at the modal natural frequencies have relatively small differences, which will be used to estimate the modal damping. The

estimated modal damping values are shown in Table 3-3. The estimated damping values seem to have an increasing trend with the mode number.

The hydrodynamic damping coefficient C_d for a cylinder is defined as

$$C_d = \frac{c_a}{\frac{1}{2} \rho D z'_0} \quad (3-20)$$

where c_a is the linear hydrodynamic damping coefficient, and z'_0 is the maximum amplitude of vibration velocity. For a harmonic vibration, the amplitude of vibration velocity can be calculated by

$$z'_0 = \omega z_0 \quad (3-21)$$

where ω is the vibration frequency, and z_0 is the vibration amplitude. Assume that the riser has uniform structural and hydrodynamic properties over its length and the structural damping is much less than the hydrodynamic damping so that the structural damping can be ignored; thus from equation (3-6), we have

$$B_{nn} \approx \frac{L}{2} c_a \quad (3-22)$$

where B_{nn} is the modal damping. Combination of equations (3-20), (3-21) and (3-22) leads to

$$C_d \approx \frac{4B_{nn}}{\rho D L \omega z_0} \quad (3-23)$$

Assuming $z_0 = 0.5D$, the estimated damping coefficients of the model riser at a pretension of 500N are shown in Table 3-4. As seen in Table 3-4, the estimated damping coefficient ranges in the region from 0.56 to 1.78. Sarpkaya (1976) conducted an experiment of a rigid cylinder in oscillating water, and it was found that the damping

coefficients for that rigid cylinder ranged from 0.5 to 2.0, which are similar to the values for the flexible cylinder used for this research.

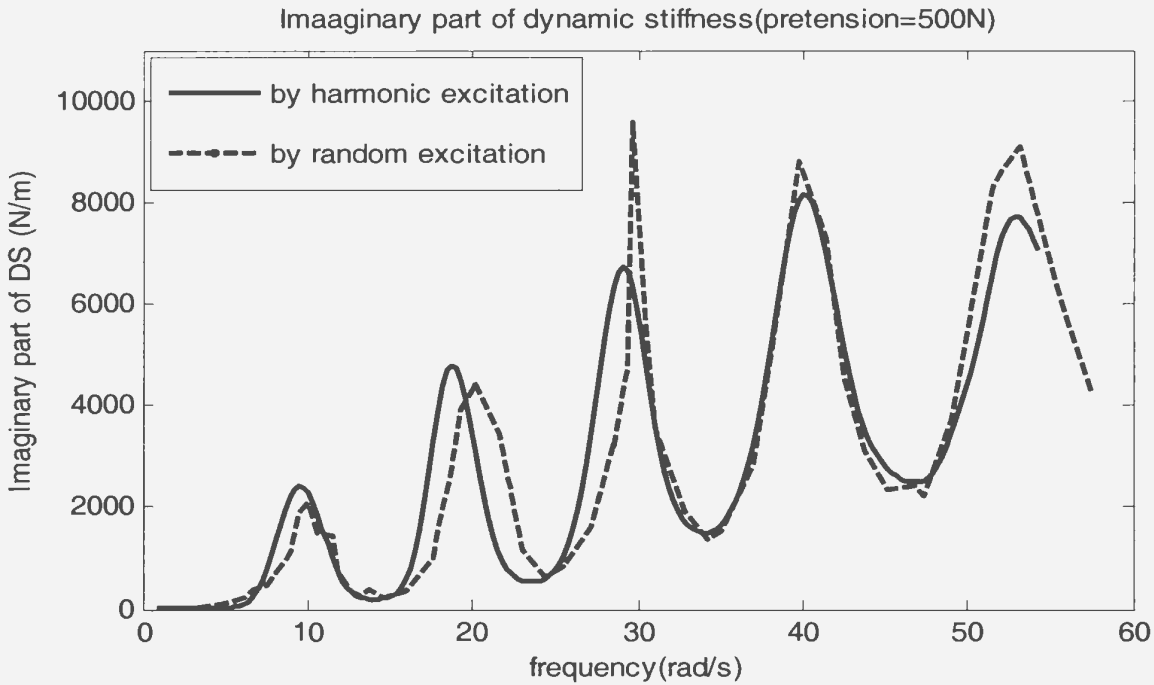


Figure 3-21 Imaginary part of DS function between the excitation force and the displacement at the middle of the riser

Table 3-3 Modal damping estimated from the harmonic and random excitation tests(N.s/m)

| Pretension | Excitation pattern | Mode 1 | Mode 3 | Mode 5 | Mode 7 | Mode 9 |
|------------|--------------------|--------|--------|--------|--------|--------|
| 500(N) | Harmonic | 16.2 | 18.1 | 25.7 | 40.1 | 51.6 |
| | Random | 6.8 | 15.7 | 26.7 | 50.3 | 64.2 |

Table 3-4 Damping coefficients estimated from the harmonic and random excitation tests

| Pretension | Excitation pattern | Mode 1 | Mode 3 | Mode 5 | Mode 7 | Mode 9 |
|------------|--------------------|--------|--------|--------|--------|--------|
| 500(N) | Harmonic | 1.78 | 0.66 | 0.56 | 0.63 | 0.63 |
| | Random | 0.80 | 0.68 | 0.69 | 0.91 | 0.88 |

3. 4. 2 Test Results for Pretension of 700N

The second pretension tested was 700N. Except for the pretension, all test conditions were identical to the test conditions at the pretension of 500N. Fifty harmonic frequencies were tested, but no random excitation tests were conducted for this pretension.

3. 4. 2. 1 Frequency Response Functions

For the pretension of 700N, only the harmonic excitation tests were conducted. Figure 3-22 presents the results of frequency response function between the shaker force and the shaker displacement from the harmonic excitation tests. Similarly in the case of the pretension of 500N, several peaks and minima are found in the frequency response function, which respectively correspond to the resonance frequencies and the anti-resonance frequencies. As seen in Figure 3-22, the low mode shapes have relatively large peak magnitude values, while the high mode shapes have relatively small peak magnitude values.

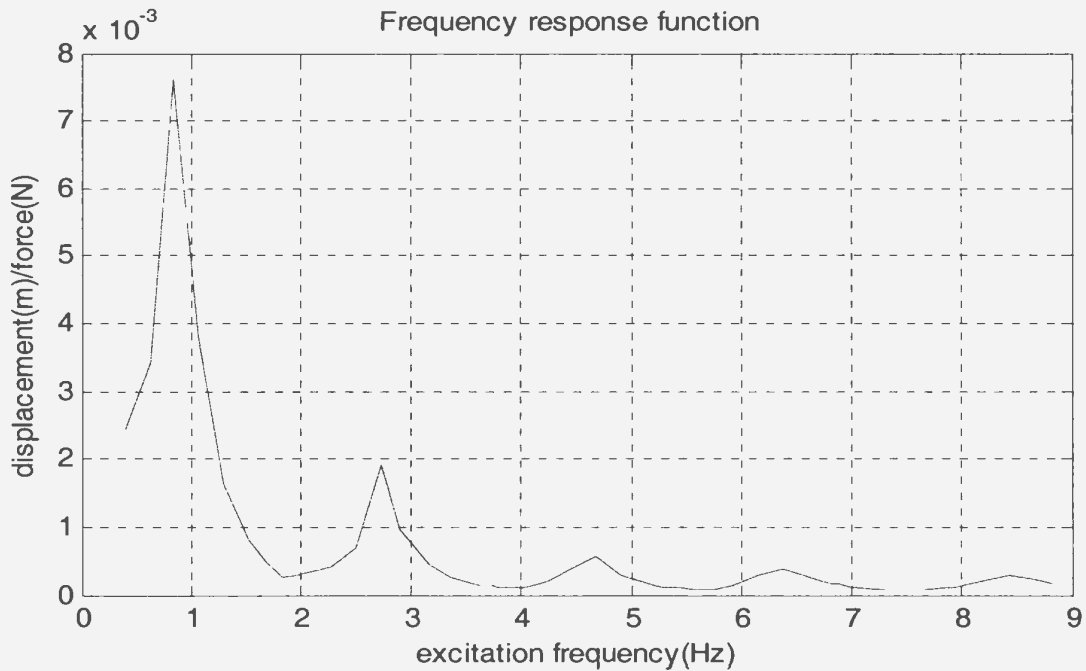


Figure 3-22 Amplitude of frequency response function of the riser in calm water at a pretension of 700N

3. 4. 2. 2 Vibration Modes

Nine excitation frequencies of 0.88, 1.96, 2.80, 4.00, 4.60, 5.44, 6.28, 7.48 and 8.44Hz were selected to check the vibration shapes over the riser length. Figures 3-23 to 3-31 give the vibration shapes and the corresponding time series of the shaker motion for these frequencies. Also, the cut-offs in the time series of the shaker motion are not true, as these cut-offs result from the smaller sampling frequencies for plotting than the sampling frequency for data acquisition. The vibration shape at the locations from $x=5.27\text{m}$ to $x=6.47\text{m}$ may have been skewed due to the lack of the measurement at these locations. It is noted that in the test the pair of accelerometers at the location of $x=2.429\text{m}$ started to work unstably, so that the vibration shapes at the locations from $x=2.0\text{m}$ to 2.8m may also be skewed in some figures, such as Figures 3-23, 3-24 and 3-25. The malfunction of this pair of accelerometers also affected the measured results of vibration shapes for the pretension of 900N, which will be presented and discussed later.

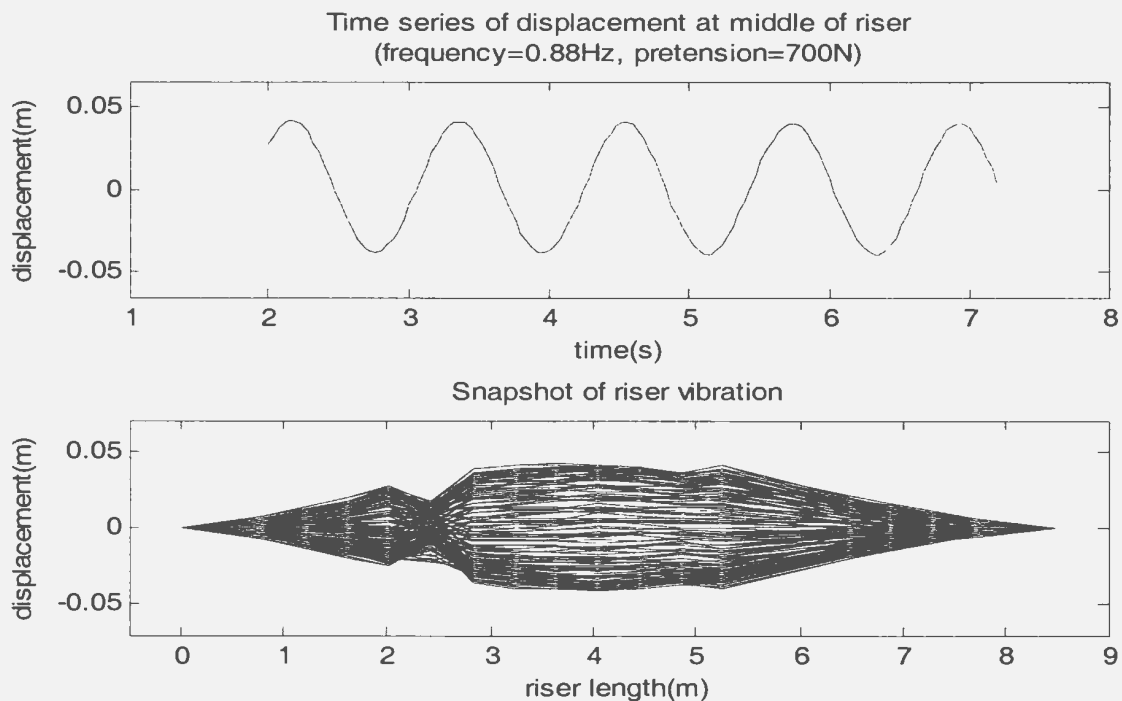


Figure 3-23 Vibration shape at an excitation frequency of 0.88Hz

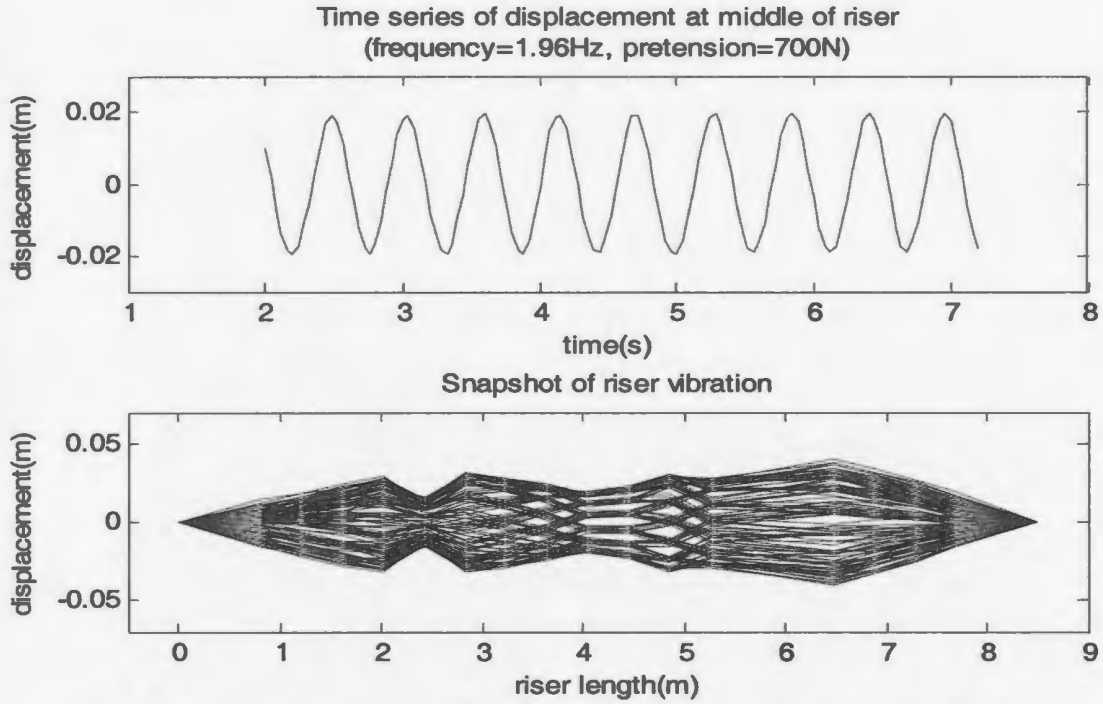


Figure 3-24 Vibration shape at an excitation frequency of 1.96Hz

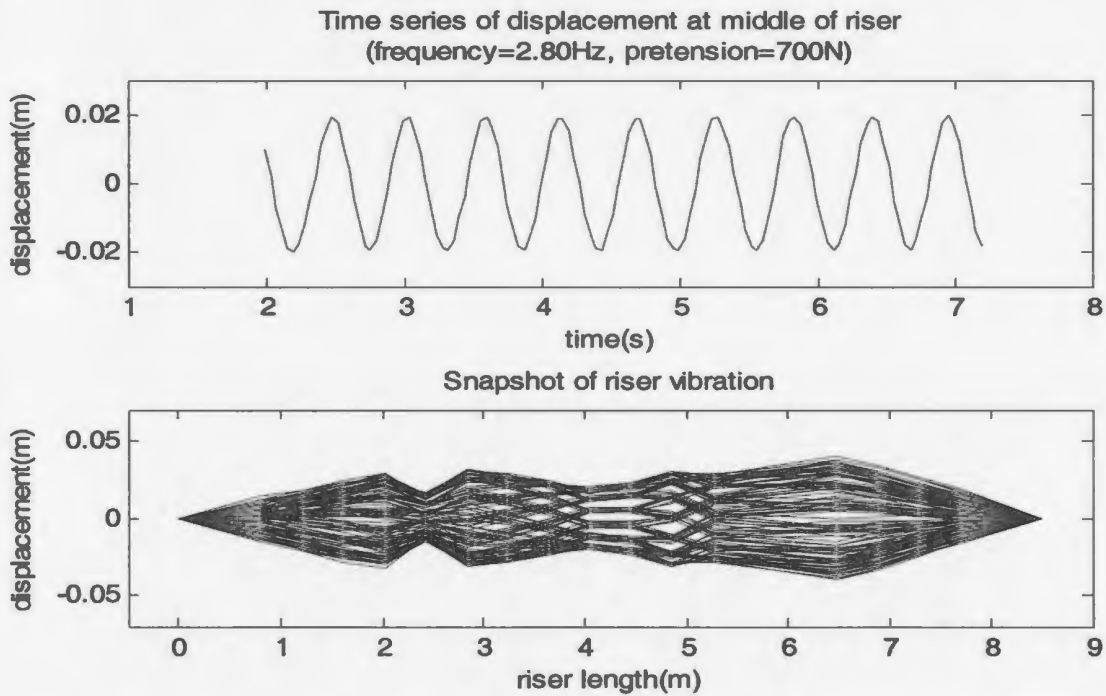


Figure 3-25 Vibration shape at an excitation frequency of 2.80Hz

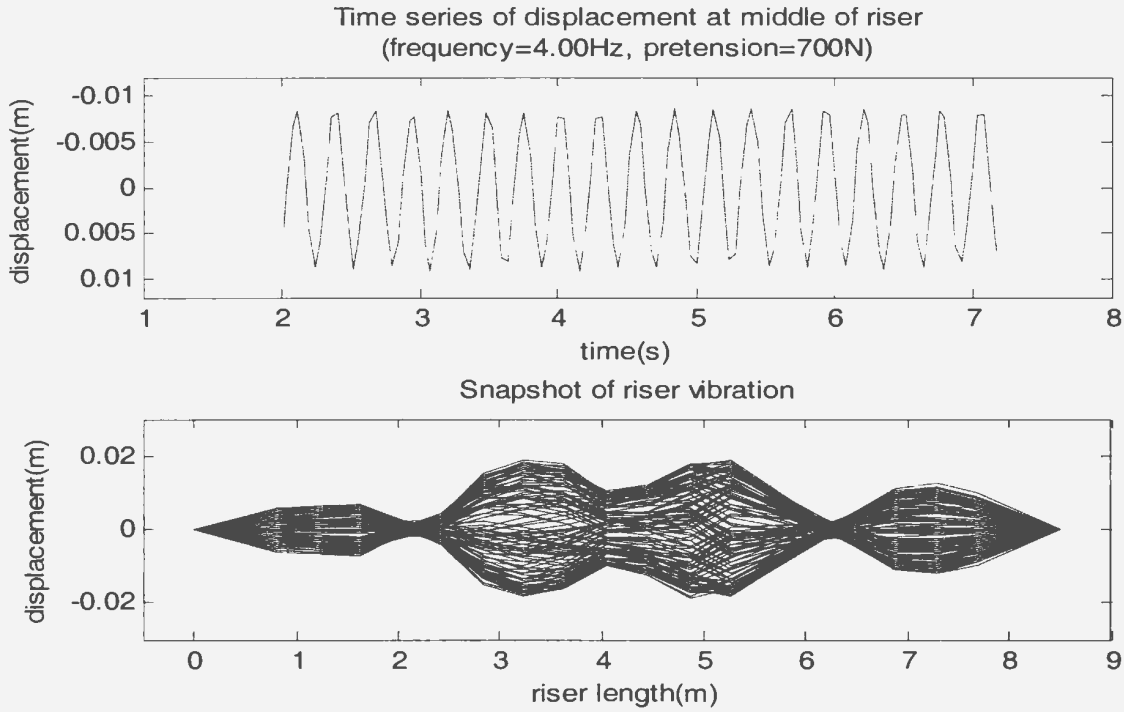


Figure 3-26 Vibration shape at an excitation frequency of 4.00Hz

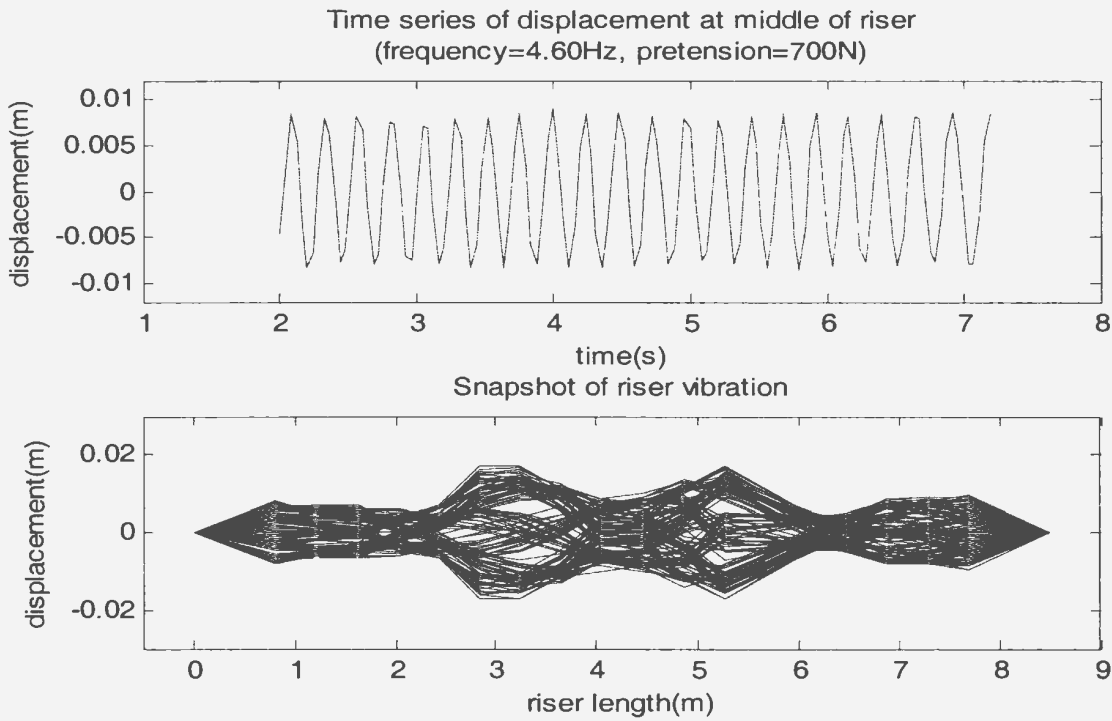


Figure 3-27 Vibration shape at an excitation frequency of 4.60Hz

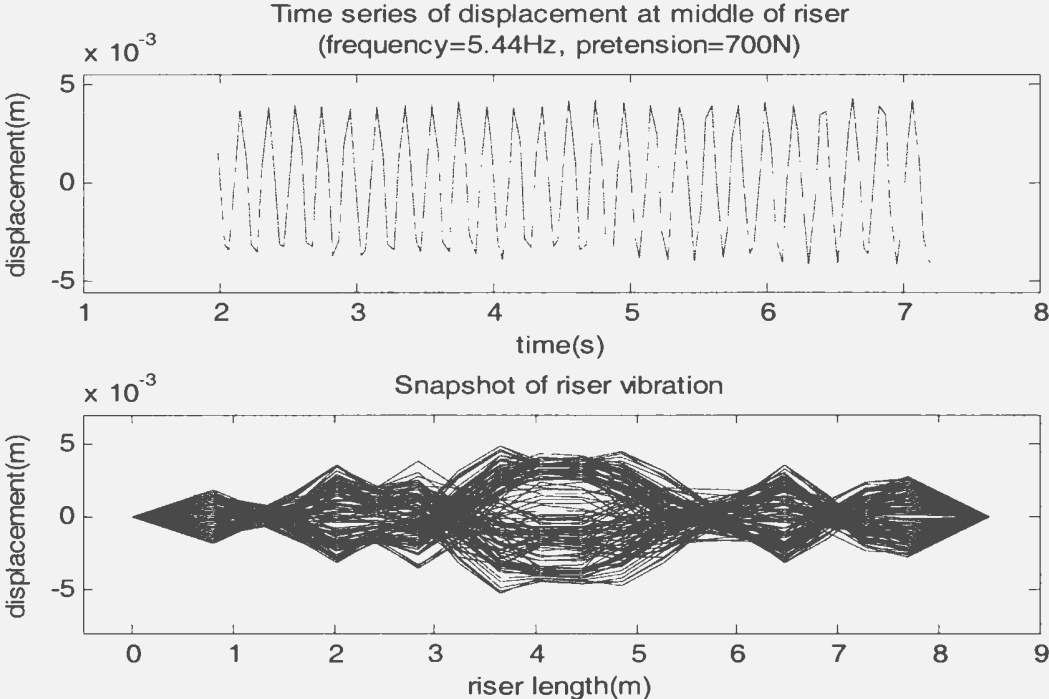


Figure 3-28 Vibration shape at an excitation frequency of 5.44Hz

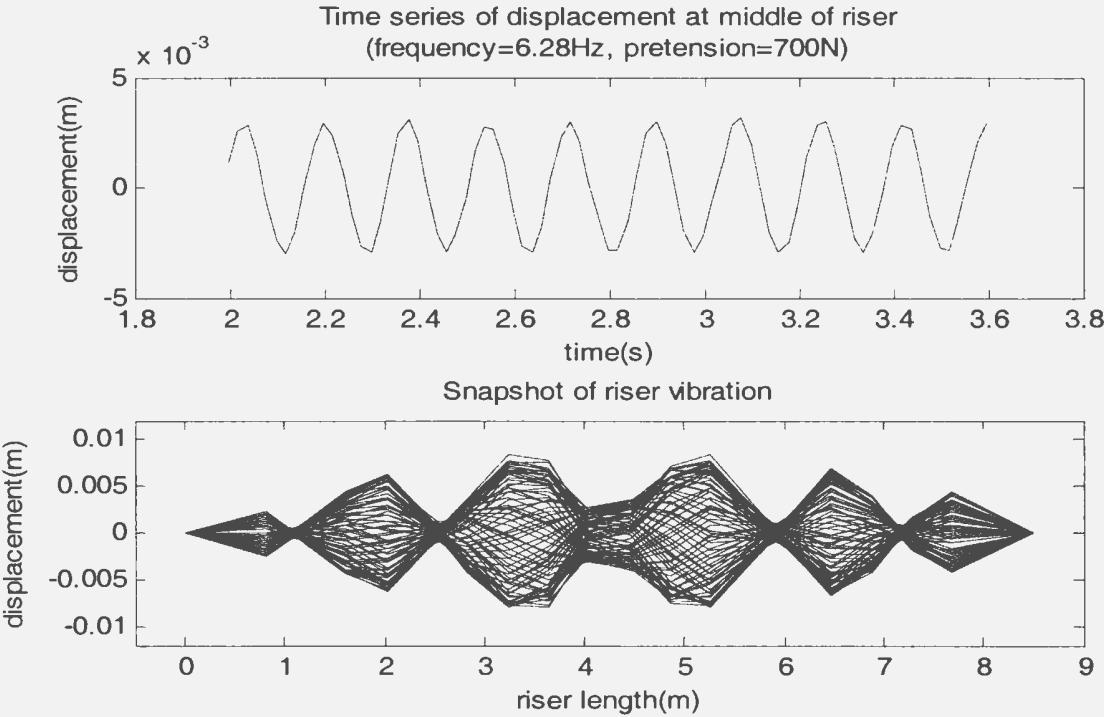


Figure 3-29 Vibration shape at an excitation frequency of 6.28Hz

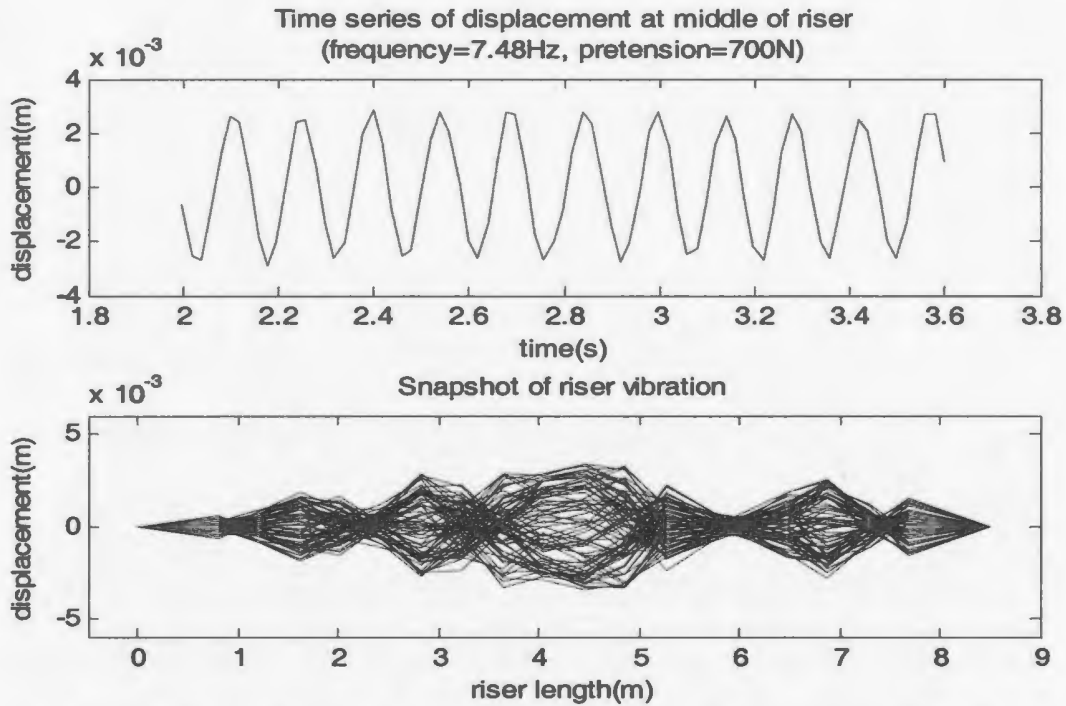


Figure 3-30 Vibration shape at an excitation frequency of 7.48Hz

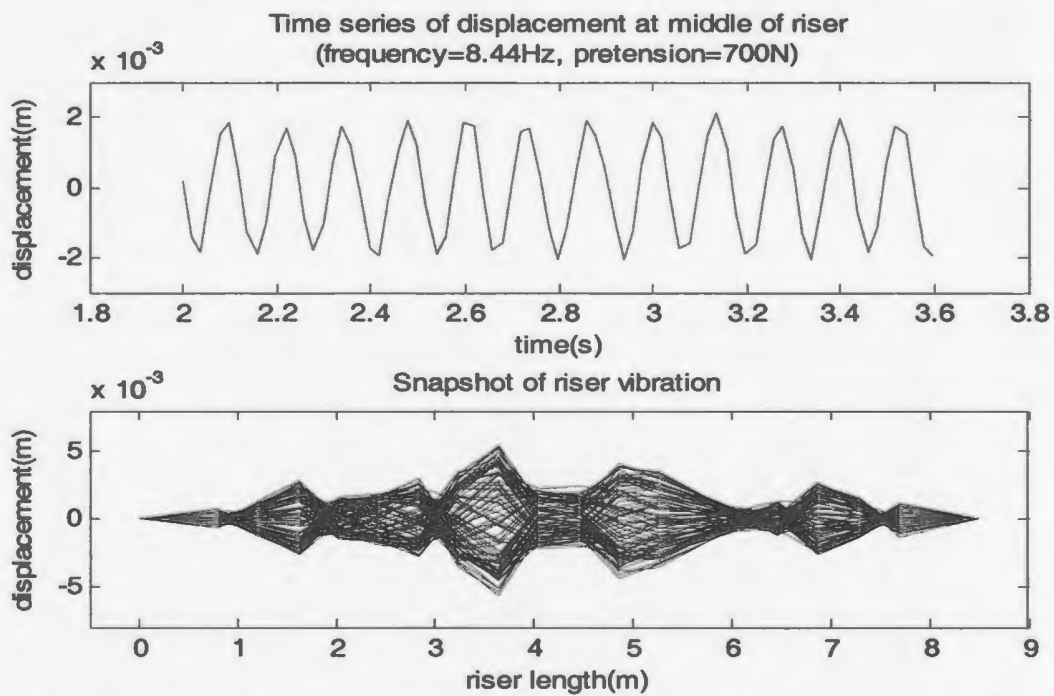


Figure 3-31 Vibration shape at an excitation frequency of 8.44Hz

From the frequency responses function shown in Figure 3-22, we know that the excitation frequencies of 0.88, 2.80, 4.60, 6.28 and 8.44Hz are close to the natural frequencies of mode 1, 3, 5, 7 and 9. Figures 3-23, 3-25, 3-27, 3-29 and 3-31 respectively exhibit the vibration shapes for these frequencies. From these figures, it is observed that the pretension of 700N results in vibration shapes more different from a sinusoidal shape than the pretension of 500N. The nodes become more unclear at some excitation frequencies compared to the vibration shapes for the pretension of 500N. Figures 3-24, 3-26, 3-28 and 3-30 respectively show the vibration shapes for the excitation frequencies of 1.96, 4.00, 5.44 and 7.48Hz. As these frequencies are far away from the modal natural frequencies, the vibrations with mixed dominant mode shapes are observed. Similarly in the case of the low pretension of 500N, the low excitation frequencies result in low mode shapes, while the high excitation frequencies result in the high mode shapes.

3. 4. 2. 3 Modal Parameters

Figure 3-32 presents the real part of dynamic stiffness functions versus the frequency-squared at a pretension of 700N, which were estimated from the harmonic excitation tests. The linear fit lines are also shown in this figure. Similar to the results in the case of the pretension of 500N, the real part of the dynamic stiffness starts with a positive value at the lowest frequency, and then it decreases with the excitation frequency. Over the excitation frequency range tested, five resonance regions were found. In each resonance region, the real part of the dynamic stiffness function changes its sign at the corresponding modal natural frequency, and the values of the real part of the dynamic stiffness function exhibit a good linear characteristic.

The estimated modal masses, modal stiffness and modal natural frequencies are listed in Table 3-5. Similarly in the case of the pretension of 500N, the modal masses, modal stiffness and modal natural frequencies depend on the mode number. The mass coefficients estimated from equation (3-19) are shown in Table 3-6. As seen in Table 3-6, the estimated mass coefficients have a big scatter ranging from 1.2 to 3.3. Also, these estimated mass coefficients for the flexible riser are bigger than those for the rigid cylinder provided by Chakrabarti (2005).

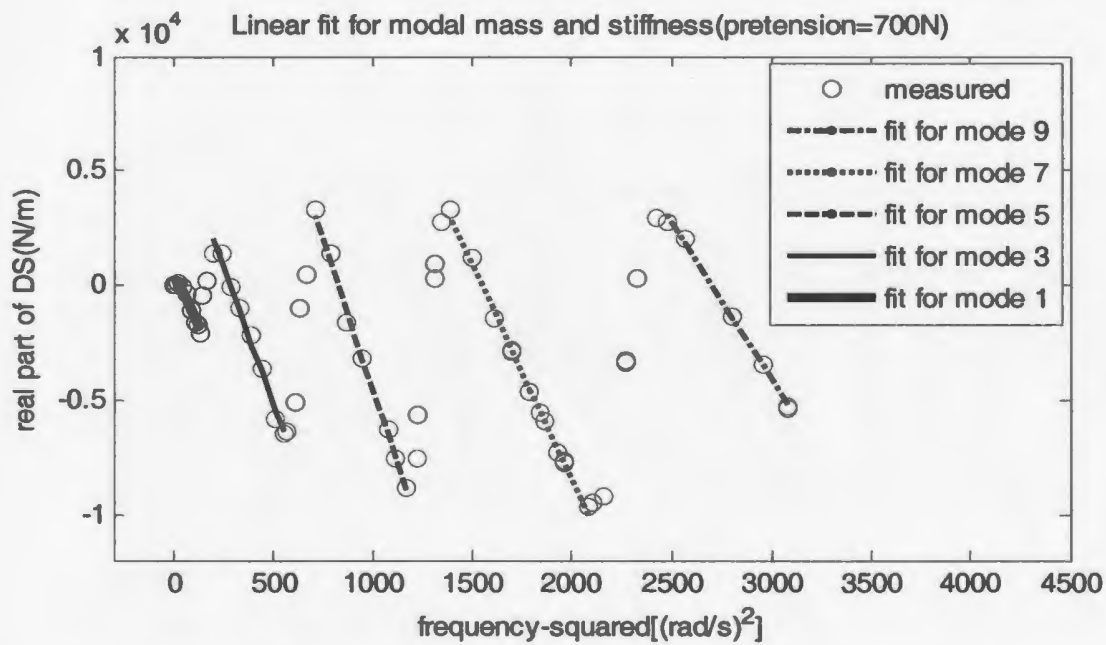


Figure 3-32 Real part of DS function estimated from the harmonic excitations at a pretension of 700N

Table 3-5 Modal parameters estimated from the harmonic and random excitation tests at a pretension of 700N

| Pattern | Item | Mode 1 | Mode 3 | Mode 5 | Mode 7 | Mode 9 |
|----------|-----------------------|--------|--------|--------|--------|--------|
| Harmonic | Modal mass(kg) | 18.0 | 24.1 | 25.0 | 18.7 | 13.9 |
| | Modal stiffness(N/m) | 554 | 6900 | 21393 | 28825 | 37614 |
| | Natural frequency(Hz) | 0.88 | 2.70 | 4.57 | 6.26 | 8.27 |

Table 3-6 Added mass coefficients estimated from the harmonic excitation tests at a pretension of 700N

| Pretension | Excitation pattern | Mode 1 | Mode 3 | Mode 5 | Mode 7 | Mode 9 |
|------------|--------------------|--------|--------|--------|--------|--------|
| 700(N) | Harmonic | 2.01 | 3.15 | 3.32 | 2.14 | 1.24 |

Figure 3-33 shows the imaginary part of the dynamic stiffness functions versus the frequency at a pretension of 700N, which were obtained from the harmonic excitation tests. Similar to the results in the case of the pretension of 500N, the minimum values appear in the modal resonance regions, while the maximum values appear in the regions where the dominant mode transits.

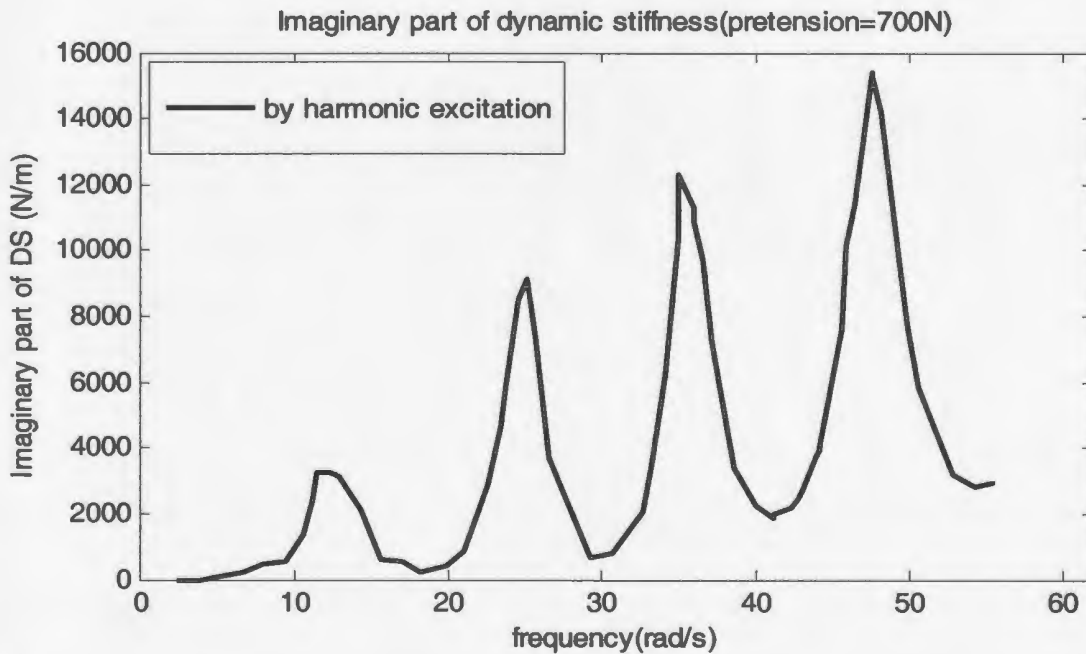


Figure 3-33 Imaginary part of DS function between the excitation force and the displacement at the middle of the riser

The estimated modal damping is shown in Table 3-7. The estimated modal damping has an increasing trend with the mode number, except for mode 1. The damping

coefficients can be estimated based on equation (3-23) and the results are shown in Table 3-8. The estimated damping coefficient ranges from 0.45 to 0.65, except for the value of mode 1. These values are similar to the values for a rigid cylinder, which were found by Sarpkaya (1976).

Table 3-7 Modal damping estimated from the harmonic and random excitation tests(N.s/m)

| Pretension | Excitation pattern | Mode 1 | Mode 3 | Mode 5 | Mode 7 | Mode 9 |
|------------|--------------------|--------|--------|--------|--------|--------|
| 700(N) | Harmonic | 25.5 | 13.5 | 25.3 | 45.5 | 52.1 |

Table 3-8 Damping coefficients estimated from the harmonic and random excitation tests(N.s/m)

| Pretension | Excitation pattern | Mode 1 | Mode 3 | Mode 5 | Mode 7 | Mode 9 |
|------------|--------------------|--------|--------|--------|--------|--------|
| 700(N) | Harmonic | 2.51 | 0.44 | 0.50 | 0.64 | 0.57 |

3. 4. 3 Test Results at Pretension of 900N

The third pretension tested was 900N. It was the biggest pretension for the shaker-excitation tests. Both harmonic and random excitations were applied to the riser at this pretension. Fifty excitation frequencies were used for the harmonic excitation tests, and one random excitation was used for the random excitation tests.

3. 4. 3. 1 Frequency Response Functions

The measured time histories of the random shaker force and motion are shown in Figure 3-34. As seen in Figure 3-34, the shaker displacement is approximately equal to that in the case of the pretension of 500N, but the shaker force is greater than that in the

case of the pretension of 500N due to the increased pretension. Figures 3-35 and 3-36 respectively present the auto-spectral density function of the shaker displacement and the cross-spectral density function of the shaker force and shaker displacement. Both the auto- and cross-spectral density functions were estimated using the methods shown in Appendix B. The Parzen window function was used to reduce the leakage errors. Also, the auto-spectral function of the shaker motion are close to zero when the frequency exceeds 7.8Hz, and this means that the shaker could not generate the random vibration components with the frequencies beyond 7.8Hz even though the digital signals contained these components. Four peaks are found in Figure 3-36, meaning that only modes 1, 3, 5 and 7 experienced the resonances and the resonance for mode 9 was not excited by the shaker motions. This is because the increased pretension gave rise to higher natural frequencies than in the case of a pretension of 500N and, as a result, the maximum excitation frequency did not reach the resonance region of the highest mode in the case of the pretension of 500N.

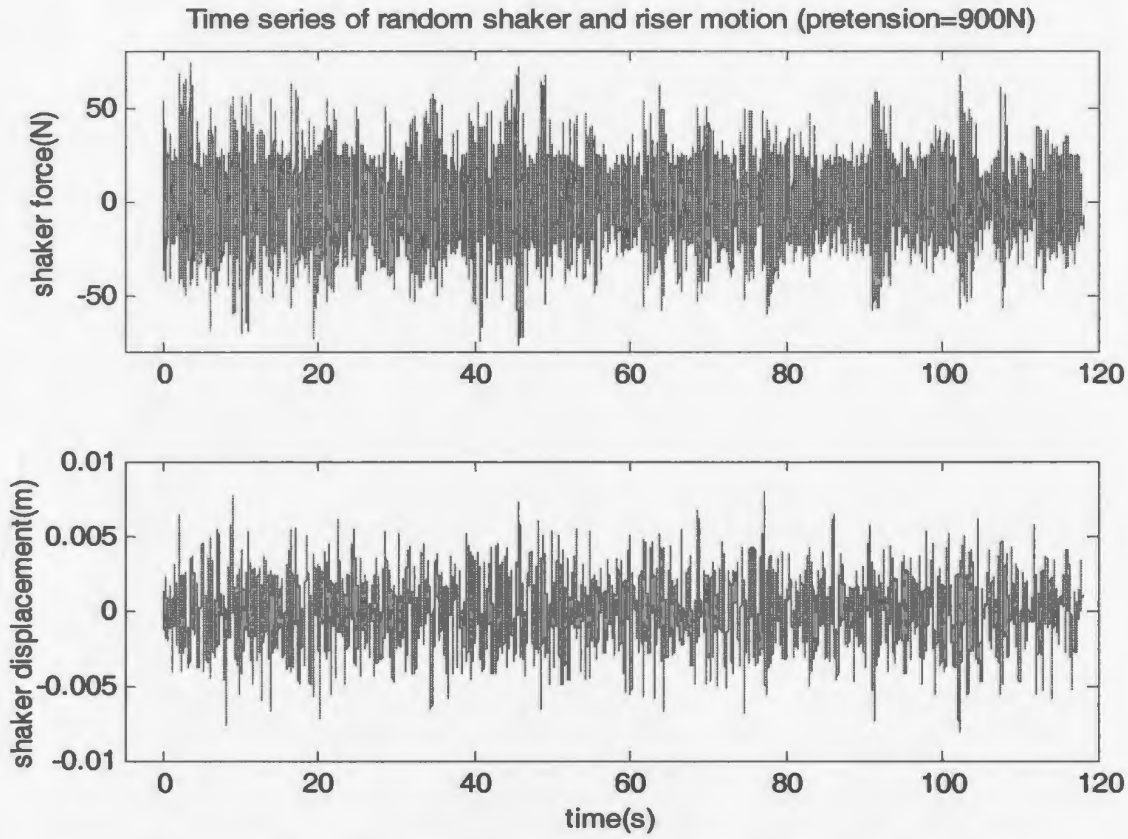


Figure 3-34 The measured shaker force and shaker motion at a pretension of 900N

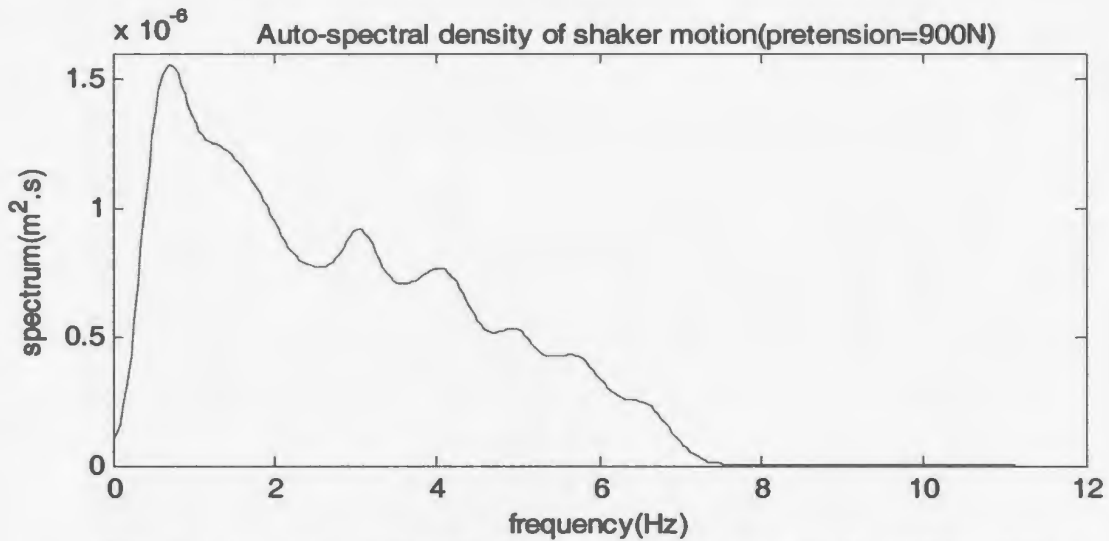


Figure 3-35 The estimated auto-spectral density function of the shaker motion at a pretension of 900N

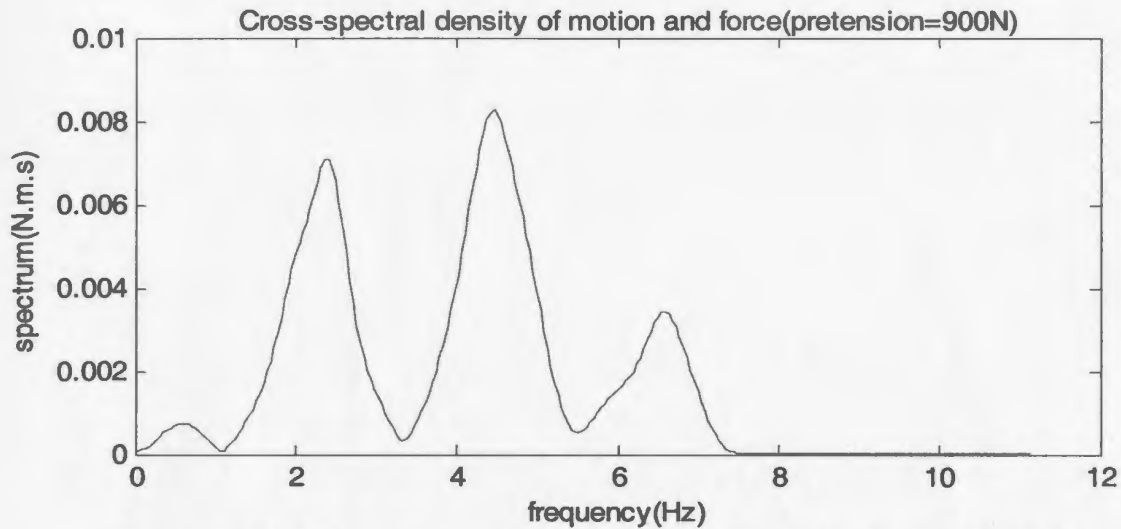


Figure 3-36 The estimated cross-spectral density function of the shaker motion and the shaker force at a pretension of 900N

Figure 3-37 presents the frequency response functions estimated from the harmonic and random excitation tests. In Figure 3-37, there are several peaks meaning resonances and several minima meaning anti-resonances. The low mode shapes result in relatively great peaks, while the high mode shapes result in relatively small peaks. This means relatively small damping for the low modes and relatively large damping for the high modes.

Figure 3-37 also gives a comparison between the results respectively from the harmonic and the random excitation tests. Similar to the results in the case of the pretension of 500N, there are considerable differences in the peak regions between the results estimated from the harmonic and random excitation tests.

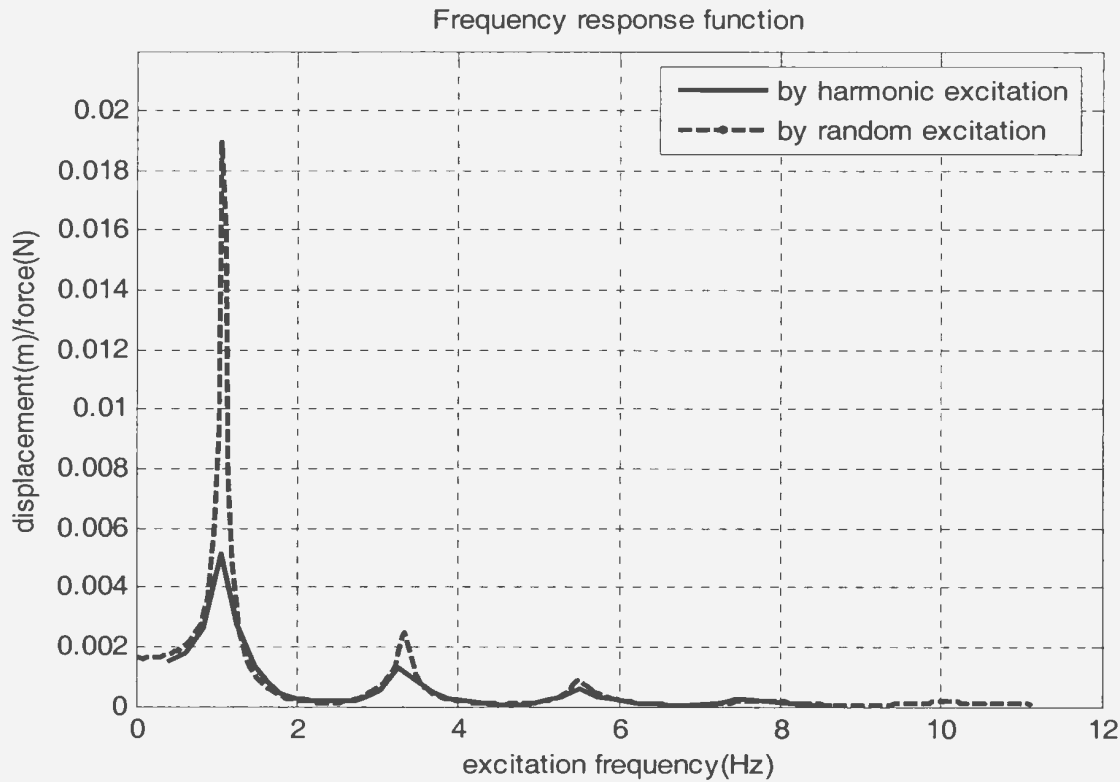


Figure 3-37 Amplitude of frequency response function of the riser in calm water at a pretension of 900N

3. 4. 3. 2 Vibration Modes

In the case of a pretension of 900N, eight excitation frequencies of 0.40, 2.20, 3.16, 4.48, 5.44, 6.88, 7.48 and 8.56Hz were selected to check the vibration shapes over the riser length. The frequencies of 3.16, 5.44 and 7.48Hz are close to the natural frequencies, and the other frequencies are far away from the natural frequencies. Figures 3-38 to 3-45 exhibit the vibration shapes for these excitation frequencies. The corresponding shaker displacements are also shown in these figures. The vibration shapes at the locations from $x=5.27\text{m}$ to $x=6.47\text{m}$ may have been skewed due to the lack of the measurement at these locations, and as the pair of accelerometers at the location of $x=2.429\text{m}$ worked unstably, the vibration shapes at the locations from $x=2.0\text{m}$ to 2.8m

may also be skewed in some figures such as Figures 3-38, 3-39 and 3-40. Similar to the results in the cases of pretensions of 500N and 700N, the low excitation frequencies result in low mode shapes, while the high excitation frequencies result in the high mode shapes. It is noted that the vibration shapes have considerable differences from the sinusoidal shapes.

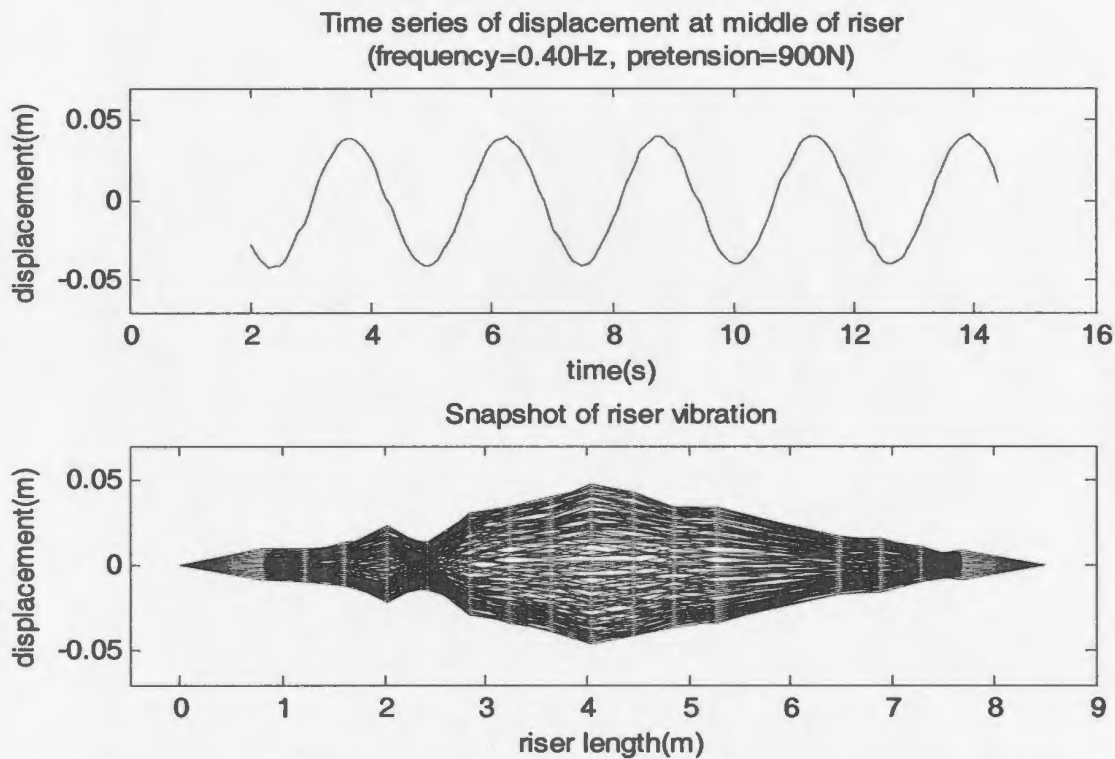


Figure 3-38 Vibration shape at an excitation frequency of 0.40Hz

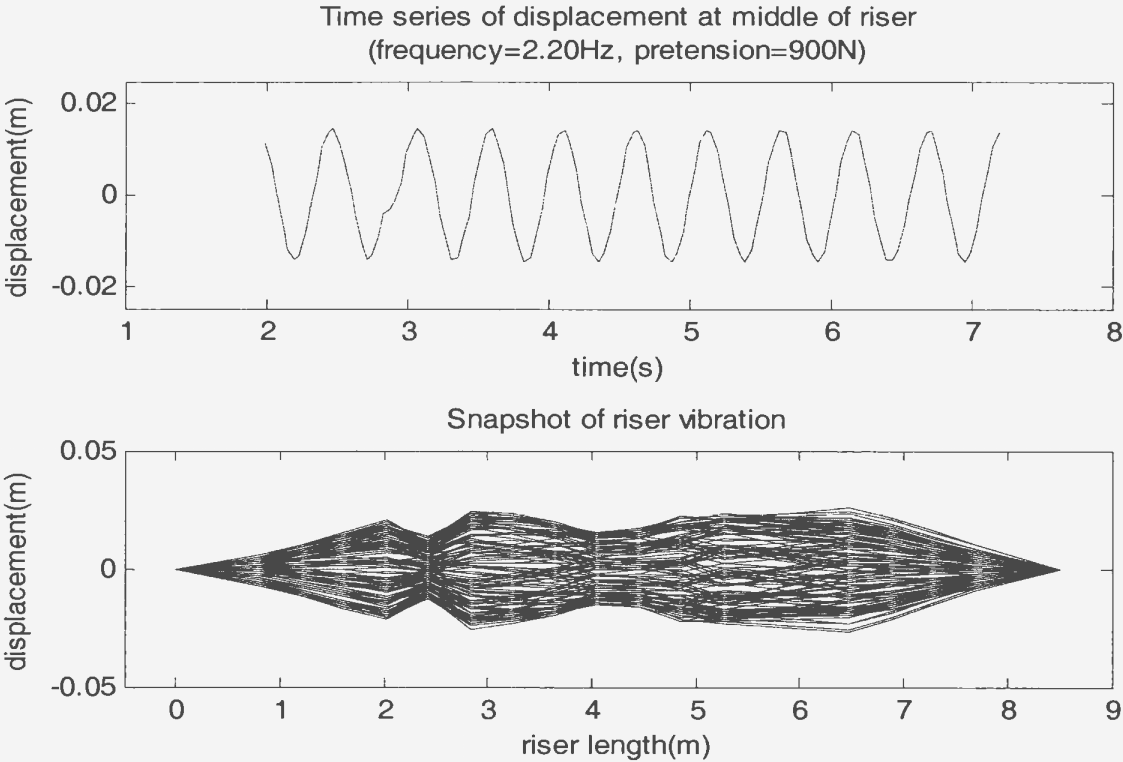


Figure 3-39 Vibration shape at an excitation frequency of 2.20Hz

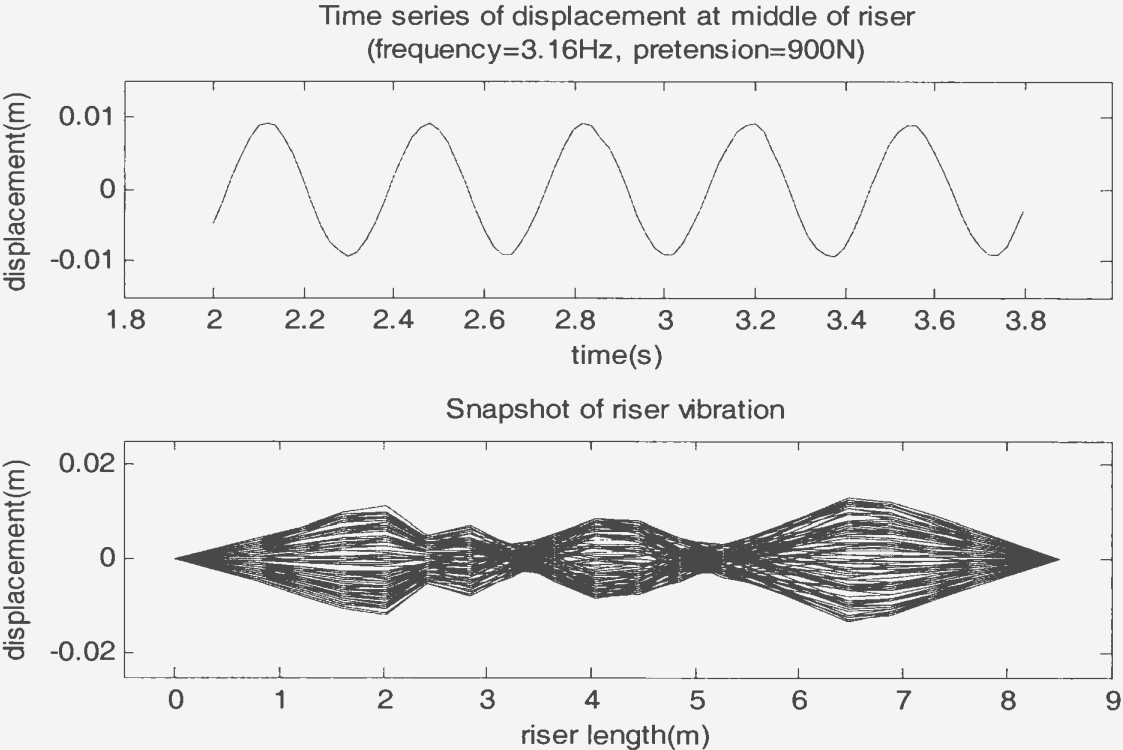


Figure 3-40 Vibration shape at an excitation frequency of 3.16Hz

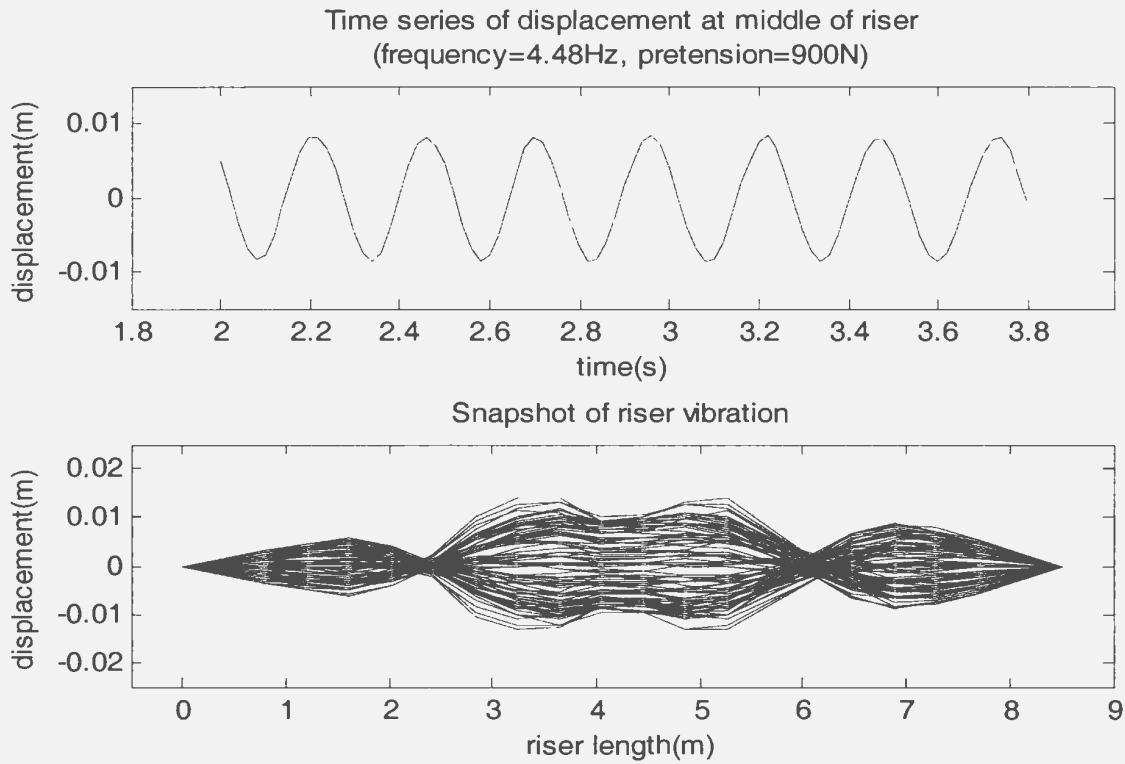


Figure 3-41 Vibration shape at an excitation frequency of 4.48Hz

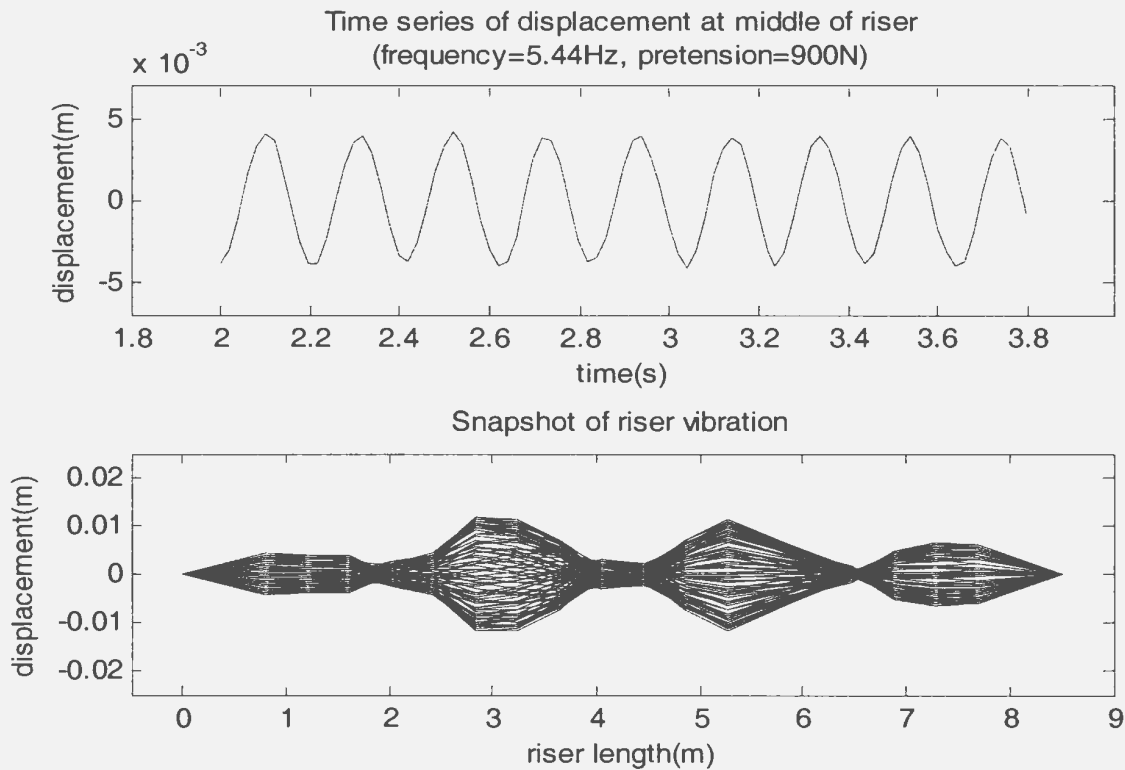


Figure 3-42 Vibration shape at an excitation frequency of 5.44Hz

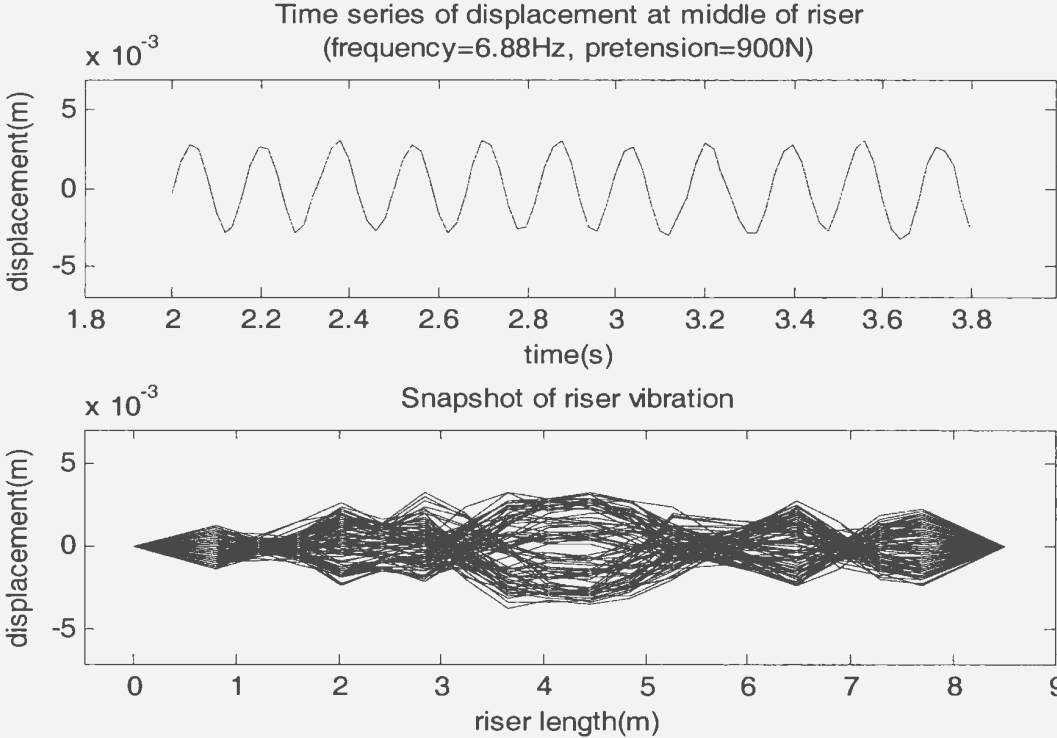


Figure 3-43 Vibration shape at an excitation frequency of 6.88Hz

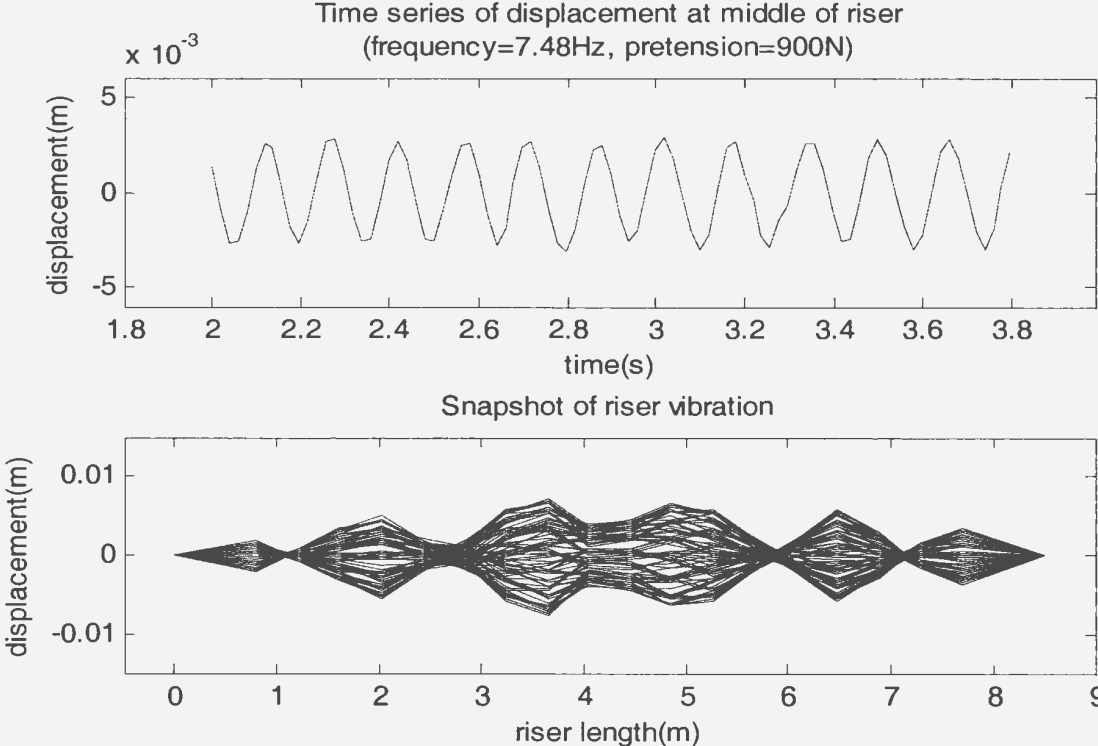


Figure 3-44 Vibration shape at an excitation frequency of 7.48Hz

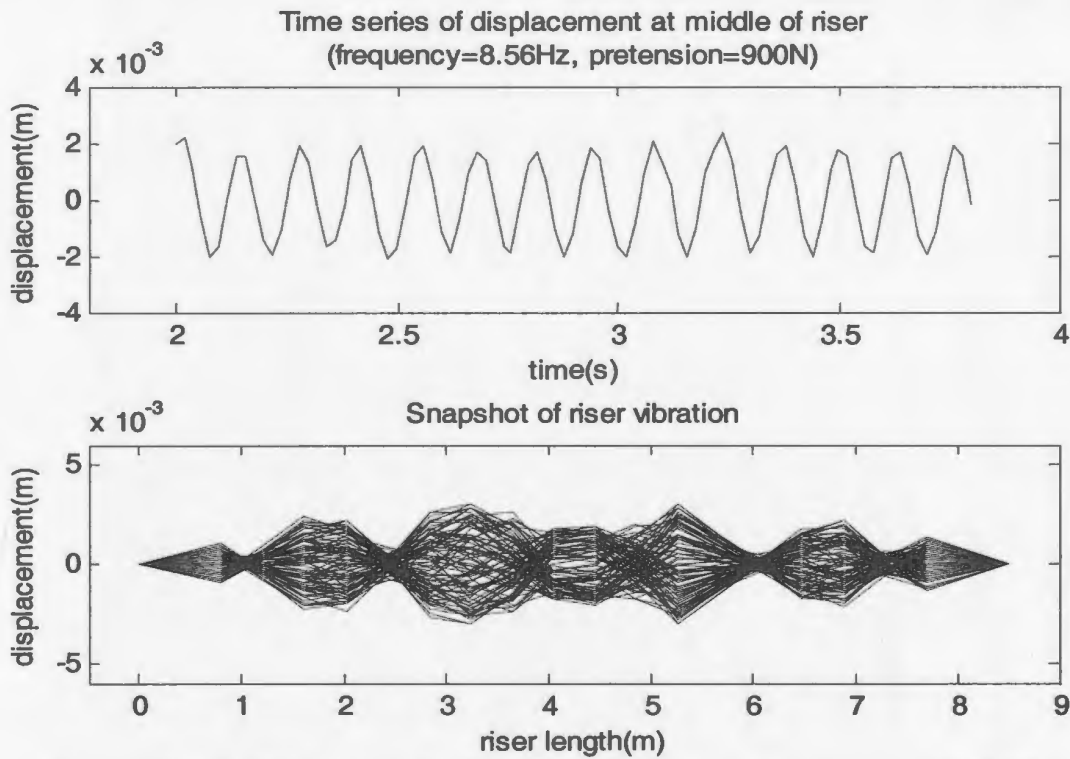


Figure 3-45 Vibration shape at an excitation frequency of 8.56Hz

3. 4. 3. 3 Modal Parameters

Figure 3-46 shows the real part of the dynamic stiffness functions versus the frequency-squared at the pretension of 900N, which were obtained from the harmonic excitation tests. The linear fit lines for estimation of the modal mass and modal stiffness are also presented in Figure 3-46. In the resonance regions, the values still follow a linear line well so that good fitted results can be obtained. Since the resonance at the natural frequency for mode 9 was not excited, only the modal parameters for mode 1, 3, 5 and 7 could be estimated for this pretension.

Figure 3-47 shows the real part of the dynamic stiffness functions versus the frequency-squared at the pretension of 900N, which were obtained from the random excitation tests. In the case of random excitation, the maximum excitation frequency also did not reach

the natural frequency of the ninth mode such that the modal parameters for the ninth mode could not be estimated. Comparing the results respectively from the harmonic and random excitation tests, the different patterns of excitations do not produce big differences in the estimated values of the real part of DS functions, but the linearity in the high mode resonance regions seems to become worse in the results from the random excitation tests than in those from the harmonic excitation tests.

The estimated modal parameters are listed in Table 3-9, and the corresponding mass coefficients are shown in Table 3-10. The estimated mass coefficients have a big scatter ranging from 1.9 to 3.9. These values are larger than those provided by Chakrabarti (2005).

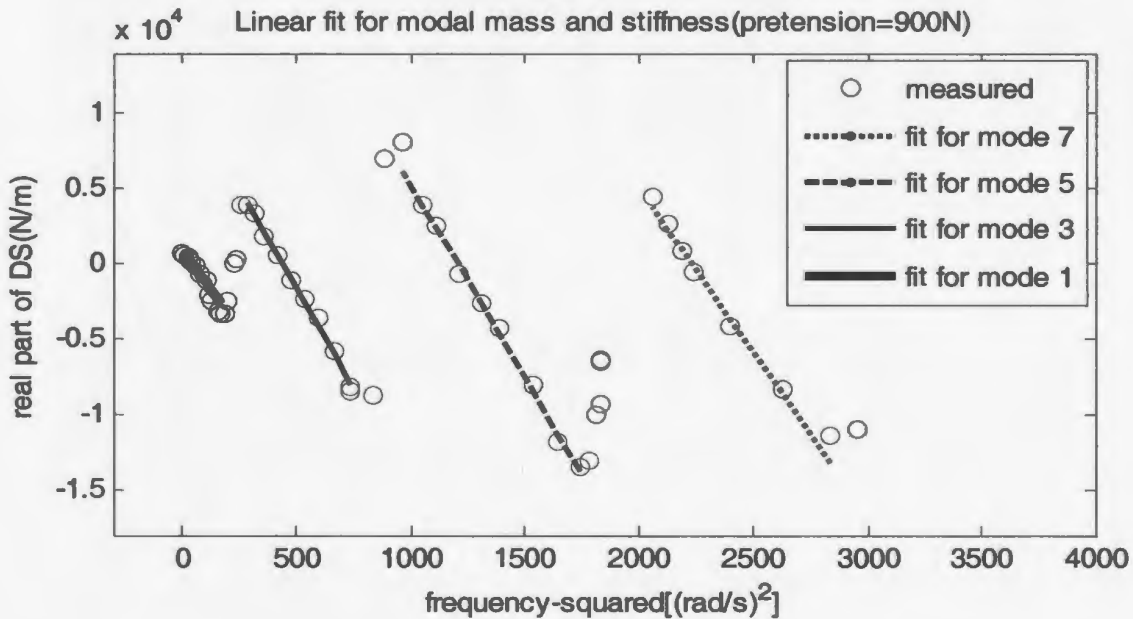


Figure 3-46 Real part of DS estimated from the harmonic excitation tests

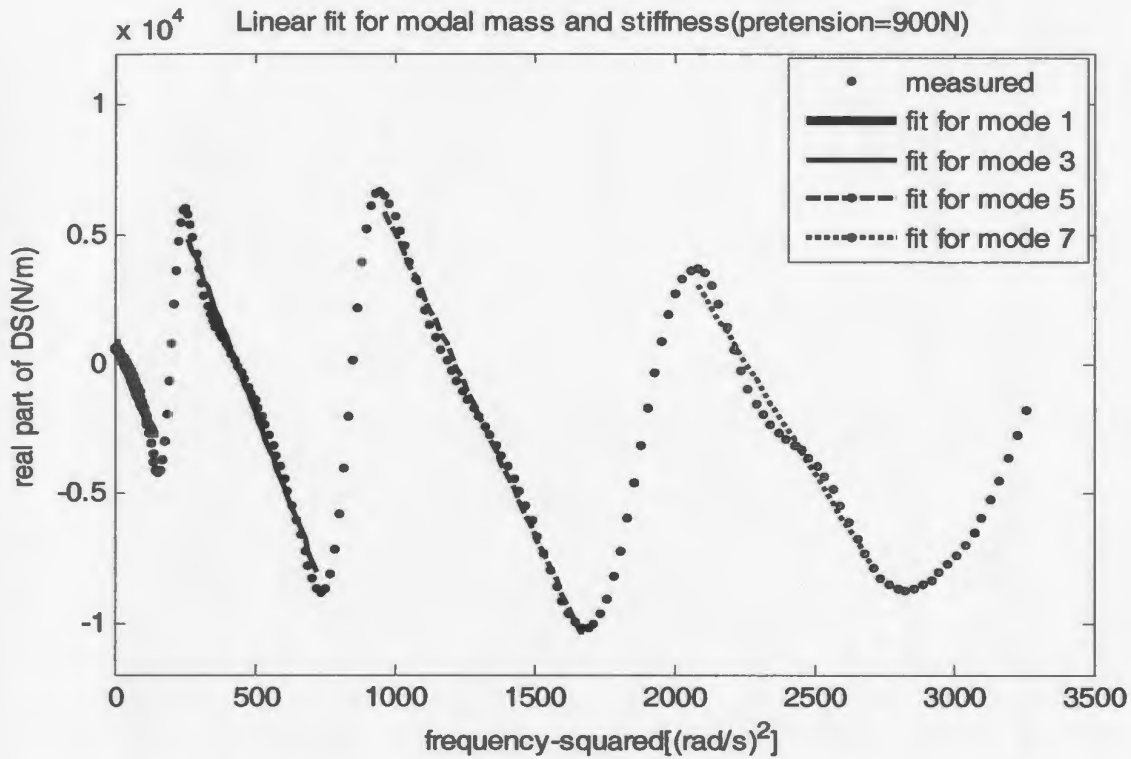


Figure 3-47 Real part of DS estimated from the random excitation tests

Table 3-9 Modal parameters estimated from the harmonic and random excitation tests at a pretension of 900N

| Pattern | Item | Mode 1 | Mode 3 | Mode 5 | Mode 7 | Mode 9 |
|----------|------------------------|--------|--------|--------|--------|--------|
| Harmonic | Modal mass(kg) | 21.1 | 27.0 | 25.6 | 22.0 | - |
| | Modal stiffness(N/m) | 976 | 11931 | 30860 | 49077 | - |
| | Natural frequency (Hz) | 1.08 | 3.34 | 5.52 | 7.52 | - |
| Random | Modal mass(kg) | 26.1 | 28.1 | 23.1 | 17.3 | - |
| | Modal stiffness(N/m) | 944 | 12250 | 28213 | 39112 | - |
| | Natural frequency(Hz) | 0.96 | 3.32 | 5.56 | 7.57 | - |

Table 3-10 Added mass coefficients estimated from the harmonic and random excitation tests

| Pretension | Excitation pattern | Mode 1 | Mode 3 | Mode 5 | Mode 7 | Mode 9 |
|------------|--------------------|--------|--------|--------|--------|--------|
| 900(N) | Harmonic | 2.59 | 3.69 | 3.43 | 2.76 | - |
| | Random | 3.52 | 3.90 | 2.96 | 1.88 | - |

Figure 3-48 shows the imaginary part of the dynamic stiffness versus the frequency at a pretension of 900N, which were estimated from the harmonic and the random excitation tests. Similar to the results in the cases of the pretensions of 500N and 700N, the minimum values appear in the modal resonance regions, while the maximum values appear in the modal anti-resonance regions. The estimated values of the imaginary part of the dynamic stiffness are sensitive to the excitation patterns, as there are considerable differences between the results respectively from the harmonic and the random excitation tests. However, the differences occurring in the resonance regions are smaller than those occurring in the anti-resonance regions.

The estimated values of modal damping are shown in Table 3-11. Also, the different excitation patterns may result in significant differences in the estimated damping values. Assuming $z_0=0.5D$, the estimated damping coefficients based on equation (3-23) are shown in Table 3-12, which ranges from 1.8 to 3.9. Sarpkaya (1976) conducted an experiment of a rigid cylinder in oscillating water and found that damping coefficients for that cylinder ranged from 0.5 to 2.0, which are smaller than the values found in this case.

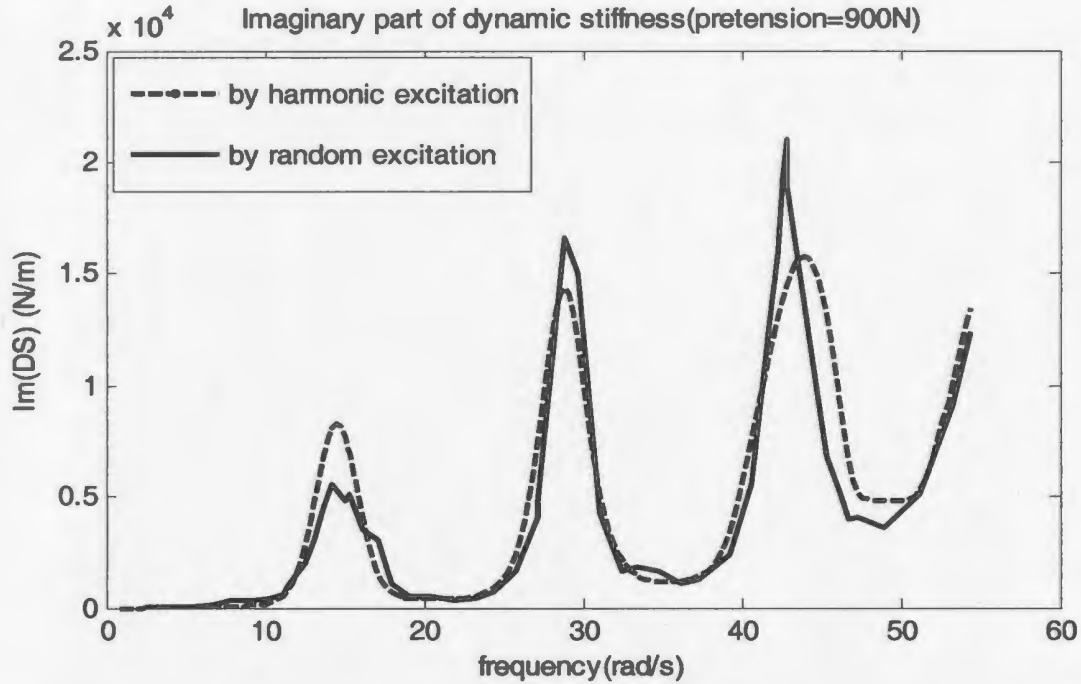


Figure 3-48 Imaginary part of DS function between the excitation force and the displacement at the middle of the riser

Table 3-11 Modal damping estimated from the harmonic and random excitation tests(N.s/m)

| Pretension | Excitation pattern | Mode 1 | Mode 3 | Mode 5 | Mode 7 | Mode 9 |
|------------|--------------------|--------|--------|--------|--------|--------|
| 900(N) | Harmonic | 14.0 | 15.3 | 28.6 | 86.3 | - |
| | Random | 6.3 | 19.0 | 34.2 | 64.2 | - |

Table 3-12 Damping coefficients estimated from the harmonic and random excitation tests

| Pretension | Excitation pattern | Mode 1 | Mode 3 | Mode 5 | Mode 7 | Mode 9 |
|------------|--------------------|--------|--------|--------|--------|--------|
| 900(N) | Harmonic | 1.27 | 0.47 | 0.52 | 1.13 | - |
| | Random | 0.57 | 0.57 | 0.62 | 0.84 | - |

3.4.4 Non-linear Component Analysis

The governing equation (3-1) is a linear model for the shaker-excitation/riser response system tested, but in reality the shaker-excitation/riser response system is a non-linear system, as at least the hydrodynamic damping is usually considered to be proportional to vibration velocity-squared; thus equation (3-1) is modified as a non-linear governing equation with a non-linear damping term as

$$\begin{aligned}
 & [m_s + m_a(x)] \frac{\partial^2 z(t, x)}{\partial t^2} + c_a \frac{\partial z(t, x)}{\partial t} + c_b \left| \frac{\partial z(t, x)}{\partial t} \right| \frac{\partial z(t, x)}{\partial t} + k_b \frac{\partial^4 z(t, x)}{\partial x^4} - T \frac{\partial^2 z(t, x)}{\partial x^2} \\
 & = p(t) \delta(x_s)
 \end{aligned} \tag{3-24}$$

where c_a denotes the linear damping coefficient of the riser, and c_b denotes the non-linear damping coefficient of the riser. Manipulating in the manner similar to Section 3.3.1, the following equation can be obtained:

$$\begin{aligned}
 & \frac{(m_s + m_{a0})L}{2} \ddot{z}_n(t) + \frac{c_{a0}L}{2} \dot{z}_n(t) + \frac{L}{2} \left[k_b \left(\frac{n\pi}{L} \right)^4 + T \left(\frac{n\pi}{L} \right)^2 \right] z_n(t) + \sum_{k=1}^{\infty} \sum_{j=1}^{\infty} I_{nj} m_{aj} \ddot{z}_k(t) \\
 & + \sum_{k=1}^{\infty} \sum_{j=1}^{\infty} I_{nj} c_{aj} \dot{z}_k(t) + c_b \int_0^L \left[\sum_{k=1}^{\infty} z_k(t) \sin\left(\frac{k\pi x}{L}\right) \left| \sum_{k=1}^{\infty} z_k(t) \sin\left(\frac{k\pi x}{L}\right) \right| \right] \sin\left(\frac{n\pi x}{L}\right) dx \\
 & = p(t) \sin\left(\frac{n\pi x_s}{L}\right)
 \end{aligned} \tag{3-25}$$

Assume that the structural and hydrodynamic properties are constant over the riser length, and the coefficients m_{aj} and c_{aj} , $j=1,2,3,\dots$, in equation (3-25) are then equal to zero, and m_{a0} and c_{a0} are respectively equal to m_a and c_a . Thus, equation (3-25) becomes

$$\begin{aligned}
 & \frac{(m_s + m_a)L}{2} \ddot{z}_n(t) + \frac{c_a L}{2} \dot{z}_n(t) + \frac{L}{2} \left[k_b \left(\frac{n\pi}{L} \right)^4 + T \left(\frac{n\pi}{L} \right)^2 \right] z_n(t) + c_b |\dot{z}_n(t)| \dot{z}_n(t) J_n \\
 & = p(t) \sin\left(\frac{n\pi x_s}{L}\right)
 \end{aligned} \tag{3-26}$$

where

$$J_n = \int_0^L \left| \sin\left(\frac{n\pi x}{L}\right) \right| \sin^2\left(\frac{n\pi x}{L}\right) dx$$

Consider the resonance region for the n -th mode. In this region, we assume that the responses of the n -th mode are much larger than the responses of other modes, so that the responses of other modes can be ignored, namely equation (3-3) becomes

$$z(t, x) \approx z_n(t) \sin\left(\frac{n\pi x}{L}\right) \quad (3-27)$$

As the shaker motion displacement $z_s(t)$ is equal to the riser vibration displacement at the shaker location, equation (3-27) gives the shaker motion displacements in the form as

$$z_s(t) \approx z_n(t) \sin\left(\frac{n\pi x_s}{L}\right) \quad (3-28)$$

For the odd modes, letting $x_s=0.5L$ and substituting equation (3-28) into equation (3-26) yields

$$\begin{aligned} & \frac{(m_s + m_a)L}{2} \ddot{z}_s(t) + \frac{c_a L}{2} \dot{z}_s(t) + \frac{L}{2} \left[k_b \left(\frac{n\pi}{L} \right)^4 + T \left(\frac{n\pi}{L} \right)^2 \right] z_s(t) + c_b L |\dot{z}_s(t)| \dot{z}_s(t) \\ & = p(t) \end{aligned} \quad (3-29)$$

It is noted that equation (3-29) defines a single-input/single-output non-linear system, which is described in Appendix D. The input for the linear subsystem is the shaker displacement $z_s(t)$, and the input for the nonlinear subsystem is

$$q[z_s(t)] = |\dot{z}_s(t)| \dot{z}_s(t)$$

Thus, the methods presented in Appendix D can be employed to estimate the nonlinear damping c_b based on the measured random shaker forces and motions.

Figures 3-49 to 3-53 present the auto- and cross-spectral density functions of the input $z_s(t)$ for the linear subsystem, the input $q[z_s(t)]$ for the nonlinear subsystem and the total output $p(t)$, which were obtained from the random excitation tests at a pretension of 500N. Figure 3-54 shows the frequency response function for the nonlinear subsystem. As seen in Figure 3-54, relatively big values appear in the regions of low frequency and resonance, and this means that in these regions the non-linear components are relatively large, i.e. the non-linear effect in the responses is relatively strong. In the regions of the low frequency and resonance, the vibration amplitudes are relatively large; therefore, relatively strong non-linear effects exist in these regions. This conclusion agrees with that extracted from the linear model analysis, which was addressed earlier.

Figure 3-55 illustrates the line fit plot for estimation of non-linear damping coefficient. The resonance region of mode 1 was used. As seen in Figure 3-55, the intercept value is $20.2(\text{N}\cdot\text{s}^2/\text{m})$, and the estimated non-linear damping is $8.5(\text{N}\cdot\text{s}^2/\text{m}^2)$.

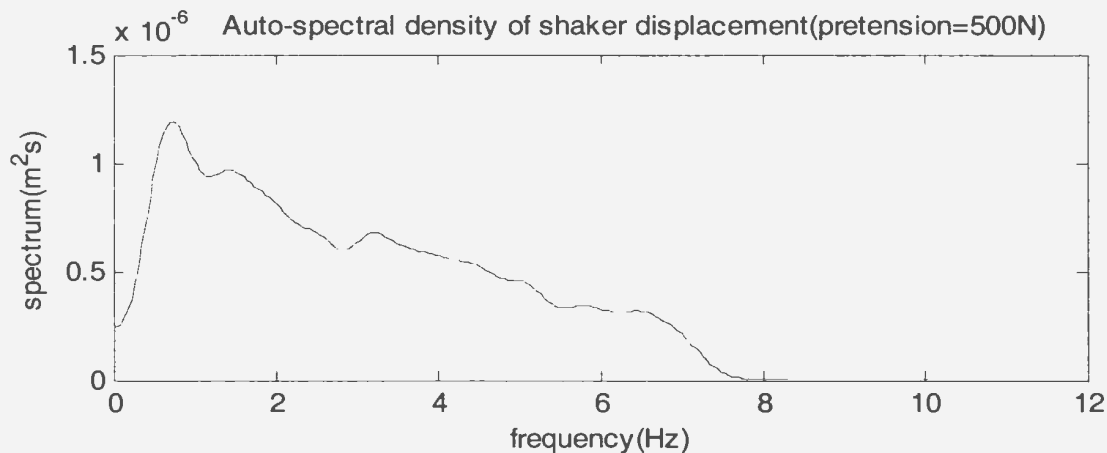


Figure 3-49 Auto-spectral density function of random shaker displacement

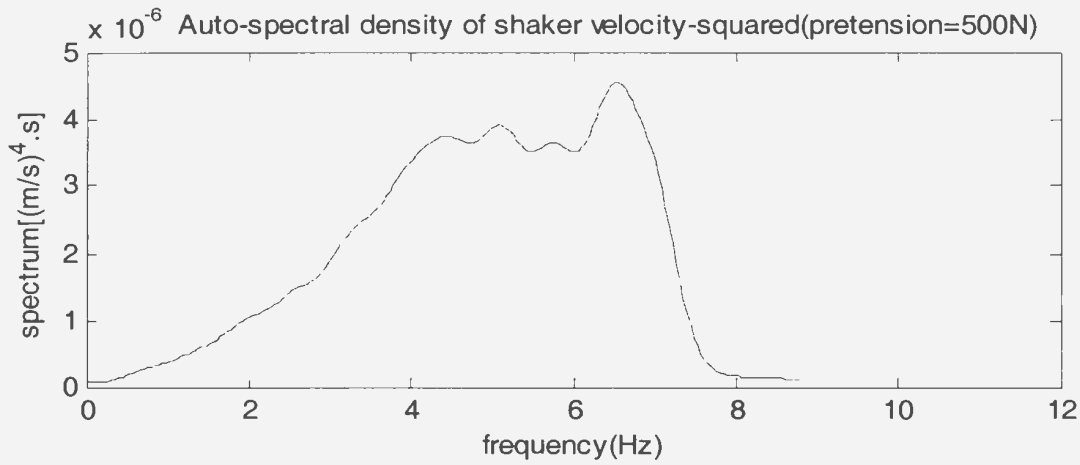


Figure 3-50 Auto-spectral density function of random shaker velocity-squared

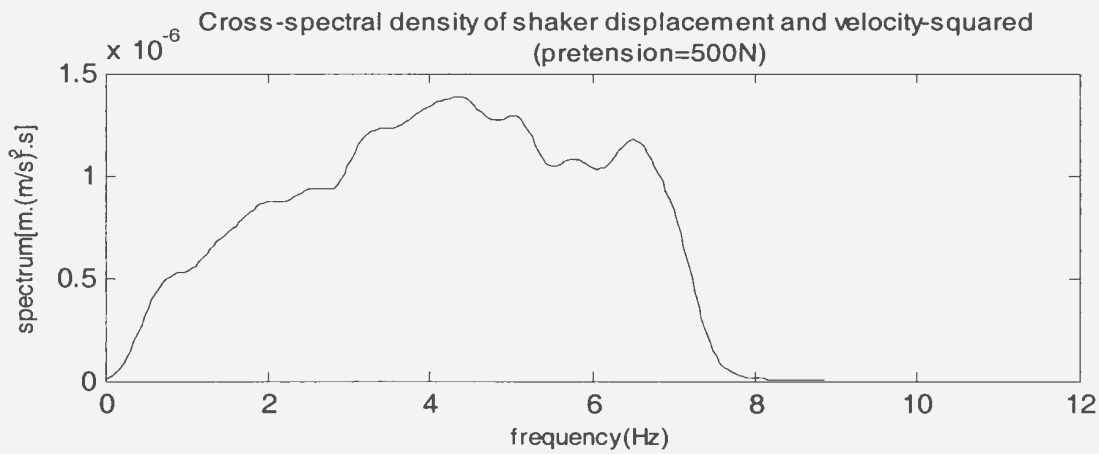


Figure 3-51 Cross-spectral density function of random shaker displacement and velocity-squared

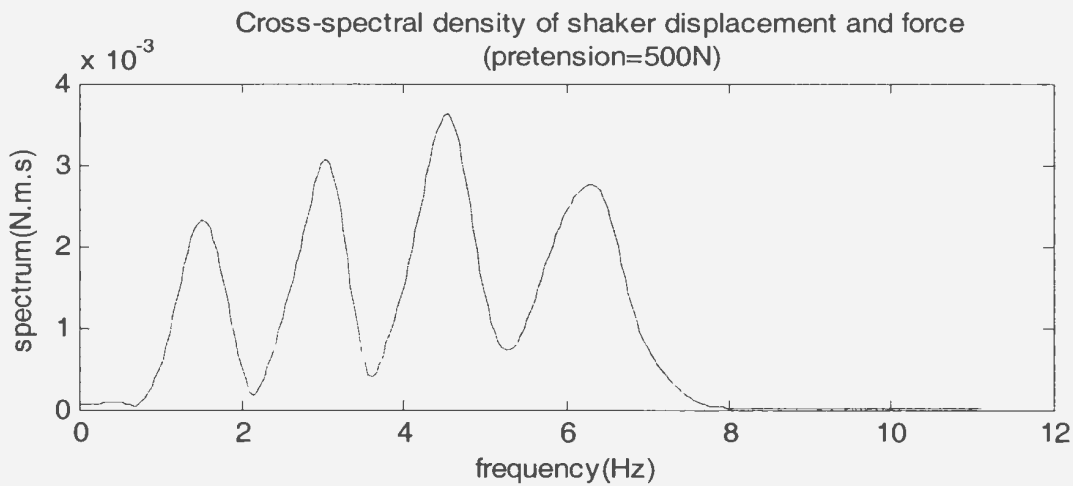


Figure 3-52 Cross-spectral density function of random shaker displacement and force

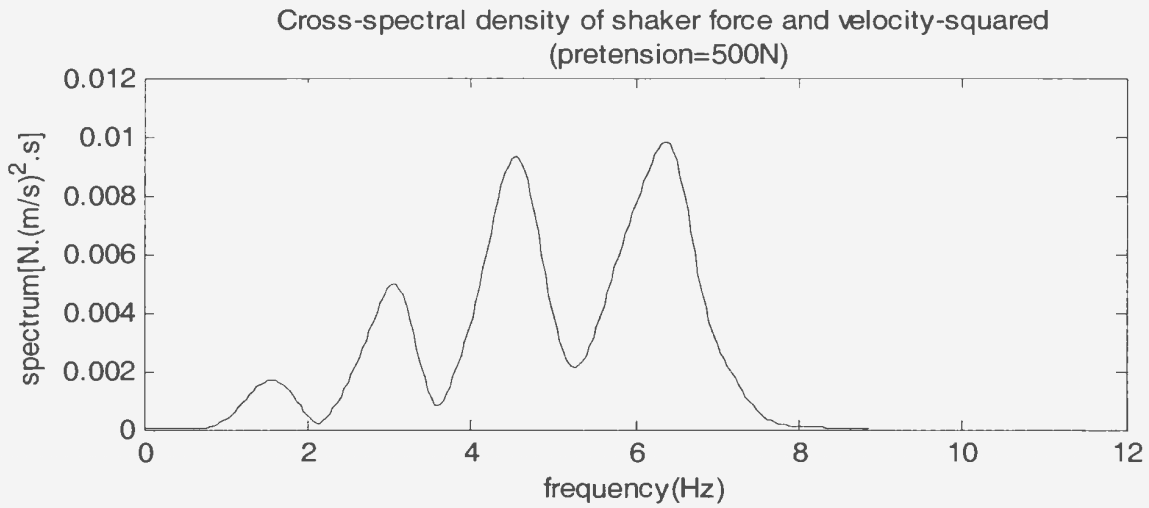


Figure 3-53 Cross-spectral density function of random shaker force and velocity-squared

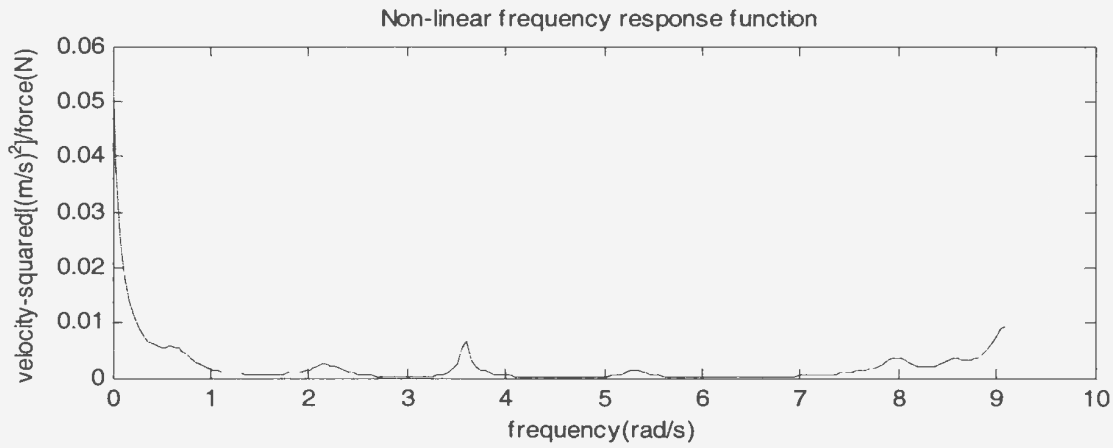


Figure 3-54 Non-linear component versus frequency

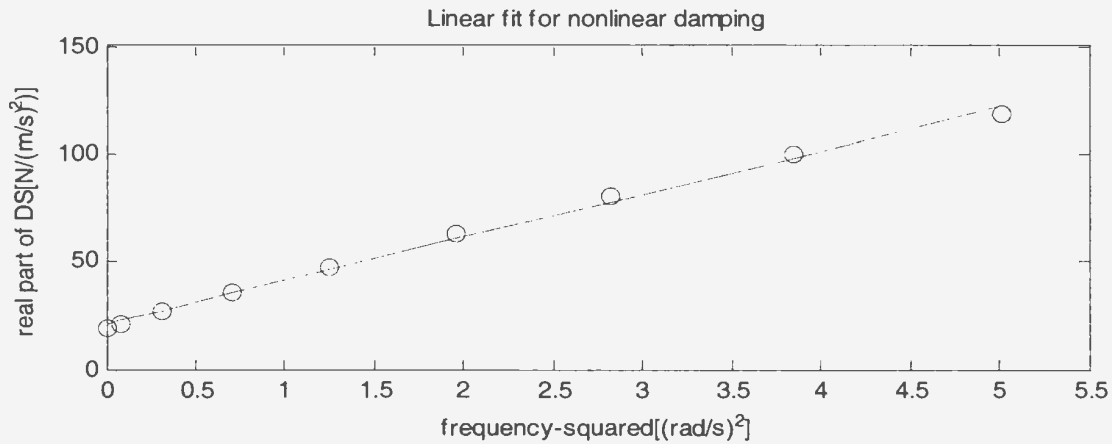


Figure 3-55 Linear fit for estimation of nonlinear damping

3. 4. 5 Summary of Shaker-Excitation Test Results

Frequency Response Functions

Frequency response functions reveal the basic characteristics of riser structural responses to vortex-shedding loads, including the resonances and anti-resonances. A flexible riser has a number of natural frequencies and a number of resonance and anti-resonance regions, which correspond to a number of mode shapes. The low modes have low natural frequencies, while the high modes have high natural frequencies.

Figure 3-56 summarizes the frequency response functions at the three pretensions tested. As seen in Figure 3-56, the increased tensions cause peaks and troughs to move towards higher frequency regions for the same mode of vibration. Increased tensions also cause peak magnitude to reduce.

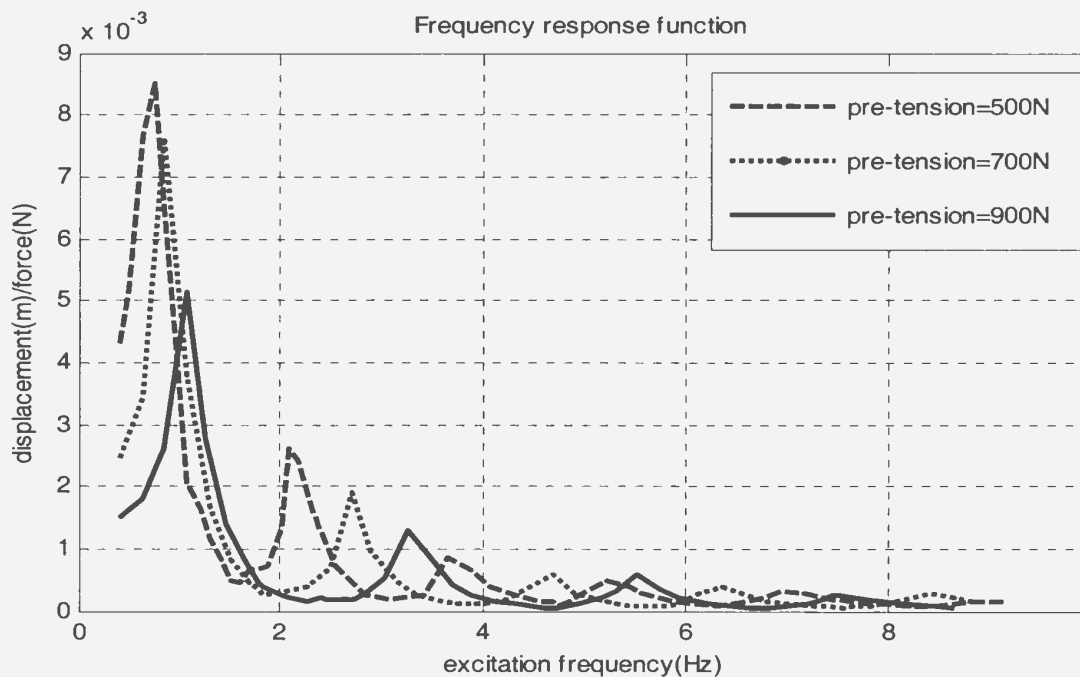


Figure 3-56 Tension effects on the frequency response functions

Modal Stiffness and Modal Masses

Table 3-13 summarizes the modal stiffness at the three pretensions tested. As seen in Table 3-13, the modal stiffness strongly depends on the pretensions. The modal stiffness increases rapidly as the tensions increase. The modal stiffness also depends on the mode shapes.

Table 3-13 Summary of the modal stiffness (N/m)

| Pretension | Mode 1 | Mode 3 | Mode 5 | Mode 7 | Mode 9 |
|------------|--------|--------|--------|--------|--------|
| 500(N) | 317 | 3519 | 8948 | 19350 | 25264 |
| 700(N) | 554 | 6900 | 21393 | 28825 | 37614 |
| 900(N) | 976 | 11931 | 30860 | 49077 | - |

Table 3-14 summarizes the modal mass at the three pretensions tested. As seen in Table 3-14, the modal masses depend weakly on the tensions. The modal masses increase slowly as the tensions increase. The modal masses also depend on the mode shapes. A maximum of modal mass appears in mode 3 or mode 5, and the modal mass decreases for higher or lower modes than the two modes. Table 3-15 summarizes the estimated added mass coefficients. The added mass coefficients range from 1.0 to 3.7 and exhibit the same characteristics as the modal mass.

Table 3-14 Summary of the modal mass (kg)

| Pretension | Mode 1 | Mode 3 | Mode 5 | Mode 7 | Mode 9 |
|------------|--------|--------|--------|--------|--------|
| 500(N) | 12.6 | 19.2 | 17.2 | 18.4 | 13.7 |
| 700(N) | 18.0 | 24.1 | 25.0 | 18.7 | 13.9 |
| 900(N) | 21.1 | 27.0 | 25.6 | 22.0 | - |

Table 3-15 Summary of added mass coefficients

| Pretension | Mode 1 | Mode 3 | Mode 5 | Mode 7 | Mode 9 |
|------------|--------|--------|--------|--------|--------|
| 500(N) | 1.00 | 2.23 | 1.86 | 2.08 | 1.20 |
| 700(N) | 2.01 | 3.15 | 3.32 | 2.14 | 1.24 |
| 900(N) | 2.59 | 3.69 | 3.43 | 2.76 | - |

Modal Natural Frequencies

Modal natural frequencies play an important role in understanding the frequency “lock-in” and amplitude resonance phenomena for a flexible riser. Table 3-16 summarizes the modal natural frequencies at the three pretensions tested. As seen in Table 3-16, the modal natural frequencies depend on the pretensions. The increased pretensions result in increased modal natural frequencies for all modes. The high modes have high natural frequencies, while the low modes have low natural frequencies.

Equation (2-9) provides a way to estimate the modal natural frequencies, and the results estimated from this equation are shown in Table 3-17. The measured bending stiffness value of 1.52 N. m² was used. It is noted that the measured modal natural frequencies are similar to the estimated modal natural frequencies.

As addressed in Section 2. 1. 1, Vandiver (2003) provided a simplified formula to estimate the modal natural frequencies, which ignores bending stiffness. The results estimated from Vandiver’s formula are shown in Table 3-18. The differences between the values in Table 3-17 and 3-18 are small, and this means that bending stiffness only has a slight effect on the natural frequencies for the flexible riser tested.

Table 3-16 Summary of the modal natural frequency (Hz)

| Pretension | Mode 1 | Mode 3 | Mode 5 | Mode 7 | Mode 9 |
|------------|--------|--------|--------|--------|--------|
| 500(N) | 0.80 | 2.16 | 3.63 | 5.16 | 6.83 |
| 700(N) | 0.88 | 2.70 | 4.57 | 6.26 | 8.27 |
| 900(N) | 1.08 | 3.34 | 5.52 | 7.52 | - |

Table 3-17 Modal natural frequency (Hz) estimated from equation (2-9)

| Pretension | Mode 1 | Mode 3 | Mode 5 | Mode 7 | Mode 9 |
|------------|--------|--------|--------|--------|--------|
| 500(N) | 0.85 | 2.56 | 4.28 | 6.02 | 7.80 |
| 700(N) | 0.95 | 2.87 | 4.79 | 6.73 | 8.69 |
| 900(N) | 1.03 | 3.08 | 5.14 | 7.22 | - |

Table 3-18 Modal natural frequency (Hz) estimated from Vandiver's equation

| Pretension | Mode 1 | Mode 3 | Mode 5 | Mode 7 | Mode 9 |
|------------|--------|--------|--------|--------|--------|
| 500(N) | 0.85 | 2.55 | 4.26 | 5.97 | 7.67 |
| 700(N) | 0.95 | 2.86 | 4.77 | 6.68 | 8.59 |
| 900(N) | 1.03 | 3.08 | 5.13 | 7.18 | - |

Modal Damping

Damping has a crucial role in the vibration responses over a modal resonance region for a flexible riser. Damping also has a role in understanding the frequency “lock-in” and amplitude resonance phenomena for a flexible riser. One of the conditions for the occurrence of the frequency “lock-in” and the amplitude resonance is that risers have

small damping. Table 3-19 summarizes the modal damping at the three pretensions tested. As seen in Table 3-19, the modal damping does not show a regular change with respect to the pretensions, and this can be interpreted as there being no correlation between pretensions and damping. The modal damping depends on the mode shapes. Increased mode number results in increased modal damping. This may mean that high mode resonances are weaker than their low mode counterparts. Table 3-20 summarizes the corresponding damping coefficients. These coefficients range from 0.5 to 2.5, and have a same characteristic as the modal damping.

Table 3-19 Summary of the modal damping (N.s/m)

| Pretension | Mode 1 | Mode 3 | Mode 5 | Mode 7 | Mode 9 |
|------------|--------|--------|--------|--------|--------|
| 500(N) | 16.2 | 18.1 | 25.7 | 40.1 | 51.6 |
| 700(N) | 25.5 | 13.5 | 25.3 | 45.5 | 52.1 |
| 900(N) | 14.0 | 15.3 | 28.6 | 86.3 | - |

Table 3-20 Summary of damping coefficients

| Pretension | Mode 1 | Mode 3 | Mode 5 | Mode 7 | Mode 9 |
|------------|--------|--------|--------|--------|--------|
| 500(N) | 1.78 | 0.66 | 0.56 | 0.63 | 0.63 |
| 700(N) | 2.51 | 0.44 | 0.50 | 0.64 | 0.57 |
| 900(N) | 1.27 | 0.47 | 0.52 | 1.13 | - |

Non-linear Effects

The results from the nonlinear analysis show that the nonlinear effects mainly exist in the low frequency and the modal resonance regions. The reason for this is that in these regions the riser vibrations have relatively big amplitudes. The conclusions from the nonlinear analysis agree with the conclusions from the linear analysis.

CHAPTER 4

VORTEX-INDUCED VIBRATION TESTS

4. Vortex-Induced Vibration Tests

The structural and hydrodynamic properties of the model riser in calm water have been investigated through the shaker-excitation tests described in Chapter 3. This Chapter will present and discuss the results of the current-excitation tests (vortex-induced vibration tests).

4.1 Experimental Design and Performance

The model riser design was presented in Section 2. In this section, the current and pretension designs will be discussed.

As addressed earlier, when a flexible riser experiences a flow with enough current velocity, the vortex-shedding phenomenon occurs. The vortex-shedding forces will cause

the riser to vibrate in the in-line and the cross-flow directions, namely vortex-induced vibrations (VIV). As deep-water risers have long and flexible structures, the vibration may contain several modal components, namely the multi-modal vibrations. Multi-modal vibration responses depend on the structural parameters of the riser and the characteristics of vortex-shedding; these parameters and characteristics are, therefore, important for the design of a VIV test. Some structural parameters, such as mass and bending stiffness, have been discussed in the design of model risers, which were presented in Chapter 2. In this section, two of the other parameters important for VIV tests will be discussed. One is the current velocities and the other is the pretensions.

In theory, the current velocities can be designed based on similarity of the Reynolds number, defined as $R_e = UD/\nu$, where: ν is the kinematic viscosity of water, D is riser diameter and U is current velocity, between the prototype and the model riser systems. The R_e for typical real production risers, for example in the Gulf of Mexico (Allen and Henning, 2001), ranges from about 1.5×10^5 to 3.4×10^5 ; however, these R_e values are too big to be modeled in the laboratory due to limited current velocities. In the present work, uniform current velocities were generated by moving the tank carriage, the maximum current velocity was, therefore, designed based on the tank length and the required data acquisition time. Twenty-seven current velocities ranging from 0.1 to 1.5m/s were selected, and the maximum Reynolds number R_e was 0.6×10^5 , which corresponds to a prototype current velocity of 0.2m/s for the selected nominal prototype riser shown in Section 2.

The pretensions were then designed based on these selected current velocities and the required equivalent tension T , which was discussed in Chapter 2. On other words, the

pretensions were designed to satisfy the required equivalent tension T at some typical currents, which will generate drag forces affecting the tension acting on the riser. In fact, the pretension design is to achieve the similarity of the frequency ratio ω^* , defined as $\omega^* = \omega / \omega_n$, where: ω is the vortex shedding frequency and ω_n is the natural frequency, so that the expected modes can be obtained in the model riser tests. These modes must be similar between the prototype and model riser systems. In the present work, two pretensions of 200 and 600N were used.

The number of the accelerometers used can be determined based on the maximum expected mode. Assume that the mode is approximately sinusoidal in shape, and a minimum of two measurement points per wavelength is suggested by a spatial Nyquist criterion (Vandiver and Marcollo, 2003). This means that the number of measurement points must be larger than the maximum mode number. Obviously, the minimum number of measurement points suggested by the spatial Nyquist criterion is only an acceptable solution, not the best solution, as this minimum number of measurement points only roughly describes the vibration shapes over riser length. In the present work, the goals were to measure multi-modal VIV responses with mode number up to 10, and initially double of the minimum number of measurement points (twenty pairs of accelerometers) were designed. However, four pairs of accelerometers were damaged in the model riser fabrication process, and finally only sixteen pairs of accelerometers could work. With the sixteen pairs of accelerometers, a clear multi-modal vibration shape over riser length was expected to be observed and a modal analysis with a sufficient accuracy was expected to be achieved.

Vortex-Induced Vibration Tests

The tests were performed in the Ice Tank at the Institute for Ocean Technology, the National Research Council of Canada. The riser was mounted horizontally on the steel frame, and then was placed at a water depth of 1.0m. The vertical lever mechanism on the supporting frame was used to adjust the pretensions applied to the riser. Figure 4-1 is a photo of the current-excitation test scene.

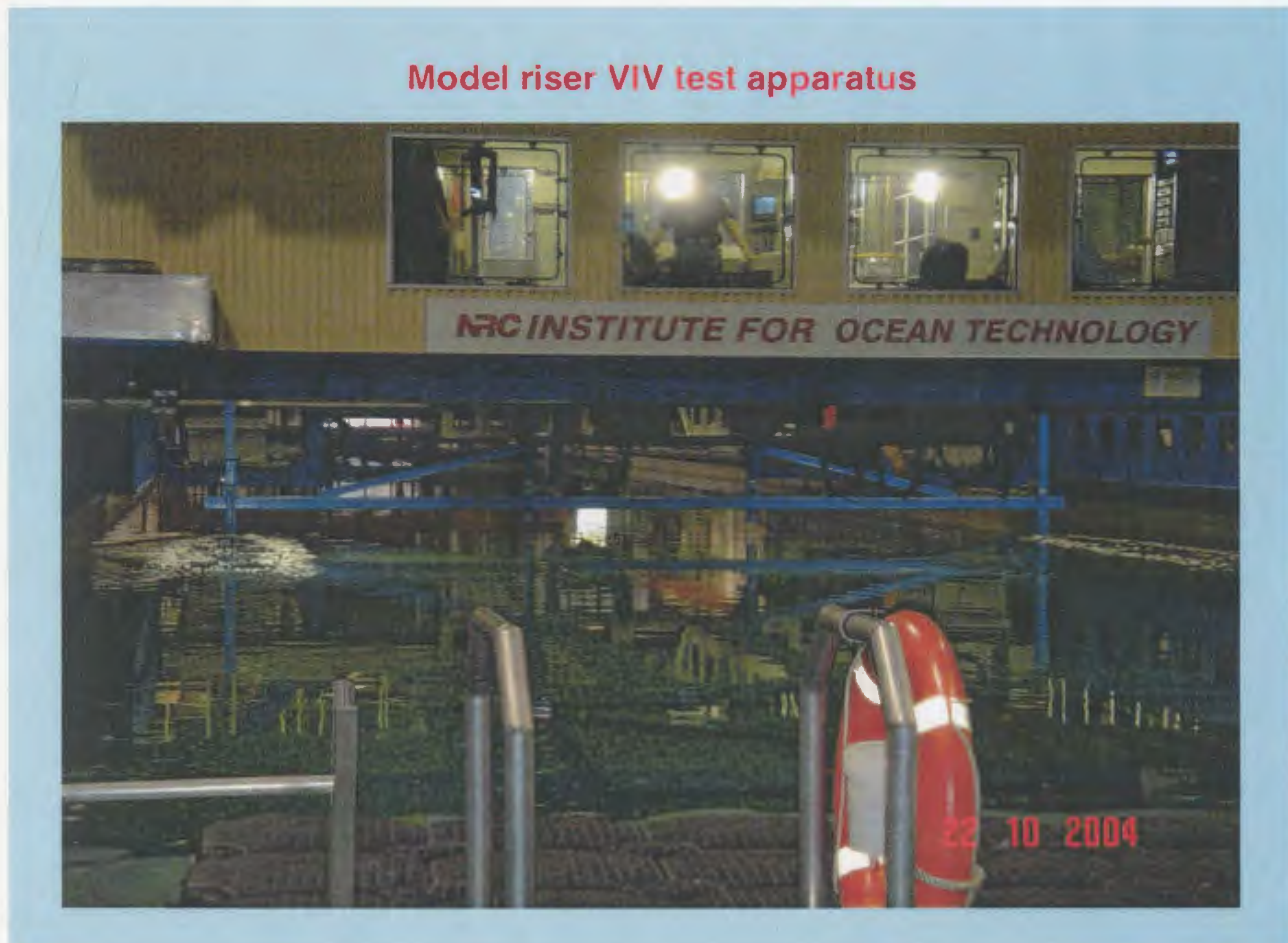


Figure 4-1 Current-excitation tests

The measured data were analyzed in the time-domain, the frequency-domain and the space-domain. The analysis in the time-domain produced the results: i) average peak-pick-up amplitude versus current velocity; and ii) average peak-pick-up frequency versus

current velocity. In this analysis, the peak was defined as a positive sampled value greater than twenty neighboring sampled values. As the data sampling frequency was 50Hz in the tests, this definition of peak ensured that a frequency component of 5Hz was not omitted. This frequency is larger than the Strouhal frequency of 0.45Hz at the maximum current velocity of 1.5m/s. The average peak-pick-up amplitude was defined as the average of all peaks, and the inverse of the average time interval of these peaks was defined as the average peak-pick-up frequency.

The analysis in the time-domain revealed the amplitude and frequency characteristics of the VIV responses against the currents. In fact, the peak-pick-up frequencies were only a rough description of the frequency characteristics of the VIV responses, and they did not provide complete information about the frequency characteristics of the VIV responses. The analysis in the frequency-domain gave a more detailed picture of frequency components in the VIV responses than the results from the analysis in the time-domain. The tool for the frequency-domain analysis was the spectral analysis technique shown in Appendix B.

The analysis in the space-domain produced the results: i) the vibration shapes over the riser length; ii) the vibration trajectories in the cross-section plane of the riser; iii) the modal responses versus the current velocity; and iv) the modal components in the VIV responses. In this analysis, the modal components were calculated through integration of the VIV displacements over riser length based on equation (2-5).

4. 2 Test Results

4. 2. 1 Tensions and Modal Natural Frequencies at Different Currents

Multi-modal VIV responses contain some complicated phenomena, such as modal resonances and frequency lock-in, and the modal parameters estimated in Chapter 3 will be employed to understand these complicated phenomena. Of these modal parameters, the modal natural frequency is the most important parameter. Table (3-16) gives the modal natural frequencies in calm water at three tensions of 500, 700 and 900N, and the modal natural frequency versus tension can be obtained by fitting these values based on the second-order polynomials. The fitting results are shown in Figure 4-2.

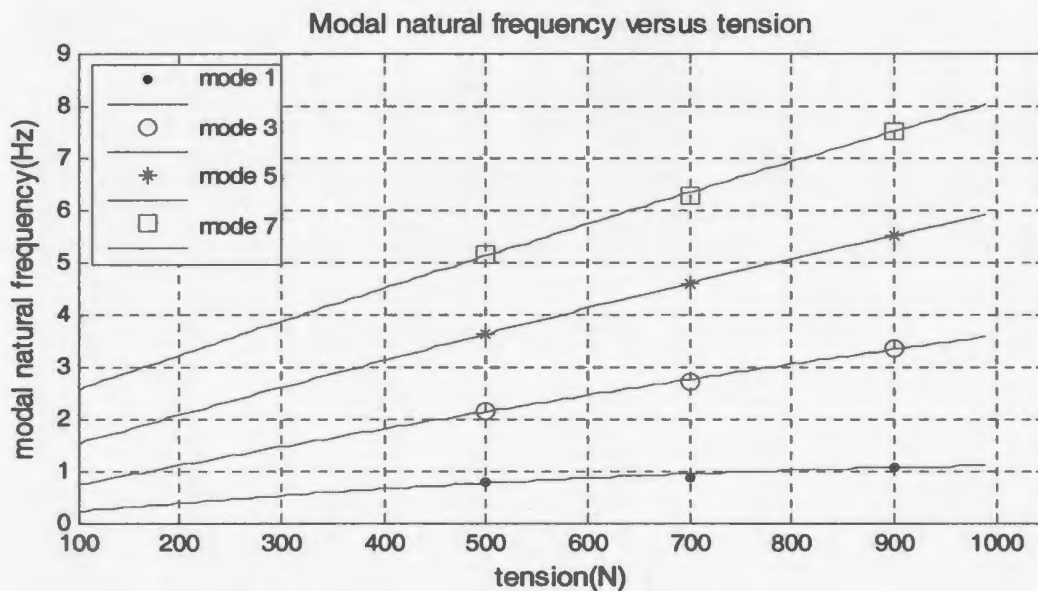


Figure 4-2 Modal natural frequency versus tension

Assume that the existence of currents does not affect the added mass of the riser, and the modal natural frequencies in currents can be estimated based on the modal natural frequencies in calm water and the tensions resulting from the drag forces in currents. In this research, the tensions resulting from the drag forces were measured at the pretension

of 600N, shown in Figure 4-3. Combination of the results respectively shown in Figure 4-2 and Figure 4-3 yields the modal natural frequency versus the current velocity at the pretension of 600N, shown in Figure 4-4. The symbol f^* denotes the ratio f_{nk}/f_{n1} , where: f_{nk} is the natural frequency of the k -th mode, and f_{n1} is the natural frequency of the first mode. From Figure 4-2, the value of f_{n1} is equal to 0.85Hz, and this value was used to plot the curves in Figure 4-4. The symbol V^* denotes the reduced velocity, defined as $V^*=U/f_{n1}D$, where: U is the current velocity, D is the riser diameter. The Strouhal frequencies with $S_r = 0.12$ are also shown in Figure 4-4, which represent the vortex-shedding frequencies. The natural frequencies for the even modes with number k ($=2, 4$ and 6) were not obtained from the shaker-excitation tests, and the natural frequencies for the even modes in Figure 4-4 were calculated by a simple average, namely

$$f_{nk} = \frac{1}{2}(f_{nk-1} + f_{nk+1})$$

$$k = 2,4,6$$

where f_{nk} denotes the natural frequency for an even mode (the k -th mode), and f_{nk-1} and f_{nk+1} denote the natural frequencies for its two adjacent odd modes.

The relationship between the tension and the current velocity at a pretension of 200N was not measured in this research. The tension versus current velocity at the pretension of 200N was simply deduced from the measured tensions at the pretension of 600N. Specifically, under the assumption that i) the tensions at currents contain two components of the pretension and the additional tension resulting from the drag force and ii) the pretension does not affect the additional tension, the tensions in currents at the pretension of 200N can be estimated by subtracting 400N, which is the difference between the two pretensions, from the tensions in currents at the pretension of 600N. The estimated modal

natural frequency versus the current velocity at the pretension of 200N is shown in Figure 4-5. From Figure 4-2, the natural frequency f_{n1} is 0.376Hz in the case of the pretension of 200N, and this value was used to plot the curves in Figure 4-5. The Strouhal frequencies with $S_r = 0.12$ are also shown in Figure 4-5. The natural frequencies shown in Figures 4-4 and 4-5 will be used to analyze the results from the current-excitation tests.

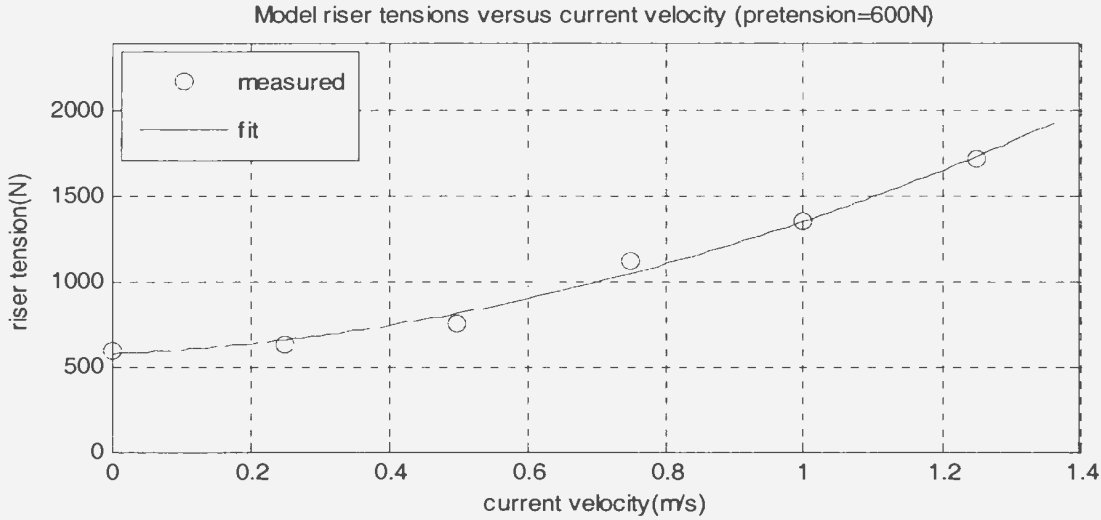


Figure 4-3 The relationship between the tension and the current velocity at a pretension of 600N

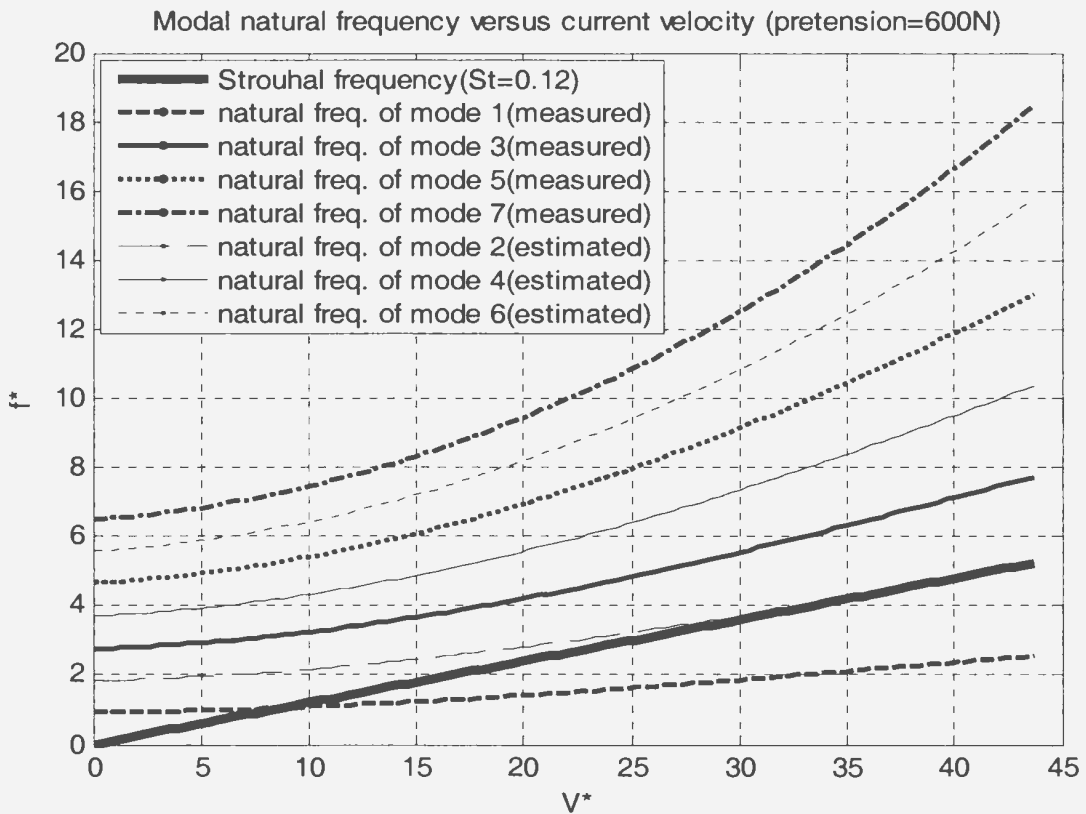


Figure 4-4 The relationship between the modal natural frequency and the current velocity at a pretension of 600N

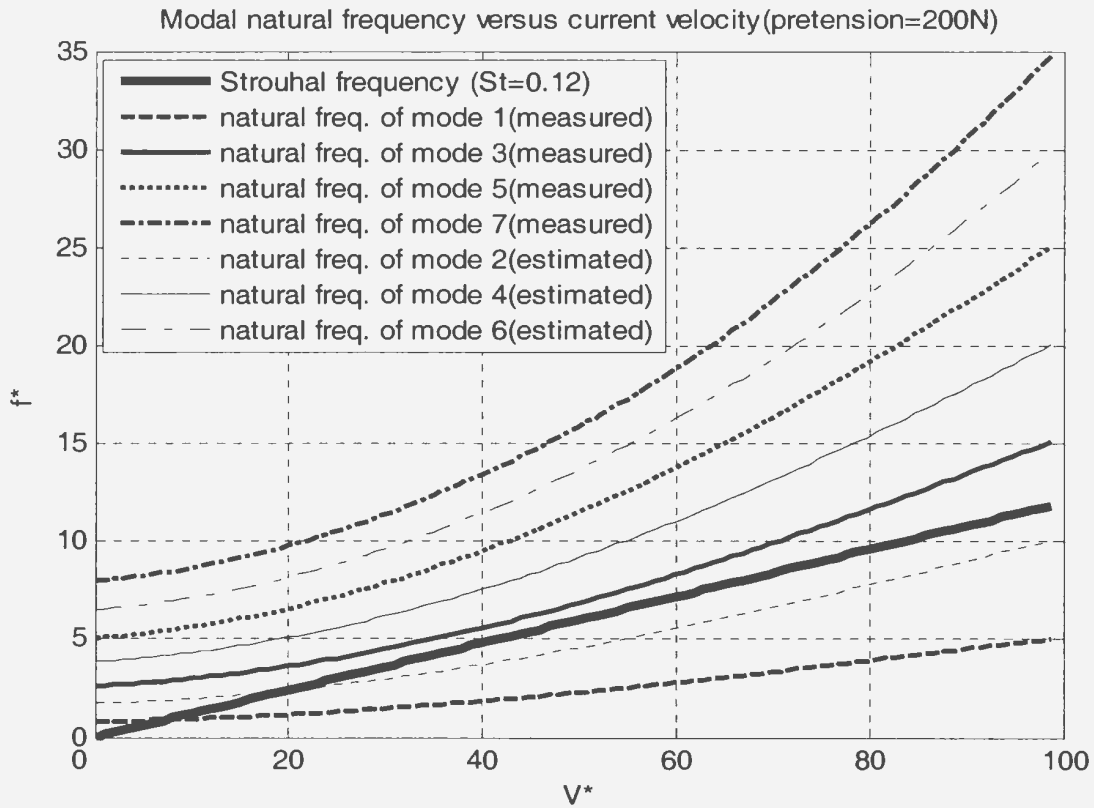


Figure 4-5 The relationship between the modal natural frequency and the current velocity at a pretension of 200N

4. 2. 2 Test Results at Low Pretension of 200N

The first pretension tested was 200N. The required pretension was achieved using the pretension adjustment lever mechanism prior to the tests. As the distributing weight of the riser in water was relatively small (about 38N) compared to the pretension, this weight did not produce the large sag on the riser. Twenty-eight current velocities ranging from 0.75 to 1.5m/s were tested for this pretension.

4. 2. 2. 1 Amplitude and Frequency versus Current Velocity

Figure 4-6 presents the average peak-pick-up amplitude and the average peak-pick-up frequency versus current velocity at the pretension of 200N. V^* is the reduced velocity,

defined as $V^*=U/f_{n1}D$, where: U is the current velocity, D is the riser diameter, $f_{n1} = 0.376\text{Hz}$, which is the natural frequency of the first mode in calm water. f^* is the frequency ratio, defined as $f^*=f/f_{n1}$, where: f is the riser vibration frequencies in currents. A^* is the non-dimensional vibration amplitude, defined as $A^*=A/D$, where: A is the average peak-pick-up amplitude over the measured period and riser length.

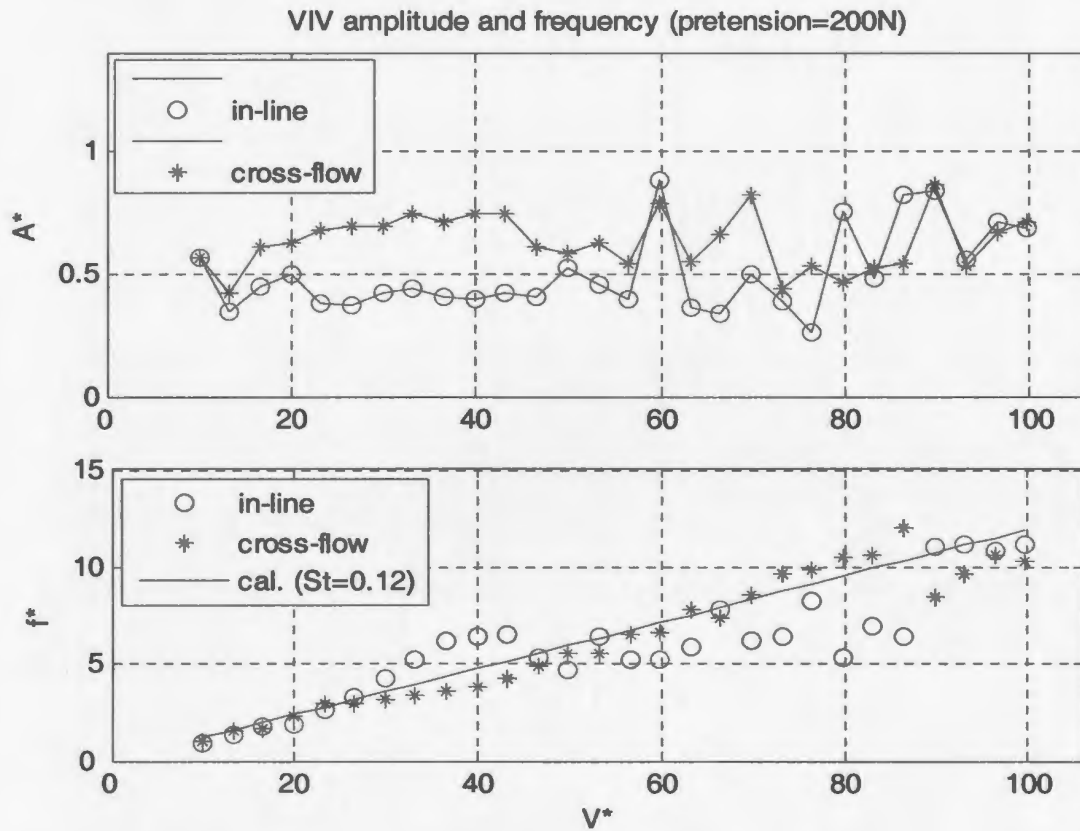


Figure 4-6 The average peak-pick-up amplitude and frequency of in-line and cross-flow VIV at a pretension of 200N

As seen in Figure 4-6, the average peak-pick-up frequencies of cross-flow VIV follow the Strouhal frequencies at the majority of current velocities. The fitted Strouhal number is about 0.12. However, in the reduced velocity region from $V^*=25$ to 47, the average peak-pick-up frequencies of cross-flow VIV are smaller than the Strouhal frequencies, and this may represent a frequency lock-in phenomenon, although the frequency lock-in

seems to be weak, as the frequency still varies with the reduced velocity over whole lock-in region and does not lock in at a constant frequency. The lock-in frequency is about 1.1Hz. There are four reasons for the judgment of the occurrence of a frequency lock-in in the reduced velocity region. The first is that the vibration frequencies start to depart from the Strouhal frequency at a reduced velocity of 25, which corresponds to the natural frequency for mode 2 according to Figure 4-5. The second is that the lock-in frequency (=1.1Hz) is close to the natural frequency ($f_{n2}=1.05\text{Hz}$) for mode 2. The third is that according to Figure 4-5 the bandwidth of vortex-shedding frequency over the reduced velocity region from $V^*=25$ to 47 may only cover a natural frequency of mode 2. In fact, one of the conditions for the occurrence of frequency lock-in for a rigid cylinder is that only one natural frequency is contained in the bandwidth of the vortex-shedding frequency (Vandiver, 1993), and the conclusion may be extended for a flexible riser. The fourth is that the reduced velocity (using f_{n2}) at the end point of the lock-in region is smaller than the maximum upper limit value calculated from the formula provided by Govardhan and Williamson (2000). They gave a formula to estimate the maximum upper limit value of the reduced velocity for the lock-in region for a rigid cylinder as follows:

$$V_{\max}^* = 9.25 \sqrt{\frac{m^* + C_a}{m^* - 0.54}} \quad (4-1)$$

where C_a is the added mass coefficient. The mass ratio, m^* , is defined as

$$m^* = \frac{m}{\frac{1}{4} \pi \rho D^2}$$

where m is the structural mass per unit length of the cylinder, ρ is the water density, and D is the diameter of the cylinder. The mass ratio m^* for the model riser tested is 1.36. At

the reduced velocity $V^*=25$, the estimated tension acting on the riser is 500N. Let the added mass coefficient C_a for mode 2 take the value of 1.7, which is an average of the added mass coefficients for mode 1 and mode 3 at the pretension of 500N shown in Table 3-17, and from equation (4-1) the maximum upper limit value of the reduced velocity for the lock-in region is 17.8. According to Figure 4-6, the lock-in region ends at a reduced velocity (using f_{n1}) of 47. If we use the natural frequency f_{n2} to re-calculate the reduced velocity, the lock-in region ends at a reduced velocity of 16.83, which is a little smaller than the maximum upper limit value of 17.8 estimated from equation (4-1).

As seen in Figure 4-6, in the reduced velocity region from $V^*=25$ to 47, the in-line response frequencies show a trend of frequency lock-in at the natural frequency of mode 3, so that the in-line response frequencies are larger than the cross-flow response frequencies. According to Figure 4-5, the natural frequencies for mode 2 and 3 are relatively close in this region and the vortex-shedding frequencies in the in-line direction may be bigger than the Strouhal frequencies, as discussed earlier, and this causes that there may be two alternative lock-in modes, i.e. mode 2 and 3, for the in-line VIV responses in this region. The test results showed that the in-line responses trended to lock-in in mode 3.

It is noted that no frequency lock-in is found in both the cross-flow and the in-line directions near the reduced velocity of about 9.0, which corresponds to the natural frequency of mode 1 according to Figure 4-5. The reason is that the reduced velocities of resonance for mode 1 and 2 are too close so that the resonance regions for the two modes may overlap in the region from $V^*=9$ to 25. In the unlock-in region, the in-line vibration frequencies are approximately equal to the cross-flow vibration frequencies.

In the region where the reduced velocities range from 45 to 90, the in-line vibration frequencies become smaller than the Strouhal frequencies and also demonstrate a characteristic of frequency lock-in. For example, according to Figure 4-5 the frequencies approximately remain a constant of 2.1Hz, and this frequency is close to the natural frequency f_{n3} of 2.44Hz for mode 3 at the reduced velocity V^* of 45. The reduced velocity (using f_{n3}) at the end point of the lock-in region is also smaller than the maximum upper limit value estimated from equation (4-1). Use the natural frequency f_{n3} to re-calculate the reduced velocity, and the lock-in region ends at a reduced velocity of 13.87. As addressed earlier, the tension versus current velocity at the pretension of 200N can be simply deduced from the measured tensions at the pretension of 600N, and the deduced tension is approximately equal to 600N at the reduced velocity (using f_{n1}) of 90 for this case. Then the added mass coefficient for mode 3 at the tension of 600N can be estimated by taking an average of the added mass coefficient of mode 3 at the pretensions of 500N and 700N, which is shown in Table 4-15, and the estimated average value of the added mass coefficient for mode 3 is 2.69. Use this value to calculate the maximum upper limit value of the reduced velocity based on equation (4-1), and the resultant reduced velocity is 20.53, which is greater than the measured value of 13.87 at the end point of the lock-in region.

Since the frequency lock-in for the in-line direction occurs in a relatively high current velocity region, the in-line response frequencies exhibit a big scatter. It is noted that in this region the cross-flow response frequencies still follow the Strouhal frequencies, and this means that the frequency lock-in occurs only in one direction.

As seen in Figure 4-6, both the average peak-pick-up amplitudes of the in-line and cross-flow VIV fluctuate in a regime ranging from $0.25D$ to $0.9D$. An apparent feature is that the increased current velocities do not cause increased amplitudes although the vortex-shedding forces may increase as current velocities increase. It is also noted that no obvious peaks exist over the current velocity range tested, even though mode 2 encounters a resonance. As energy is shared by several modes, the resonance for a single mode does not produce an obvious resonance in the total responses for multi-modal VIV. The single-modal VIV responses have very small amplitudes in the regions where vortex-shedding frequencies are far away from the natural frequency, as shown in Figure 1-4. However, the multi-modal VIV responses do not show such a characteristic, because there are many natural frequencies for a flexible cylinder so that no current velocity regions where vortex-shedding frequencies are far away from these natural frequencies exist, except for the very low current velocity region.

According to Figure 4-6, three current velocity regions can be found: i) Region A: the region where no frequency lock-in occurs; ii) Region B: the region where the frequency lock-in occurs in one direction; and iii) Region C: the region where the frequency lock-in occurs in two directions.

In Region A, the average peak-pick-up frequencies for in-line VIV responses are nearly identical to the average peak-pick-up frequencies for cross-flow VIV responses, and these frequencies match the Strouhal frequencies. In Region B, frequency lock-in only occurs at one of the in-line and the cross-flow directions, and the average peak-pick-up frequencies for the in-line VIV responses are different from the average peak-pick-up frequencies for the cross-flow VIV responses. In Region C, the frequency lock-in occurs

in both the in-line and the cross-flow directions, but the lock-in modes in the two directions may be different. If the lock-in modes in the two directions are different, the average peak-pick-up frequencies for the in-line VIV responses will be different from the average peak-pick-up frequencies for the cross-flow VIV responses.

4.2.2.2 Vibration Power Spectra

A detailed analysis of the frequency components existing in VIV responses helps understand the complicated behaviors of multi-modal VIV responses for a flexible riser. The spectral analysis technique shown in Appendix B can be used to reveal the frequency components in a VIV response, and the result is a continuous power spectral function with respect to frequency. The frequencies corresponding to peaks in the power spectral function are the dominant or secondary-dominant frequencies of the VIV response.

As discussed in Section 4.2.2.1, there are three regions, i.e. Region A, Region B and Region C, in the plots of average peak-pick-up frequency and amplitude versus reduced velocity for the VIV responses. In this section, the vibration power spectra of VIV responses in these regions will be examined.

Vibration power spectra in Region A

According to Figure 4-6, Region A ranges from $V^*=9$ to 25. Let us check the power spectra of VIV responses at a reduced velocity of 13.30, which corresponds to a current velocity of 0.2m/s. Figure 4-7 gives the power spectrum of cross-flow VIV responses at the middle of the riser at this reduced velocity. This power spectrum demonstrates a

single dominant frequency of 0.4Hz, which is close to the corresponding average peak-pick-up frequency of 0.5Hz, as shown in Figure 4-6.

Figure 4-8 gives the power spectrum of in-line VIV responses at the middle of the riser at the reduced velocity of 13.30. This power spectrum demonstrates a single dominant frequency of 0.4 Hz, which is equal to its counterpart for the cross-flow VIV responses. This dominant frequency is also close to the average peak-pick-up frequency of 0.5Hz for the in-line VIV responses at the same reduced velocity, as shown in Figure 4-6.

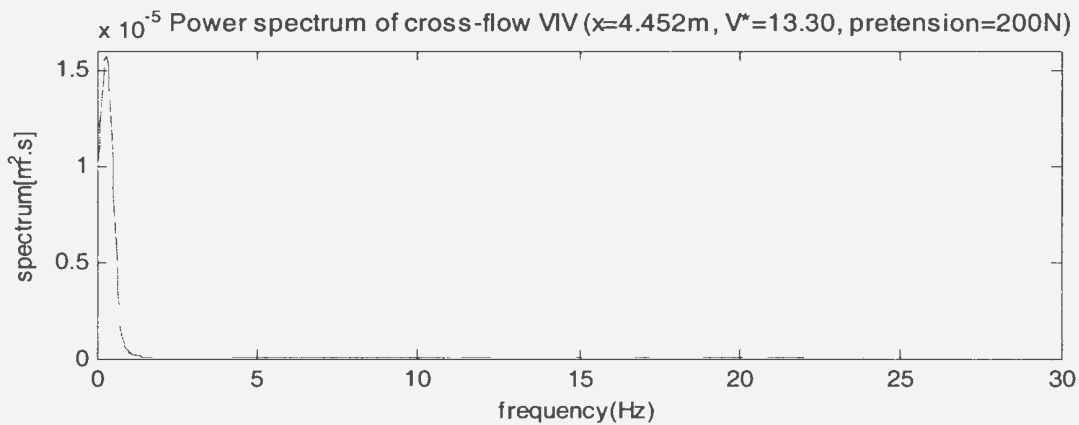


Figure 4-7 Power spectrum of cross-flow VIV at the middle of riser at a current velocity of 0.2m/s and a pretension of 200N

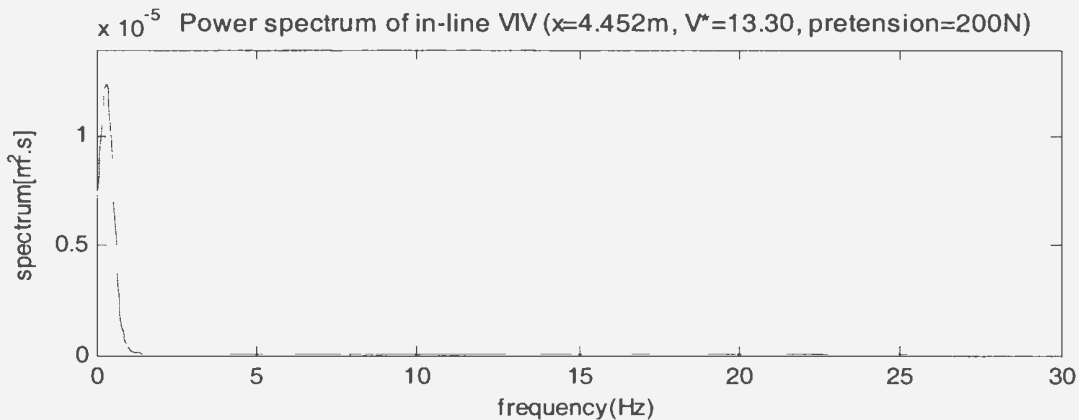


Figure 4-8 Power spectrum of in-line VIV at the middle of riser at a current velocity of 0.2m/s and a pretension of 200N

Vibration power spectra in Region B

According to Figure 4-6, the VIV responses at the reduced velocities from $V^*=45$ to 90 are the responses in Region B. Let us check the power spectra of VIV responses at three reduced velocities of 53.20, 73.15 and 86.44, which respectively correspond to the current velocities of 0.8, 1.1 and 1.3m/s.

Figure 4-9 presents the power spectrum of cross-flow VIV responses at the reduced velocity of 53.20. This reduced velocity is close to the starting point of Region B. As seen in Figure 4-9, there is a strong dominant frequency of 2.5Hz and a weak secondary-dominant frequency of 0.4Hz. As the secondary-dominant frequency contains a small amount of energy, it has little contribution to the VIV responses. According to Figure 4-6, at this reduced velocity, the average peak-pick-up frequency and the Strouhal frequency are respectively 2.1 and 2.4 Hz, which are close to the dominant frequency.

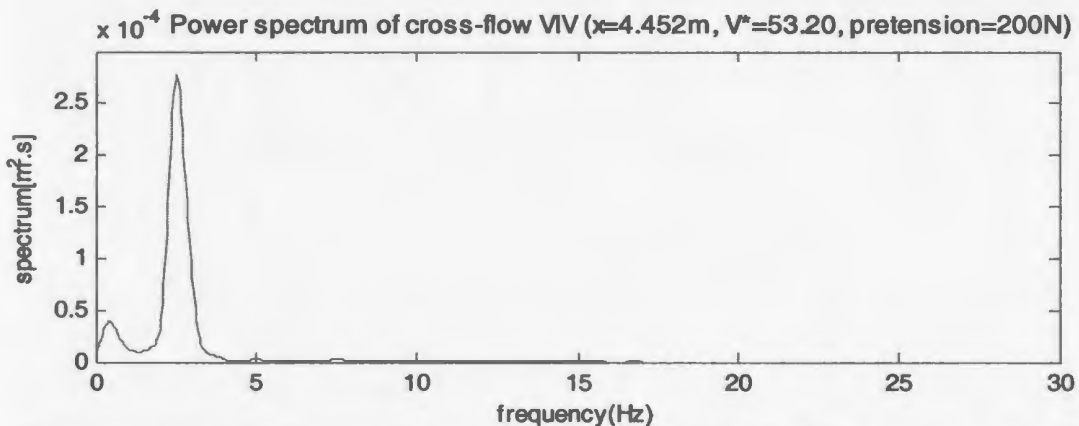


Figure 4-9 Power spectrum of cross-flow VIV at the middle of riser at a current velocity of 0.8m/s and a pretension of 200N

Figure 4-10 presents the power spectrum of in-line VIV responses at the reduced velocity of 53.20. As seen in Figure 4-10, there are a strong dominant frequency of 0.4Hz and three weak secondary-dominant frequencies of 2.5, 5.0 and 5.8Hz. According to

Figure 4-6, at this reduced velocity, both the average peak-pick-up frequency and the Strouhal frequency is 2.4Hz, which is close to one of the secondary-dominant frequencies.

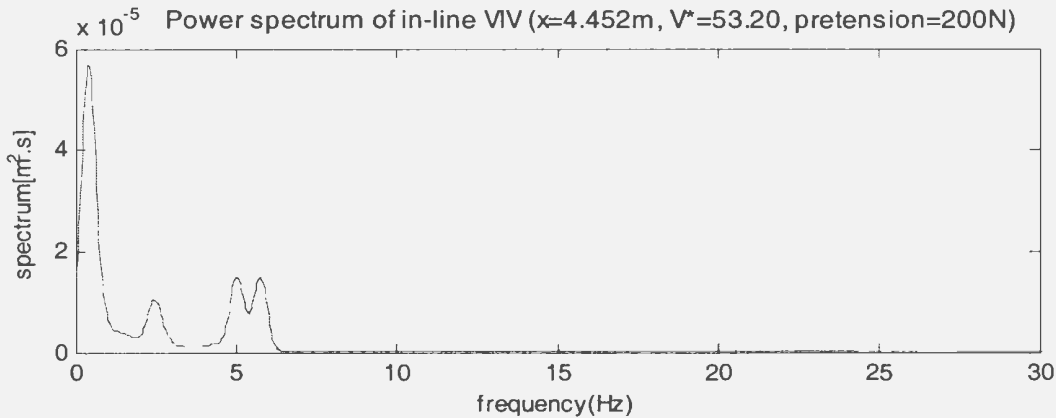


Figure 4-10 Power spectrum of in-line VIV at the middle of riser at a current velocity of 0.8m/s and a pretension of 200N

Figure 4-11 presents the power spectrum of cross-flow VIV responses at the reduced velocity of 73.15. As seen in Figure 4-11, there is a strong dominant frequency of 4.3Hz and a secondary-dominant frequency of 0.8Hz. According to Figure 4-6, at this reduced velocity, the average peak-pick-up frequency and the Strouhal frequency are respectively 3.7 and 3.3Hz, and the two frequencies are smaller the dominant frequency and larger than the secondary-dominant frequency.

Figure 4-12 presents the power spectrum of in-line VIV responses at the reduced velocity of 73.15. As seen in Figure 4-12, there are a strong dominant frequency of 0.8Hz and two weak secondary-dominant frequencies of 5.0 and 8.8Hz. Figure 4-6 shows that the corresponding average peak-pick-up frequency is 2.4Hz, which is close to the natural frequency of mode 3 (2.44Hz). Obviously, the low dominant frequency of 0.8Hz causes the average peak-pick-up frequency to depart from the Strouhal frequency, but the

average peak-pick-up frequency does not match any dominant or secondary-dominant frequencies.

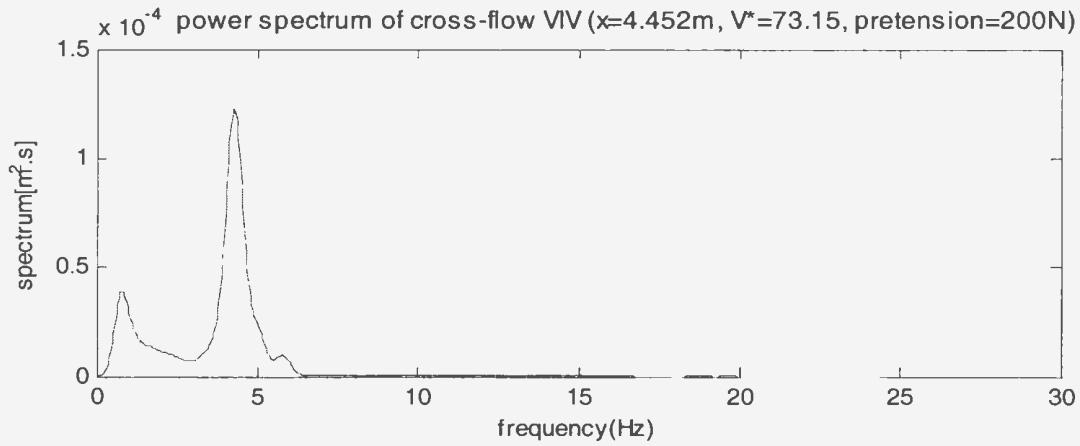


Figure 4-11 Power spectrum of cross-flow VIV at the middle of riser at a current velocity of 1.1m/s and a pretension of 200N

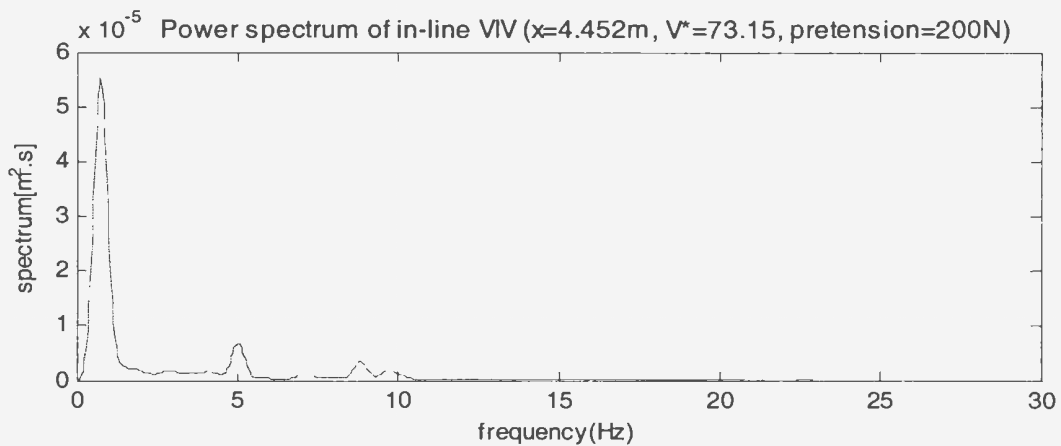


Figure 4-12 Power spectrum of in-line VIV at the middle of riser at a current velocity of 1.1m/s and a pretension of 200N

Figure 4-13 presents the power spectrum of cross-flow VIV responses at the reduced velocity of 86.44. This reduced velocity is close to high reduced velocity boundary of Region B. As seen in Figure 4-13, there are two strong dominant frequencies of 0.6 and 5.6Hz. According to Figure 4-6, the average peak-pick-up frequency and the Strouhal frequency are respectively 4.5 and 3.9Hz, which do not match any dominant frequencies.

Figure 4-14 presents the power spectrum of in-line VIV responses at the reduced velocity of 86.44. As seen in Figure 4-14, there is a strong dominant frequency of 0.6Hz and a weak secondary-dominant frequency of 11.2Hz. From Figure 4-6, the average peak-pick-up frequency is 2.4Hz. Also, at this reduced velocity the low dominant frequency of 0.6Hz causes the average peak-pick-up frequency to depart from the Strouhal frequency, but the average peak-pick-up frequency does not match any dominant or secondary-dominant frequencies.

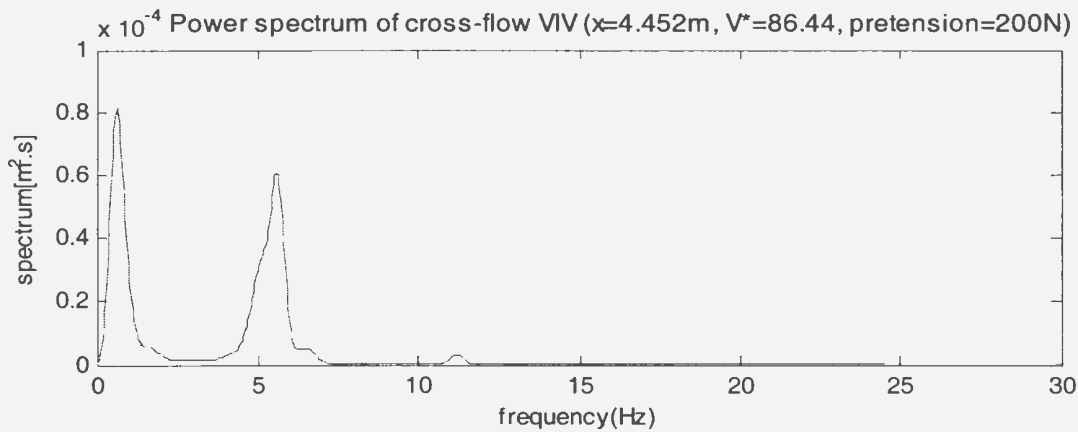


Figure 4-13 Power spectrum of cross-flow VIV at the middle of riser at a current velocity of 1.3m/s and a pretension of 200N

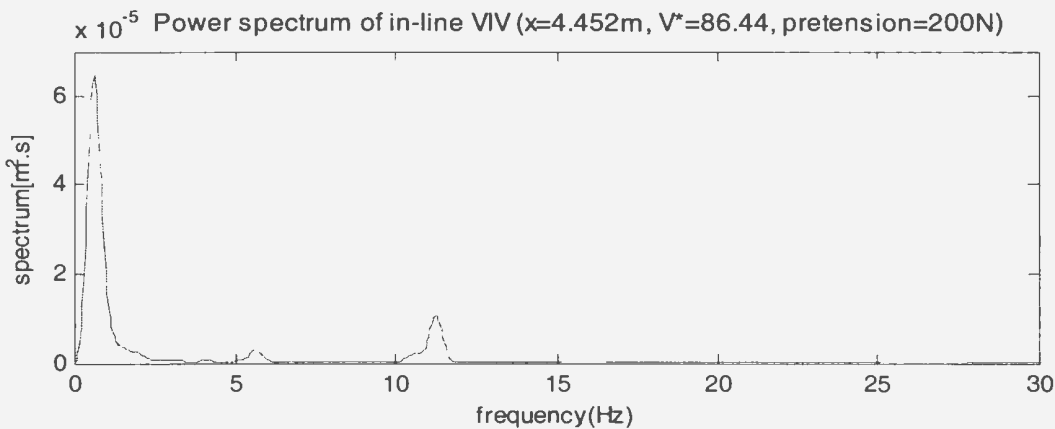


Figure 4-14 Power spectrum of in-line VIV at the middle of riser at a current velocity of 1.3m/s and a pretension of 200N

According to the discussions above, we know that in Region B both the in-line and cross-flow VIV responses contain more than one dominant and secondary-dominant frequency. The average peak-pick-up frequency is close to an average of these dominant and secondary-dominant frequencies. The lock-in frequency only matches the modal natural frequency, and does not match any dominant or secondary-dominant frequencies.

Vibration power spectra in Region C

According to Figure 4-6, Region C ranges from $V^*=25$ to 45. Let us examine the power spectra of VIV responses at two reduced velocities of 26.59 and 39.90, which respectively correspond to the current velocities of 0.4 and 0.6m/s.

Figure 4-15 presents the power spectrum of cross-flow VIV responses at the reduced velocity of 26.59. This reduced velocity is close to the starting point of Region C. As seen in Figure 4-15, there is a strong dominant frequency of 1.3Hz and a weak secondary-dominant frequency of 3.9Hz. As the secondary-dominant frequency contains a small amount of energy, it has little contribution to the VIV responses, so that the VIV responses are dominated by the dominant frequency. The dominant frequency is close to the corresponding average peak-pick-up frequency of 1.1Hz and the Strouhal frequency of 1.2Hz at the corresponding reduced velocity, as shown in Figure 4-6.

Figure 4-16 presents the power spectrum of in-line VIV responses at the reduced velocity of 26.59. It is noted that this power spectrum is obviously different from its counterpart in the cross-flow direction, which is shown in Figure 4-15. As seen in Figure 4-16, there are a dominant frequency of 2.6Hz and two secondary-dominant frequencies of 0.3Hz and 1.3Hz. The average of these dominant and secondary dominant frequencies

is 1.4Hz. The average peak-pick-up frequency at the corresponding reduced velocity is 1.3Hz, as shown in Figure 4-6, and this average peak-pick-up frequency is close to the average of the dominant and secondary dominant frequencies.

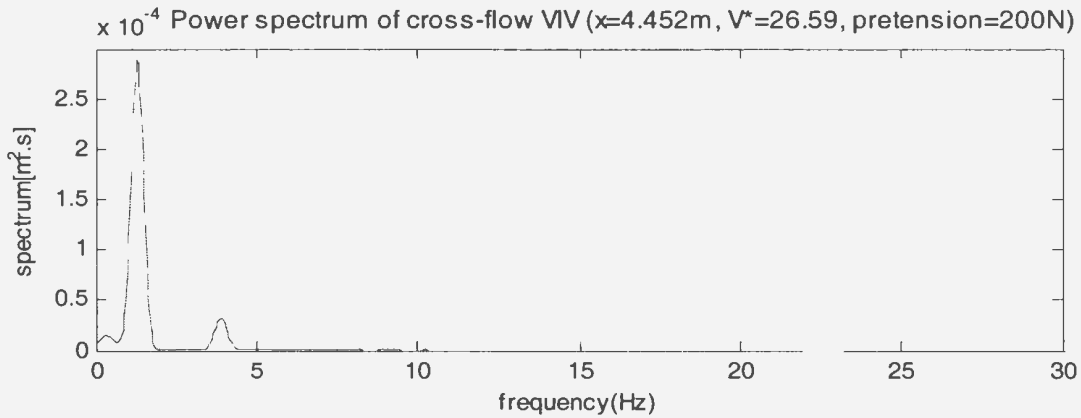


Figure 4-15 Power spectrum of cross-flow VIV at the middle of riser at a current velocity of 0.4m/s and a pretension of 200N

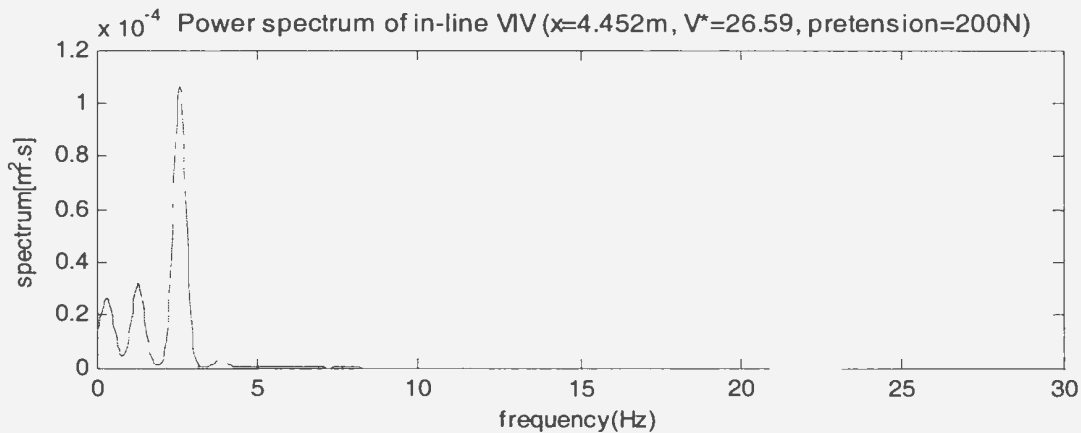


Figure 4-16 Power spectrum of in-line VIV at the middle of riser at a current velocity of 0.4m/s and a pretension of 200N

Figure 4-17 presents the power spectra of cross-flow VIV responses at the reduced velocity of 39.90. This reduced velocity corresponds to the mid-point of Region C. This power spectrum shows a strong dominant frequency of 1.7Hz and a weak secondary-dominant frequency of 5.24Hz. Compared to the dominant frequency of cross-flow VIV

responses at the reduced velocity of 26.59, the dominant frequency becomes larger as the current velocity increases, but it is smaller than the Strouhal frequency of 1.8Hz at this reduced velocity. The corresponding average peak-pick-up frequency is 1.5Hz, as shown in Figure 4-6, and the Strouhal frequency is larger than both the dominant frequency and average peak-pick-up frequency.

Figure 4-18 presents the power spectrum of in-line VIV responses at the reduced velocity of 39.90. As seen in Figure 4-18, there is a strong dominant frequency of 3.5Hz and a weak secondary-dominant frequency of 0.4Hz. As the peak corresponding to the dominant frequency is much bigger than the peak corresponding to the secondary-dominant frequency, the average peak-pick-up frequency of 2.4Hz is closer to the dominant frequency than the secondary-dominant frequency, as shown in Figure 4-6. Compare the results in Figure 4-18 with those in Figure 4-16, and it is found that the second secondary-dominant frequency disappears.

According to the discussion above, we can see that, in Region C, a strong dominant frequency and several secondary-dominant frequencies exist in the cross-flow VIV responses, but these secondary dominant frequencies often have small energy so that few effects contribute to the cross-flow responses. The spectra of in-line VIV responses in this region seem complicated. At the low reduced velocity boundary of this region, the frequency close to the dominant frequency of cross-flow responses becomes a secondary-dominant frequency, and a new dominant frequency higher than the dominant frequency cross-flow responses is developed. As the new dominant frequency appears, the in-line vibration frequency starts to become larger than the cross-flow vibration frequencies. At

the middle of the lock-in region, the secondary-dominant frequency disappears, and the new dominant frequency completely dominates the in-line VIV responses.

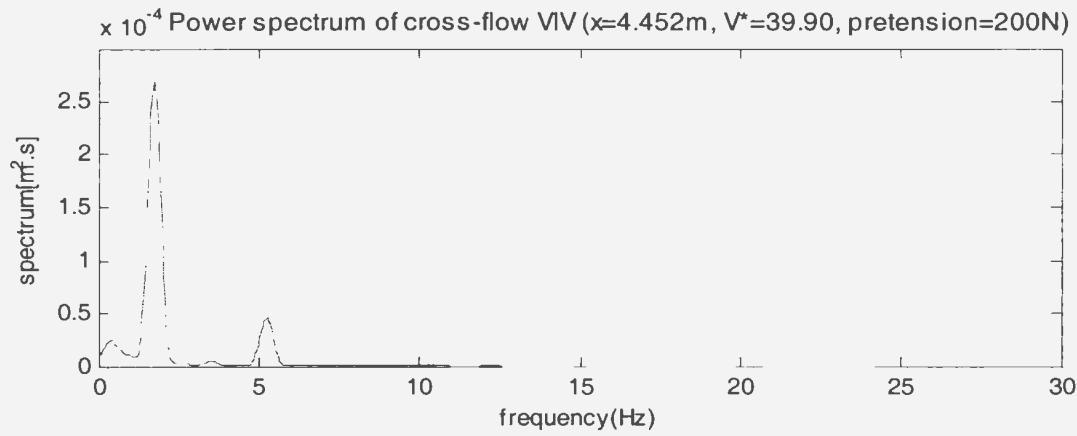


Figure 4-17 Power spectrum of cross-flow VIV at the middle of riser at a current velocity of 0.6m/s and a pretension of 200N

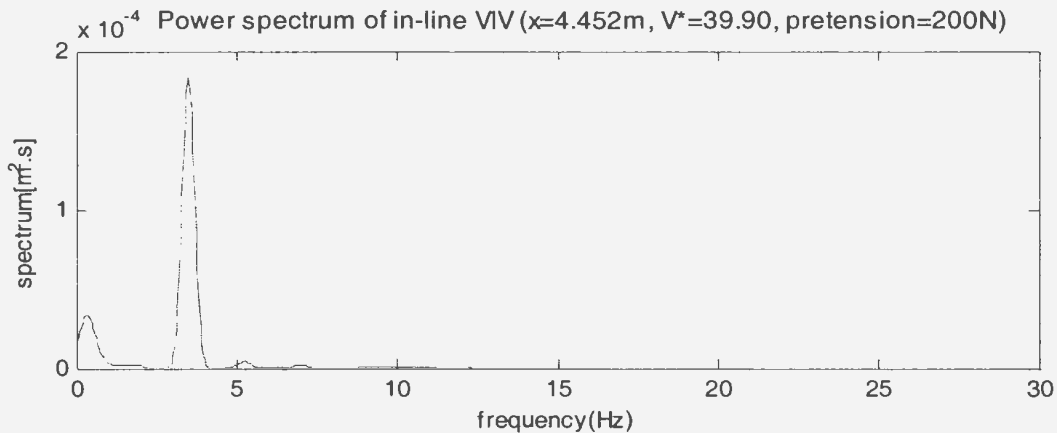


Figure 4-18 Power spectrum of in-line VIV at the middle of riser at a current velocity of 0.6m/s and a pretension of 200N

Vibration power spectra over riser length

Now examine the power spectra over the riser length. Four reduced velocities of 26.59, 39.90, 59.85 and 86.44 and three locations of $x=2.024$, 4.452 and 6.881m were selected for this examination. The first location is at about one-quarter of the riser length, the

second location is at about half of the riser length, and the third location is at about three-quarters of the riser length.

Figure 4-19 gives the power spectra of in-line VIV responses at the three locations at a reduced velocity of 26.59, which corresponds to a current velocity of 0.4m/s. As seen in Figure 4-19, at the low current velocities the spectral shapes are similar along the riser length, but the peak magnitude values vary over the riser length.

Figure 4-20 shows the power spectra of in-line VIV responses at the three locations at a reduced velocity of 39.90, which corresponds to a current velocity of 0.6m/s. Compared to the power spectra at two of the other locations, a secondary-dominant frequency disappears at the location of $x=4.452\text{m}$. This means that the secondary-dominant frequency is more dependent on the locations than the dominant frequency.

Figure 4-21 presents the power spectra of in-line VIV responses at the three locations at a reduced velocity of 59.85, which corresponds to a current velocity of 0.9m/s. At this current velocity, the patterns of power spectra have significant differences over the riser length. This means that the increased currents result in increased variations of VIV responses over the riser length.

Figure 4-22 gives the power spectra of in-line VIV responses at the three locations at a reduced velocity of 86.44, which corresponds to a current velocity of 1.3m/s. As seen in Figure 4-22, the spectra over the riser length still have a similar pattern, but the secondary-dominant frequency disappears at some locations.

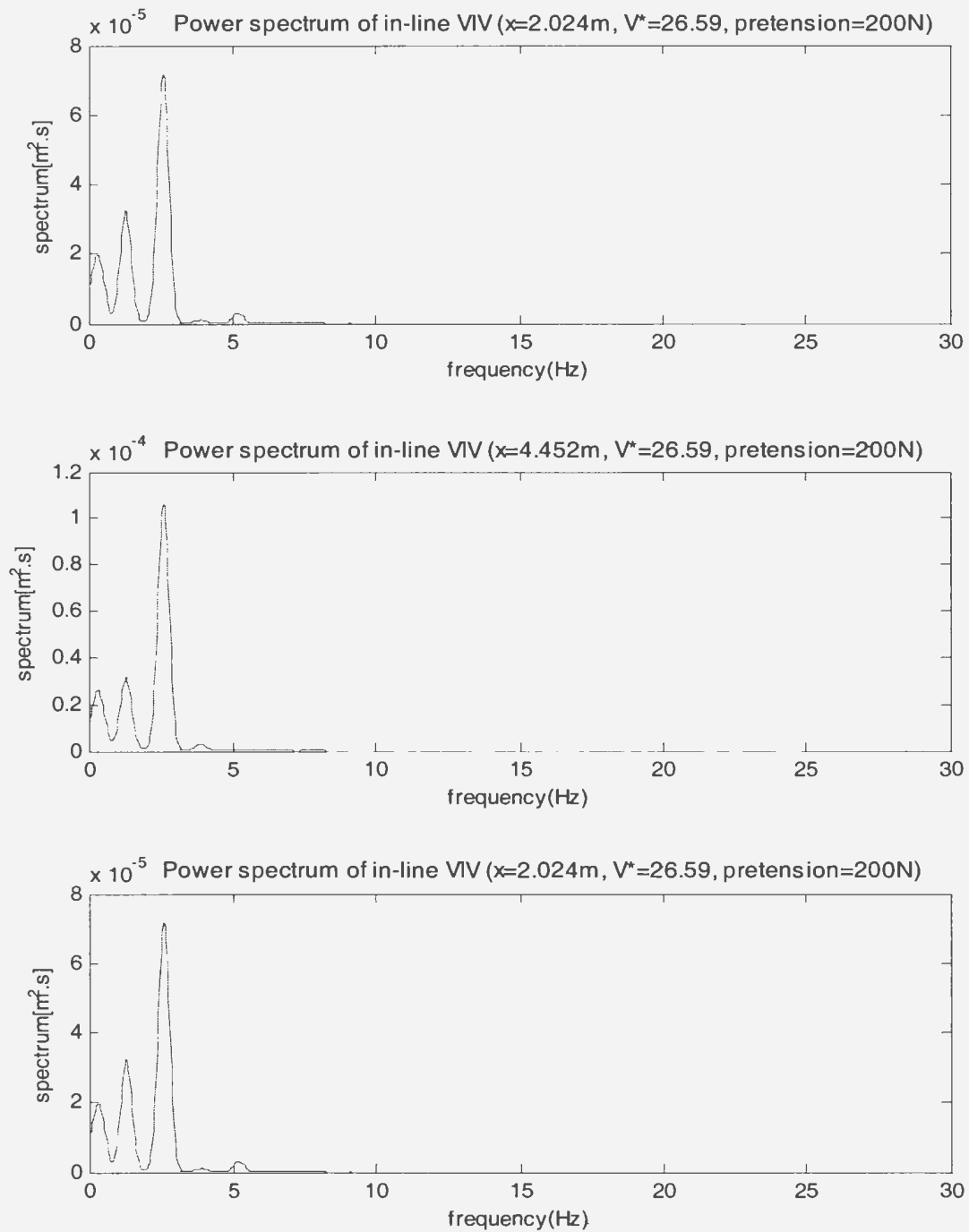


Figure 4-19 Power spectra of in-line VIV at different location on riser at a current velocity of 0.4m/s and a pretension of 200N

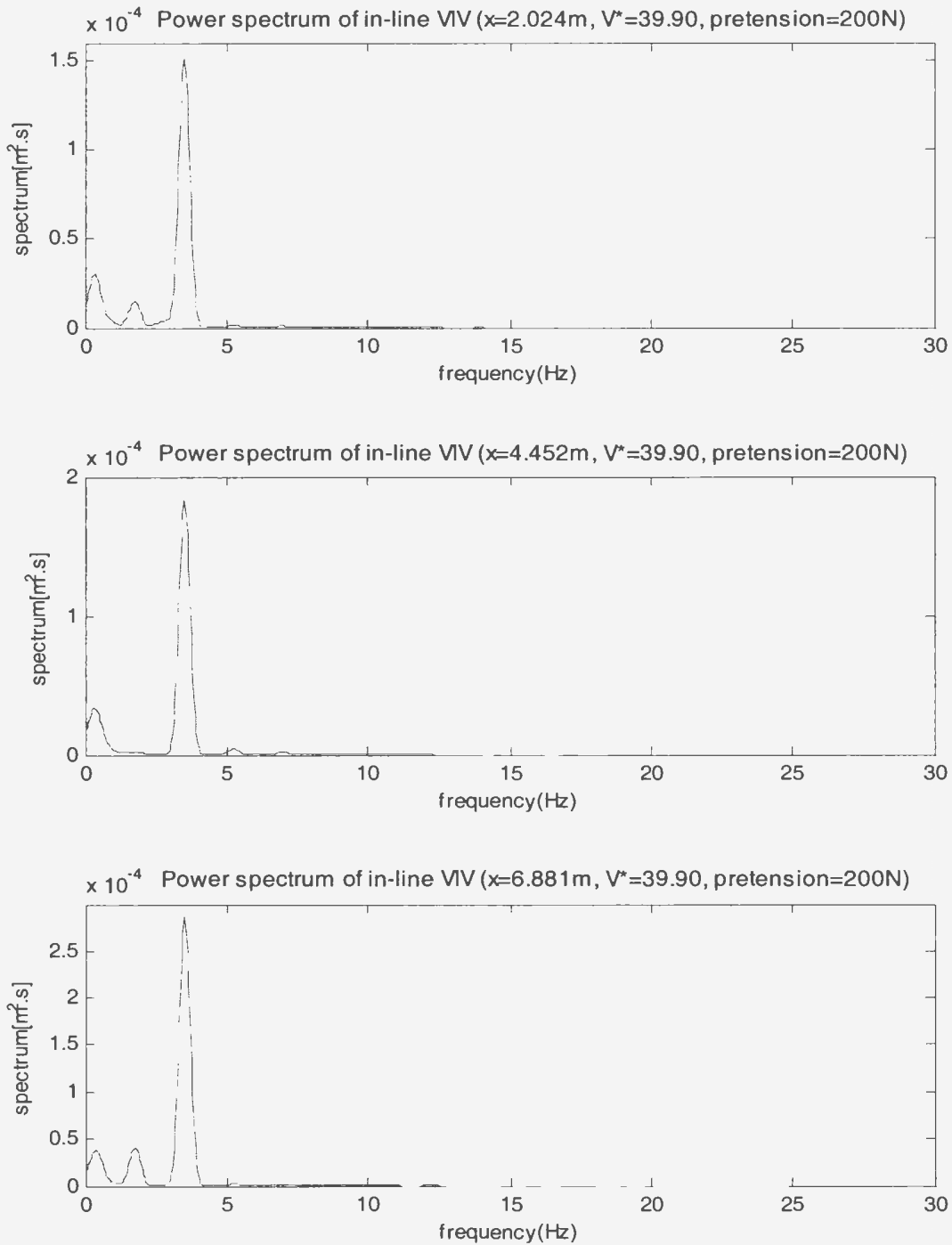


Figure 4-20 Power spectra of in-line VIV at different location on riser at a current velocity of 0.6m/s and a pretension of 200N

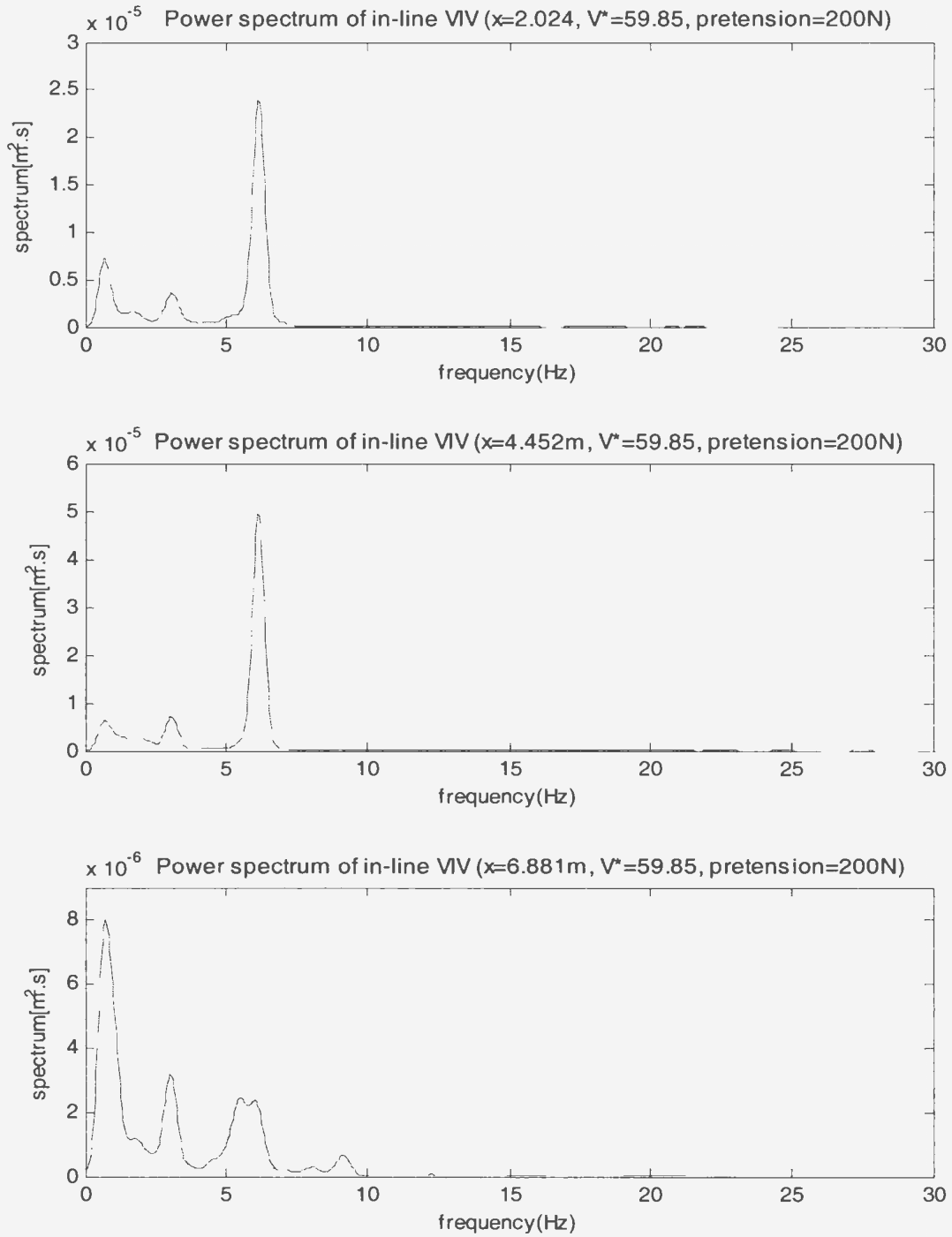


Figure 4-21 Power spectra of in-line VIV at different location on riser at a current velocity of 0.9m/s and a pretension of 200N

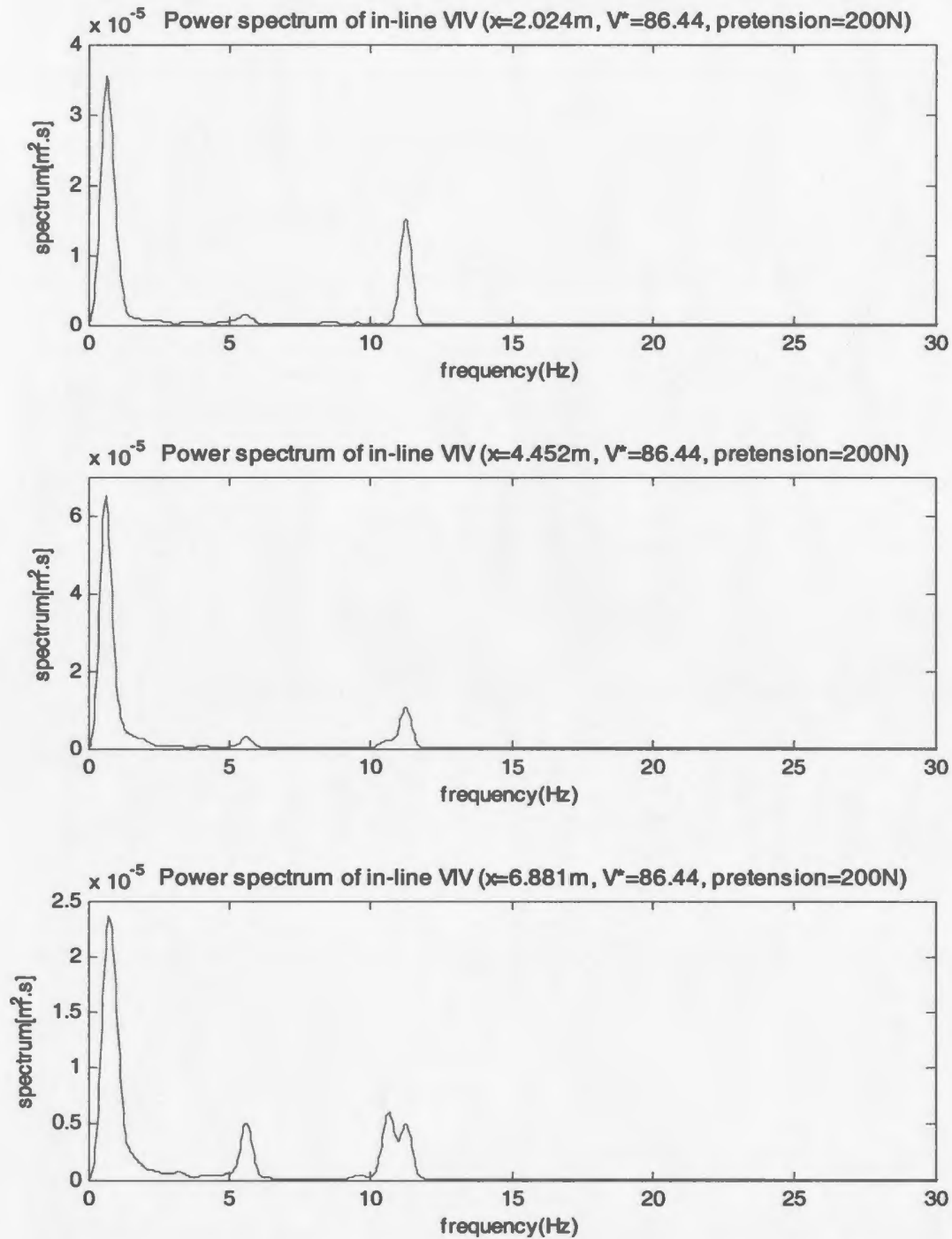


Figure 4-22 Power spectra of in-line VIV at different location on riser at a current velocity of 1.3m/s and a pretension of 200N

Figure 4-23 shows the power spectra of cross-flow VIV responses at the three locations on the riser at a reduced velocity of 26.59, which corresponds to a current velocity of 0.4m/s. As seen in Figure 4-23, at the low current velocity, the power spectra of the cross-flow VIV have a similar pattern over the riser length.

Figure 4-24 presents the power spectra of cross-flow VIV responses at the three locations at a reduced velocity of 59.85, which corresponds to a current velocity of 0.9m/s. At this current velocity, the power spectra of cross-flow VIV still have a similar pattern over riser length.

Figure 4-25 gives the power spectra of cross-flow VIV responses at the three locations at a reduced velocity of 86.44, which corresponds to a relatively high current velocity of 1.3m/s. At this current velocity, the power spectrum of cross-flow VIV at the location of 6.881m is different from the power spectra at two of the other locations. This means that the power spectra of cross-flow vibration at relatively high currents become more dependent of locations on the riser than those at relatively low currents.

Figure 4-26 shows three power spectra at a reduced velocity of 99.74. At the location of $x=2.024\text{m}$, the cross-flow VIV response contain a dominant frequency of 0.8Hz and two secondary-dominant frequencies of 6.0Hz and 9.8Hz. The two secondary-dominant frequencies are not close to each other. At the location of $x=4.452\text{m}$, the cross-flow VIV response contain a dominant frequency of 0.8Hz and two secondary-dominant frequencies of 4.8Hz and 6.0Hz. The two secondary-dominant frequencies are very close. At the location of $x=6.881\text{m}$, the cross-flow VIV response contain a dominant frequency and two secondary-dominant frequencies, but the dominant frequency moves to the frequency of 4.8Hz, and the peak at the frequency of 0.8Hz becomes very small.

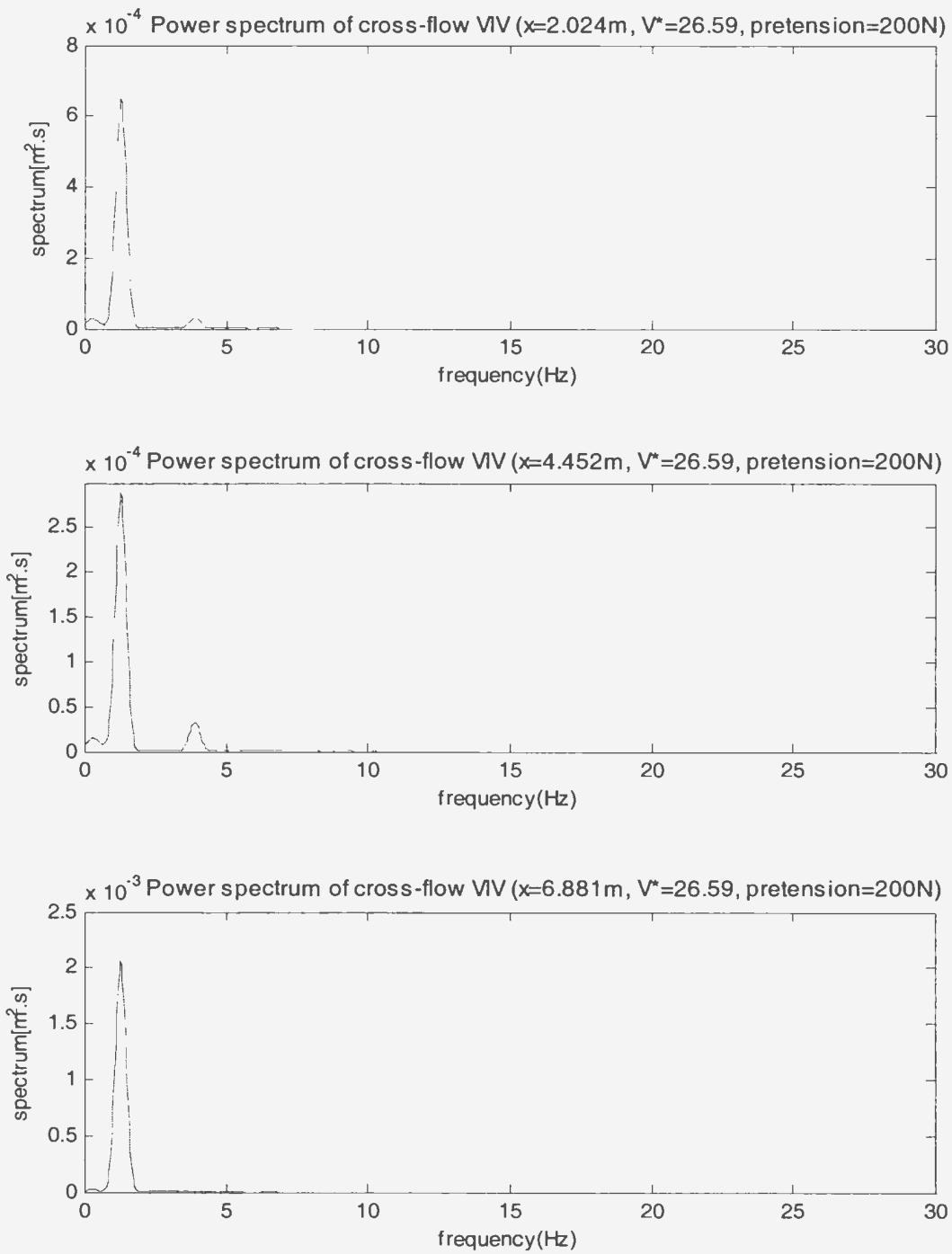


Figure 4-23 Power spectra of cross-flow VIV at different location on riser at a current velocity of 0.4m/s and a pretension of 200N

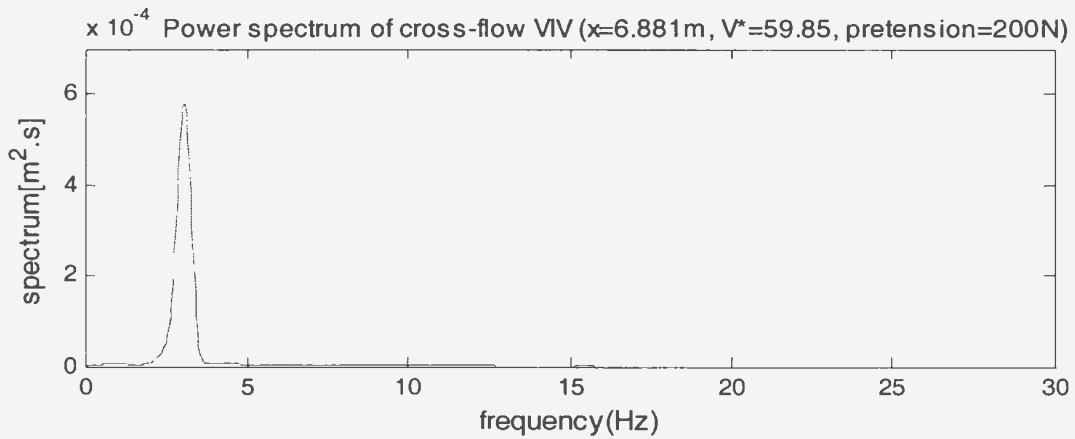
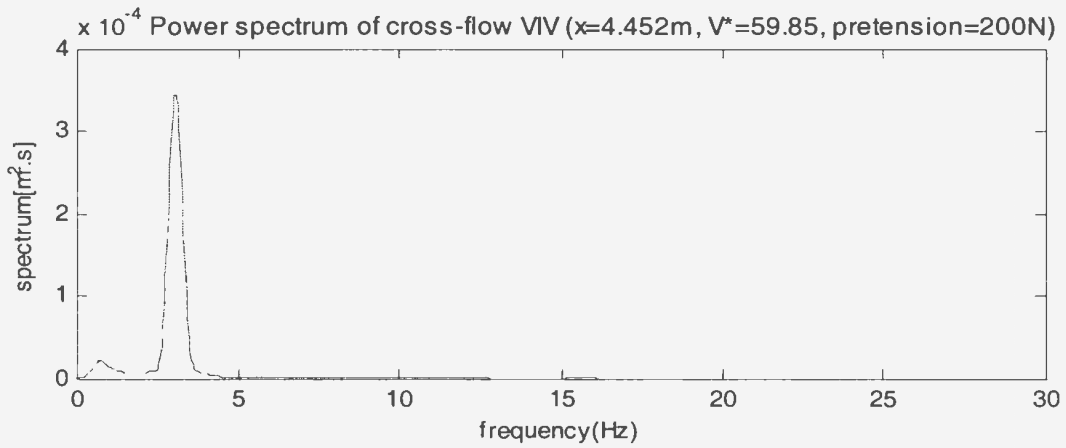
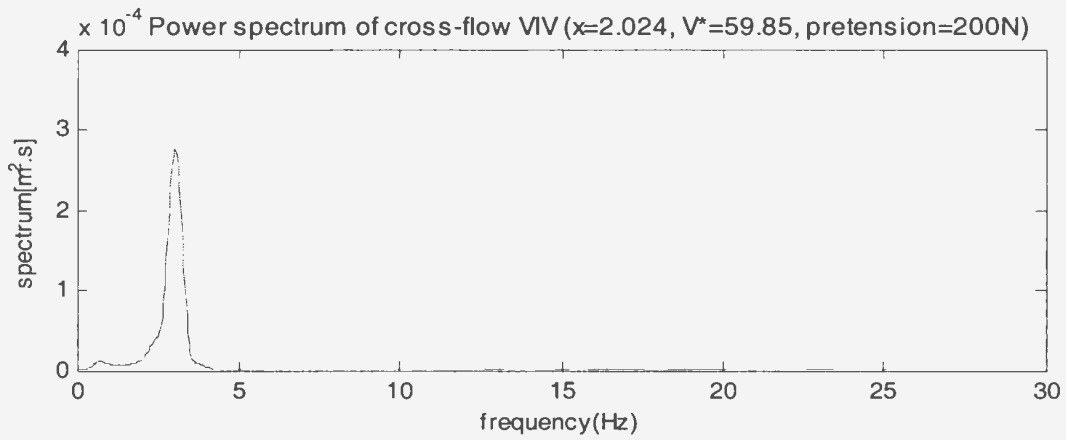


Figure 4-24 Power spectra of cross-flow VIV at different location on riser at a current velocity of 0.9m/s and a pretension of 200N

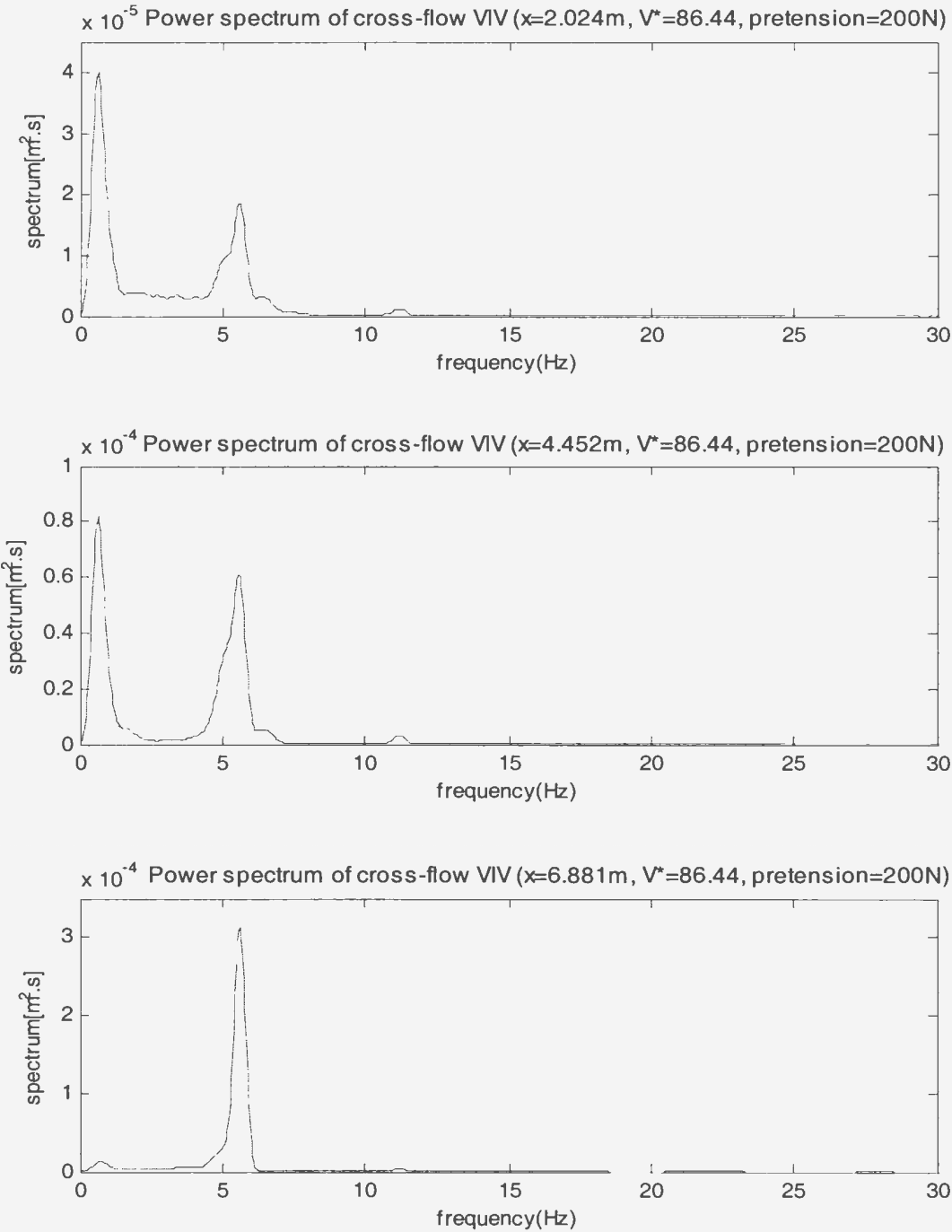


Figure 4-25 Power spectra of cross-flow VIV at different location on riser at a current velocity of 1.3m/s and a pretension of 200N

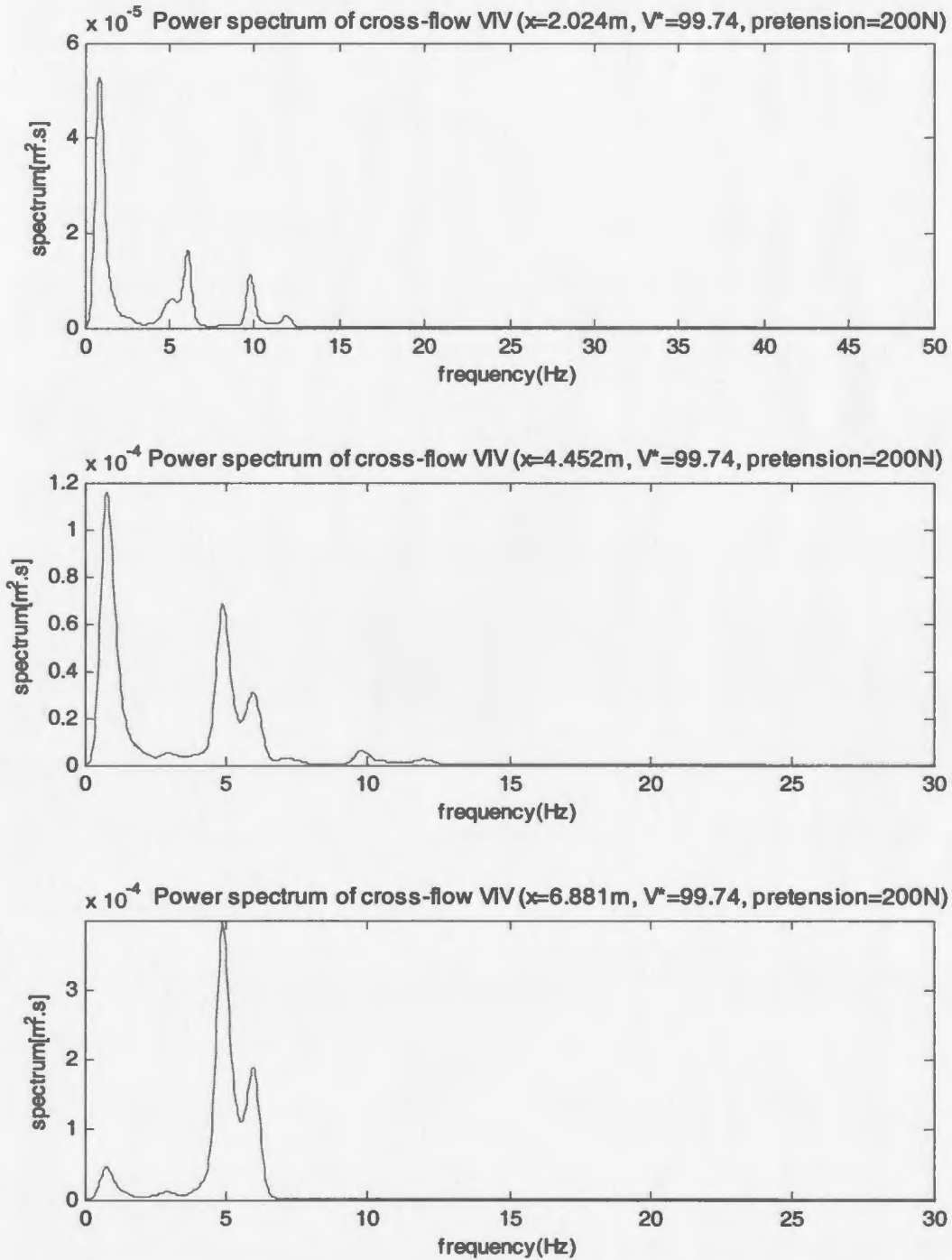


Figure 4-26 Power spectra of cross-flow VIV at different location on riser at a current velocity of 1.5m/s and a pretension of 200N

Summary of the results of vibration power spectra at the low pretension

As discussed above, the following points can be summarized:

- i) at the low currents, both the in-line and cross-flow vibration only contains one dominant frequency, and the two dominant frequencies are identical. No secondary-dominant frequencies exist.
- ii) in the low current velocity lock-in region, a strong dominant frequency and several secondary-dominant frequencies exist in the responses in the cross-flow direction, but these secondary-dominant frequencies have little energy to affect the cross-flow VIV responses.
- iii) in the low current velocity lock-in region, a strong dominant frequency and several secondary-dominant frequencies exist in the responses in the in-line direction. The energy of the lower dominant frequency become small and the energy of the higher dominant frequency become big as current velocity increases. This causes the amplitude of the in-line lock-in mode to be higher than for the cross-flow lock-in mode.
- iv) in the high current velocity lock-in region, the number of dominant frequency in cross-flow responses changes from one to two, while the number of dominant frequencies in in-line responses may be more than two. The lock-in frequency does not match any dominant and secondary-dominant frequencies.
- v) in low currents, both the in-line and cross-flow VIV responses have the same power spectral patterns over riser length.
- vi) high current velocities may complicate the characteristics of power spectra of VIV responses and cause power spectra different over riser length.

4. 2. 2. 3 Modal Components of VIV Response

The modal components contained in VIV responses can be revealed based on the modal analysis. The prerequisite of the modal analysis is that there is the sufficient number of measurement points over riser length. In the previous work, little involved the modal analysis of the measured data, as the insufficient number of the measurement points was used. In this research, the vibrations at sixteen locations on the riser were measured successfully so that the components of up to mode 10 could be analyzed. The results from the modal analysis help understand the characteristics of multi-modal VIV responses, such as lock-in modes, dominant modes and modal resonances.

Equation (2-5) gives the definition of modal responses, and this equation can be used to estimate the modal components in VIV responses. In this research, the tenth mode was the highest mode analyzed, and the results from the modal analysis were presented by two types of plots. The first is the modal components contained in the VIV responses at a current velocity, and another is the modal response versus current velocity for each mode.

Figure 4-27 shows the modal components in the VIV responses at four reduced velocities of 39.90, 59.85, 86.44 and 99.74, which correspond to the current velocities of 0.6, 0.9, 1.3 and 1.5m/s. The first is a current in Region A; the second and third are the currents in Region C; and the fourth is the highest current in Region B. B^* is the non-dimensional modal VIV response. It is defined as $z_{k0}/2D$ for the cross-flow VIV responses, where: D is the riser diameter, and z_{k0} is the average peak-pick-up amplitudes of the modal response components $z_k(t)$, defined by equation (2-5). The function $z(t,x)$ in equation (2-5) is the vibration displacements in the cross-flow directions, which were measured in the tests. The non-dimensional modal VIV response B^* is also defined as

$y_{k0}/2D$ for the in-line VIV responses, where: y_{k0} is the average peak-pick-up amplitudes of the modal response components $y_k(t)$ in the in-line direction.

As seen in Figure 4-27, both the in-line and cross-flow VIV responses contain all of the modal components from the first mode to the tenth mode, but some modal components have larger contributions to the VIV responses than the others. The modal component with the largest contribution to the VIV responses is called the dominant modal component, and the corresponding mode called the dominant mode. At lower current velocities, there is a clear dominant mode, while at higher current velocities, the dominant mode become vague. For example, for the cross-flow VIV responses, at the reduced velocity of 39.90, the VIV responses contain a clear dominant component of mode 2, which matches the lock-in mode discussed earlier. Since the value of the dominant modal component is much larger than the values of the other modal components, the VIV response is close to a single modal vibration. At the reduced velocities of 59.85 and 86.44, the VIV responses contain a relatively large modal components of mode 2 and 4, and this means that in the reduced velocity region the dominant cross-flow vibration mode changes from mode 2 to mode 4. At the highest current tested, the dominant mode becomes unclear.

For the in-line VIV responses, at the reduced velocity of 39.90, the VIV responses contain a clear dominant component of mode 3, which matches the lock-in mode in this direction. This dominant mode is higher than the dominant mode in the cross-flow direction, and this causes the fact that in the current velocity region the in-line average peak-pick-up frequencies are larger than the cross-flow peak-pick-up frequencies, as seen in Figure 4-6. Since the dominant modal component has much larger energy than the

energy of other modal components, the VIV response is close to a single modal vibration. In the highest current tested, the dominant mode in the in-line VIV responses is also unclear.

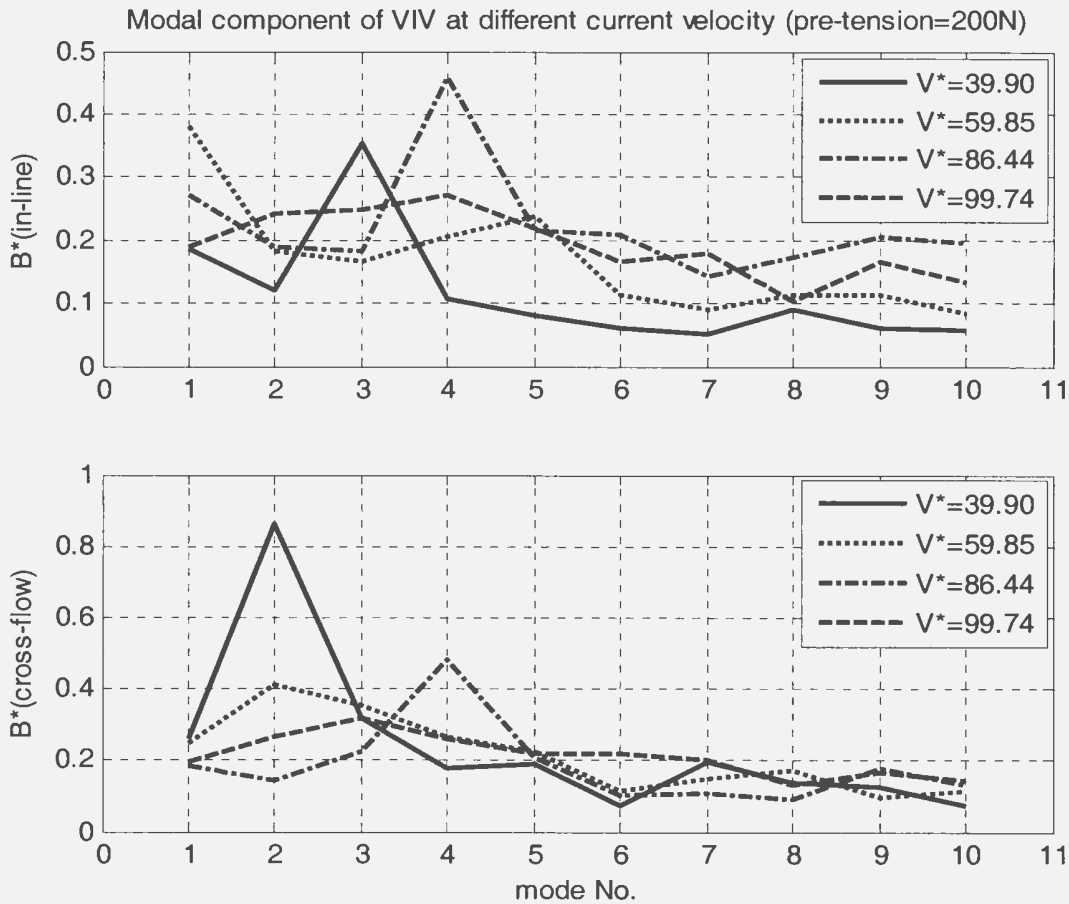


Figure 4-27 The modal component distribution of the in-line and cross-flow VIV responses at a pretension of 200N

Figures 4-28 to 4-31 show the modal components versus current velocity from mode 1 to mode 9 in the in-line and cross-flow directions. Figure 4-28 presents the modal components of the in-line and cross-flow responses for mode 1. As seen in Figure 4-28, in both the in-line and the cross-flow direction the largest modal response appears at $V^*=16$, and this implies that a modal resonance for mode 1 occurs near $V^*=16$. According to Figure 4-5, at $V^*=10$ the Strouhal frequency matches the natural frequency of mode 1.

The maximum value of the modal responses for mode 1 appears at the reduced velocity a little larger than the reduced velocity corresponding to the natural frequency of mode 1. It is noted that this modal resonance is not reflected in the total VIV response, shown in Figure 4-6. This means that the modal resonance contains relatively small energy so that the total VIV responses may not be influenced.

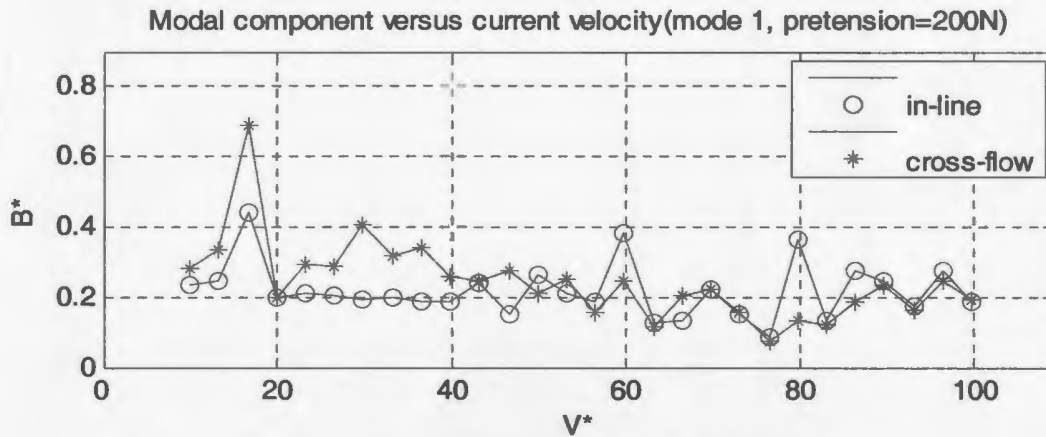


Figure 4-28 The component of mode 1 in VIV responses at a pretension of 200N

Figure 4-29 gives the modal responses for mode 2 in the in-line and cross-flow directions. As seen in Figure 4-29, the modal responses in the cross-flow direction for mode 2 have a relatively big response region from $V^*=21$ to 45. This region corresponds to the lock-in region for the cross-flow VIV responses, shown in Figure 4-6. This clarifies that for the cross-flow VIV responses the lock-in mode is mode 2 in this region. The modal responses in the in-line direction for mode 2 do not exhibit relatively large values over the whole reduced velocity range tested, and this means that no modal resonance occurs in the in-line responses for mode 2.

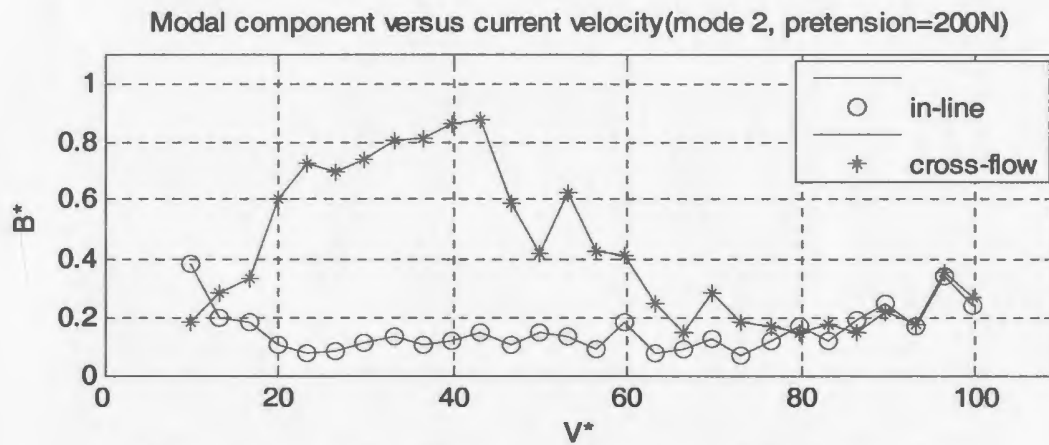


Figure 4-29 The component of mode 2 in VIV responses at a pretension of 200N

Figure 4-30 presents the modal responses for mode 3 in the in-line and cross-flow directions. As seen in Figure 4-30, there is a relatively large modal response region from $V^*=60$ to 75 for the cross-flow VIV responses. According to Figure 4-5, in this region the Strouhal frequencies are close to the natural frequencies of mode 3 and, as a result, the modal responses for mode 3 have relatively large values in the cross-flow direction over the region. However, in the region $V^*=60$ to 75, no relatively large modal responses for mode 3 are found in the in-line direction, and this implies that the frequency lock-in at the natural frequency of mode 3 in the in-line direction does not causes big modal response for mode 3. This is a characteristic completely different from the lock-in phenomenon occurring in the region from $V^*=21$ to 45, where relatively large modal responses for mode 3 appear in the in-line direction, and this verifies that in the region mode 3 is the lock-in mode for the in-line VIV responses.

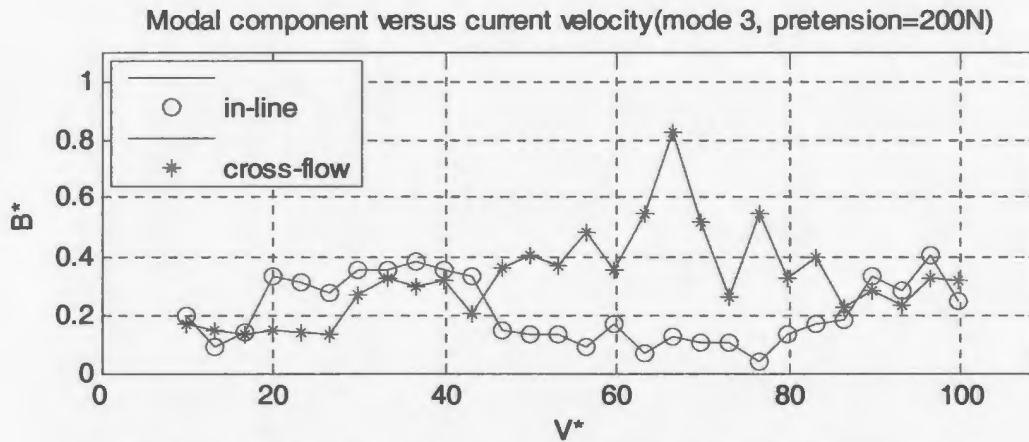


Figure 4-30 The component of mode 3 in VIV responses at a pretension of 200N

Figure 4-31 presents the modal responses for mode 4 in the in-line and cross-flow directions. As seen in Figure 4-31, there is relatively large modal response region from $V^*=68$ to 89 for the cross-flow VIV responses, while there is a relatively big modal response region near the reduced velocity of 90 for the in-line VIV responses. This may imply that a modal resonance of mode 4 in the cross-flow direction exists in the region from $V^*=76$ to 90 and a modal resonance for mode 4 in the in-line direction exists in the region from $V^*=88$ to 95. These resonances were not predicted by the natural frequencies of mode 4 shown in Figure 4-5, and this may reflect the difference between the natural frequencies measured in calm water and the natural frequencies at relatively high currents.

Figures 4-32 to 4-36 are respectively the in-line and cross-flow modal responses for mode 5, mode 6, mode 7, mode 8 and mode 9. As seen in these figures, no relatively big modal responses exist over the entire reduced velocity region tested.

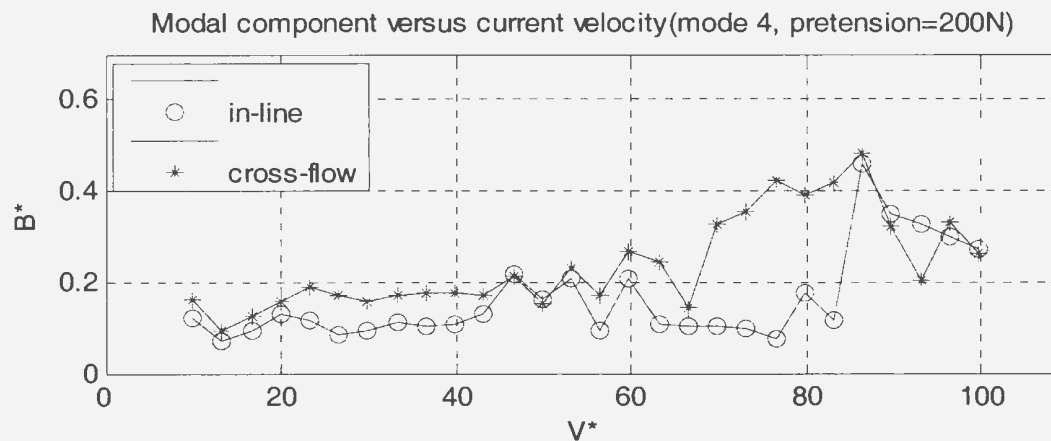


Figure 4-31 The component of mode 4 in VIV responses at a pretension of 200N

Summarizing the results above, we know that:

- i) both the in-line and cross-flow VIV responses contain all of the modal components from the first mode to the tenth mode, but there may be a dominant mode, especially for relatively low currents.
- ii) in the low current velocity lock-in region, in both the in-line and cross-flow VIV directions the lock-in modes are identical to the dominant modes.
- iii) the modal analysis found a modal resonance for mode 1 in the in-line and cross-flow responses at the reduced velocity of about 16, but this modal resonance had relatively small energy so that it did not obviously affect the total VIV response.
- vi) the modal analysis results clearly reveal that in the low current velocity lock-in region, the resonance mode in the cross-flow direction is mode 2, while the resonance mode in the in-line direction is mode 3.
- v) in the high current velocity lock-in region, the in-line VIV responses lock in at the modal natural frequency of mode 3, but this does not cause a large modal response for mode 3.

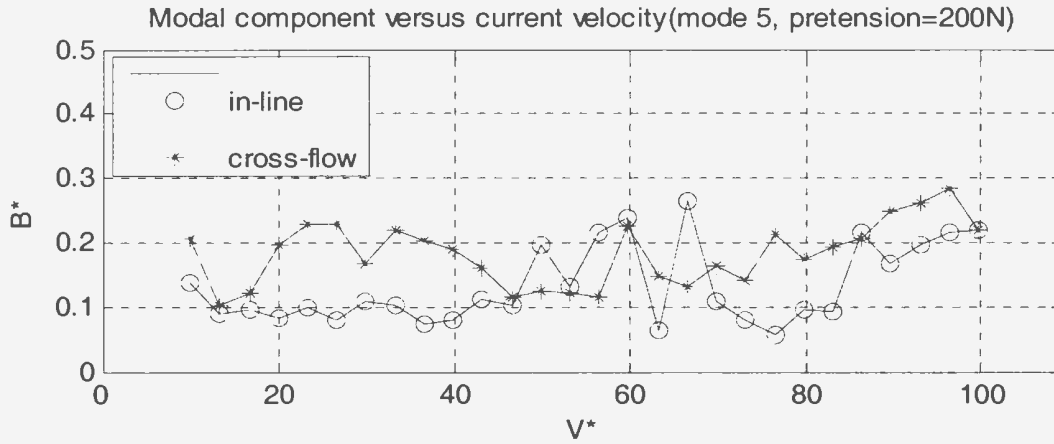


Figure 4-32 The component of mode 5 in VIV responses at a pretension of 200N

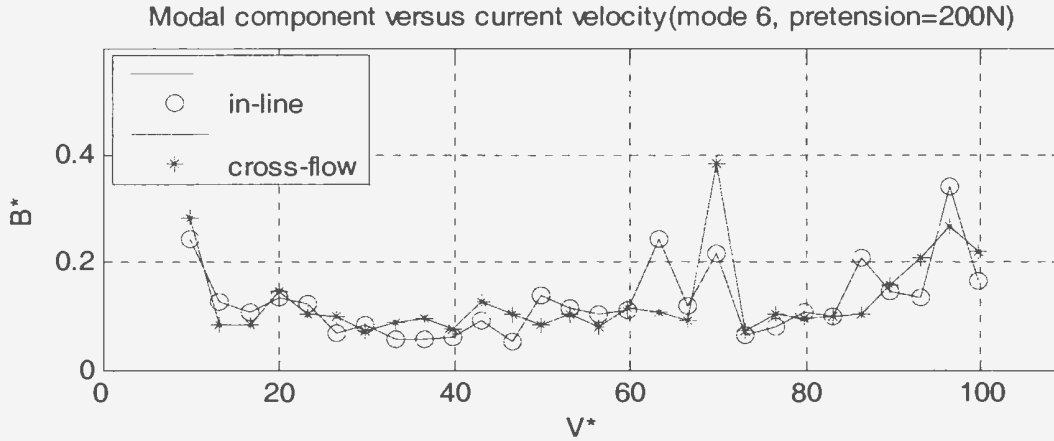


Figure 4-33 The component of mode 6 in VIV responses at a pretension of 200N

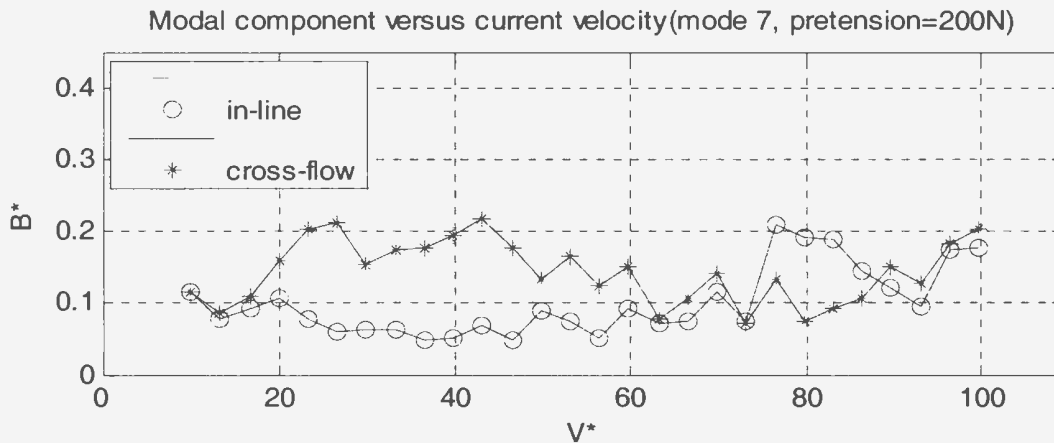


Figure 4-34 The component of mode 7 in VIV responses at a pretension of 200N

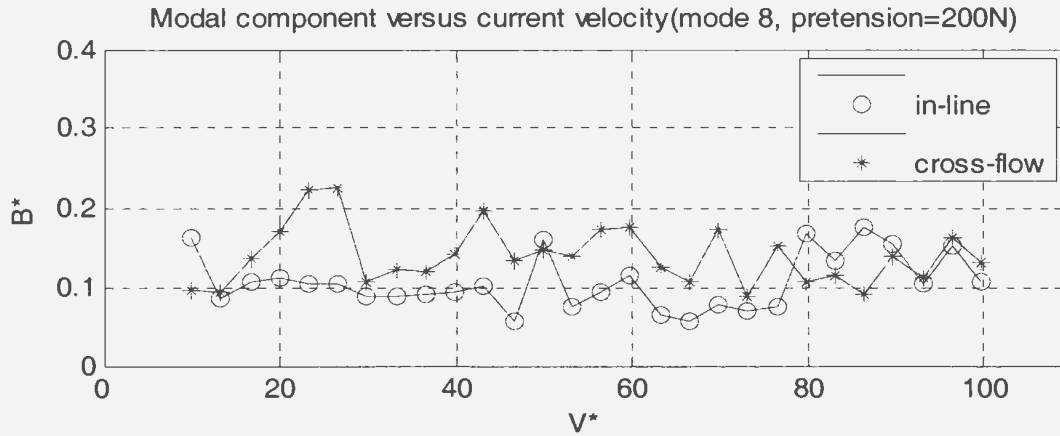


Figure 4-35 The component of mode 8 in VIV responses at a pretension of 200N

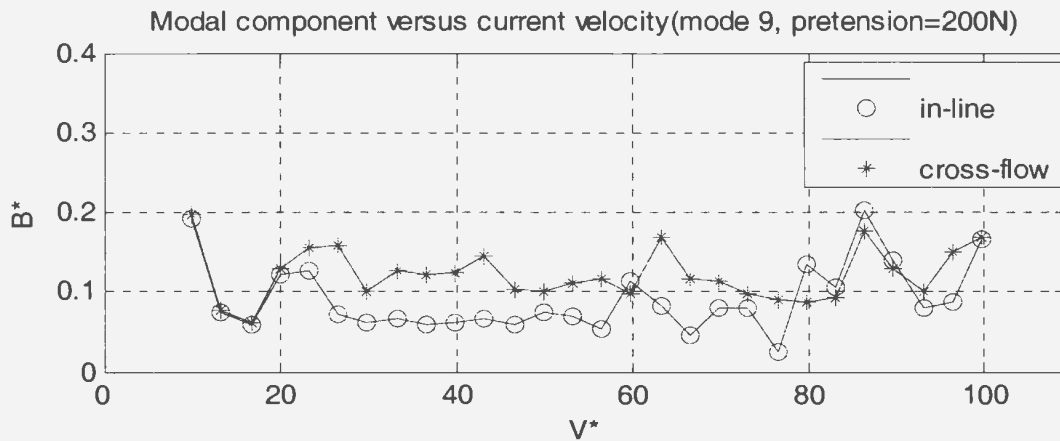


Figure 4-36 The component of mode 9 in VIV responses at a pretension of 200N

4. 2. 2. 4 Vibration Time Histories

Time histories of VIV responses directly provide the wave shapes of vibrations. In this research, the time histories of VIV acceleration in the in-line and cross-flow directions were measured by the accelerometers based on the calibration factors and the orientation angles shown in Table 2-4 and Table 2-5. The time histories of the VIV displacement in

the in-line and cross-flow directions were obtained by double-integration of the acceleration data.

Figures 4-37 to 4-41 present the time histories of cross-flow VIV responses at five reduced velocities of 26.59, 39.90, 53.20, 86.44 and 99.74, which respectively correspond to five current velocities of 0.4, 0.6, 0.8, 1.3 and 1.5m/s. These time histories were measured at the location of $x=4.452\text{m}$.

As seen in these figures, the patterns of time history of cross-flow VIV response depend on current velocities. At the reduced velocity of 26.59, the response is a relatively regular vibration, namely the vibration amplitudes have a relatively small variation in the time domain. This is a typical vibration with a single-dominant frequency. At the reduced velocity of 39.90, the vibration is still dominated by a frequency, as the vibration pattern still looks relatively regular. However, the variation of vibration amplitude in the time-domain becomes larger than in the case of reduced velocity of 26.59. The vibrations at the reduced velocities of 26.59 and 39.90 have the same pattern, i.e. the vibrations with a strong dominant frequency and several weak non-dominant frequencies. This vibration pattern is called the single-frequency type (SF type) in this thesis.

At the higher reduced velocity of 53.20, the pattern of the vibration changes. As seen in Figure 4-39, the time history exhibits a vibration with two very close frequencies. This vibration pattern is called the close-double frequency type (CD type) in this thesis.

At the reduced velocity of 86.44, the pattern of the vibration changes again. As seen in Figure 4-40, there are still two dominant frequencies, but the two dominant frequencies are separate. This vibration pattern is called the far-double frequency type (FD type).

At the highest reduced velocity of 99.74, the vibrations have a pattern similar to that in the case of the reduced velocity of 86.44, but more secondary-dominant frequencies exist in the vibrations, as seen in Figure 4-41. This vibration pattern is called the multi-frequency type (MF type) in this thesis.

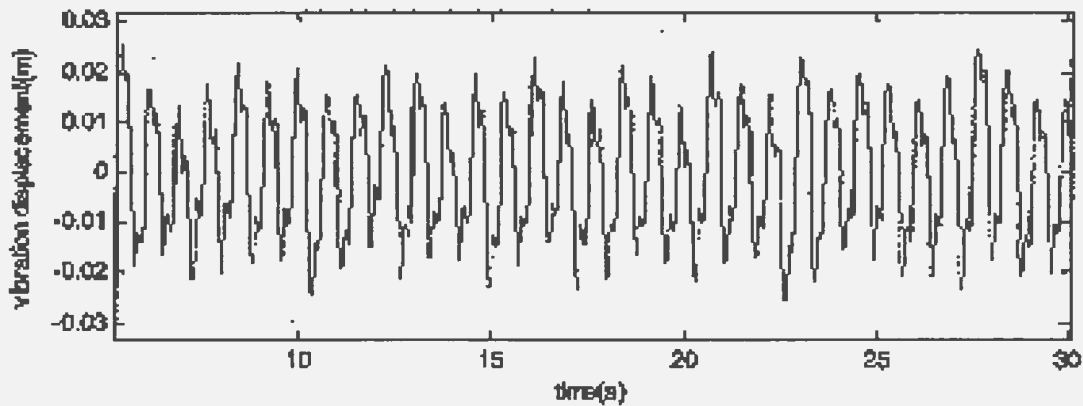


Figure 4-37 Time history of cross-flow VIV at a current velocity of 0.4m/s and a pretension of 200N

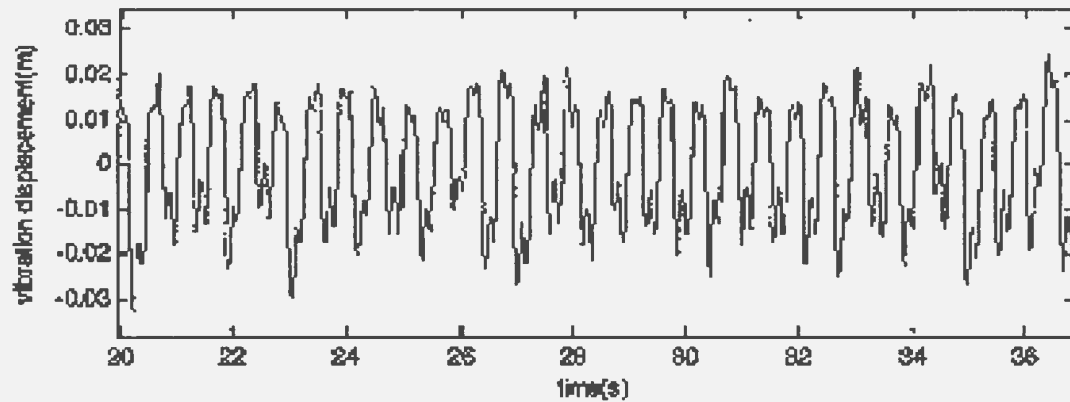


Figure 4-38 Time history of cross-flow VIV at a current velocity of 0.6m/s and a pretension of 200N

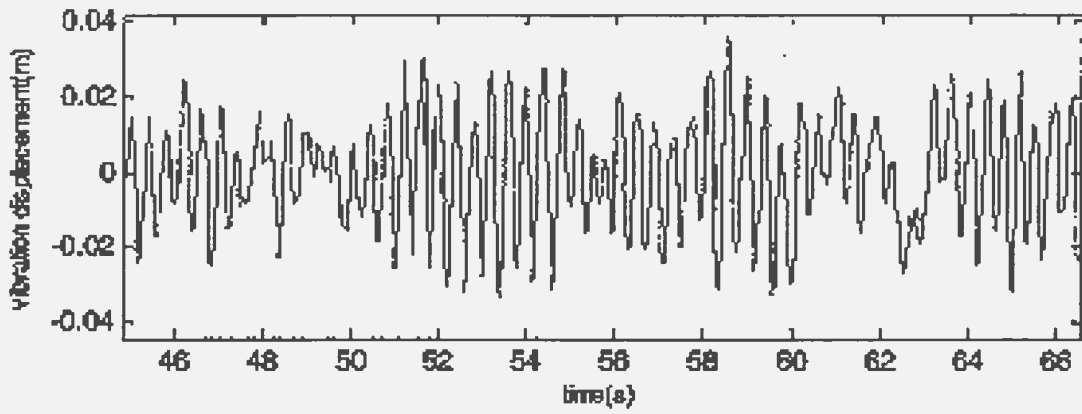


Figure 4-39 Time history of cross-flow VIV at a current velocity of 0.8m/s and a pretension of 200N

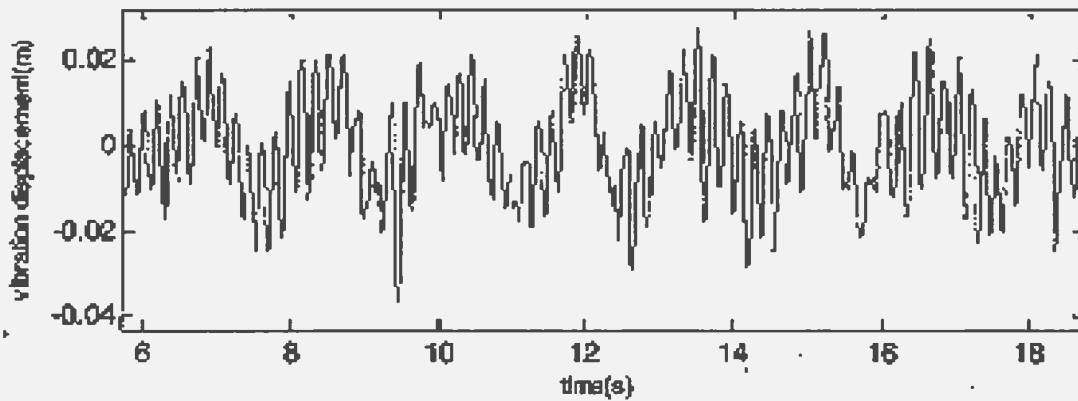


Figure 4-40 Time history of cross-flow VIV at a current velocity of 1.3m/s and a pretension of 200N

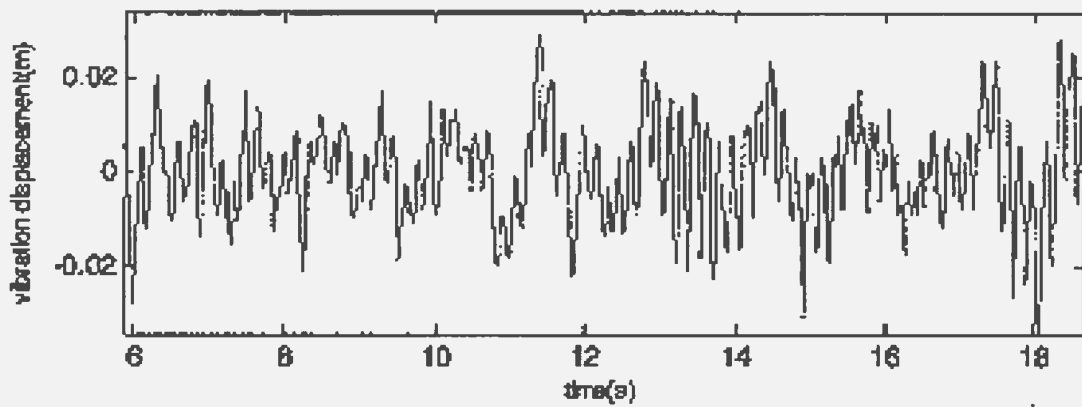


Figure 4-41 Time history of cross-flow VIV at a current velocity of 1.5m/s and a pretension of 200N

Figure 4-42 to 4-46 present the time histories of in-line VIV responses at five reduced velocities of 26.59, 53.20, 86.44 and 99.74, which were also measured at the location of $x=4.452\text{m}$.

As seen in these figures, the patterns of time history of in-line VIV response also depend on current velocities. At the reduced velocity of 26.59, the responses contain a dominant frequency, but the amplitudes have a big variation. The pattern of this time history is still the SF type. At the higher reduced velocity of 39.90, the pattern of time history also shows a SF type, and no high frequency components exist. As the reduced velocity increased to 53.20, the pattern of time history becomes the MF type. At the higher reduced velocities of 86.44 and 99.74, the patterns of time history are still the MF type.

Summarizing these results, we know that there may be four time history patterns in the multi-modal VIV responses. They are respectively the SF, CD, FD and MF types. The SF type corresponds to lower current velocities, the CD and FD types correspond to moderate current velocities, and the MF type corresponds to higher current velocities. In the case of a pretension of 200N, the cross-flow VIV responses cover all of the four types, but the in-line VIV responses do not exhibit the CD and the FD types.

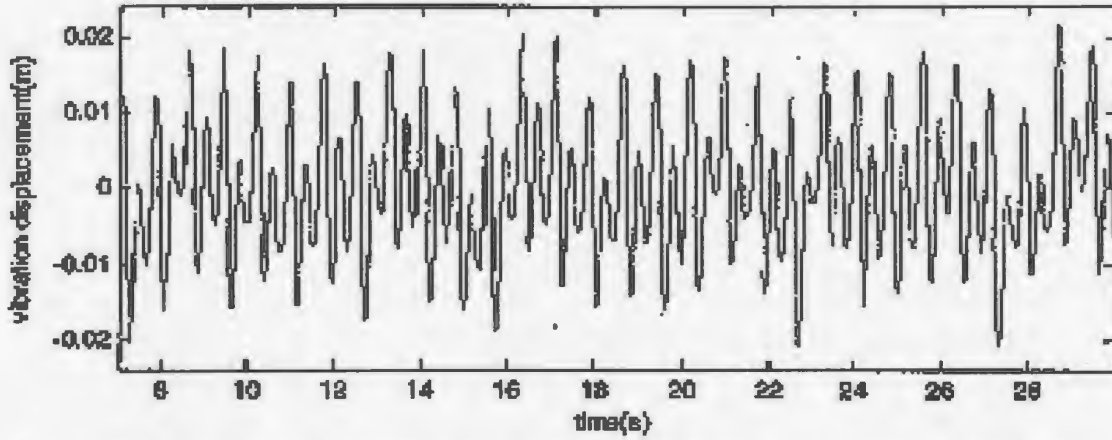


Figure 4-42 Time history of in-line VIV at a current velocity of 0.4m/s and a pretension of 200N

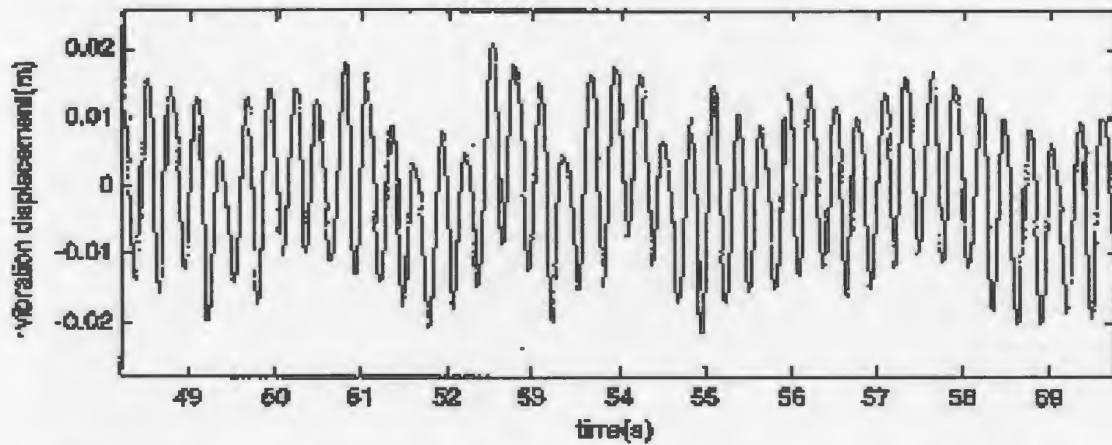


Figure 4-43 Time history of in-line VIV at a current velocity of 0.6m/s and a pretension of 200N

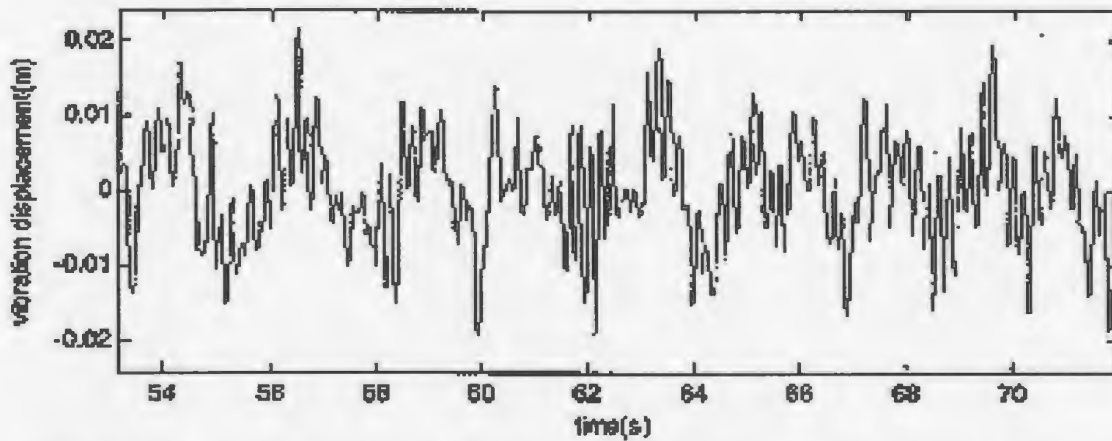


Figure 4-44 Time history of in-line VIV at a current velocity of 0.8m/s and a pretension of 200N

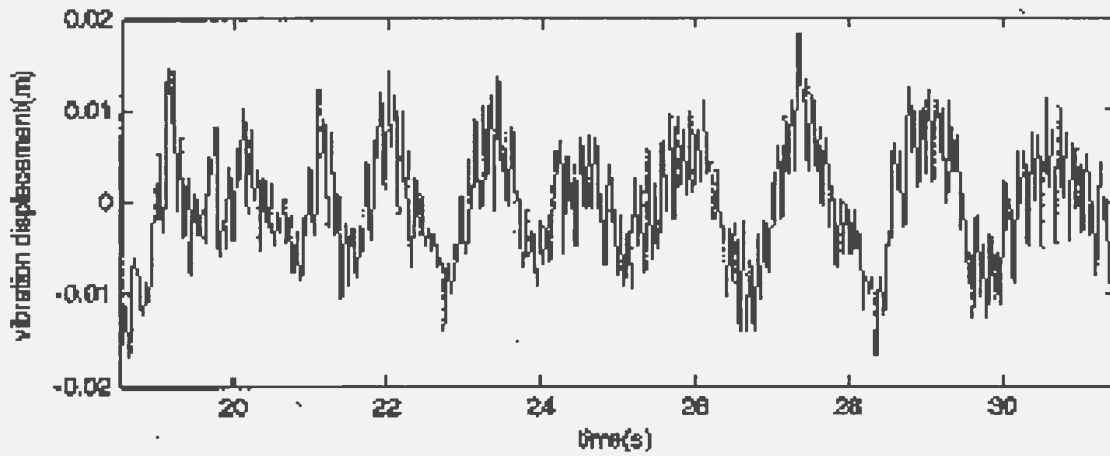


Figure 4-45 Time history of in-line VIV at a current velocity of 1.3m/s and a pretension of 200N

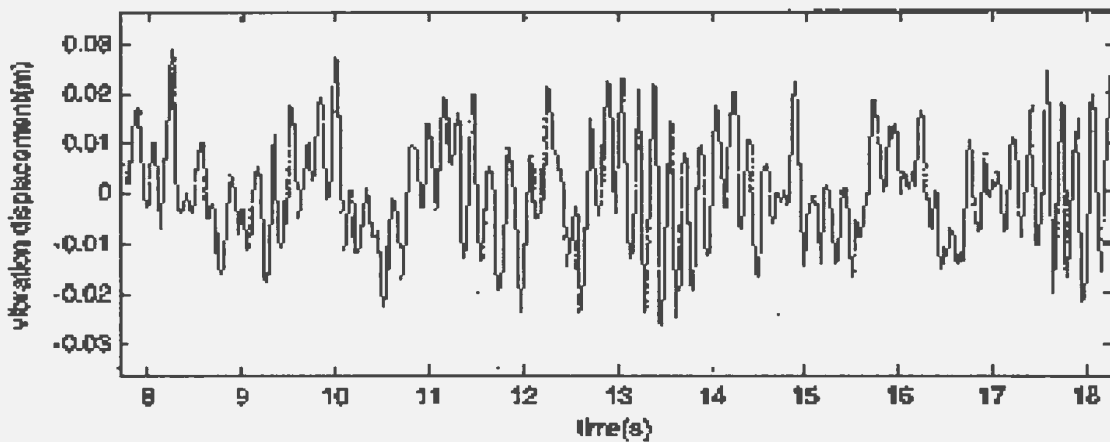


Figure 4-46 Time history of in-line VIV at a current velocity of 1.5m/s and a pretension of 200N

Figure 4-47 shows the time histories of cross-flow VIV responses at a current velocity of 0.4m/s ($V^*=26.59$) at three different locations on the riser. As seen in Figure 4-47, at the locations of $x=2.024$, 4.452 and 6.880m, the vibration patterns are all the SF type, and this means that at a low current velocity, the vibration types of cross-flow VIV are independent of the locations over the riser length.

Figure 4-48 shows the time histories of in-line VIV responses at a current velocity of 0.4m/s ($V^*=26.59$) at three different locations on the riser. As seen in Figure 4-48, at the locations of $x=2.024$, 4.452 and 6.880m, the vibration patterns are all the SF type, and

this means that at a low current velocity, the vibration types of in-line VIV are also independent of the locations over riser length.

Figures 4-49 presents the time histories of cross-flow VIV responses at three different locations on the riser at another current velocity. This current velocity is 1.5m/s ($V^*=99.74$), which was the highest current velocity tested. At the locations of $x=2.024\text{m}$ and $x=4.452\text{m}$, the time history patterns are respectively the MF type and the FD type, while at the location of $x=6.881\text{m}$, the time history patterns seem to be a mixture of the MF type and the CD type. It is apparent that the increased current velocity causes vibration patterns to contain more variations over riser length than the lower current velocities.

Figures 4-50 shows the time histories of in-line VIV responses at three different locations on the riser at the current velocity of 1.5m/s ($V^*=99.74$). As seen in Figure 4-50, at the locations of $x=2.024\text{m}$ and $x=6.881\text{m}$, the time history patterns are the MF type, while at the location of $x=4.452\text{m}$, the time history pattern becomes a mixture of the MF type and the CD type.

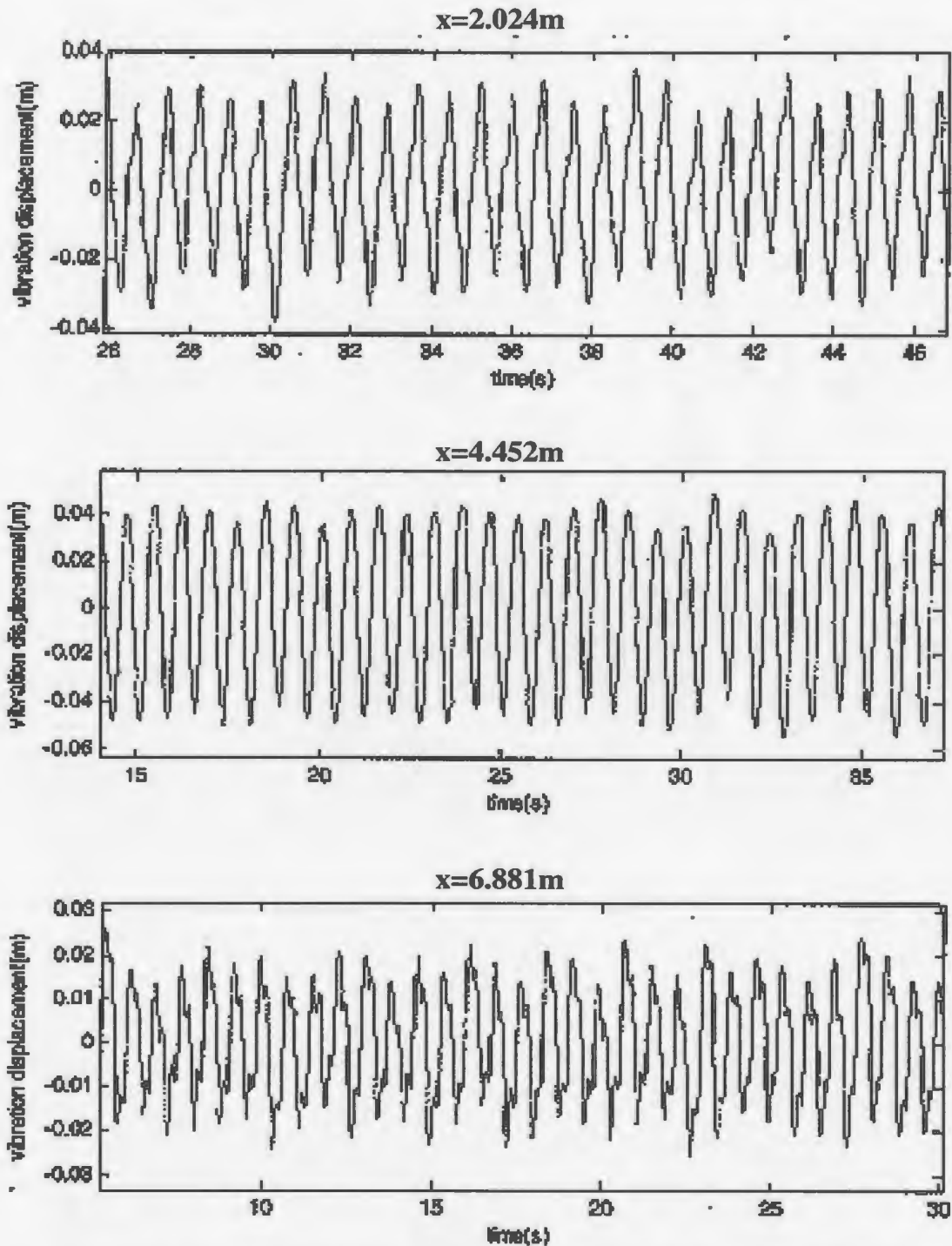


Figure 4-47 Time history of cross-flow VIV at different locations at a current velocity of 0.4m/s and a pretension of 200N

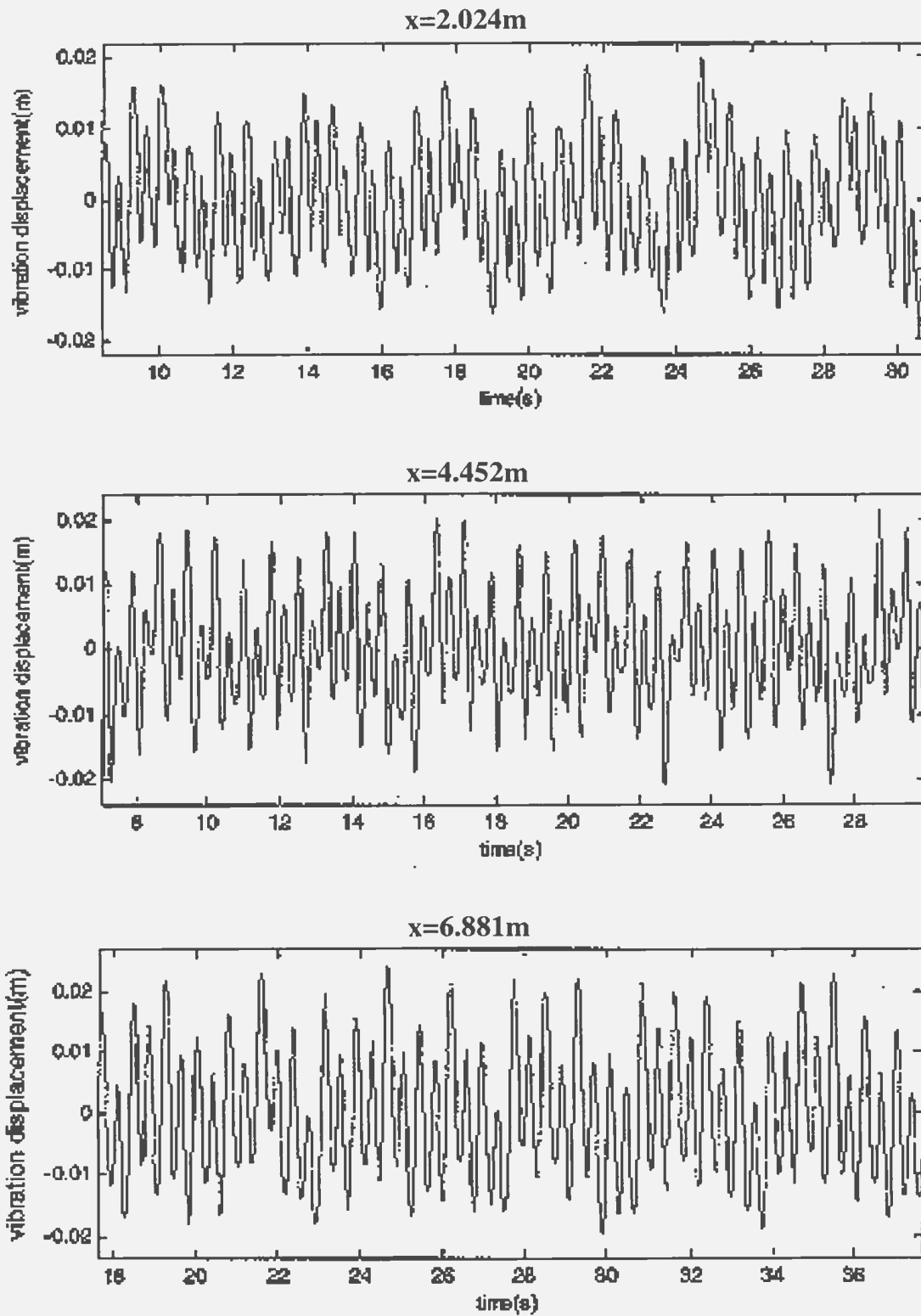


Figure 4-48 Time history of in-line VIV at different locations at a current velocity of 0.4m/s and a pretension of 200N

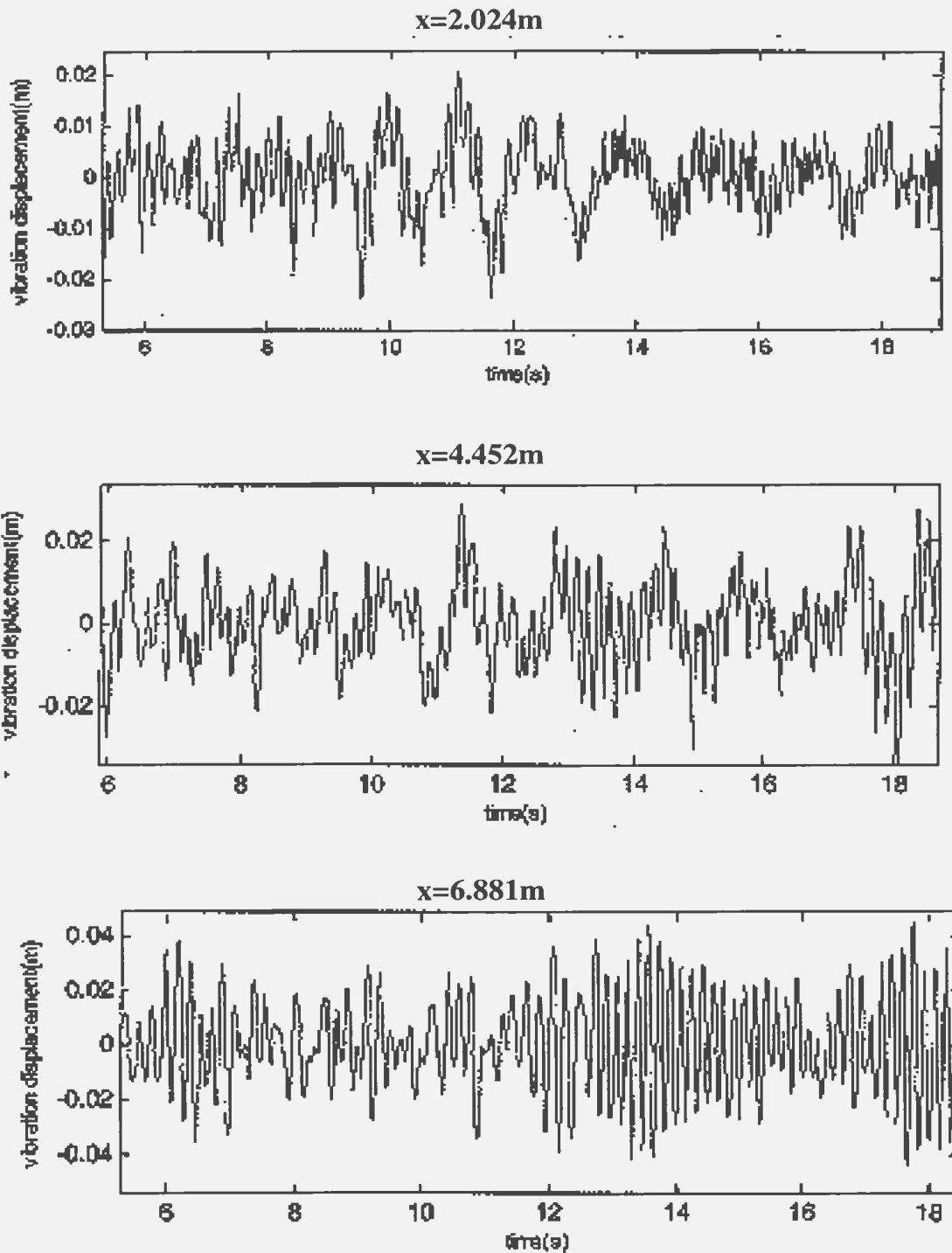


Figure 4-49 Time history of cross-flow VIV at different locations at a current velocity of 1.5m/s and a pretension of 200N

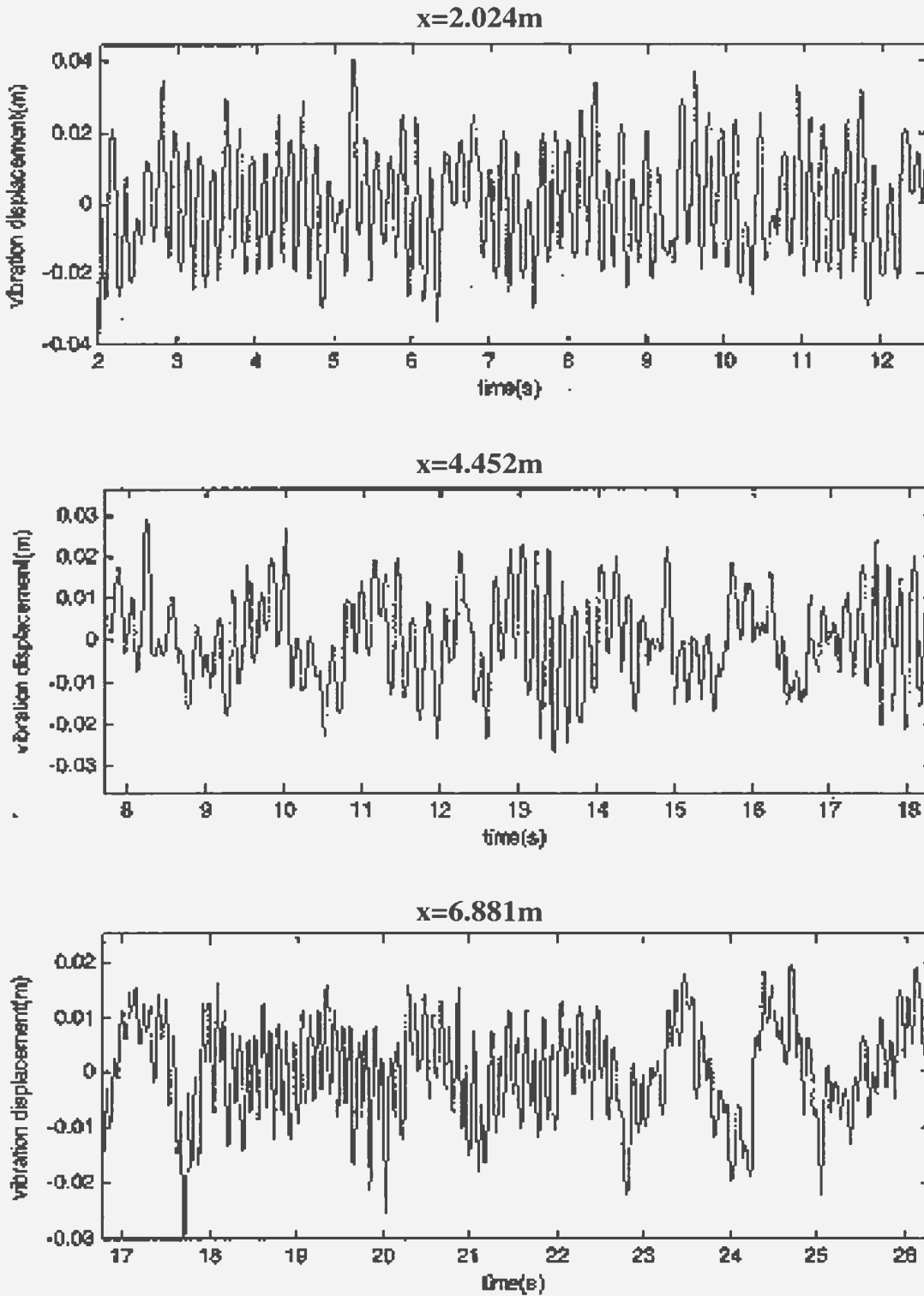


Figure 4-50 Time history of in-line VIV at different locations at a current velocity of 1.3m/s and a pretension of 200N

Summarizing the results above, we know that at low current velocities, it is most likely that the in-line and cross-flow VIV responses contain the SF type, and the vibration type is independent of the locations over the riser length. At high current velocities, it is most possible that the in-line and cross-flow VIV responses contain the MF type. Sometimes, there may be a mixture of MF and CD types in the VIV responses at high current velocities. At high current velocities, the vibration type may depend on the locations over the riser length.

4. 2. 2. 5 Vibration Shapes

Combining the vibration displacements measured by the sixteen pairs of accelerometers at a time instant can give the vibration shapes over the riser length. If several vibration shapes at different time instants are plotted on a picture, a snapshot can be made. Figures 4-51 to 4-55 present the snapshots of the in-line and cross-flow VIV responses at five current velocities of 0.4, 0.6, 0.8, 1.3 and 1.5m/s. Note that the vibration shapes in these figures may be skewed at the locations from 5.27 to 6.47m on the riser, as no measurement of the VIV displacements was made at those locations in the tests.

As seen in these figures, these snapshots directly verify that the VIV responses for a flexible riser are the multi-modal vibrations; that is, both the vibration shapes of the in-line and the cross-flow VIVs over the riser length contain several modal components. It is noted that the vibration shapes over the riser length were not symmetrical about the middle point of the riser, although the structure of the model riser and the current profiles tested were. The odd mode shapes, such as mode 1, 3, 4,..., are symmetrical about the middle point of the riser, and a mixture of these mode shapes are also symmetrical about

the middle point of the riser. A vibration shape asymmetrical with respect to the middle point of the riser means that in addition to these odd modes the even modes also exist in the VIV responses. As the riser structure and the current profile tested were symmetrical about the middle point of the riser, the cause of asymmetry of vibration shapes should be the hydrodynamic loads acting on the riser. This implies that for a flexible riser, the hydrodynamic loads may be asymmetrical with respect to its middle point. A possible interpretation for this is that a slightly asymmetrical structure of the riser results in a slightly asymmetrical vibration shape, and the slight asymmetrical motion results in the slight asymmetrical hydrodynamic loads on the riser. The slightly asymmetrical hydrodynamic loads then intensify the asymmetry of the riser vibrations, and the intensified asymmetry of the riser vibration will cause bigger asymmetry of the hydrodynamic loads again. Finally, the VIVs become completely asymmetrical. This discovery would mean that the riser vibration motion have a significant effect on the hydrodynamic loads acting on the riser and have an important role for the multi-modal VIV process.

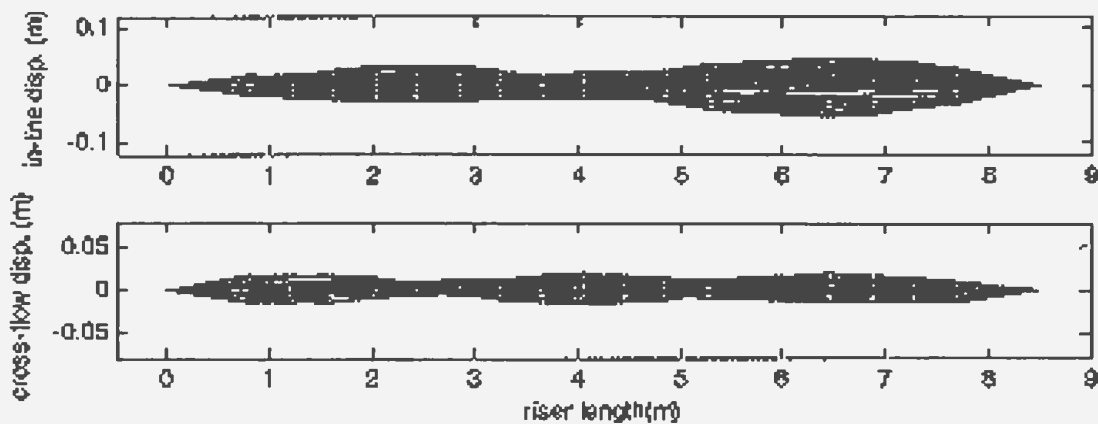


Figure 4-51 Vibration shapes at a current velocity of 0.4m/s and a pretension of 200N

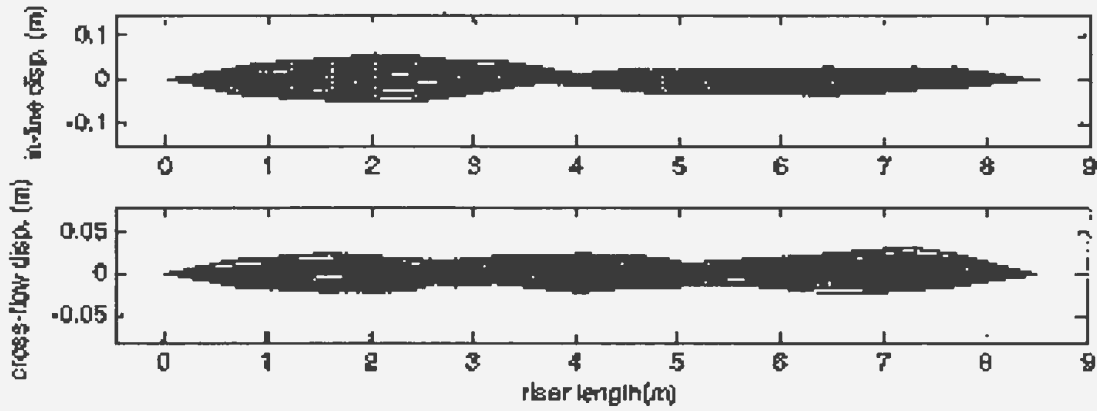


Figure 4-52 Vibration shapes at a current velocity of 0.6m/s and a pretension of 200N

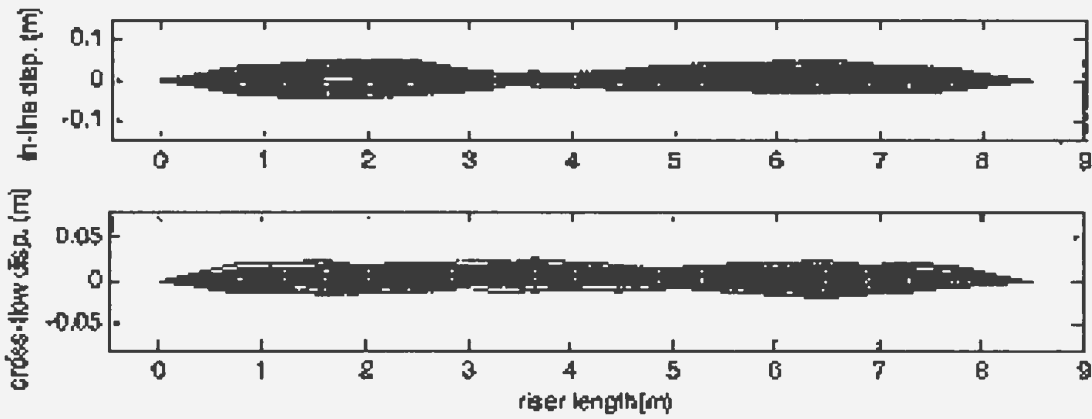


Figure 4-53 Vibration shapes at a current velocity of 0.8m/s and a pretension of 200N

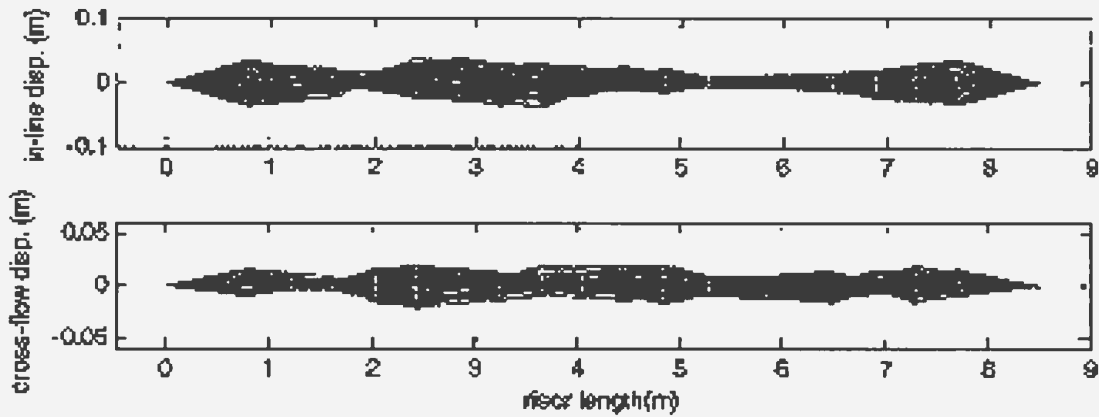


Figure 4-54 Vibration shapes at a current velocity of 1.3m/s and a pretension of 200N

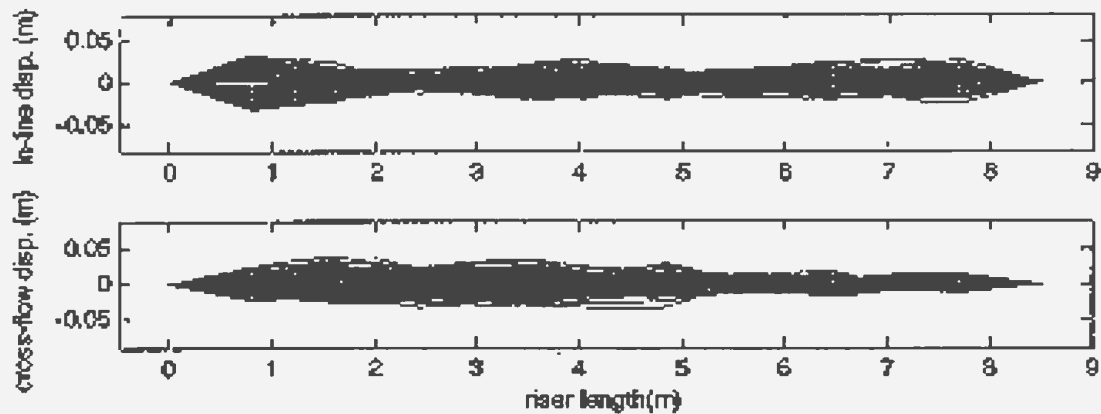


Figure 4-55 Vibration shapes at a current velocity of 1.5m/s and a pretension of 200N

It was found that the increased current velocity gives rise to more dominant modal components in the VIV responses. For example, in the currents with velocities smaller than 1.00m/s, the snapshots contain a clear dominant mode with relatively clear vibration nodes, while in the currents with velocities greater than 1.00m/s, the dominant modes and the vibration nodes become relatively unclear, and this means that the vibrations were dominated by several modes. Compared to the results from the time history analysis, we know that the vibrations with a relatively clear mode correspond to the SF type, while the vibrations without a relatively clear mode correspond to the MF type.

4. 2. 2. 6 Vibration Trajectories

Combining the vibration displacements in the in-line and the cross-flow directions measured by each pair of accelerometers at several time instants, a vibration trajectory in a cross-sectional plane of the riser can be plotted. These vibration trajectories exhibit the patterns of the riser motion in the cross-section plane and have an important effect on the vortex formation-shedding process behind the riser.

Figures 4-56 to 4-60 present the VIV motion trajectories on four cross-sectional planes along the riser at five reduced velocities of 26.59, 39.90, 61.22, 79.77 and 99.74, which correspond to five current velocities of 0.4, 0.6, 1.0, 1.2 and 1.5m/s. In these figures, the y -direction is defined as the in-line direction, and the z -direction is defined as the cross-flow direction. These trajectories are the records during about three or four cyclic periods. As the recording periods are relatively short, these trajectories are only the representatives of the entire VIV responses.

As shown in these figures, the trajectories are quite complicated and strongly depend on the current velocity and the location on the riser. These trajectories mainly contain two fundamental motions. The first is a basic figure of 8-, L- and O-shaped or other complicated vibration motion. Another is a shifted motion of the basic figure motion.

The low current velocities cause the basic figures of the 8- or L-shaped vibration motion. For example, at the current velocity of 0.4m/s, as seen in Figure 4-56, the basic figure is the 8-shaped vibration motion at the locations of $x=0.810$, 3.624 and 4.857m, while the basic figure is the L-shaped vibration motion at the location of $x=6.881$ m. At the current velocity of 0.6m/s, as seen in Figure 4-57, the basic figure is 8-shaped vibration motion at the locations of $x=3.624$ and 6.881m, while the basic figure is L-shaped vibration motions at the location of $x=0.810$ and 4.857m. The high current velocities may cause the basic figures of O-shaped or other complicated vibration motion. For example, in Figure 4-60, at the location of $x=0.810$ m, a basic figure of O-shaped vibration motion is found, while the more complicated basic figures exist in the vibrations at the other locations.

Vortex-Induced Vibration Tests

It is noted that the shifted motions of the basic figure occur not only in the in-line direction but also in the cross-flow direction. The shifted motion may be an indication of multi-modal VIV, because such a shifted motion does not usually exist for single-modal VIV.

The complicated motion trajectories mean a complicated vortex formation-shedding process. The strong dependence of the motion trajectories on the locations along riser length may cause non-uniform vortex-shedding loads acting on a uniform riser. This may be one of the causes of the even mode components contained in VIV responses for a uniform riser.

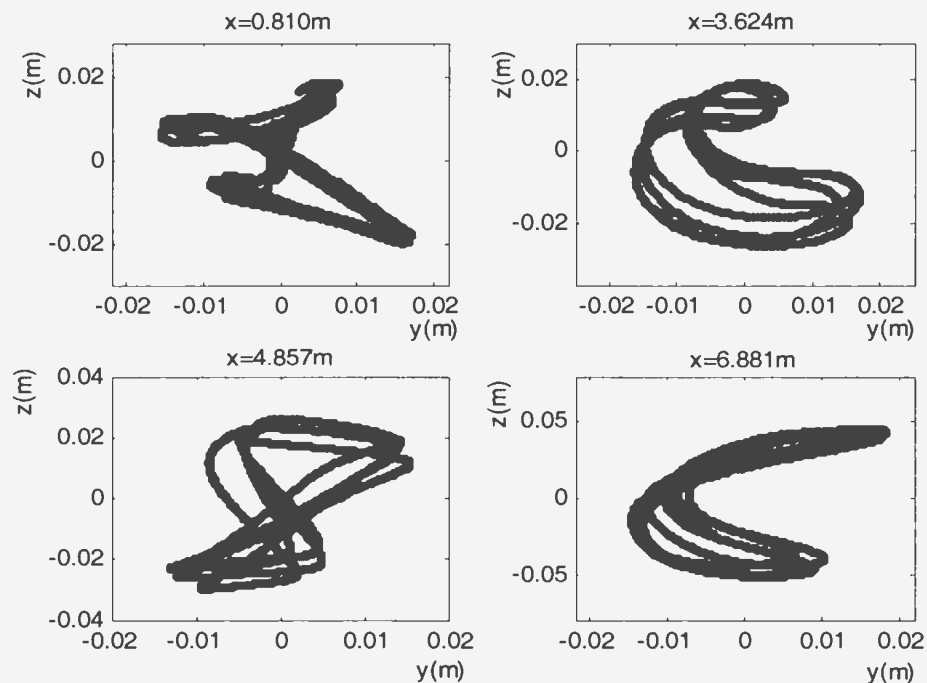


Figure 4-56 Trajectory of VIV at a current velocity of 0.4m/s and a pretension of 200N

Vortex-Induced Vibration Tests

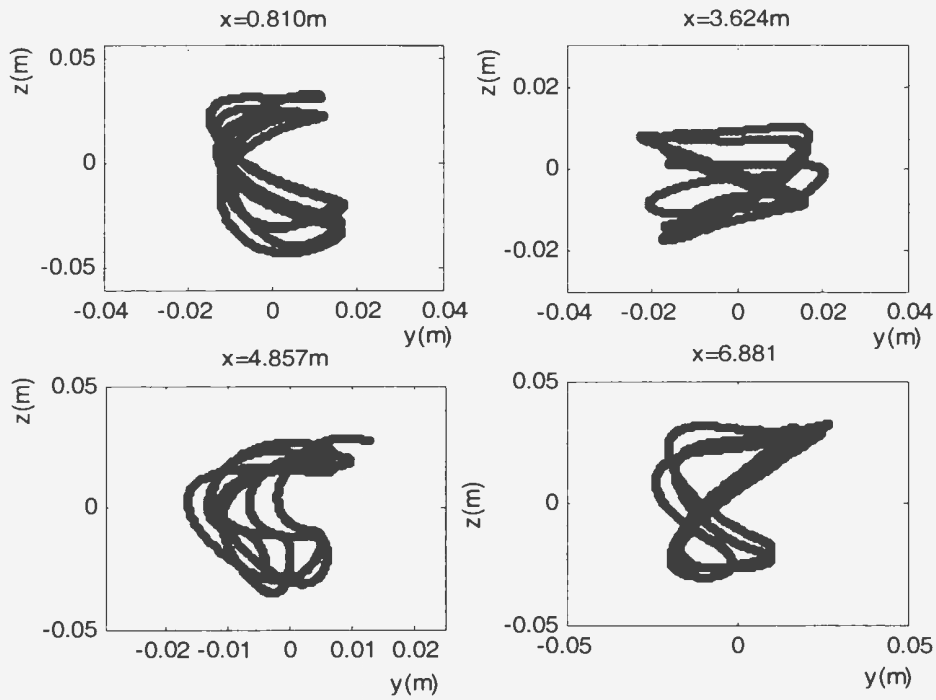


Figure 4-57 Trajectory of VIV at a current velocity of 0.6m/s and a pretension of 200N

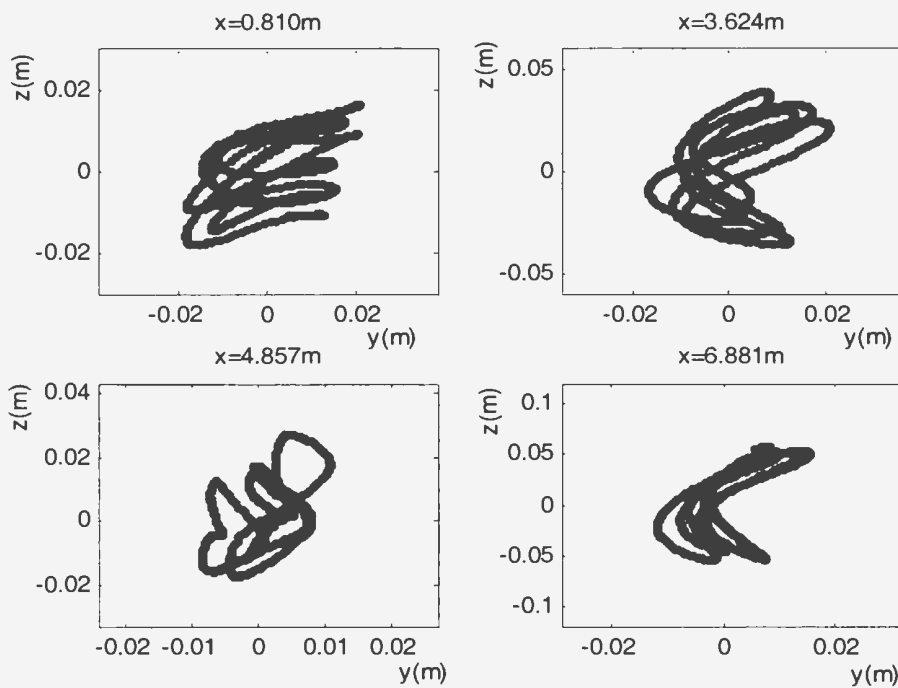


Figure 4-58 Trajectory of VIV at a current velocity of 1.00m/s and a pretension of 200N

Vortex-Induced Vibration Tests

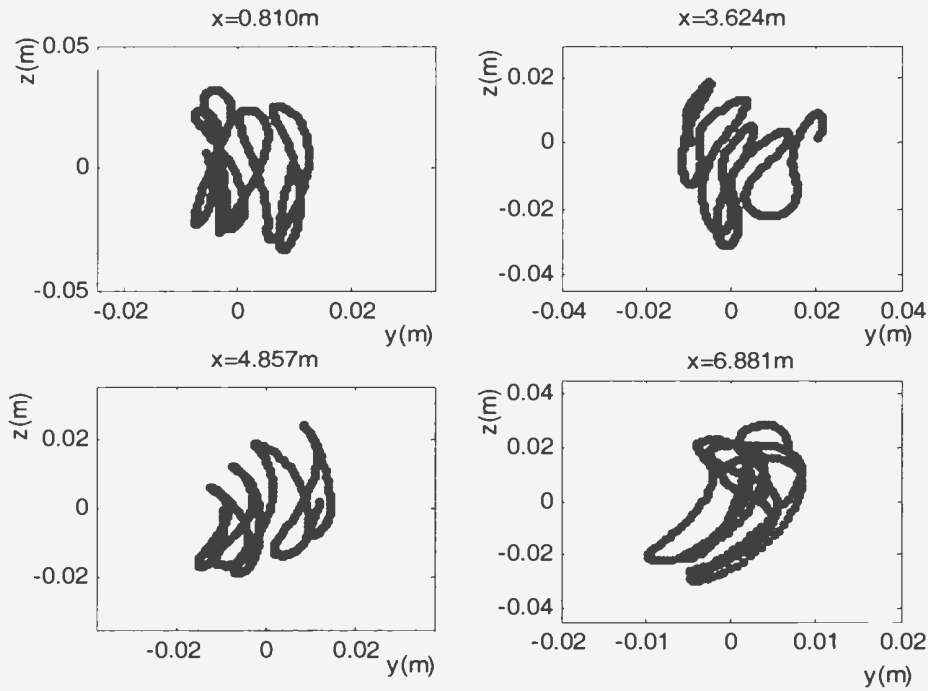


Figure 4-59 Trajectory of VIV at a current velocity of 1.20m/s and a pretension of 200N

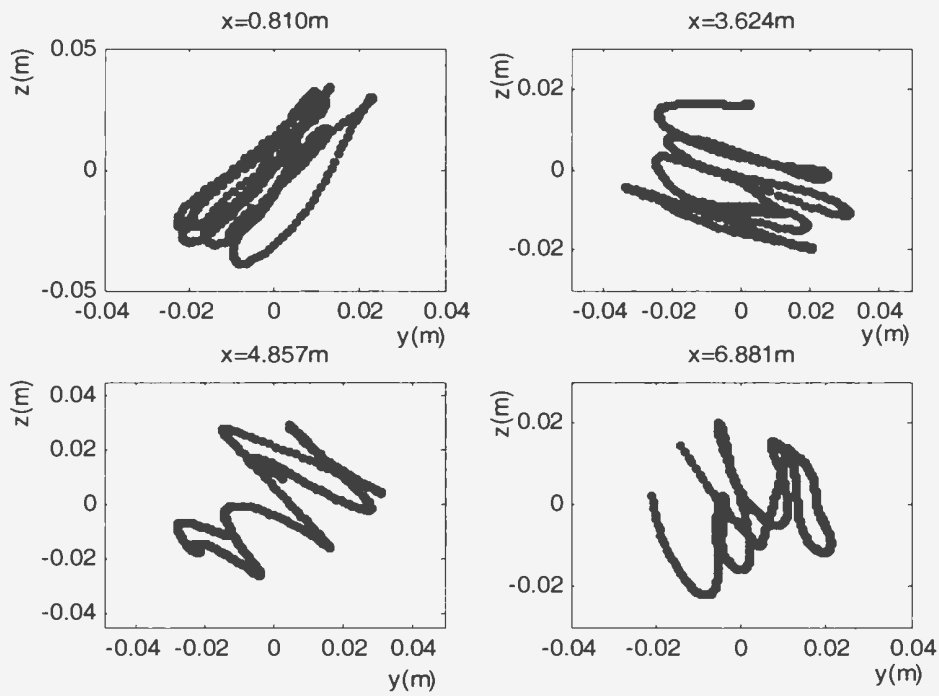


Figure 4-60 Trajectory of VIV at a current velocity of 1.50m/s and a pretension of 200N

4. 2. 3 Test Results at High Pretension of 600N

The second pretension tested was 600N. After adjusting the pretension to satisfy the required pretension value, twenty-nine current velocities ranging from 0.75 to 1.5m/s were tested. The test results will be presented and discussed in this section.

4. 2. 3. 1 Amplitude and Frequency versus Current Velocity

Figure 4-61 shows the average peak-pick-up amplitude and the average peak-pick-up frequency versus current velocity at the pretension of 600N. The peak definition and the analysis methods are the same as those in the case of a pretension of 200N. V^* is the reduced velocity, defined as $V^*=U/f_{n1}D$, where: U is the current velocity, D is the riser diameter, $f_{n1} = 0.85\text{Hz}$, which is the natural frequency of the first mode in calm water at the pretension of 600N. f^* is the frequency ratio, defined as $f^*=f/f_{n1}$, where: f is the average peak-pick-up frequencies in currents. A^* is the non-dimensional vibration amplitude, defined as $A^*=A/D$, where: A is the average peak-pick-up amplitude.

As seen in Figure 4-61, both the average peak-pick-up frequencies of the cross-flow VIV and the in-line VIV follow the Strouhal frequencies at the majority of current velocities. In the region from $V^*=9$ to 16.5, the average peak-pick-up frequencies of the cross-flow and in-line vibrations are a little smaller than those represented by a Strouhal number of 0.12, and this indicates a frequency lock-in phenomenon occurring in both the cross-flow and in-line directions. This lock-in phenomenon is very weak, because the average peak-pick-up frequencies still vary with the current velocities and are just a little smaller than the Strouhal frequencies. The lock-in region starts at the reduced velocity of 9 at which the Strouhal frequency matches the natural frequency of mode 1, as seen in

Figure 4-4. This implies that both the lock-in mode of the cross-flow and in-line vibrations is mode 1, and this lock-in region can be categorized to Region C.

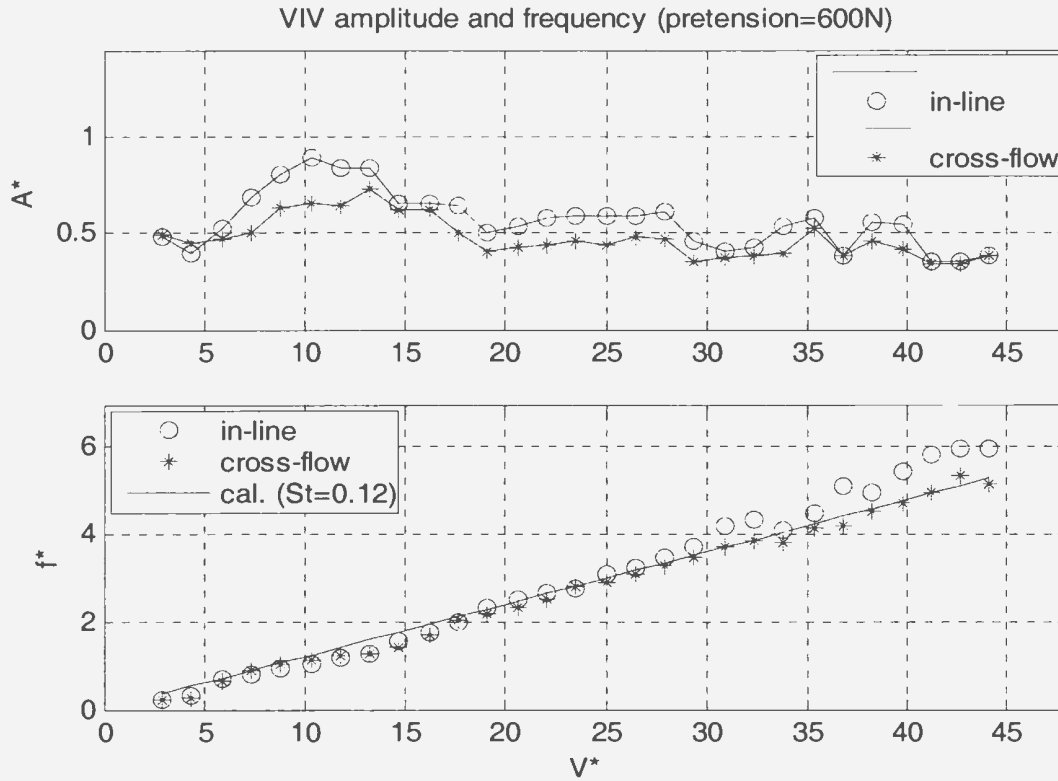


Figure 4-61 The average peak-pick-up amplitude and frequency of in-line and cross-flow VIV at a pretension of 600N

Comparing the results in Figure 4-61 with the results in Figure 4-6, we can find a different characteristic for the pretensions of 200 and 600N in the in-line vibration frequencies in this lock-in region. In the case of the pretension of 200N, the lock-in mode in the in-line direction is different from the lock-in mode in the cross-flow direction, while in the case of the pretension of 600N, the lock-in mode in the in-line direction is identical to the lock-in mode in the cross-flow direction. As opposed to the natural frequencies in the case of the pretension of 200N, in the case of the pretension of 600N the natural frequencies of mode 1 and 2 are relatively separate and, as a result, both the

vortex shedding frequencies in the cross-flow and in-line directions are close to the natural frequency of mode 1, as seen in Figure 4-4, so that both lock-in mode for the cross-flow and in-line vibrations is mode 1. According to Figure 4-3, at the reduced velocity of 9, which corresponds to a current velocity of 0.3m/s, the tension acting on the riser is 700N, and the added mass coefficient for mode 1 is 2.01 at this tension, as shown in Table (3-15). The maximum upper limit value of the reduced velocity estimated from equation (4-1) is 18.74 for this lock-in region, which is larger than the measured reduced velocity value of 16.5 at the higher boundary of this lock-in region.

According to Figure 4-4, a lock-in region for mode 2 is expected to start from $V^*=20$, but as seen in Figure 4-61, the vibration frequencies still follow the Strouhal frequencies in the region beyond $V^*=20$, i.e. the expected lock-in region disappears. This is because the Strouhal frequencies are almost equal to the natural frequencies of mode 2 in the region and this causes the frequency lock-in phenomenon to “disappear”. Therefore, this lock-in region may still exist implicitly. In this region, the in-line vibration frequencies are a little larger than the cross-flow vibration frequencies at some current velocities.

Both of the average peak-pick-up amplitudes of the in-line and cross-flow VIV responses fluctuate over a range from $0.34D$ to $0.89D$, which lie with in the same level as in the case of the low pretension of 200N. This implies that the amplitudes of multi-modal VIV response for the flexible riser is not sensitive to the pretension over the current velocity range tested. Similar to the results for the lower pretension case, increased current velocities result in a trend of reducing amplitudes although the vortex-shedding forces are usually expected to have bigger values in high current velocities compared to those in low current velocities. Also, no obvious peak exists over the current

velocity range tested, but a region of relatively big response amplitude is found from $V^*=6$ to 19. It is noted that, as opposed to the amplitudes of the in-line VIV in the case of a pretension of 200N, the amplitudes of the in-line VIV responses also have relatively big values in this region. The cause is that in the lower pretension case the lock-in mode for the in-line vibrations is different from the lock-in mode in the cross-flow responses, while in the higher pretension case the lock-in mode for the in-line vibrations is identical to the lock-in mode in the cross-flow responses. A region of medium response amplitude is found from $V^*=20$ to 28, and a region of small response amplitudes is found from $V^*=30$ to 45. In the small response amplitude region, the response amplitudes seem to have larger fluctuations than in the other regions.

Although the amplitudes of multi-modal VIV response for the flexible riser is not sensitive to the pretension over the current velocity range tested, the lock-in modes of vibrations depend strongly on the pretensions, as the modal natural frequencies depend strongly on the pretensions. The different characteristics of riser vibrations at different pretensions may change the so-called vortex wake modes, because the vortex wake modes usually depend on the current velocities and the cylinder motion patterns. Previous experimental work has showed that for a rigid cylinder with free vibrations the vortex wake modes may include 2S, 2P and S+P types in three regions of the “initial branch”, “upper branch” and “lower branch”, but more complicated modes may exist if the cylinder motions are complicated (Williamson and Govardhan, 2004). For a flexible riser with three-dimensional multi-modal vibrations, it is still unclear what vortex wake modes such motions will produce. The complexity of vortex wake modes for a flexible riser will cause complexity in the characteristics of the VIV responses.

Two reduced velocity regions i.e. Region A and Region C, could be found in the VIV responses in the case of pretension of 600N. As seen in Figure 4-61, Region A ranges from $V^*=3$ to 9, where no frequency lock-in occurs, and Region C ranges from $V^*=9$ to 20, where the frequency lock-in appears in both the in-line and cross-flow directions. The lock-in frequency corresponds to the natural frequency of mode 2. In the region from $V^*=20$ to 44, as the Strouhal frequencies are almost equal to the natural frequencies of mode 2, it is difficult to clearly judge whether a frequency lock-in occurs. This region is called Region D in this thesis.

4. 2. 3. 2 Vibration Power Spectra

The spectral analysis technique shown in Appendix B is used to analyze the frequency components in the measured VIV responses. As discussed in Section 4.2.3.1, three regions of Region A, Region C and Region D can be found from the plots of the average peak-pick-up amplitude and frequency versus reduced velocity. In this section, the power spectra of the VIV responses in the three regions will respectively be examined.

Vibration power spectra in Region A

According to Figure 4-61, Region A ranges from $V^*=3$ to 9. Select the VIV responses at a reduced velocity of 5.88, which corresponds to a low current velocity of 0.2m/s, to check power spectra. Figure 4-62 presents the power spectrum of the cross-flow VIV responses at this reduced velocity. As seen in Figure 4-62, a strong dominant frequency of 1.34Hz and a weak secondary-dominant frequency of 0.3Hz are found. Figure 4-61 shows an average peak-pick-up frequency is 0.5Hz with a Strouhal frequency of 0.6Hz at this reduced velocity. The dominant frequency is greater than the average peak-pick-up

frequency, while the secondary-dominant is smaller than the average peak-pick-up frequency.

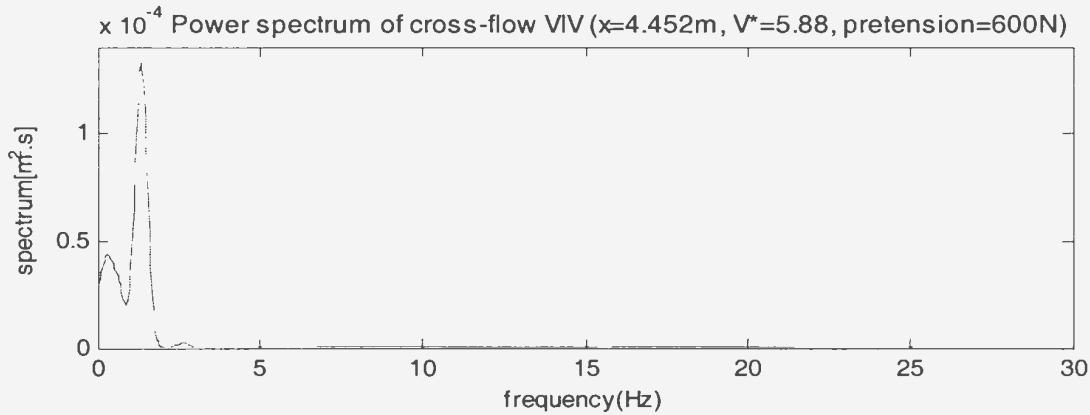


Figure 4-62 Power spectrum of cross-flow VIV at the middle of riser at a current velocity of 0.2m/s and a pretension of 600N

Figure 4-63 is the power spectrum of in-line VIV responses at the reduced velocity of 5.88. The in-line VIV responses contain a dominant frequency of 0.7Hz. The average peak-pick-up frequency of the in-line VIV responses at this reduced velocity is 0.6Hz, as seen in Figure 4-61. The dominant frequency is close to the average peak-pick-up frequency.

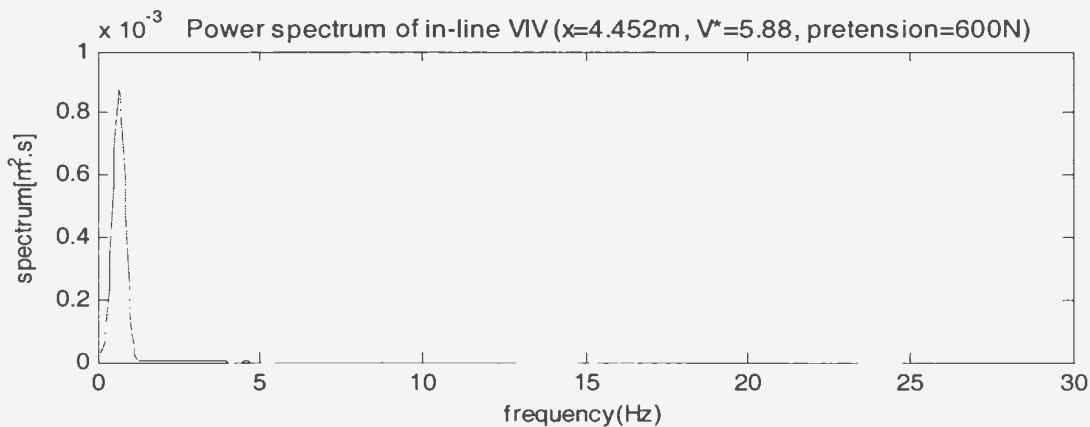


Figure 4-63 Power spectrum of in-line VIV at the middle of riser at a current velocity of 0.2m/s and a pretension of 600N

Vibration power spectra in Region C

According to Figure 4-61, Region C ranges from $V^*=9$ to 20. Now examine the power spectra at two reduced velocities of 11.76 and 17.65, which correspond to two current velocities of 0.4 and 0.6m/s.

Figure 4-64 shows the power spectrum of the cross-flow VIV responses at the reduced velocity of 11.76. At this reduced velocity, the cross-flow VIV responses contain two dominant frequencies of 0.3 and 2.2Hz and a secondary-dominant frequency of 1.1Hz. The corresponding average peak-pick-up frequency and Strouhal frequency are respectively 1.0 and 1.2, as seen in Figure 4-61, which is close to the average of the dominant and the secondary-dominant frequencies.

Figure 4-65 gives the power spectrum of the in-line VIV responses at the reduced velocity of 11.76. As seen in Figure 4-65, the in-line VIV responses only contain a dominant frequency of 1.1Hz. Figure 4-61 shows that the average peak-pick-up frequency of the in-line VIV responses shown is 1.0Hz at this reduced velocity, which is close to the dominant frequency.

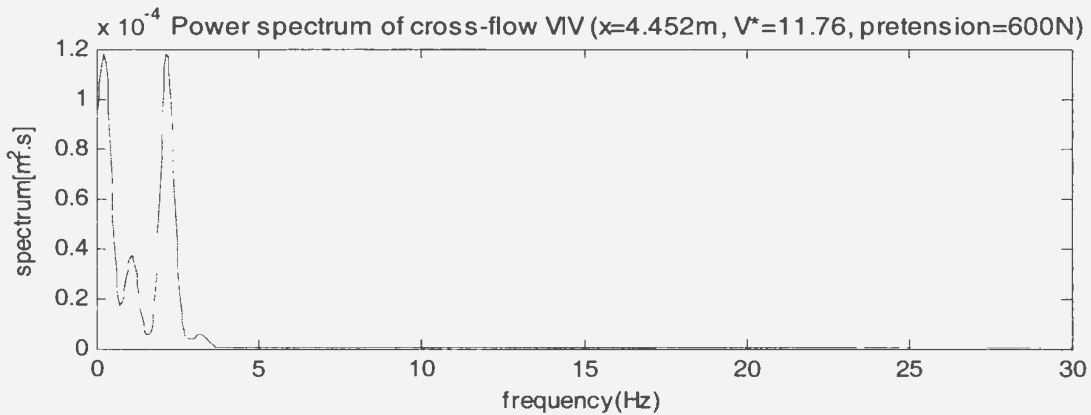


Figure 4-64 Power spectrum of cross-flow VIV at the middle of riser at a current velocity of 0.4m/s and a pretension of 600N

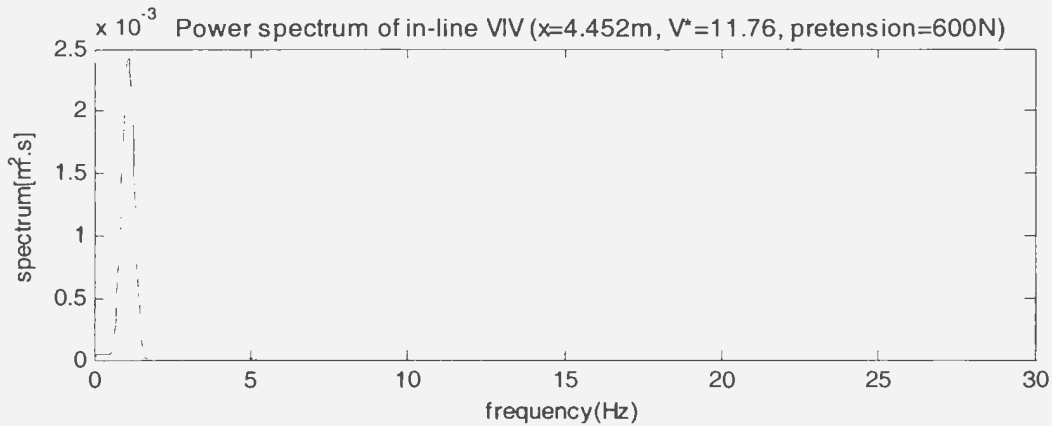


Figure 4-65 Power spectrum of in-line VIV at the middle of riser at a current velocity of 0.4m/s and a pretension of 600N

Figure 4-66 shows the power spectrum of the cross-flow VIV responses at a reduced velocity of 17.65. As seen in Figure 4-66, a dominant frequency of 4.0Hz and two secondary-dominant frequencies of 0.4 and 2.0Hz are found. According to Figure 4-61, the average peak-pick-up frequency and the Strouhal frequency are respectively 1.7 and 1.8Hz, which are close to one of two secondary-dominant frequencies. The increased current velocity causes the vibration energy at the low dominant frequencies to decrease and the vibration energy at the high dominant frequency to increase.

Figure 4-67 presents the power spectrum of the in-line VIV responses at the reduced velocity of 17.65. At this reduced velocity, the in-line VIV responses contain a dominant frequency of 2.0Hz. As shown in Figure 4-61, the average peak-pick-up frequency of the in-line VIV responses is 1.7Hz, which is close to the dominant frequency. The increased current velocity pushes the dominant frequency to higher frequency region.

Summarize the results of spectral analysis in Region C at two pretensions of 200 and 600N, and we know that in Region C, the VIV responses contain the different number of the dominant and secondary-dominant frequencies in the in-line and cross-flow

directions. In a direction there is a dominant frequency, while in the other direction there are several dominant and secondary-dominant frequencies.

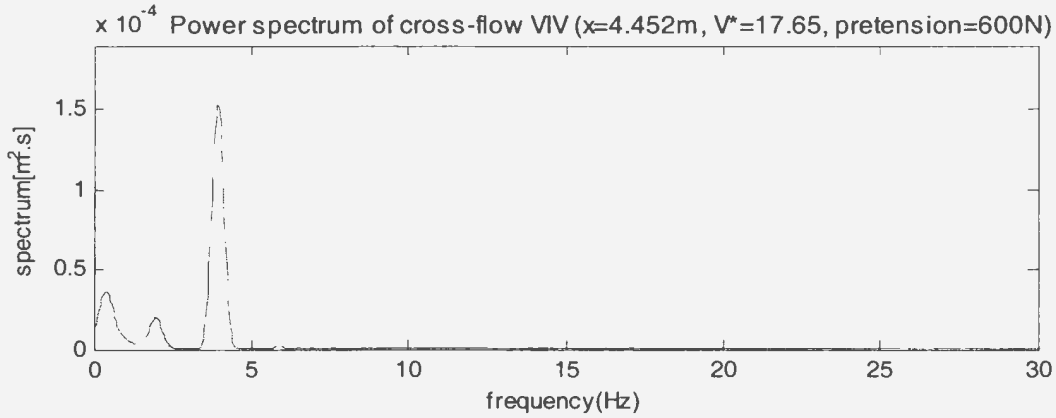


Figure 4-66 Power spectrum of cross-flow VIV at the middle of riser at a current velocity of 0.6m/s and a pretension of 600N

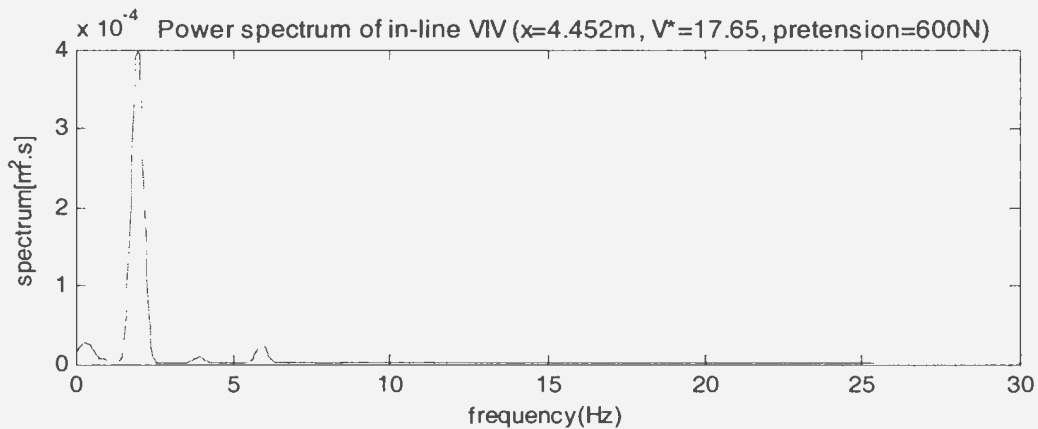


Figure 4-67 Power spectrum of in-line VIV at the middle of riser at a current velocity of 0.6m/s and a pretension of 600N

Vibration power spectra in Region D

According to Figure 4-61, Region D ranges from $V^*=20$ to 44. Now examine the power spectra at three reduced velocities of 23.53, 35.29 and 44.12, which corresponding to three current velocities of 0.8, 1.2 and 1.5m/s.

Figure 4-68 presents the power spectrum of the cross-flow VIV responses at the reduced velocity of 23.53. As seen in Figure 4-68, there is a dominant frequency of 2.8Hz and two secondary-dominant frequencies of 0.4Hz and 5.5Hz. According to Figure 4-61, the corresponding average peak-pick-up frequency and Strouhal frequency are respectively 2.3 and 2.4Hz, which is close to the dominant frequency.

Figure 4-69 shows the power spectrum of the in-line VIV responses at the reduced velocity of 23.53. At this reduced velocity, the in-line VIV responses contain a dominant frequency of 2.8Hz, and the average peak-pick-up frequency of the in-line VIV responses is 2.4Hz, as shown in Figure 4-61. The dominant frequency is a little bigger than the average peak-pick-up frequency.

Compared to the spectra of the VIV responses at the lower pretension of 200N at the current velocity of 0.8m/s, shown in Figures 4-9 and 4-10, the different pretensions cause obvious differences for the patterns of spectra of the VIV responses.

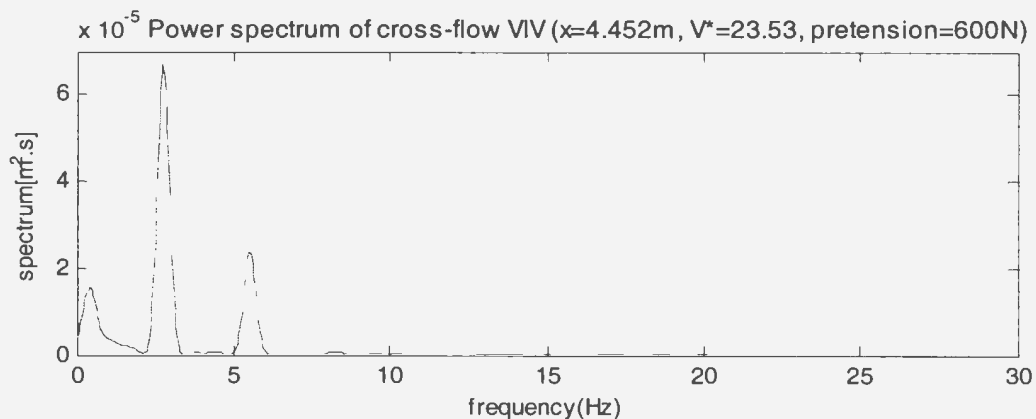


Figure 4-68 Power spectrum of cross-flow VIV at the middle of riser at a current velocity of 0.8m/s and a pretension of 600N

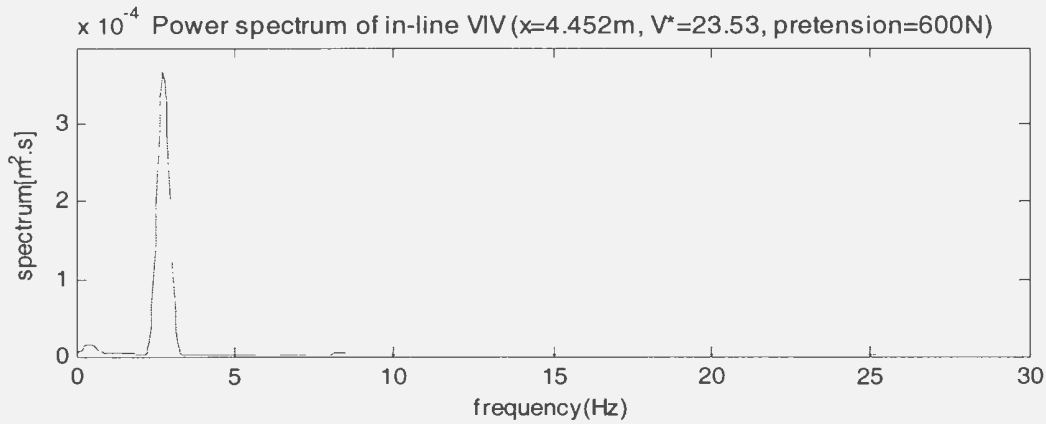


Figure 4-69 Power spectrum of in-line VIV at the middle of riser at a current velocity of 0.8m/s and a pretension of 600N

Figure 4-70 presents the power spectrum of the cross-flow VIV responses at the reduced velocity of 35.29. As seen in Figure 4-70, there is a dominant frequency of 4.6Hz and a secondary-dominant frequency of 0.7Hz. Figure 4-61 shows an average peak-pick-up frequency is 3.5Hz and a Strouhal frequency of 3.6Hz at this reduced velocity. Compared to the power spectrum shown in Figure 4-68, the second peak moves to higher frequency region, and the third peak disappears.

Figure 4-71 shows the power spectrum of the in-line VIV responses at the reduced velocity of 35.29. The in-line VIV responses contain a dominant frequency of 0.6Hz and a secondary-dominant frequency of 9.2Hz. The corresponding average peak-pick-up frequency of the in-line VIV responses is 3.8Hz, as shown in Figure 4-61. Compared to the spectrum shown in Figure 4-69, at this current velocity the VIV responses in the in-line direction contain a dominant frequency and a secondary-dominant frequency, and the increased current velocity results in more dominant frequencies in the in-line VIV responses than at lower current velocities.

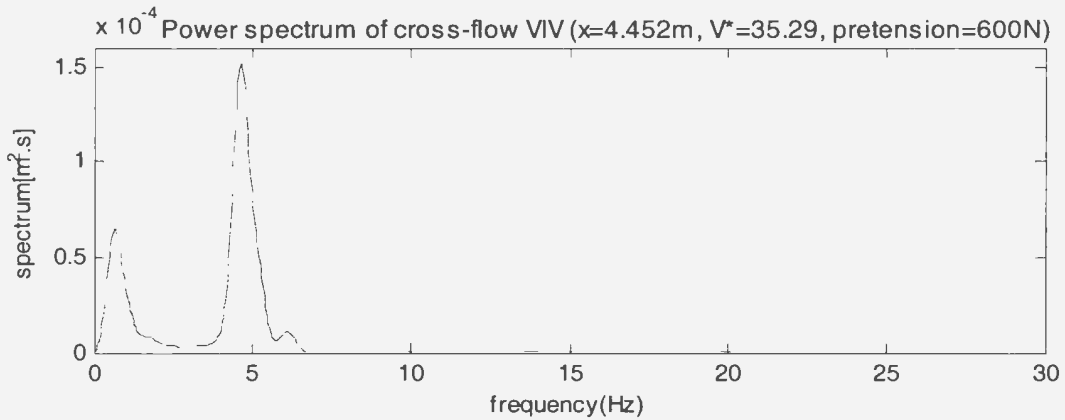


Figure 4-70 Power spectrum of cross-flow VIV at the middle of riser at a current velocity of 1.2m/s and a pretension of 600N

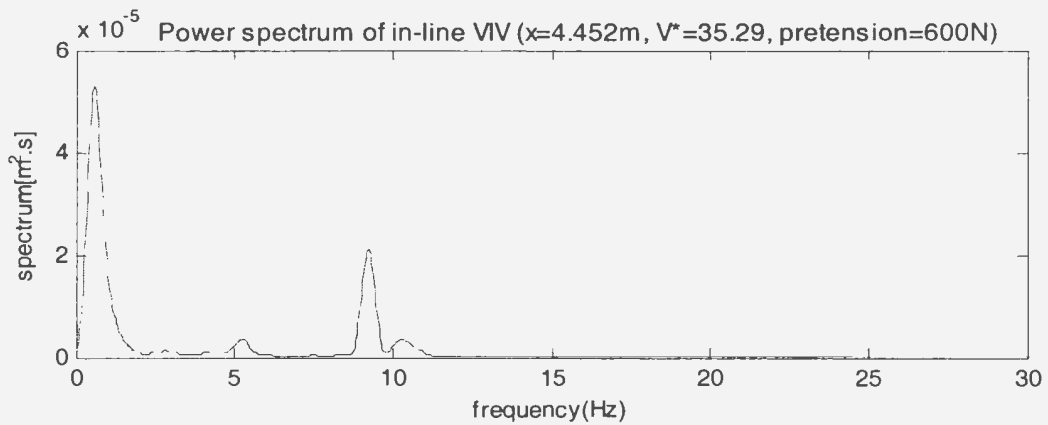


Figure 4-71 Power spectrum of in-line VIV at the middle of riser at a current velocity of 1.2m/s and a pretension of 600N

Figure 4-72 shows the power spectrum of the cross-flow VIV responses at the reduced velocity of 44.12. This is the highest current velocity in the VIV tests. As seen in Figure 4-72, there is a dominant frequency of 0.9Hz and a secondary-dominant frequency of 6.4Hz. The average peak-pick-up frequency of the cross-flow VIV responses is 4.4Hz and the Strouhal frequency is 4.5Hz, as shown in Figure 4-61. Compared to the power spectrum shown in Figure 4-70, the second peak moves to higher frequency region, while a number of frequency components with small energy appear between the dominant and secondary-dominant frequencies. This implies that higher current velocities may cause

the vibration energy to be shared by more frequency components than at lower current velocities.

Figure 4-73 presents the power spectrum of the in-line VIV responses at the reduced velocity of 44.12. The in-line VIV responses contain a dominant frequency of 0.8Hz and a secondary-dominant frequency of 6.4Hz. The average peak-pick-up frequency of the in-line VIV responses is 5.1Hz, as shown in Figure 4-61. It is noted that the vibration responses contain a number of frequency components with small energy ranging from 0 to 5.8Hz, and this is similar to the spectrum of the cross-flow VIV responses shown in Figure 4-72.

According to the discussions above, in Region D the responses contain several dominant and secondary-dominant frequencies in both the in-line and cross-flow directions. At the highest current velocity, many frequency components with small energy exist in the in-line and cross-flow VIV responses, meaning that vibration energy to be shared by a large number of frequency components.

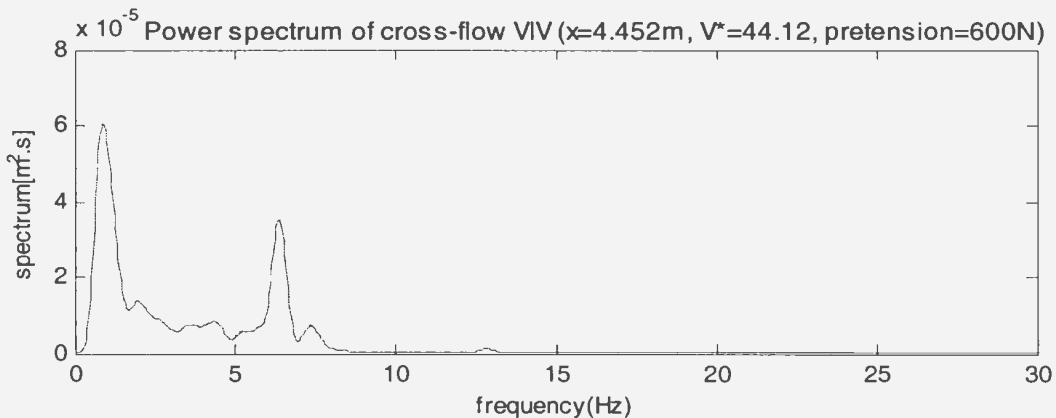


Figure 4-72 Power spectrum of cross-flow VIV at the middle of riser at a current velocity of 1.5m/s and a pretension of 600N

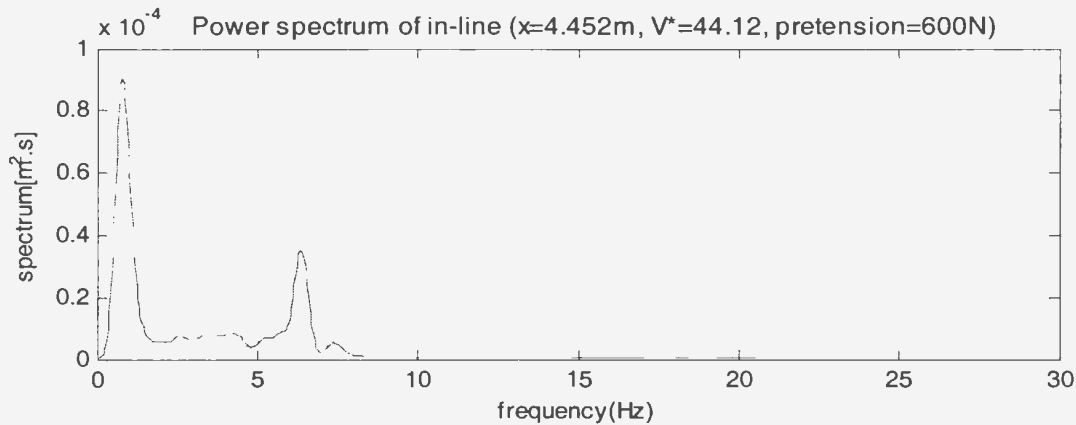


Figure 4-73 Power spectrum of in-line VIV at the middle of riser at a current velocity of 1.5m/s and a pretension of 600N

Vibration power spectra over riser length

Now examine the power spectra of the VIV responses at different locations over the riser length. Firstly, check the power spectra of the in-line VIV response. Figures 4-74 to 4-76 give spectra at three locations of $x=2.024$, 4.452 and 6.881 m and at three reduced velocities of 11.76 , 35.29 and 44.12 , which corresponding to three current velocities of 0.4 , 0.8 and 1.5 m/s.

Figure 4-74 presents the power spectra of the in-line VIV responses at the three locations at the low reduced velocity of 11.76 . As seen in Figure 4-74, the difference in location does not produce a big difference in power spectrum. This means that for small current velocities, the spectral characteristics of VIV responses over riser length are nearly identical in the present case.

Figure 4-75 gives the power spectra of the in-line VIV responses at the three locations at a moderate reduced velocity of 35.29 . As seen in Figure 4-75, the three spectra are also similar to each other, and this means that for moderate current velocities, the

characteristics of power spectra over the riser length are still nearly identical in the present case.

Figure 4-76 shows the power spectra of the in-line VIV responses at the three locations at the highest reduced velocity of 44.12. As seen in Figure 4-76, there are obvious differences in the three spectra. At the location of $x=2.024\text{m}$, only one peak exists at the frequency of 7.5Hz in the power spectrum. At the location of $x=4.452\text{m}$, two peaks exist at the frequency of 1.0Hz and 7.5Hz in the power spectrum. At the location of $x=6.881\text{m}$, only one peak exists at the frequency of 1.0Hz in the power spectrum. This means that at high current velocities the spectral characteristics of the in-line VIV responses over the riser length are different.

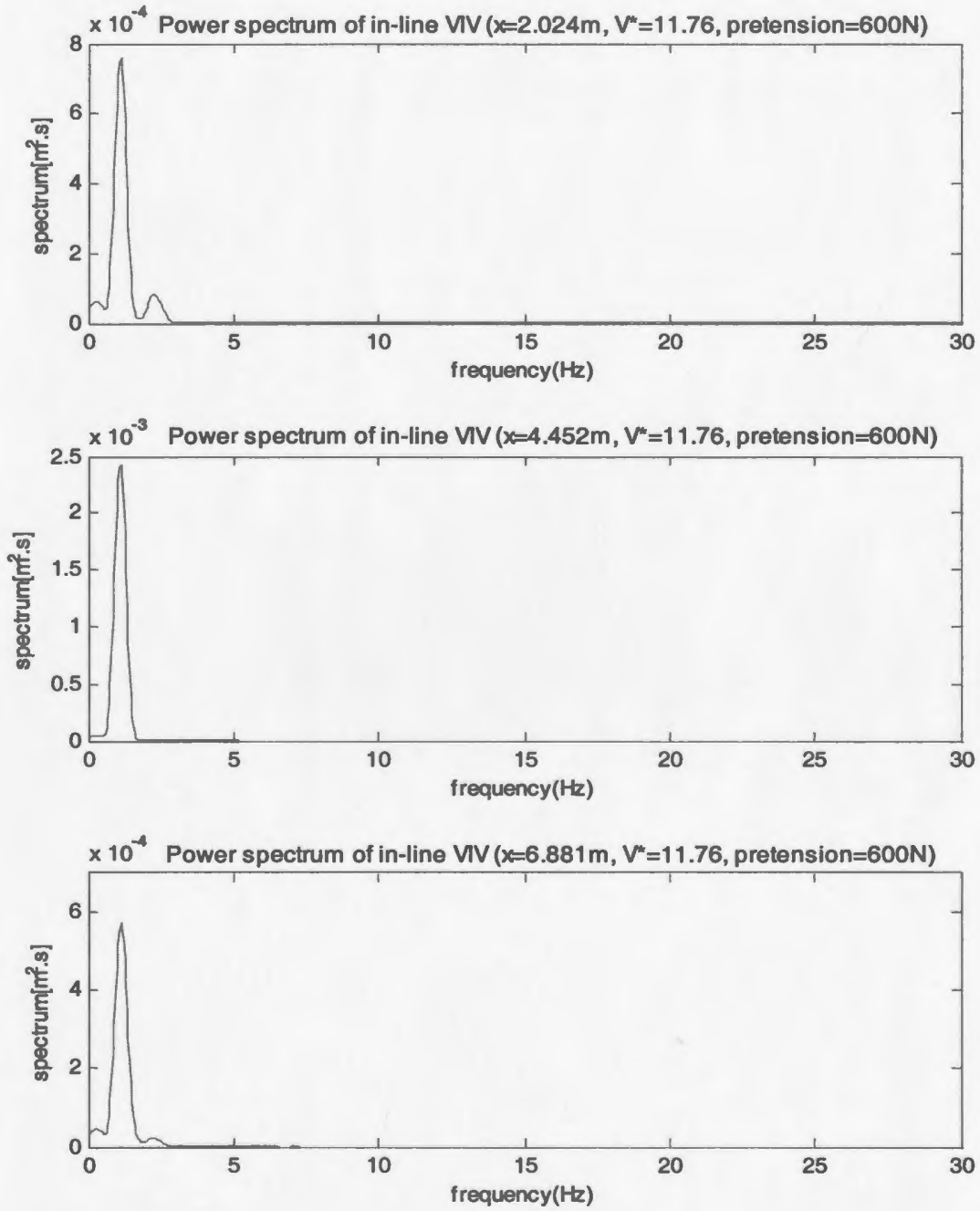


Figure 4-74 Power spectra of in-line VIV at different location on riser at a current velocity of 0.4m/s and a pretension of 600N

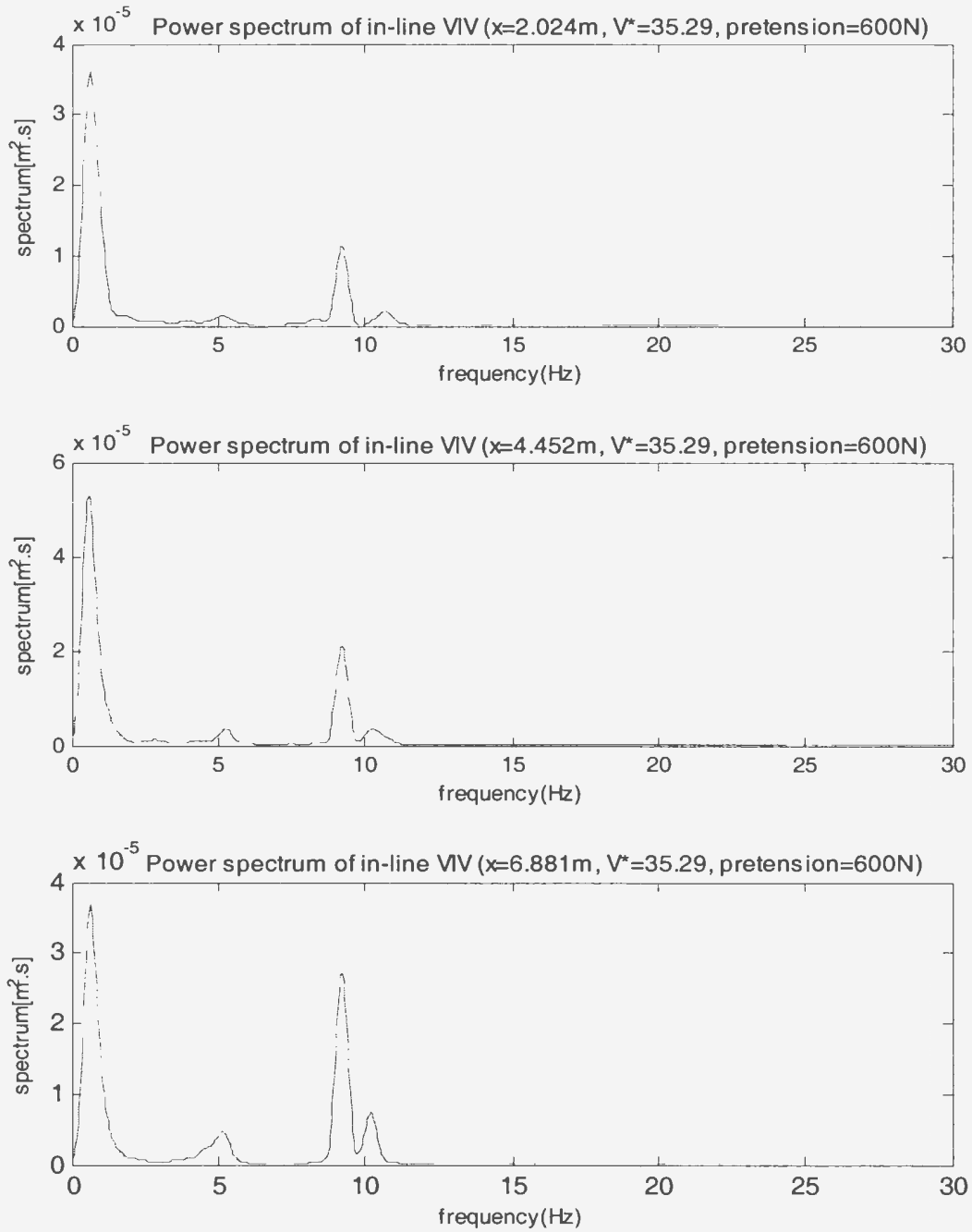


Figure 4-75 Power spectra of in-line VIV at different location on riser at a current velocity of 0.8m/s and a pretension of 600N

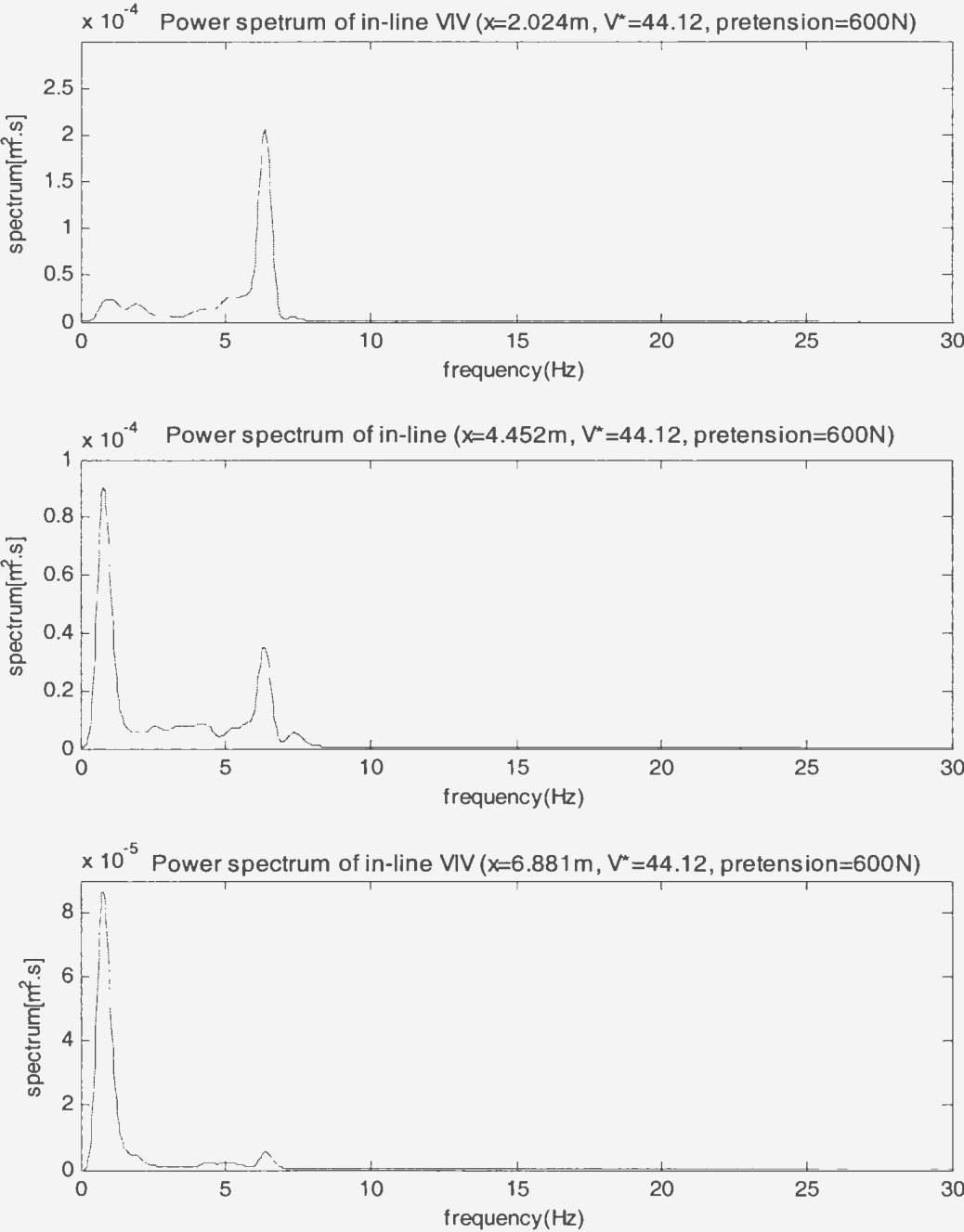


Figure 4-76 Power spectra of in-line VIV at different location on riser at a current velocity of 1.5m/s and a pretension of 600N

Now check the power spectra of the cross-flow VIV response over the riser length. Figures 4-77 to 4-78 give the results of spectral analysis at three locations of $x=2.024$, 4.452 and 6.881m and at three reduced velocities of 11.76 , 35.29 and 44.12 , which corresponding to three current velocities of 0.4 , 0.8 and 1.5m/s .

Figure 4-77 presents the power spectra at the three locations at the lowest reduced velocity of 11.76 . It is noted that the low current velocity also leads to significant differences of the power spectra over the riser length, as seen in Figure 4-77. Only one dominant frequency exists in the power spectrum of cross-flow VIV responses at the location of $x=2.024\text{m}$, while three dominant frequencies exist in the power spectra of cross-flow VIV response at the locations of $x=4.452$ and 6.881m . This result is different either from that in the case of the in-line VIV response at the same pretension, or from that in the case of the cross-flow VIV responses at the lower pretension of 200N .

The power spectra at the three locations at the moderate reduced velocity of 35.29 are shown in Figure 4-78. As seen in Figure 4-78, the spectra at this particular reduced velocity are somewhat similar to the results at the reduced velocity of 11.76 , namely the spectra contain significant differences at the different locations over the riser length. This finding is also different either from that in the case of the in-line VIV response at the same pretension, or in the case of the cross-flow VIV responses from that at the lower pretension of 200N .

Figure 4-79 shows the power spectra at the three locations at the highest reduced velocity of 44.12 . At this reduced velocity, the power spectra at the locations of $x=2.024$ and 4.452m have the same characteristics, while the power spectrum at the location of 6.881m is different from the spectra at the other locations.

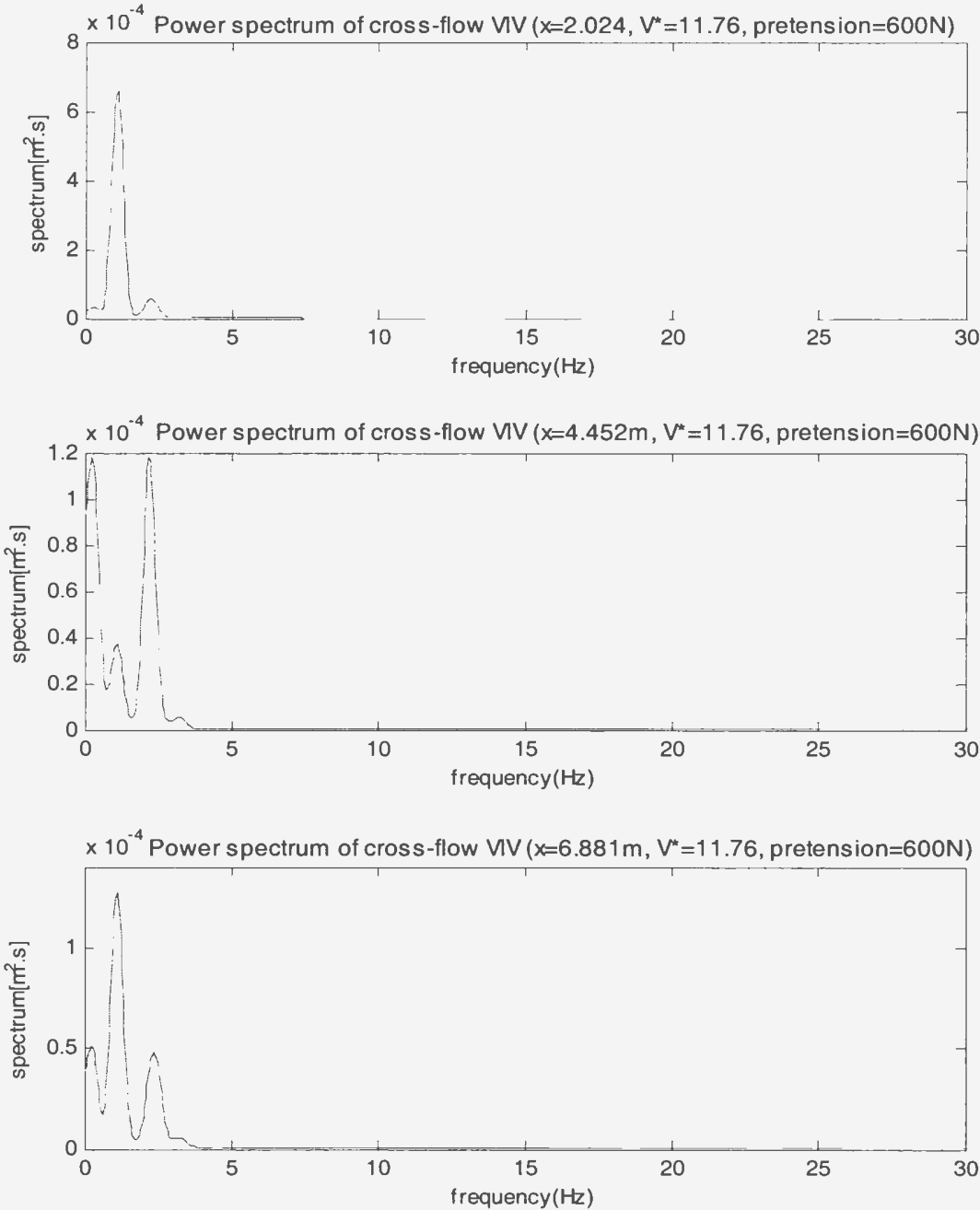


Figure 4-77 Power spectra of cross-flow VIV at different location on riser at a current velocity of 0.4m/s and a pretension of 600N

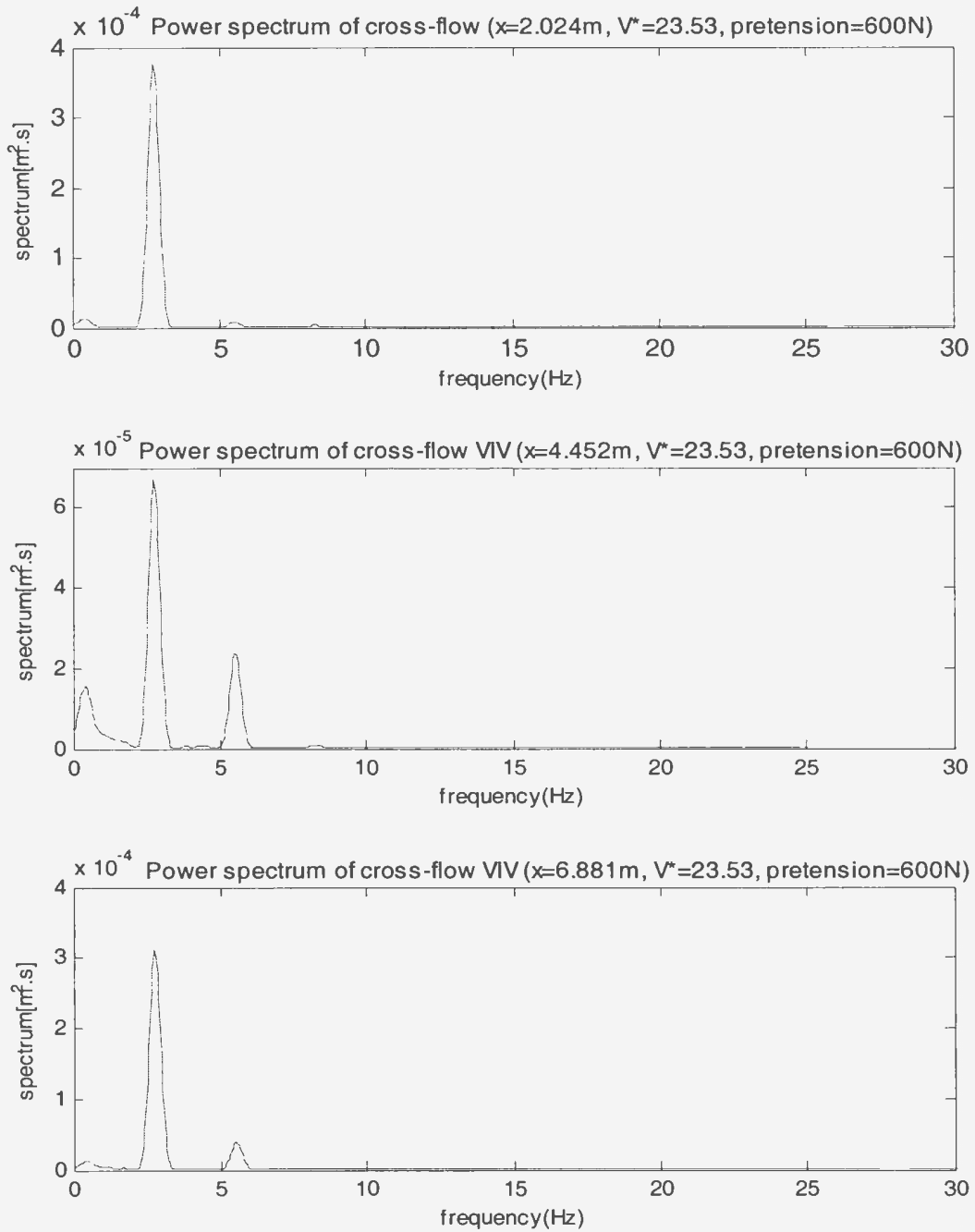


Figure 4-78 Power spectra of cross-flow VIV at different location on riser at a current velocity of 0.8m/s and a pretension of 600N

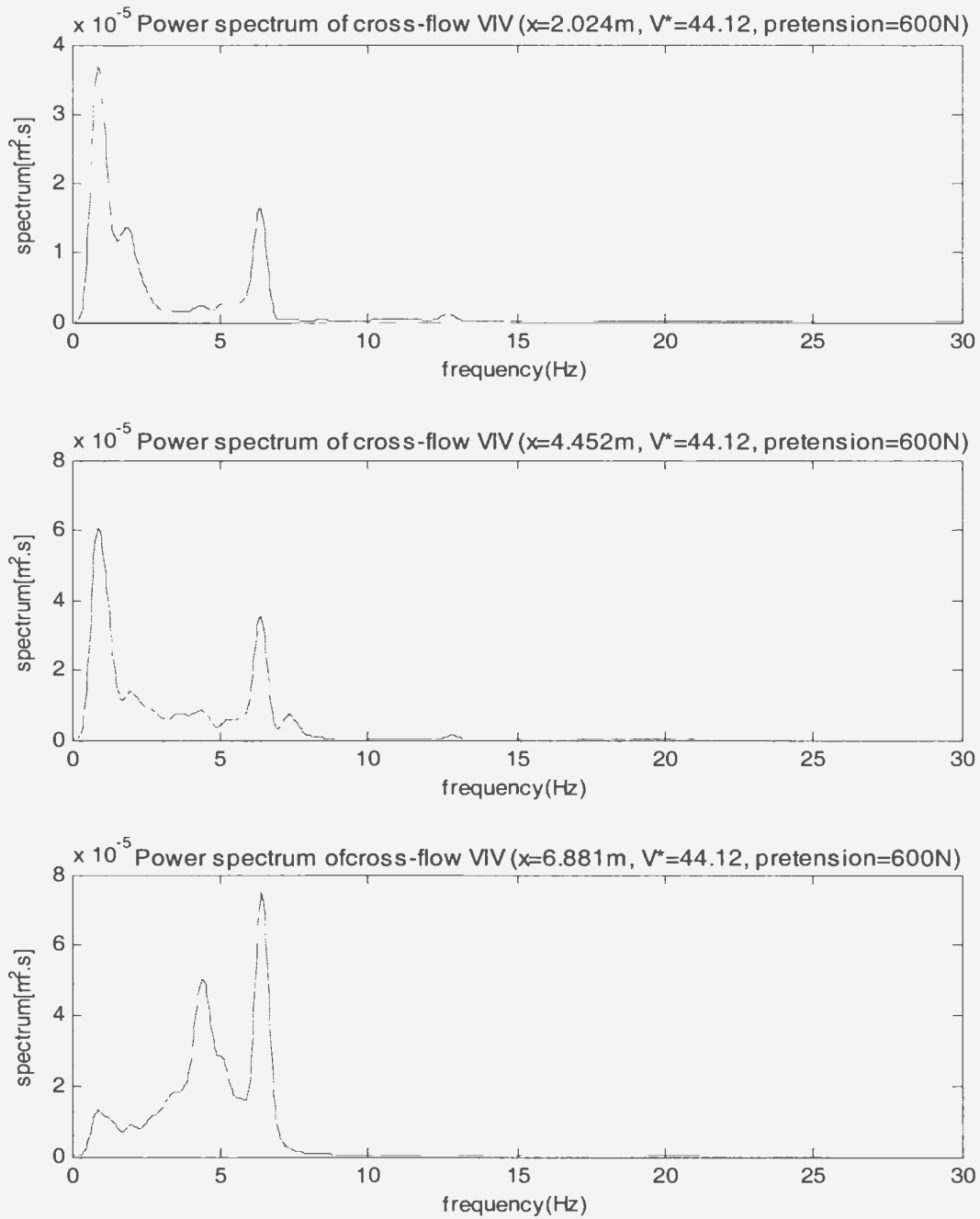


Figure 4-79 Power spectra of cross-flow VIV at different location on riser at a current velocity of 1.5m/s and a pretension of 600N

Summary of the results of vibration power spectra at the high pretension

As discussed above, the following points can be summarized:

- i) at the high pretension the patterns of power spectra in the in-line and cross-flow VIV responses are different over entire current velocity range tested.
- ii) in the low current velocity lock-in region (Region C), a strong dominant frequency and several secondary-dominant frequencies exist in the responses in the in-line direction, but these secondary-dominant frequencies have small energy to affect the cross-flow VIV responses.
- iii) in the low current velocity lock-in region (Region C), a strong dominant frequency and several secondary-dominant frequencies exist in the responses in the cross-flow direction. The energy of the lower dominant or secondary-dominant frequency becomes small and the energy of the higher dominant or secondary-dominant frequency becomes large as current velocities increase.
- iv) at high current velocities, many frequency components with small energy exist in the in-line and cross-flow VIV responses, and vibration energy is shared by a large number of frequency components.
- v) at low current velocities, the in-line responses have nearly identical power spectral patterns over the riser length, but the cross-flow responses have different power spectral patterns over the riser length.
- vi) at high current velocities both the in-line and cross-flow responses have different power spectral patterns over the riser length.

4. 2. 3. 3 Modal Components of VIV Response

The modal components of the VIV responses were analyzed based on equation (2-5) for the case of the high pretension. Figure 4-80 shows the modal components of the VIV responses at four reduced velocities of 13.23, 23.53, 32.34 and 44.12, which correspond to four current velocities of 0.55, 0.80, 1.15 and 1.50m/s. B^* is the non-dimensional modal VIV response, defined as $z_{k0}/2D$ for the cross-flow VIV responses, where: D is the riser diameter, and z_{k0} is the average peak-pick-up amplitudes of the modal response components $z_k(t)$, defined by equation (2-5). The function $z(t,x)$ in equation (2-5) is the vibration displacements in the cross-flow directions, which were measured from the VIV tests. The non-dimensional modal VIV response B^* is also defined as $y_{k0}/2D$ for the in-line VIV responses, where: y_{k0} is the average peak-pick-up amplitudes of the modal response components $y_k(t)$ in the in-line direction.

As seen in Figure 4-80, at this high pretension the VIV responses contain all modal components from mode 1 to 10, but the higher modes, such as mode 9 and 10, have less contribution to the responses than the lower modes, such as mode 1 and 2 at all reduced velocities. For both the in-line and cross-flow VIV responses, a dominant mode exists in the VIV responses at the lower currents, while the dominant mode becomes unclear at the higher currents. For example, for the in-line responses, at the lower reduced velocity of 13.23, mode 2 and 3 are respectively the dominant modes, while at the highest reduced velocity of 44.12, the dominant mode becomes unclear, as five modes, i.e. mode 1, 2, 3, 4 and 5, have relatively big contributions to the VIV responses. Similarly, for the cross-flow VIV responses, at the reduced velocities of 13.23, the dominant mode is mode 1, while at the reduced velocities of 32.34 and 44.12, the dominant mode become unclear.

It is noted that the increased pretension does not change the fundamental characteristics of the VIV responses. For example, the in-line and cross-flow VIV responses still contain all of the modal components from the first mode to the tenth mode; the increased current velocities cause increased dominant mode numbers; and the number of dominant modes for the in-line VIV responses are different from the number of dominant modes for the cross-flow VIV responses.

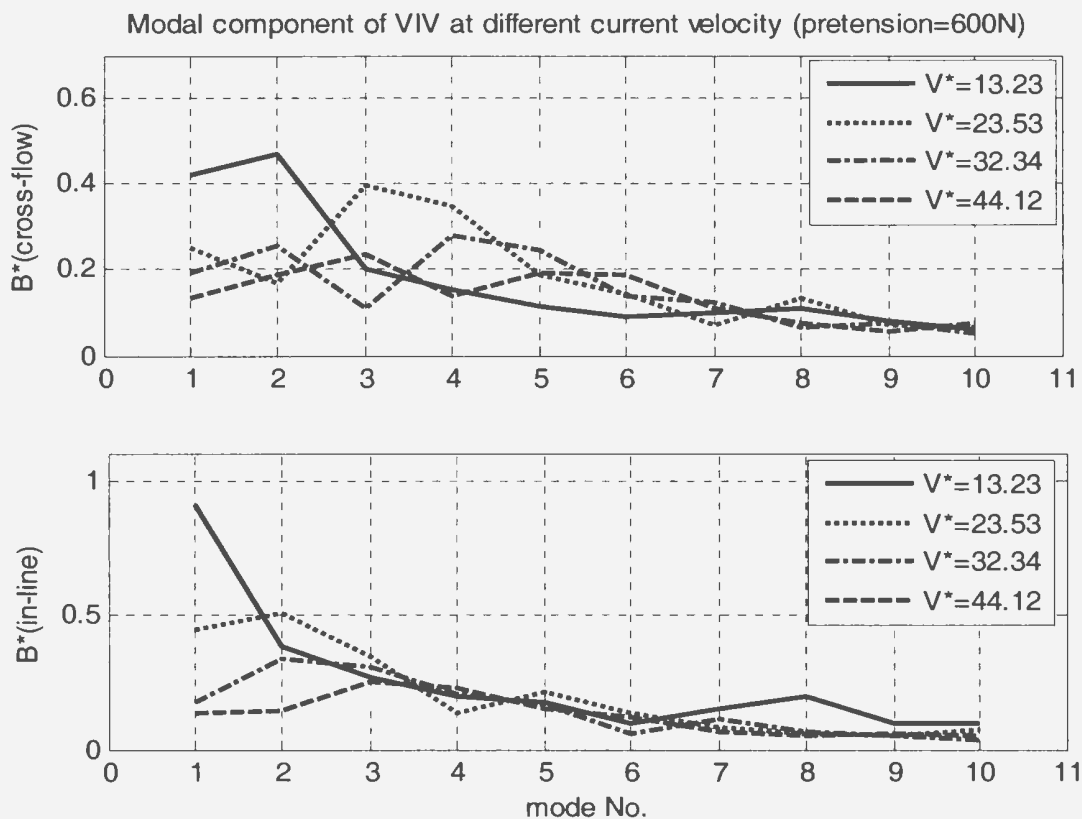


Figure 4-80 Modal component distributions of the in-line VIV and cross-flow VIV at a pretension of 600N

Figures 4-81 to 4-89 show the modal components in the in-line and cross-flow responses versus current velocity from mode 1 to mode 9. Figure 4-81 gives the in-line and cross-flow modal responses for mode 1. As seen in Figure 4-81, the relatively large modal responses in both of the in-line and cross-flow directions occur in the region from

$V^*=6$ to 14, which corresponds to the low current velocity lock-in region (Region C), and the modal responses in the in-line direction are larger than those in the cross-flow direction. The results of the modal analysis again clarify that in this region there is a resonance for mode 1 in both the in-line and cross-flow directions. In the region from $V^*=28$ to 44, the modal responses for mode 1 in both the in-line and cross-flow directions are small, and this means that the vortex-shedding frequencies are far away from the natural frequencies of mode 1. In the region from $V^*=14$ to 28, the cross-flow responses of mode 1 also have small values, but the in-line responses of mode 1 have moderate values compared to the responses in other regions. This means that the vortex-shedding frequencies in the in-line direction may be smaller than the vortex-shedding frequencies in the cross-flow direction, so that the vortex-shedding frequencies in the cross-flow direction are closer to the natural frequencies of mode 2 than the vortex-shedding frequencies in the cross-flow direction.

Figure 4-82 presents the modal responses in the in-line and cross-flow directions for mode 2. As seen in Figure 4-82, the relatively big modal response region for mode 2 in the cross-flow direction is still the region from $V^*=6$ to 14. This implies that in this region the cross-flow responses contain two dominant modes, i.e. mode 1 and mode 2, as both the modal responses for mode 1 and 2 are relatively large in this region. The relatively big in-line modal responses for mode 2 appear in the region from $V^*=14$ to 28. As the in-line modal responses for mode 1 also have the relatively large values in this region, the in-line responses may contain a dominant mode, i.e. mode 2, and a secondary-dominant mode, namely mode 1.

Figure 4-83 shows the modal responses in the in-line and cross-flow directions for mode 3. As seen in Figure 4-83, the relatively big modal responses for mode 3 in the cross-flow direction move to the region from $V^*=14$ to 28, while the relatively big modal responses in the in-line direction move to the region from $V^*=22$ to 35. Obviously, the higher mode resonates at the higher current velocities.

Figure 4-84 shows the modal responses in the in-line and cross-flow directions for mode 4. As seen in Figure 4-84, the relatively big modal response in cross-flow direction still appear in the region from $V^*=22$ to 35, where the cross-flow responses for mode 3 also have relatively large values, and this means that in this region the cross-flow responses have two dominant modes, namely mode 3 and 4. The relatively big in-line response for mode 4 exist in the region from $V^*=35$ to 40. The resonance for mode 4 obviously occurs at the higher currents compared to the resonance for mode 3.

Figures 4-85 to 4-89 show the modal responses in the in-line and cross-flow directions for modes 5 to 9. As seen in these figures, the modal responses over the whole current velocity range have relatively small values, and this means that the vortex-shedding frequencies in both the in-line and cross-flow directions are far away from the natural frequencies of these modes.

Based on the discussions above, the following points can be extracted:

- i) The VIV responses contain all modes from 1 to 10, but the higher modes have less contribution to the responses than the lower modes;
- ii) one or two dominant modes exist in the VIV responses at lower currents, while the dominant mode becomes unclear at higher currents;
- iii) High modes resonate in higher currents than low modes.

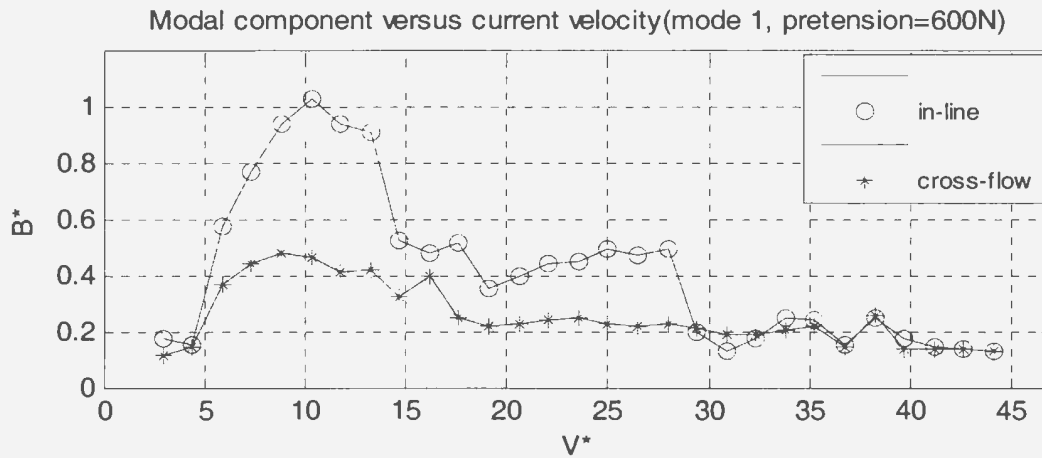


Figure 4-81 The component of mode 1 in VIV responses at a pretension of 600N

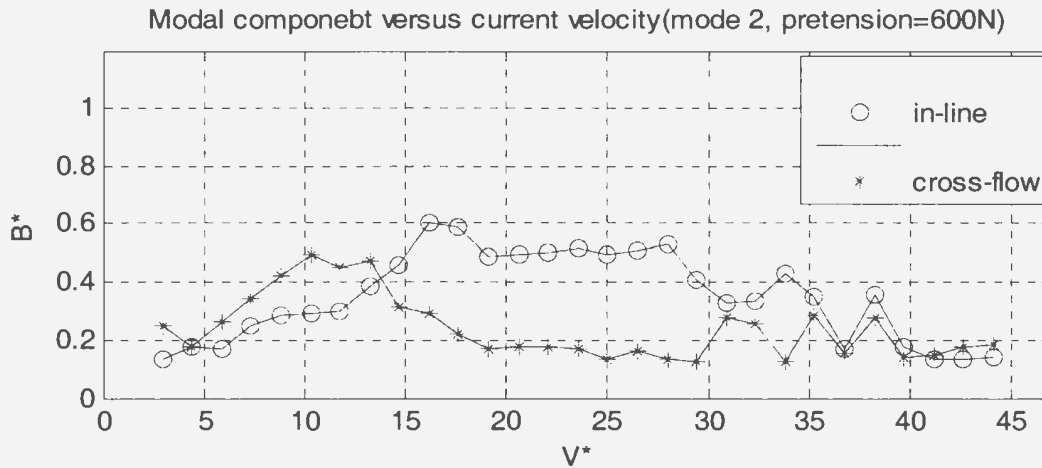


Figure 4-82 The component of mode 2 in VIV responses at a pretension of 600N

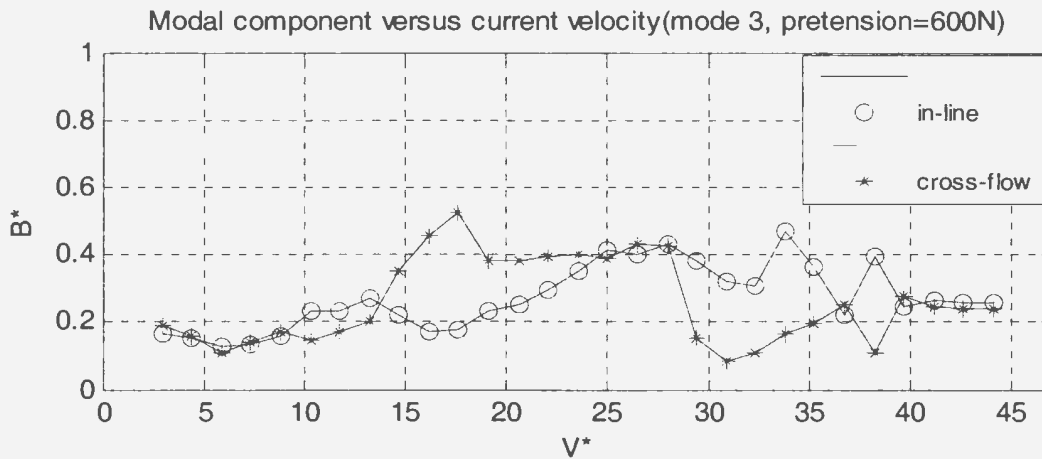


Figure 4-83 The component of mode 3 in VIV responses at a pretension of 600N

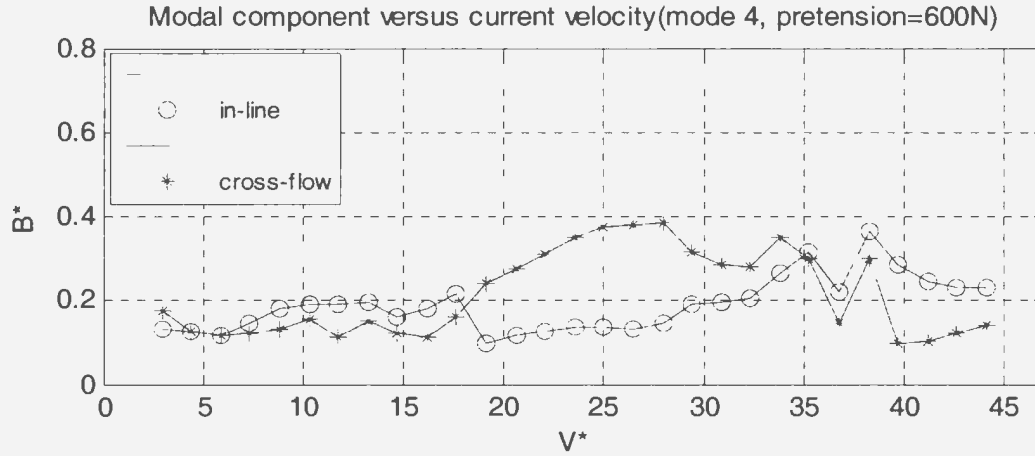


Figure 4-84 The component of mode 4 in VIV responses at a pretension of 600N

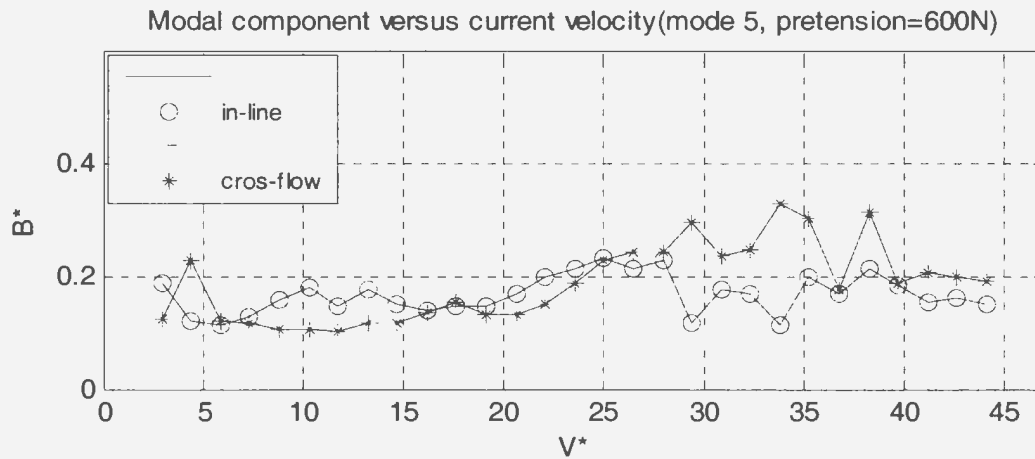


Figure 4-85 The component of mode 5 in VIV responses at a pretension of 600N

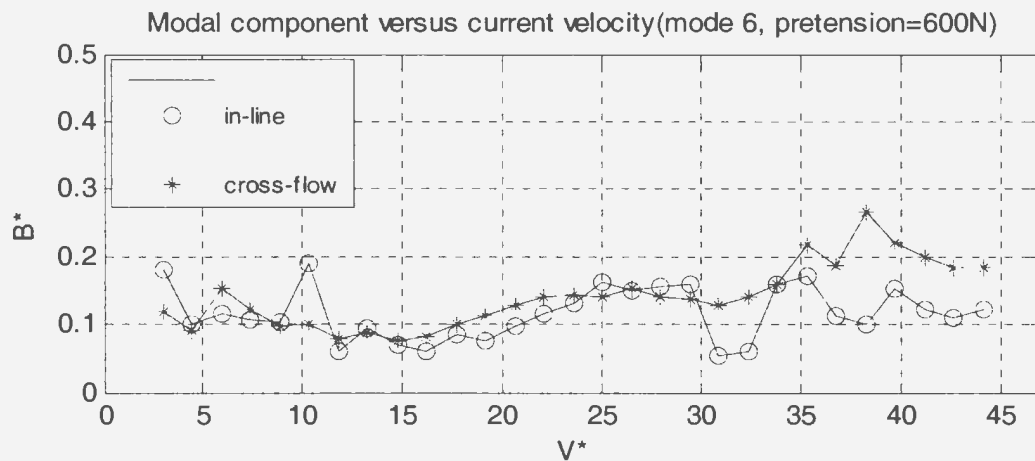


Figure 4-86 The component of mode 6 in VIV responses at a pretension of 600N

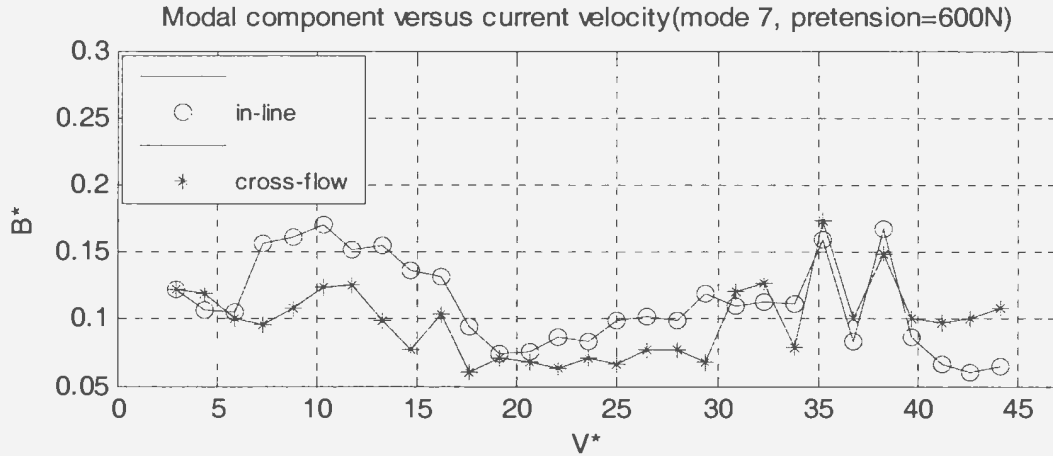


Figure 4-87 The component of mode 7 in VIV responses at a pretension of 600N

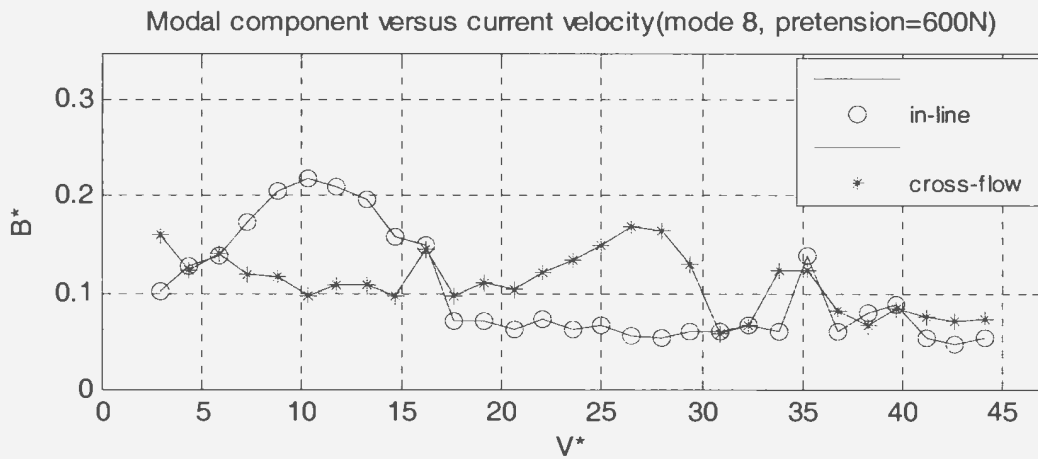


Figure 4-88 The component of mode 8 in VIV responses at a pretension of 600N

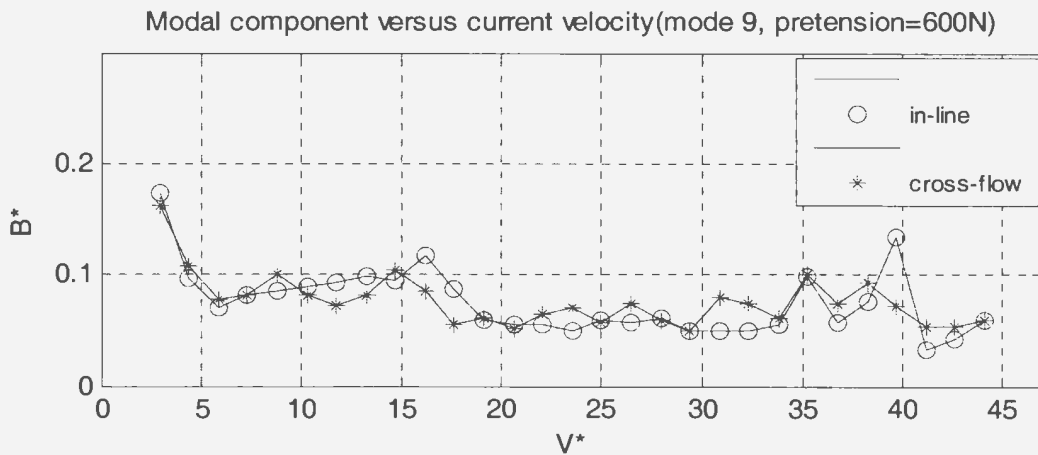


Figure 4-89 The component of mode 9 in VIV responses at a pretension of 600N

4. 2. 3. 4 Vibration Time Histories

Similarly in the case of pretension=200N, the time histories of VIV displacement were obtained by double-integration of the acceleration data. Figures 4-90 to 4-94 present the time histories of the in-line VIV responses at five reduced velocities of 11.76, 17.65, 23.53, 35.29 and 44.12, which correspond to five current velocities of 0.4, 0.6, 0.8, 1.2 and 1.5m/s. These time histories were measured at the location of $x=4.452\text{m}$.

As seen in these figures, the patterns of the time history of the in-line VIV response depend on the current velocities. At the lower reduced velocities of 11.76, 17.65 and 23.53, the patterns of the time history are the SF type, which contain a dominant frequency, while at the higher reduced velocities of 35.29 and 44.12, the patterns are the MF type, which contain more than two dominant frequencies.

Compared to the patterns of the time history of the in-line VIV responses at the lower pretension of 200N, it can be seen that at some current velocities the higher pretension causes the patterns to contain less frequency components. For example, at the current velocity of 0.8m/s, the pattern of the time history of the in-line VIV at the pretension of 600N is the SF type, while the pattern of the time history of the in-line VIV at the pretension of 200N is the MF.

Figure 4-95 to 4-98 show the time histories of the cross-flow VIV responses at four reduced velocities of 17.65, 23.53, 35.29 and 44.12, which were measured at the location of $x=4.452\text{m}$.

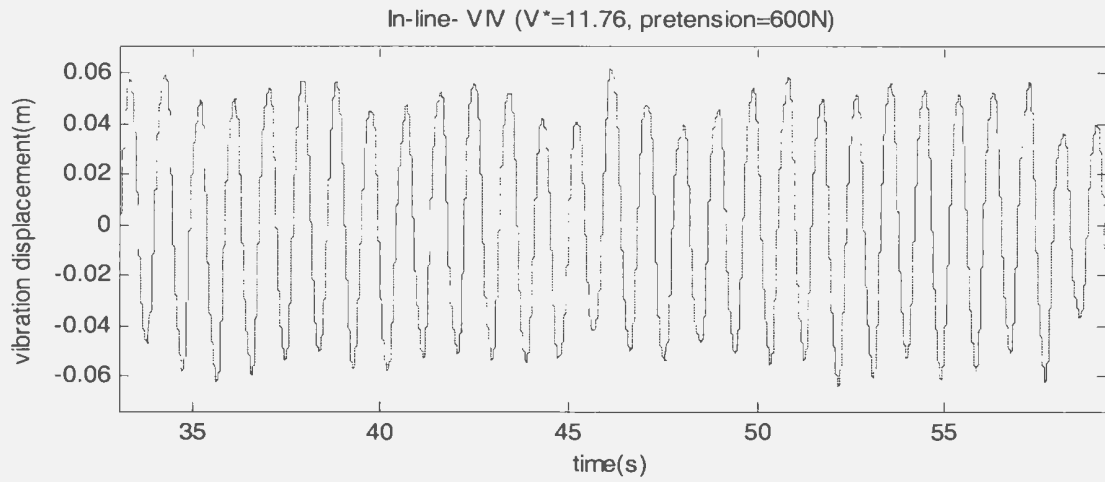


Figure 4-90 Time history of in-line VIV at a current velocity of 0.4m/s and a pretension of 600N

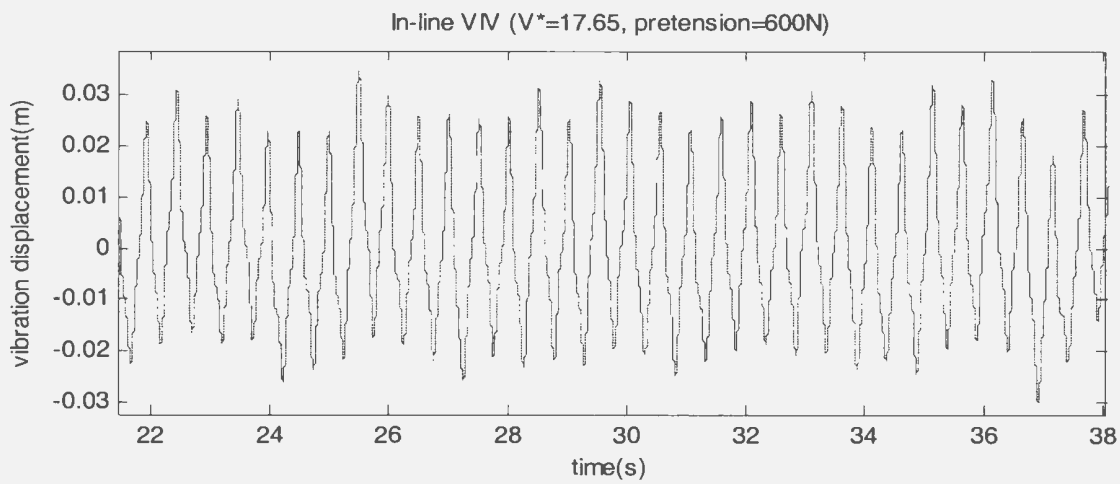


Figure 4-91 Time history of in-line VIV at a current velocity of 0.6m/s and a pretension of 600N

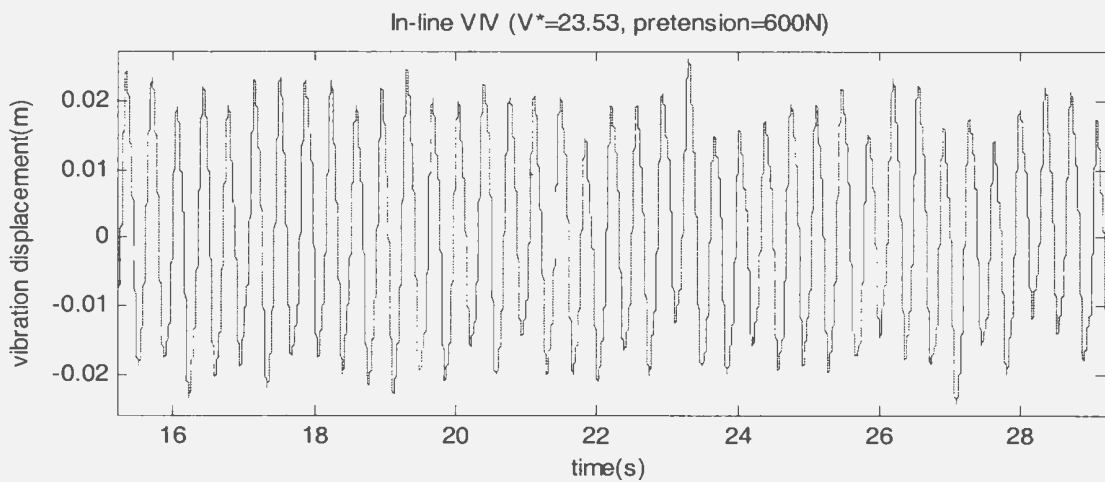


Figure 4-92 Time history of in-line VIV at a current velocity of 0.8m/s and a pretension of 600N

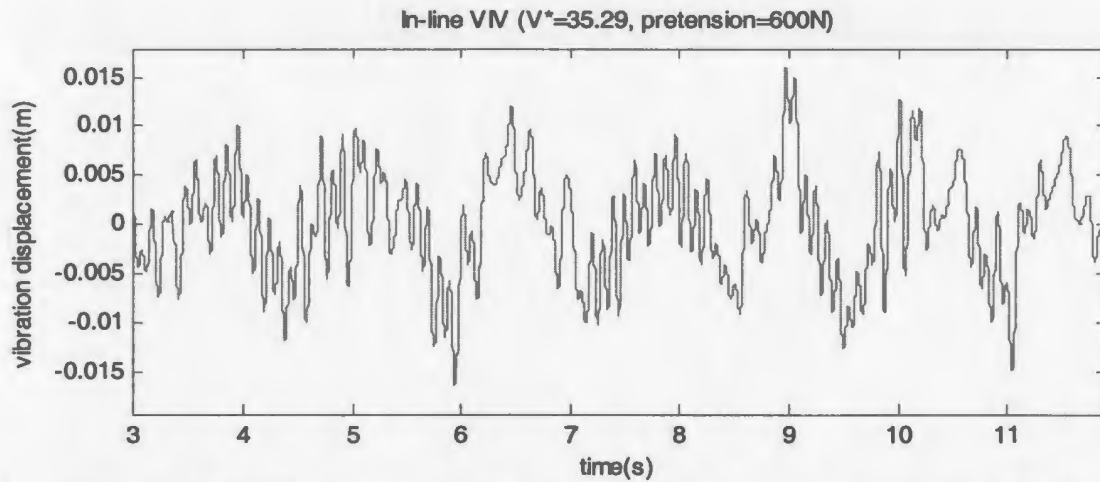


Figure 4-93 Time history of in-line VIV at a current velocity of 1.2m/s and a pretension of 600N

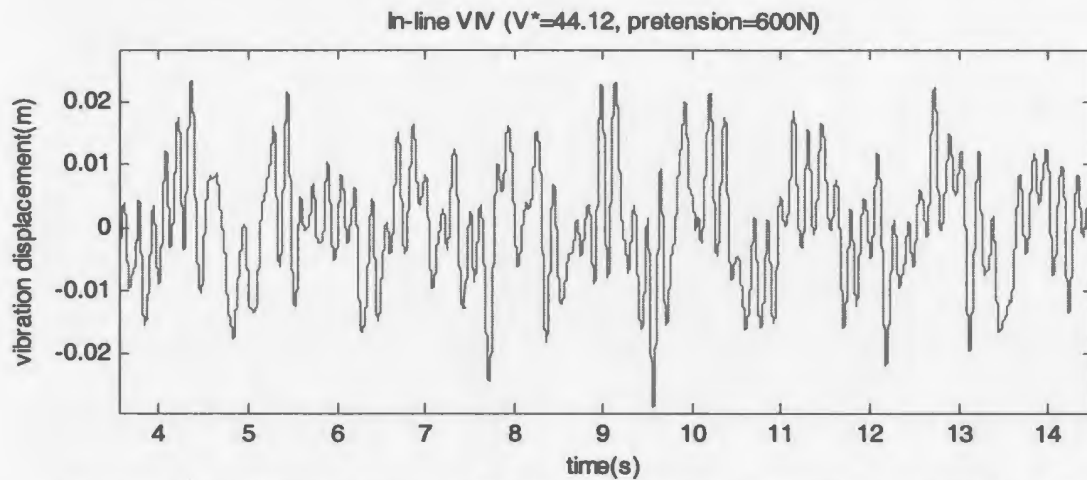


Figure 4-94 Time history of in-line VIV at a current velocity of 1.5m/s and a pretension of 600N

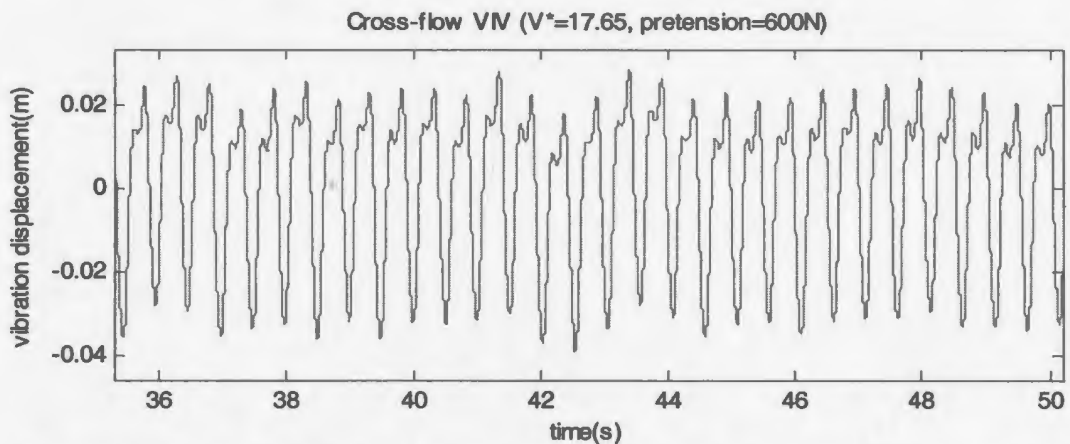


Figure 4-95 Time history of cross-flow VIV at a current velocity of 0.6m/s and a pretension of 600N

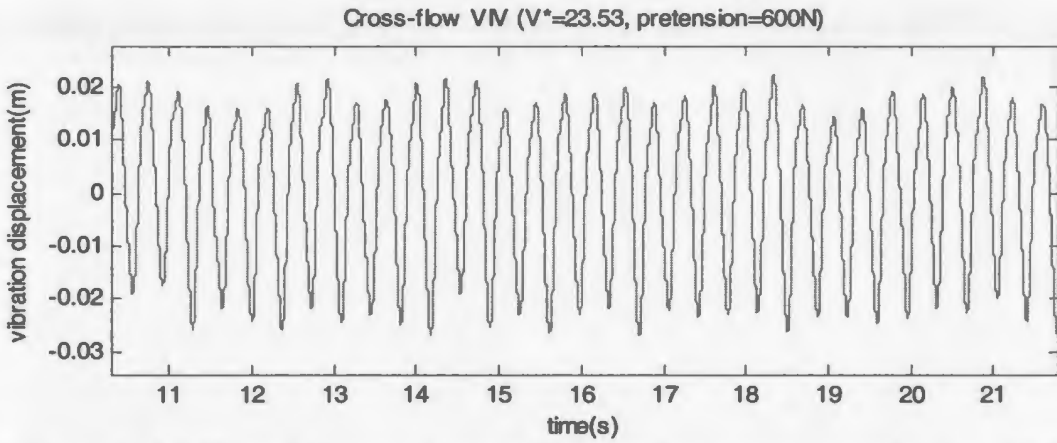


Figure 4-96 Time history of cross-flow VIV at a current velocity of 0.8m/s and a pretension of 600N

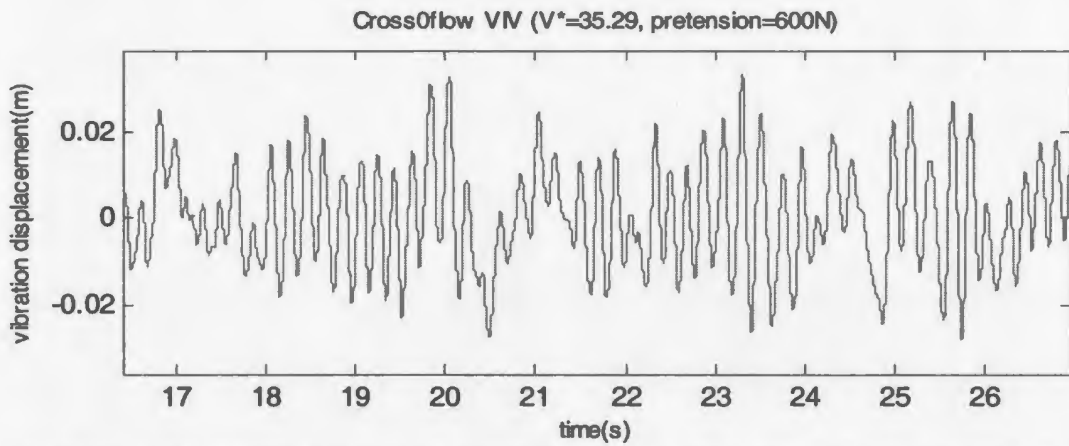


Figure 4-97 Time history of cross-flow VIV at a current velocity of 1.2m/s and a pretension of 600N

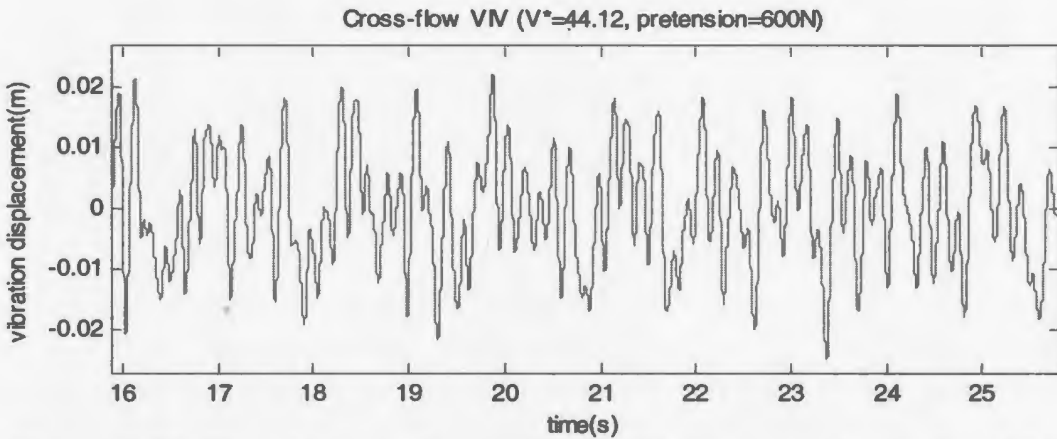


Figure 4-98 Time history of cross-flow VIV at a current velocity of 1.5m/s and a pretension of 600N

Similarly in the case of in-line VIV responses at the pretension of 600N, the patterns of time history of cross-flow VIV response depend on current velocities. At the low reduced velocities, such as 17.65 and 23.53, the patterns of the time history are the SF type, containing a dominant frequency, while at the high reduced velocities, such as 35.29 and 44.12, the patterns of the time history are the MF type, containing more than two dominant frequencies. The higher pretension also causes the patterns of time history of in-line VIV responses to contain less frequency components than those in the case of a lower pretension.

Now check the time histories of the VIV responses at different locations on the riser. Chose three locations of $x=2.024$, 4.452 and 6.881m and two reduced velocities of 11.76 and 35.29.

Figure 4-99 presents the time histories of the in-line VIV response at the three locations. As seen in Figure 4-99, at the reduced velocity of 11.76, the patterns of time history at the three locations are all the SF types. It is noted that at this high pretension the patterns of the time history does not change over the riser length, but the amplitude variations become large at the locations of $x=2.04$ m and $x=6.881$ m.

Figure 4-100 shows the time histories of the cross-flow VIV responses at the three locations at the reduced velocity is 11.76. As seen in Figure 4-100, at this reduced velocity, the patterns of the time history at the three locations are all the MF types.

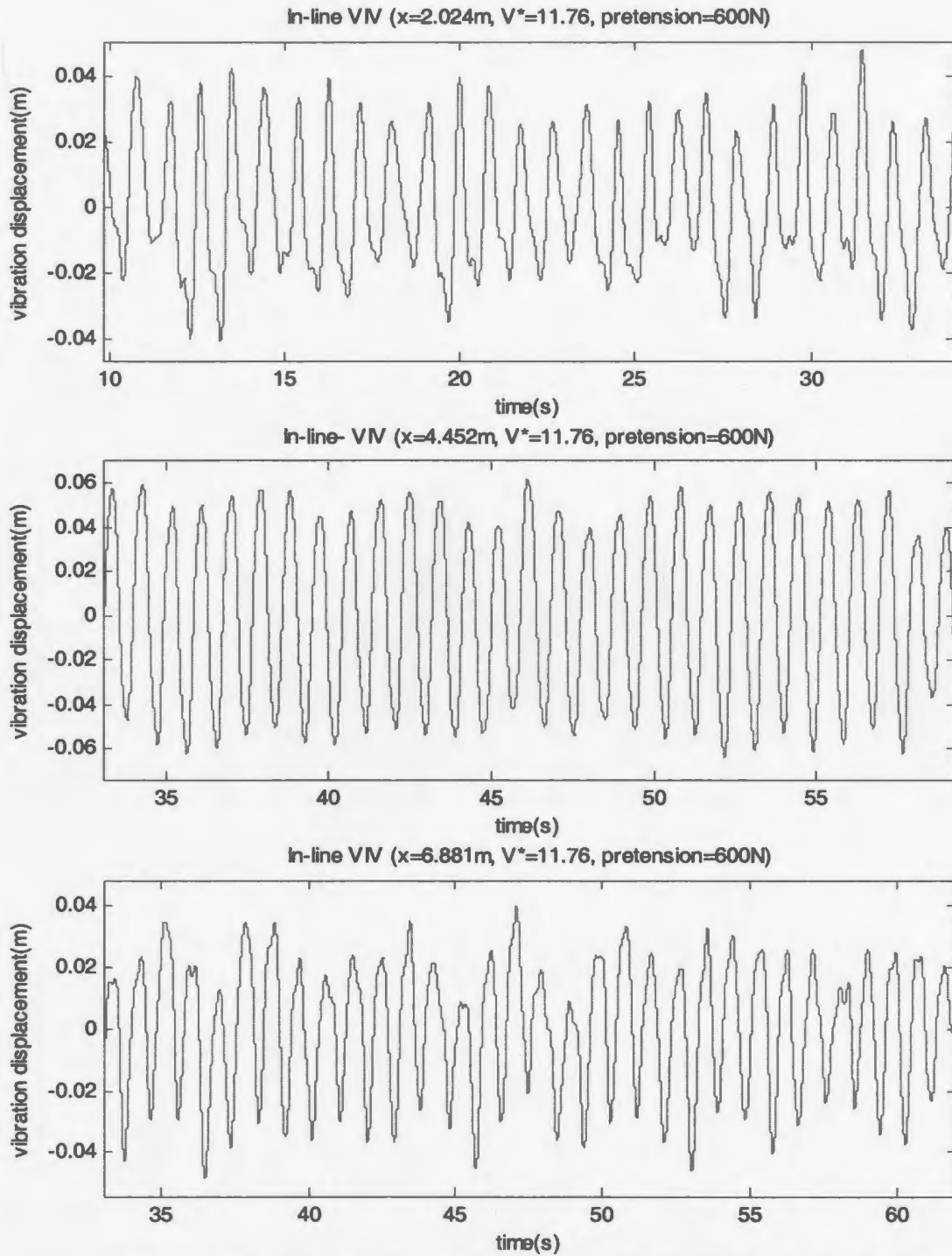


Figure 4-99 Time history of in-line VIV at different locations at a current velocity of 0.4m/s and a pretension of 600N

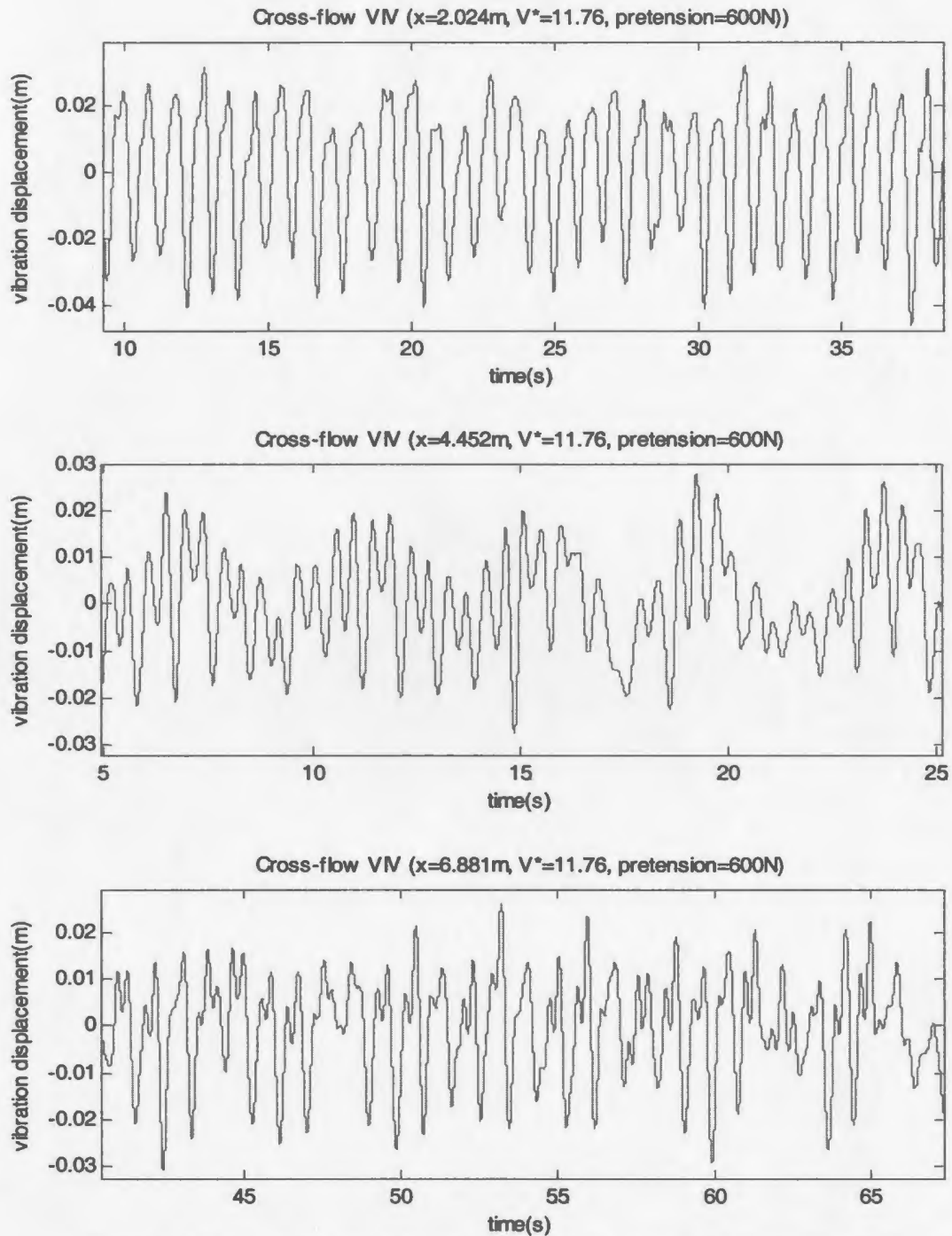


Figure 4-100 Time history of cross-flow VIV at different locations at a current velocity of 0.4m/s and a pretension of 600N

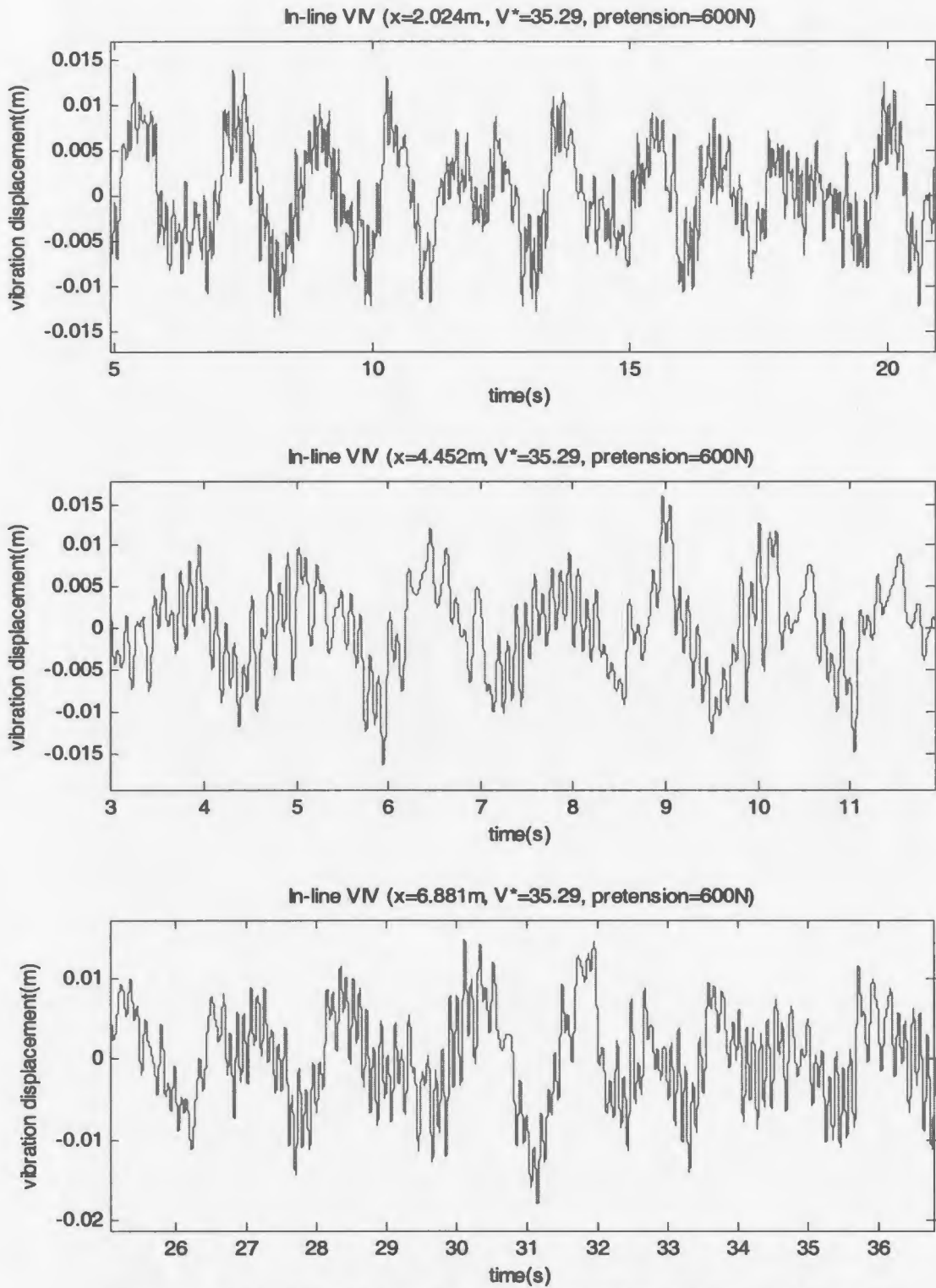


Figure 4-101 Time history of in-line VIV at different locations at a current velocity of 1.2m/s and a pretension of 600N

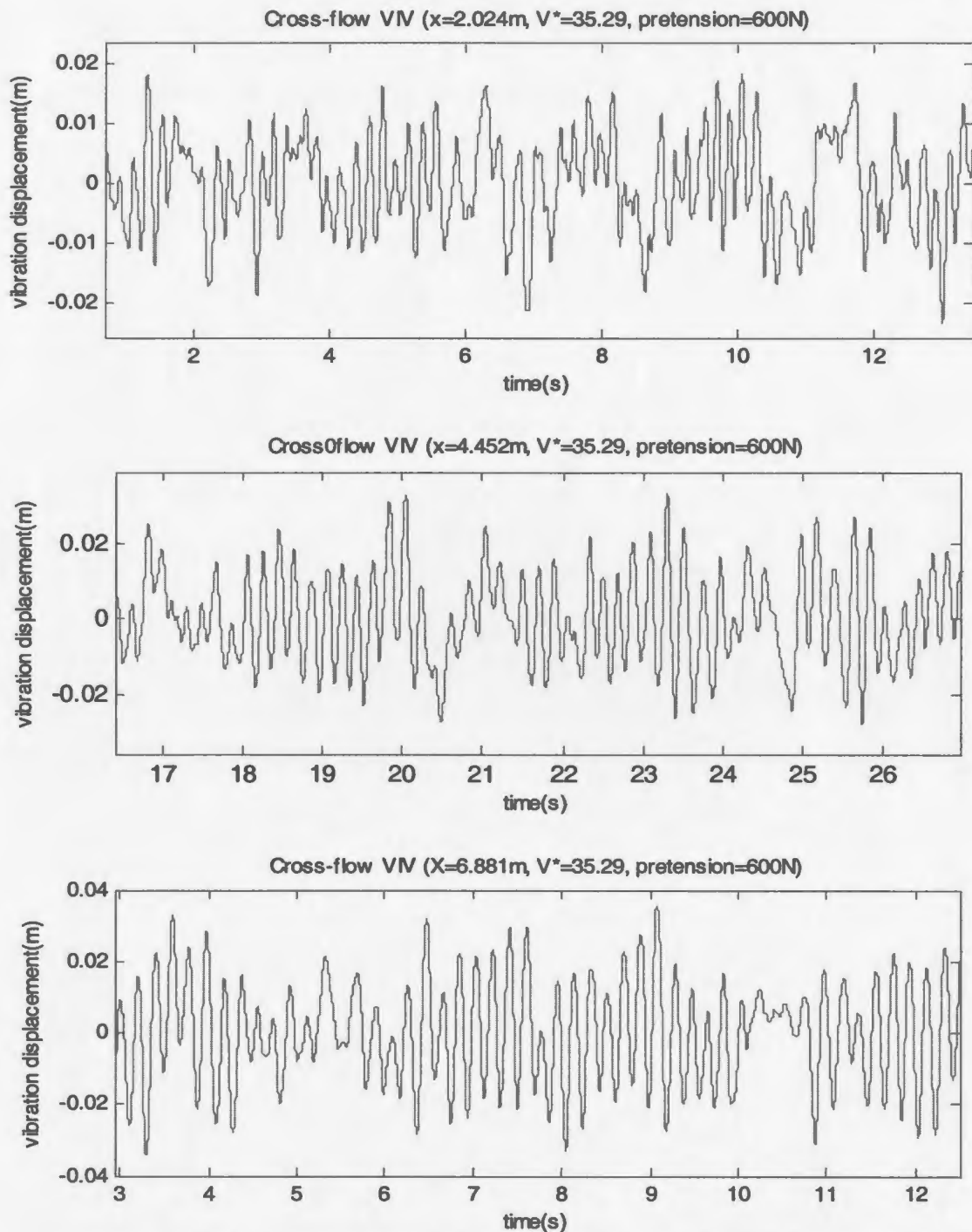


Figure 4-102 Time history of cross-flow VIV at different locations at a current velocity of 1.2m/s and a pretension of 600N

Figure 4-101 gives the time histories of the in-line VIV response at the three locations at the reduced velocity is 35.29. As seen in Figure 4-101, at this reduced velocity, the vibration patterns at the three locations are different. At the locations of $x=2.024$ and 6.881m , the patterns of the time history are close to a SF type, although the amplitudes exhibit a relatively large variation. At the location of $x=4.452\text{m}$, the pattern of the time history is close to a MF type. It is noted that the increased pretension complicates the patterns of the time history of the cross-flow VIV responses while simplifies the patterns of the time history of the in-line VIV responses.

Figure 4-102 presents the time histories of the cross-flow VIV responses at the three locations at the reduced velocity is 35.29. It is seen that the vibration patterns at the three locations are all the FD types.

4. 2. 3. 5 Vibration Shapes

Similarly in the case of the lower pretension of 200N, the vibration shape was obtained through the combination of the VIV displacements at sixteen locations on the riser at the a time instant, and then a snapshot was obtained through plotting several vibration shapes on a picture. Figures 4-103 to 4-107 present the snapshots of the in-line VIV and cross-flow VIV at five reduced velocities of 5.88, 17.65, 23.53, 29.41 and 35.29, which correspond to five current velocities of 0.2, 0.6, 0.8, 1.0 and 1.2m/s. As the displacements at the locations from $x=5.27$ to 6.47m on the riser were not measured, the vibration shapes may be skewed at those locations.

As seen in these figures, both the vibration shapes of the in-line VIV and the cross-flow VIV over the riser length are a mixture of several modal components, meaning that the

VIV responses at the high pretension are also the multi-modal vibrations. The vibration shapes over the riser length are also asymmetrical about the mid-point of the riser and contained the components of even modes, although the riser structure and the current profile were uniform over the riser length. The increased current gives rise to higher dominant modal components in the VIV responses. At the lower current velocities, the dominant modes are clearer than at the higher current velocities. For example, at the lower current velocity of 0.2m/s, mode 1 and mode 2 are clearly shown in the snapshot plots of the cross-flow and in-line VIV responses, as seen in Figure 4-103. At the higher current velocity of 1.0m/s, the dominant modes become vague, as seen in Figure 4-106. This means that there is more than one dominant mode in the VIV responses at the higher current velocities.

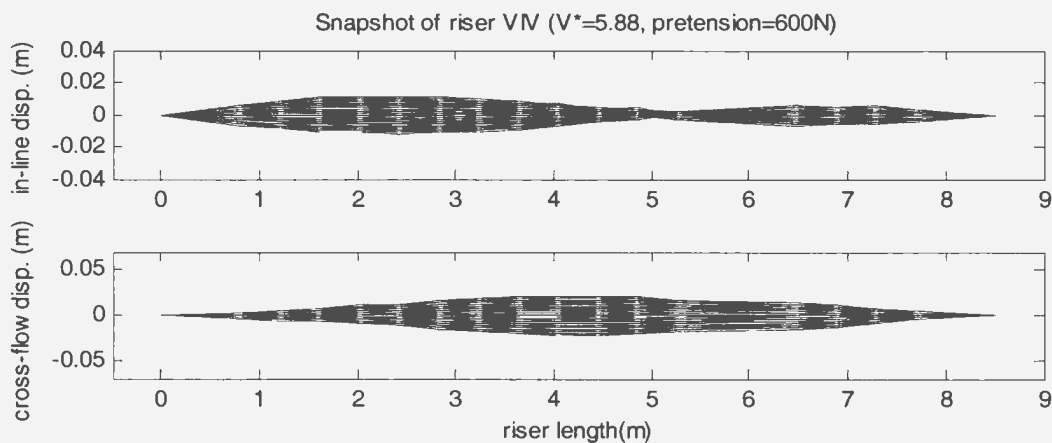


Figure 4-103 Vibration shapes at a current velocity of 0.2m/s and a pretension of 600N

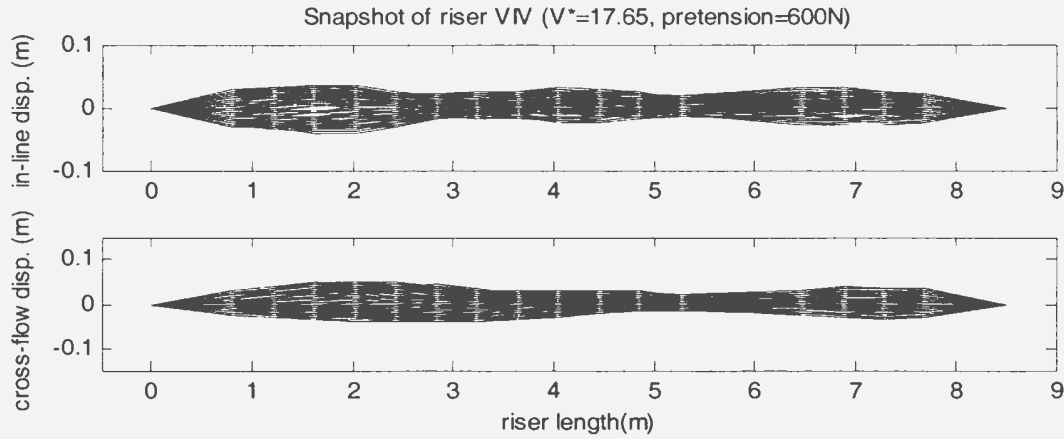


Figure 4-104 Vibration shapes at a current velocity of 0.6m/s and a pretension of 600N

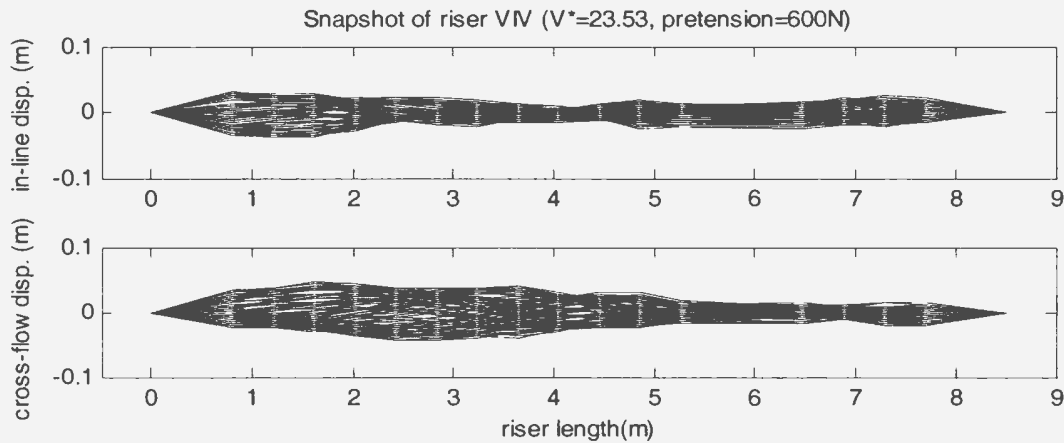


Figure 4-105 Vibration shapes at a current velocity of 0.8m/s and a pretension of 600N

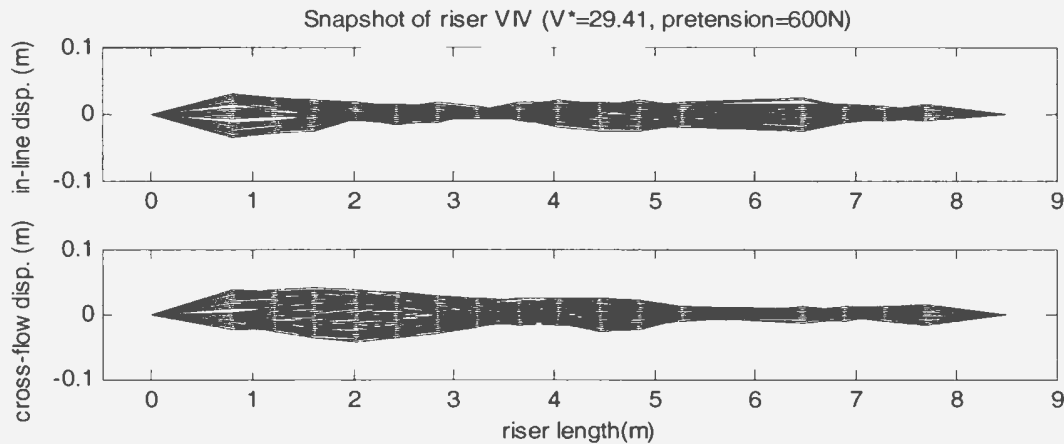


Figure 4-106 Vibration shapes at a current velocity of 1.0m/s and a pretension of 600N

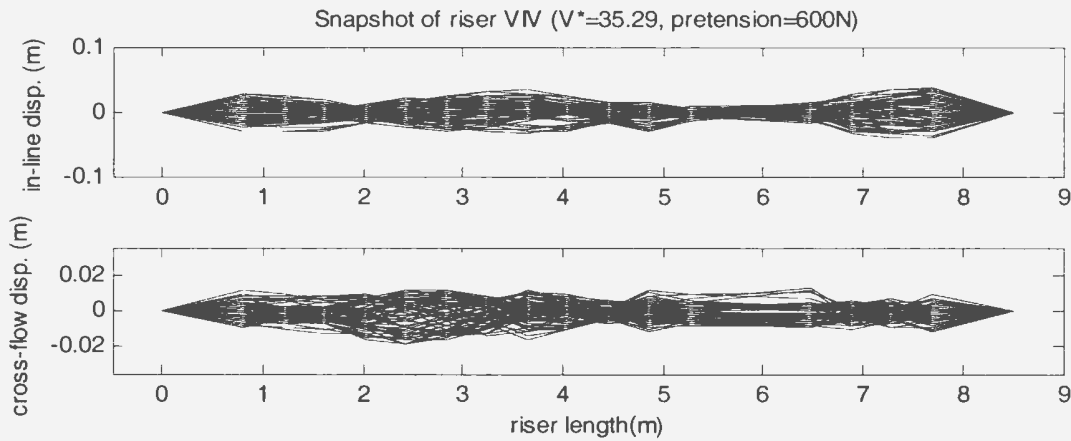


Figure 4-107 Vibration shapes at a current velocity of 1.2m/s and a pretension of 600N

It is noted that at this high pretension the vibration shapes in the in-line VIV responses exhibit higher dominant mode shape than in the cross-flow VIV responses. For example, as seen in Figure 4-103, at the current velocity of 0.2m/s, the dominant mode the in-line VIV responses is mode 2, while the dominant mode in the cross-flow VIV responses is mode 1. At the current velocity of 0.6m/s, the dominant mode in the in-line VIV responses is mode 3, while the dominant mode in the cross-flow VIV responses is mode 2.

4. 2. 3. 6 Vibration Trajectories

The combination of the VIV displacements in the in-line direction and the cross-flow direction at several time instants produces the vibration trajectory on a cross-section plane of the riser. Figure 4-108 to 4-112 show the VIV motion trajectories on the cross-section planes at four locations of $x=0.810, 3.624, 4.857$ and 6.881 m along the riser for five current velocities of 0.4, 0.6, 0.8 1.2 and 1.5m/s. In these figures, the y-direction is defined as the in-line direction and the z-direction as the cross-flow direction. These

trajectories are the records during about three or four cyclic periods and they are only the representatives of the VIV responses during the whole vibration period.

Similar to the results in the case of pretension=200N, the trajectories depend on current velocities and locations on the riser. Low current velocities always cause the basic figures of 8- or L-shaped vibration motion. For example, in Figure 4-108, at all of the locations the basic figures are the 8-shaped vibration motion. In Figure 4-109, at the locations of $x=0.810$, 4.857 and 6.881m the basic figures are 8-shaped vibration motion, while at the location of $x=3.624$ m the basic figure is L-shaped vibration motions. In Figure 4-110, at the locations of $x=0.810$ and 3.624m the basic figures are 8-shaped vibration motion, while at the location of $x=4.857$ and 6.881m the basic figures are L-shaped vibration motions. High current velocities may cause the basic figures of O-shaped or other complicated vibration motion. For example, in Figure 4-111, at the location of $x=0.810$ m, there is a basic figure of O-shaped vibration motion. In Figure 4-112 other complicated figures exist. Usually, if a vibration exhibits a clear dominant mode, its trajectory shows the 8-shaped or L-shaped basic figures, while if the vibration contains more than one dominant mode, the trajectory may contain other complicated basic figures. Similar to the results in the case of pretension=200N, the shifted motions of the basic figure occur not only in the in-line direction but also in the cross-flow direction.

Vortex-Induced Vibration Tests

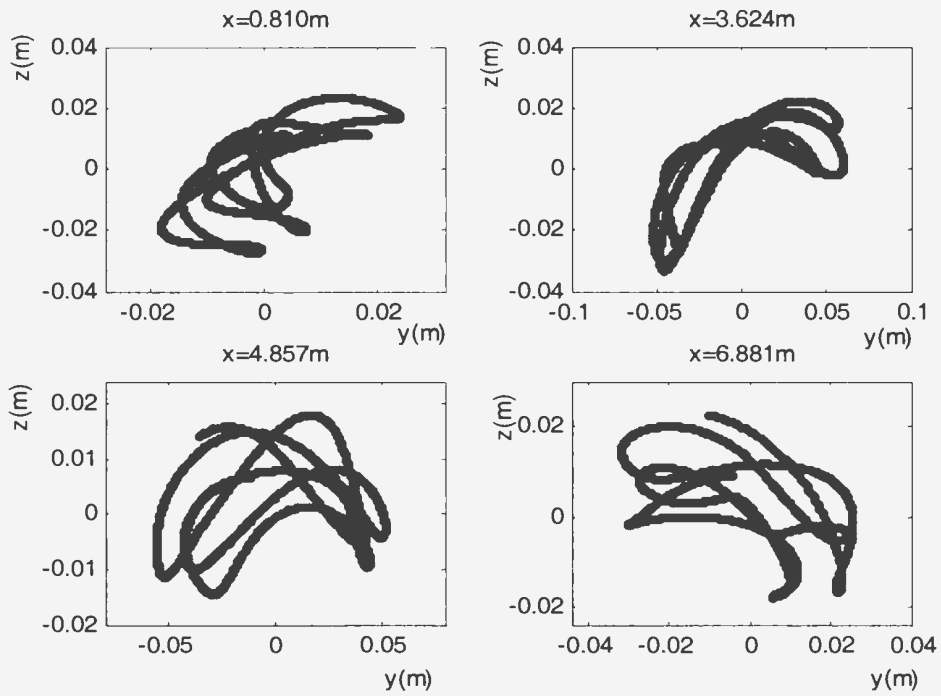


Figure 4-108 Trajectory of VIV at a current velocity of 0.4m/s and a pretension of 600N

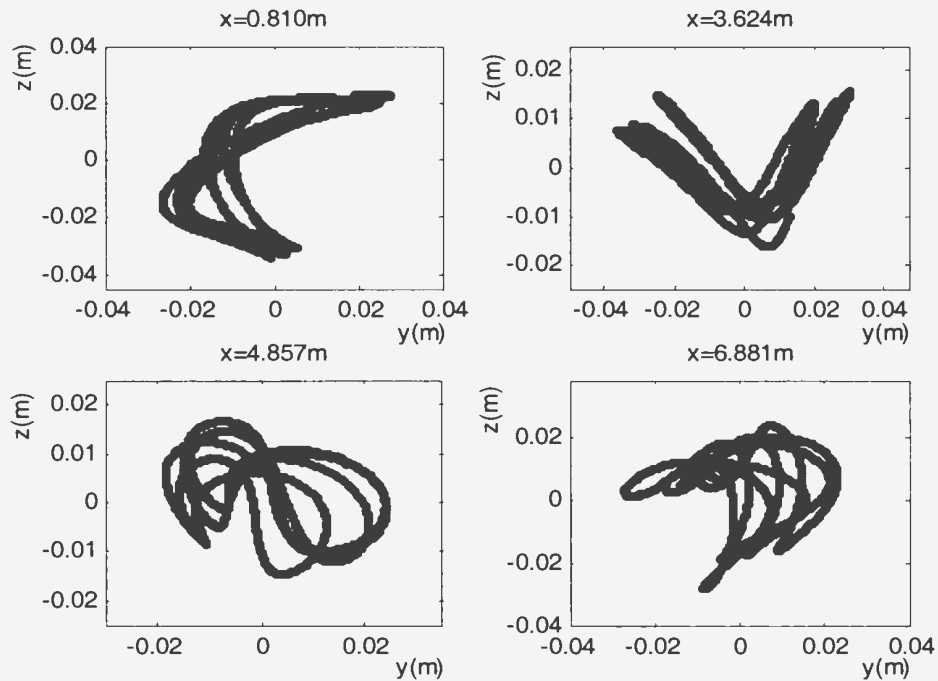


Figure 4-109 Trajectory of VIV at a current velocity of 0.6m/s and a pretension of 600N

Vortex-Induced Vibration Tests

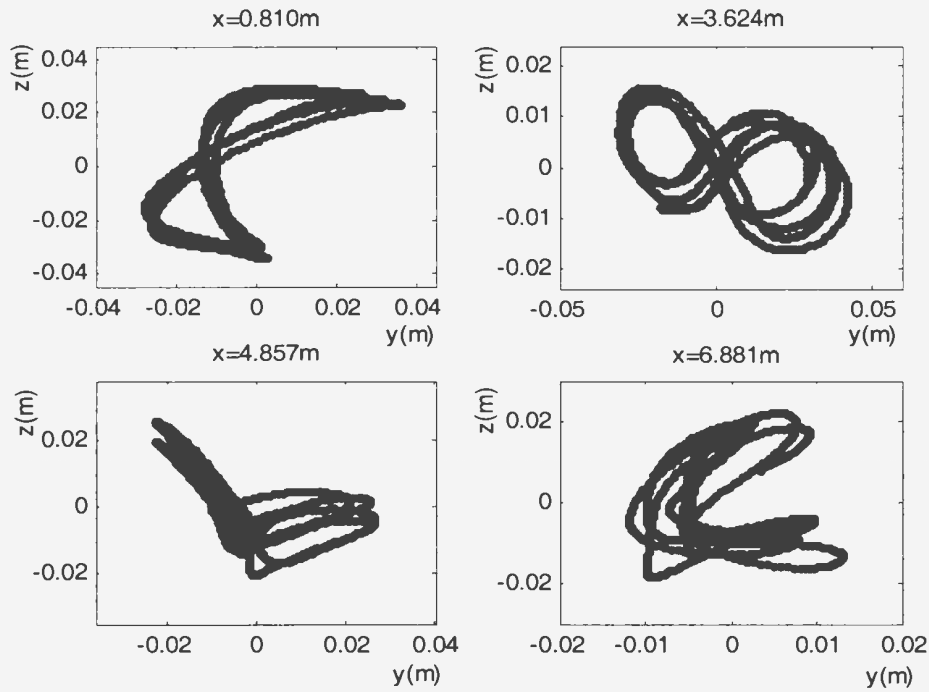


Figure 4-110 Trajectory of VIV at a current velocity of 0.8m/s and a pretension of 600N

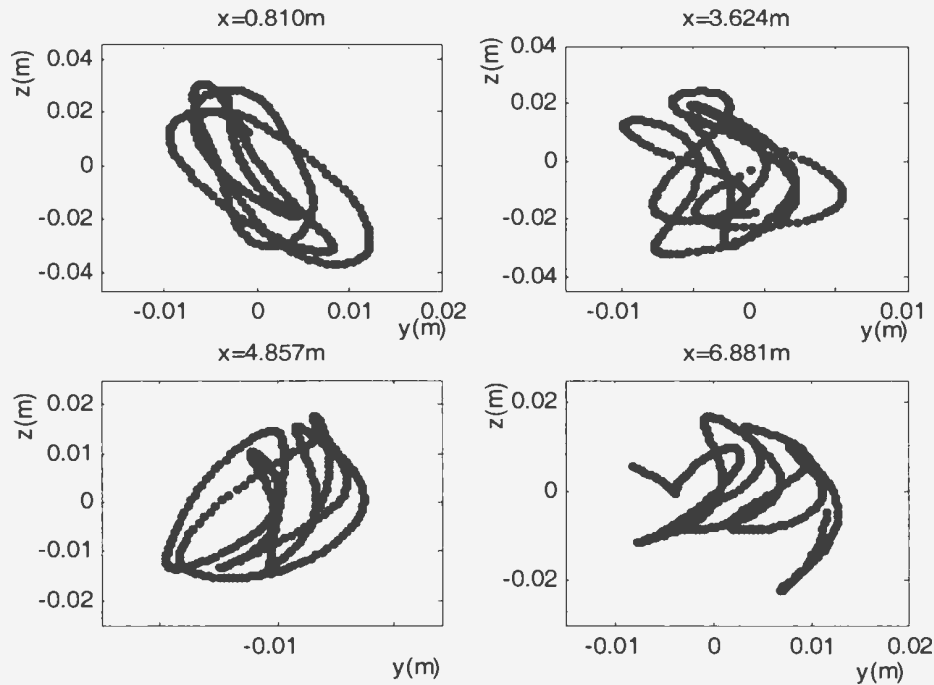


Figure 4-111 Trajectory of VIV at a current velocity of 1.2m/s and a pretension of 600N

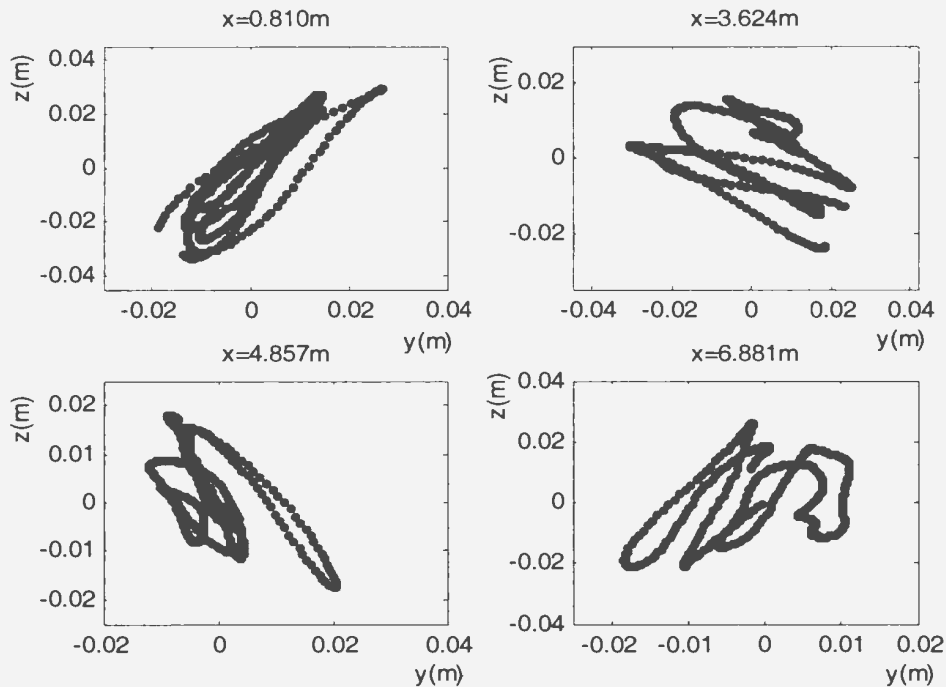


Figure 4-112 Trajectory of VIV at a current velocity of 1.5m/s and a pretension of 600N

4.3 Summary of VIV Test Results

The time histories of multi-modal VIV have four types, namely the single-dominant-frequency type (SF), the close-double-dominant-frequency type (CD), the far-double-dominant-frequency type (FD) and the multi-frequency type (MF). The SF and CD types often appear in the VIV responses at the current velocities lower than 0.8m/s, while the FD and MF types often appear in the VIV responses at the current velocities higher than 0.8m/s in the current velocity range tested.

The motion trajectories on the cross-section plane contain two fundamental motions. The first is a basic figure of 8-, L- and O-shaped or other complicated vibration motion. Another motion is a shifted motion of the basic figure motion. The basic figures of 8- and L-shaped correspond to the vibrations at lower current velocities with a strong single

dominant frequency, while other basic figures correspond to the vibrations at higher current velocities with multi-dominant frequencies.

The snapshots of the VIV responses over the riser length clearly demonstrate that the VIV responses for a flexible riser are the multi-modal vibrations. In the multi-modal vibrations, there are a dominant mode and several secondary-dominant modes. At lower current velocities, the vibration shapes over the riser length often exhibit a clear dominant mode with clear nodes, while at higher current velocities, the dominant modes become vague.

In the un-lock-in regions, the average peak-pick-up frequencies of the cross-flow multi-modal VIV follow the Strouhal frequency for the lower and higher pretensions, which correspond to a Strouhal number of about 0.12. When a current velocity at which a natural frequency matches the Strouhal frequency is not close to another current velocity at which the next natural frequency matches the Strouhal frequency, a frequency lock-in will occur at the first current velocity. The lock-in frequency in the cross-flow direction is approximately equal to the first natural frequency, and the vibration amplitudes are relatively large in the lock-in region. The lock-in frequency in the in-line direction is approximately equal to either the first natural frequency or the next natural frequency depending on which natural frequency the in-line vortex-shedding frequency is close to. If the in-line responses lock in the first natural frequency, the vibration amplitudes will be relatively big. Otherwise, the vibration amplitudes are relatively small. The reduced velocity corresponding to the end points of the lock-in region are smaller than the maximum upper limit values estimated from equation (4-1) provided by previous studies (Govardhan and Williamson, 2000).

The average peak-pick-up amplitude versus current velocity shows that the vibration amplitudes fluctuates from 0.3 to $0.9D$, and no increasing trend exists as the current velocity increases. No sharp peaks exist in the average peak-pick-up amplitude versus current velocity. The average peak-pick-up amplitudes are not sensitive to the pretensions tested.

The results from the spectral analysis verify that there are three types of VIV responses can be found: i) the vibrations with single dominant frequency; ii) the vibrations with double dominant frequencies; and iii) the vibrations with multi-dominant frequencies. In the third type, the power spectra have broad bandwidth, which usually appear at the high current velocities. The power spectra may vary over riser length or not, depending on the current velocities and the pretensions. At high currents, there is more than one dominant or secondary-dominant frequency in the VIV responses in the frequency lock-in regions, and the lock-in frequency does not match any of these dominant or secondary-dominant frequencies.

The in-line and cross-flow VIVs for a flexible riser contain a number of modal components. The higher modes have less contribution to the responses than the lower modes. A dominant mode exists in the VIV responses at lower currents, while the dominant mode becomes unclear at higher currents. The dominant modes for the in-line and cross-flow VIV responses are usually different.

CHAPTER 5

CORRELATION BETWEEN MODAL PARAMETER AND VIV RESPONSE

5. Correlation between Modal Parameter and VIV Response

This section discusses the correlation between the estimated modal parameters and the VIV responses. In this research, the modal parameters were estimated by the shaker-excitation tests, which were conducted in calm water. Strictly, VIV responses depend on the modal parameters in currents, not on the modal parameters in calm water, because currents can change the hydrodynamic loads on the riser, so that the added mass and damping in currents are different from those in calm water. Vandiver (1993) reviewed two experimental results about the effective added mass coefficient versus reduced velocity, which were respectively conducted by Sarpkaya (1977) and Chung (1989). They found that the measured effective added mass coefficients decreased as the reduced

Correlation between Modal Parameter and VIV Response

velocities increased. At high reduced velocities, the effective added mass coefficients may even be negative. The hydrodynamic damping also depends on current velocities. In lock-in regions, VIV response amplitudes depend on so-called “reduced damping” (Griffin and Ramberg, 1982). However, there may still be some correlations between the VIV responses and the modal parameters in calm water if the currents are not too high.

Now the correlations between results from the shaker-excitation and VIV tests conducted in this research are examined, namely the correlation between the modal natural frequencies and the frequency lock-in of the VIV responses, the correlation between the modal added mass coefficients and the maximum upper limit values, and the correlation between the modal natural frequencies and the resonance of the modal VIV responses.

5. 1 Correlation between Modal Natural Frequencies and Frequency Lock-in of VIV Responses

The correlations between the modal natural frequencies and the frequency lock-in of the VIV responses were discussed earlier in Chapter 4, and now these correlations are summarized. For the case of the pretension of 200N, according to Figure 4-5 and 4-6, in the region from $V^*=25$ to 45 the cross-flow VIV responses lock in at the second modal natural frequency of 1.05Hz, which is the value estimated from the shaker-excitation tests. In the region from $V^*=45$ to 90, the in-line VIV responses lock in at the third modal natural frequency of 2.44Hz, which is also the value estimated from the shaker-excitation tests. The shaker-excitation test results show that the resonance reduced velocities for mode 1 and 2 are very close so that lock-in in the region from $V^*=9$ to 25 is difficult to

Correlation between Modal Parameter and VIV Response

occur. The VIV test results showed that this prediction is correct, as no lock-in was observed in that region.

For the case of the pretension of 600N, according to Figure 4-4 and 4-61, in the region from $V^*=9$ to 16.5, the in-line VIV and cross-flow responses lock-in in the first modal natural frequency of 0.57Hz, which is the value estimated from the shaker-excitation tests. In the region from $V^*=20$ to 44, the shaker-excitation test results predict that no lock-in characteristics appear in the VIV response frequencies as the Strouhal frequencies are almost equal to the natural frequencies of mode 2 in the region, and the VIV test results showed that the prediction is correct.

5. 2 Correlation between Modal Added Mass Coefficients and Upper Limit Values

The correlations between the modal added mass coefficients and the upper limit values were also discussed earlier in Chapter 4, and now these correlations are summarized. For the case of the pretension of 200N, in the lock-in region from $V^*=25$ to 45, the reduced velocity at the end point of the lock-in region is 16.83 if the natural frequency of $f_{n2}=1.05\text{Hz}$ for mode 2 is used, while the maximum upper limit value of the reduced velocity for the lock-in region calculated from equation (4-1) is 17.8 if the added mass coefficient measured from the shaker-excitation tests is used. The measured value of 16.83 is a little smaller than the maximum upper limit value of 17.8. In the lock-in region from $V^*=45$ to 90, the reduced velocity at the end point of the lock-in region is 13.87 if the natural frequency of $f_{n3}=2.44\text{Hz}$ for mode 3 is used, while the maximum upper limit value of the reduced velocity for the lock-in region calculated from equation (4-1) is

Correlation between Modal Parameter and VIV Response

20.53 if the added mass coefficient measured from the shaker-excitation tests is used. The measured value of 13.76 is smaller than the maximum upper limit value of 20.53.

For the case of the pretension of 600N, in the region from $V^*=9$ to 16.5, the reduced velocity at the end point of the lock-in region is 16.5 if the natural frequency of $f_{n1}=0.57\text{Hz}$ for mode 1 is used, while the maximum upper limit value of the reduced velocity for the lock-in region calculated from equation (4-1) is 18.74 if the added mass coefficient measured from the shaker-excitation tests is used. The measured value of 16.5 is smaller than the maximum upper limit value of 18.74.

5.3 Correlation between Modal Natural Frequencies and Resonance of VIV Responses

The resonance of riser vibration can be predicted by the natural frequencies and the vortex shedding frequencies. For the case of the pretension of 200N, according to Figure 4-5, two resonance regions can be predicted. The first resonance is expected to occur at $V^*=10$ for mode 1, and the second resonance is expected to occur in the region from $V^*=25$ to 40 for mode 2. Figure 4-28 shows a maximum response for mode 1 at $V^*=16$ in both the in-line and cross-flow directions, and this means that the prediction is correct, even though the reduced velocity for the maximum response for mode 1 is a little bigger than the predicted value. Figure 4-29 shows a resonance occurring in the region from $V^*=21$ to 45 for mode 2 in the cross-flow direction, but not in the in-line direction. According to Figure 4-30, the in-line VIV responses resonate in this region for mode 3. This means that the expected resonance of mode 2 only occurs in the cross-flow direction, and the results from the shaker-excitation tests fail to predict the resonance for

Correlation between Modal Parameter and VIV Response

the in-line VIV responses. The reason for the failure is that the frequencies of the in-line vortex-shedding do not follow the Strouhal frequencies well in this reduced velocity region, as seen in Figure 4-6.

For the case of the pretension of 600N, according to Figure 4-4, two resonance regions can be predicted. The first resonance is expected to occur in the region from $V^*=9$ to 16.5 for mode 1, and the second resonance is expected to occur in the region from $V^*=22$ to 44 for mode 2. Figure 4-81 shows that the responses for mode 1 have relatively big values in the region from $V^*=8$ to 15, and the measured resonance region matches the predicted resonance region. Figure 4-82 shows that the in-line response resonance region is from $V^*=22$ to 35, which matches the expected resonance region for the in-line responses. However, Figure 4-82 shows that the cross-flow response resonance region is from $V^*=15$ to 28, which does not match the expected resonance region for the in-line responses. The failure may imply that the correlations between the VIV responses and the modal parameters estimated from the shaker-excitation tests in calm water are worse at the high current velocity region than at the low current velocity region.

CHAPTER 6

CONCLUSIONS

6. Conclusions

Multi-modal vortex-induced vibration for a flexible riser is a complicated process, and so far it has not been fully understood. The questions include:

- i) It is well known that the frequencies of single-modal VIV responses in currents follow the Strouhal frequencies in un-lock-in regions for a rigid cylinder. Do the frequencies of the multi-modal VIV responses in currents still follow the Strouhal frequencies for a flexible cylinder? If so, what value is the Strouhal number?
- ii) What are the characteristics of the amplitudes of the multi-modal VIV responses? Are the resonances near the modal natural frequencies? If so, how strong are those resonances?

iii) It is well known that there is a frequency lock-in region near the natural frequency in single-modal VIV responses for a rigid cylinder vibrating in currents, and the maximum reduced velocity at the end point of the lock-in region is smaller than the maximum upper limit value of the reduced velocity estimated from equation (4-1). Does the frequency lock-in occur near a modal natural frequency in the multi-modal VIV responses for a flexible riser vibrating in currents? If so, does the frequency lock in at the modal natural frequency? Is the maximum reduced velocity at the end point of the lock-in region smaller than the maximum upper limit value of the reduced velocity estimated from equation (4-1)?

iv) How many frequency components do the multi-modal VIV responses contain for a flexible riser? What is the relationship between these frequency components and the current velocities? Are the frequency components contained in the multi-modal VIV responses identical over riser length?

v) How many modal components do the multi-modal VIV responses contain for a flexible riser? What is the relationship between these modal components and the current velocities?

vi) What is the vibration shape over riser length for multi-modal VIV responses?

vii) What are the motion trajectories in the cross-section plane for a flexible riser?

The modal parameters estimated from the shaker-excitation tests play an important role in giving the answers to the questions mentioned above. These modal parameters include the modal mass, the modal stiffness, the modal damping and the modal natural frequencies. This research aims to improve the understanding of multi-modal vortex-

induced vibrations for highly flexible deepwater risers in currents, and the objectives are to answer these equations.

6.1 Modal Parameters in Calm Water

The results from the shaker-excitation tests showed the characteristic traits of the modal parameters. It was found that flexible risers have a variety of natural frequencies, which correspond to a variety of mode shapes. The modal natural frequencies depended on the tensions, i.e. increased tensions resulted in increased modal natural frequencies. The shaker-excitation tests in calm water could give the estimated values of the modal natural frequencies in calm water for all modes through using harmonic and random excitations, but the different excitation patterns produced considerable differences in the estimated modal parameters.

The modal stiffness depended on the tensions. The modal stiffness increased rapidly as tensions increased. The stiffness also depended on the mode shapes. Tension is a dominant factor affecting the resonance regions for a flexible riser.

The modal mass depended weakly on the tensions. The modal mass increased slowly as the tensions increased. The modal masses were influenced by mode shapes. A maximum value of modal mass appeared in mode 3 or mode 5 for the riser tested. The estimated added mass coefficients C_a depended on the tensions and mode shapes for the flexible riser tested, ranging from 1.0 to 3.7. These estimated values of added mass coefficients are larger than those for a rigid cylinder ranging from 0.8 to 1.5, which were provided by Chakrabarti (2005).

The modal damping did not show a regular change with respect to the tensions. The modal damping also depended on the mode shapes, i.e. increased mode number resulted in increased modal damping. The estimated damping coefficients C_d have a relatively big scatter, ranging from 0.5 to 2.5. These values are similar to those for a rigid cylinder in oscillating water ranging from 0.5 to 2.0, which were found by Sarpkaya (1976).

The vibration shapes measured at the resonance frequency were not exact sinusoidal shapes, even though the model riser had a uniform structure over its length. The estimated modal mass and damping depended on the mode number, and this implies that the hydrodynamic loads acting on a flexible riser are not uniform over the riser length and the hydrodynamic loads vary with mode number.

The added mass of the flexible model riser appeared to be weakly dependent on the frequency in the resonance regions, as the real parts of the dynamic stiffness function have an approximately linear relationship with the frequency-squared over these modal resonance regions, and this ensures that a linear fit for the estimate of modal parameters works well.

The results from non-linear analysis show that in the low frequency and the modal resonance regions non-linear effects are relatively big, as in these regions the riser vibrations have relatively big amplitudes.

6.2 Multi-Modal Vortex-Induced Vibration in Currents

The results from the current-excitation tests showed the characteristic traits of the multi-modal VIV responses. It was found that the time histories of multi-modal VIV have four types. They are the single-dominant-frequency type (SF), the close-double-

dominant-frequency type (CD), the far-double-dominant-frequency type (FD) and the multi-frequency type (MF). The SF and CD types often appeared in the VIV responses at lower current velocities, while the FD and MF type often appeared in the VIV responses at higher current velocities.

The motion trajectories on the cross-section plane contain two fundamental motions. The first motion is a basic figure of 8-, L-, O-shaped or other complicated vibration motion. Another motion is a shifted motion of the basic figure motion. The basic figures of 8- and L-shapes corresponded to the vibrations at lower current velocities with a strong dominant frequency, while other basic figures corresponded to the vibrations at higher current velocities with multi-dominant frequencies.

The snapshots of the VIV responses over the riser length verify that the VIV responses for a flexible riser are multi-modal vibrations. At lower current velocities, the vibration shapes over riser length often exhibit a clear dominant mode with clear nodes, while at higher current velocities, the dominant modes become vague. The snapshot with vague modes represents a VIV response with several dominant modes.

The frequencies of multi-modal VIV responses in both the cross-flow and in-line directions follow the Strouhal frequencies for a flexible riser. The measured Strouhal number was about 0.12. The frequency lock-in occurred in both the in-line and cross-flow directions at some of the modal natural frequencies, but not if the reduced velocities corresponding to the resonances for two neighboring modes were too close so that the resonance regions for the two modes overlap.

In the frequency lock-in regions with lower current velocities, the VIV responses contained a strong dominant frequency in one direction (in-line or cross-flow direction),

while they contained more than one dominant frequency in the other direction. In the frequency lock-in regions with higher current velocities, the VIV responses contained more than one dominant frequency in both the in-line and cross-flow directions. If the VIV responses contained a single dominant frequency in a frequency lock-in region, the dominant frequency was close to the corresponding modal natural frequency. Otherwise, no dominant frequencies were close to the corresponding modal natural frequency. The maximum reduced velocity at the end point of the lock-in region was still smaller than the maximum upper limit value of the reduced velocity estimated from Govardhan's formula for a flexible riser, but the reduced velocity must be calculated using the modal natural frequency of the corresponding mode.

The vibration amplitudes fluctuated from 0.3 to $0.9D$ in both the in-line and cross-flow directions for the flexible riser tested, and no increasing trend exists as the current velocity increases. Modal response regions can be found, but in these regions resonances are not strong as the vibration energy is shared by several modes.

Three types of power spectra can be found in the VIV responses: i) power spectra with single dominant frequency; ii) power spectra with double dominant frequencies; and iii) power spectra with multi-dominant frequencies. The third type of power spectra had a broad frequency bandwidth, namely the VIV responses contained a number of frequency components with small energy, which covered a broad frequency range. The third type of power spectra appeared at the high current velocities. Whether the power spectra varied over riser length or not depended on the current velocities and pretensions.

The dominant modes for the in-line VIV and the cross-flow VIV are usually different. The modal responses may experience a resonance region.

6. 3 Correlation between Modal Parameters and VIV Responses

Although the modal parameters were estimated from the shaker-excitation tests in calm water in this research and the modal parameters in calm water were different from those in currents, some correlations between the estimated modal parameters and the VIV responses can still be found. The first is the correlation between the estimated modal natural frequencies and the frequency lock-in of the VIV responses. Most frequency lock-in regions could be predicted successfully based on analyzing the modal natural frequencies and the Strouhal frequencies, but some frequency lock-in regions in the relatively high currents could not be predicted. This reflects the fact that at higher currents the modal parameters estimated from the tests in calm water have more errors than at lower currents.

The second is the correlation between the estimated modal added mass coefficients and the upper limit values of the reduced velocity. The maximum upper limit values of the reduced velocity calculated from equation (4-1) based on the added mass coefficients estimated from the shaker-excitation tests are larger than the values of the reduced velocity at the ends for all frequency lock-in regions, and this demonstrates the correlations between the estimated modal added mass coefficients and the actual upper limit values of the reduced velocity.

The third is the correlation between the estimated modal natural frequencies and the modal resonance of VIV responses. The modal natural frequencies estimated from the shaker tests lie within the modal resonance regions found in VIV tests in currents and this shows the correlations between the estimated modal natural frequencies and the modal resonance of VIV responses.

6. 4 Recommendations for Future Work

Although detailed experimental work was done in this research, and good results were obtained, it is still necessary to investigate some further work in future. One is to investigate multi-modal VIV responses using other model risers. The results from one model riser may be insufficient to reflect a full picture of multi-modal VIV behavior. A model riser with a relatively large scale may be important for investigation of the multi-modal VIV responses for a marine riser in reality. The Reynolds number used in this research is relatively small ($Re=0.6\times 10^5$), and it is necessary to test a model riser with higher Reynolds number in future.

In this research, the uniform currents were used. In real deep waters, currents are sheared. In a sheared current, the multi-modal VIV responses may have characteristics different from those in a uniform current; it is, therefore, important to test a riser in sheared currents in future.

The modal parameters estimated from the shaker-excitation tests play an important role in understanding the complicated multi-modal VIV responses, but there were two shortages in the shaker-excitation tests in this research. The first is that the modal parameters with even modes could not be measured from the tests, as the shaker was located at the middle of the riser. The measurement of the modal parameters with even modes can be achieved through placing the shaker at other locations on the riser. The second is that the shaker-excitation tests were conducted in calm water, and only the modal parameters in calm water were obtained. In fact, the multi-modal VIV responses depend on the modal parameters in currents, and the modal parameters in currents are

different from the modal parameters in calm water. In order to improve the understanding of modal parameters in currents, a shaker excitation test in currents is necessary in future.

References

- Allen, D. W. and Henning, D. L. (2001), "Prototype Vortex-Induced Vibration Tests for Production Risers", Proceedings of Offshore Technology Conference, Vol. 2, Houston, U.S.A, pp.499-510
- Bai, Y. (2001), "Pipelines and Risers", Elsevier Science Ltd, Kidlington, Oxford OX5 1GB, UK
- Bendat, J. S. and Piersol, A. G. (1971), "Data: Analysis and Measurement Procedure", A Wiley-Interscience Publication
- Bendat, J. S., (1998), "Nonlinear System Techniques and Applications", A Wiley-Interscience Publication, John Wiley & Sons, Inc.
- Chakrabarti, S. K. (1987), "Hydrodynamics of Offshore Structures", Computational Mechanics Publications
- Chakrabarti, S. K. (2002), "The Theory and Practice of Hydrodynamics and Vibration", World Scientific
- Chakrabarti, S. K. (2005), "Handbook of Offshore Engineering", Vol. 1, Elsevier Science Ltd, UK
- Chaplin, J. R. and Subbiah, K. (1998), "Hydrodynamic Damping of A Cylinder in Still Water and in A Transverse Current", Applied Ocean Research 20, Elsevier, pp251-259
- Clayton, B. R. and Bishop, R. E. D. (1982), "Mechanics of Marine Vehicles", E & F.N. Shon Ltd, London
- Chung, T. Y. (1989), "Vortex-induced Vibration of Flexible Cylinder Having Different Mass Ratios. Report No. UCE 440-1283ED, Korea Research Institute of Ships and Ocean Engineering
- DiMarco, S. F., Reid, R. O., Jochens, A. E., Nowlin, W. D. J. and Howard, M. K. (2001), "General Characteristics of Current in the Deepwater Gulf of Mexico", Proceedings of Offshore Technology Conference, Vol. 1, Houston, U.S.A, pp.513-525
- Furnes, G. K. (2000), "On Marine Riser Responses in Time and Depth-dependent Flows", Journal of Fluids and Structures, 14, pp. 257-273
- Govardhan, R. and Williamson, C.H.K. (2000), "Modes of Vortex Formation and Frequency Response for A Freely-vibrating Cylinder", J. Fluid Mech. 420:85-130

- Griffin, O. M. and Ramberg, S. E. (1982), "Some Recent Study of Vortex Shedding with Applications to Marine Turbulars and Risers", ASME Journal of Energy Resources Technology 104, 2-13
- He, J. and Fu, Z. (2001), "Modal Analysis", Butterworth-Heinemann, Linacre House, Jordan Hill Oxford OX2 8DP
- Heylen, W., Lammens, S. and Sas, P. (1998), "Modal Analysis Theory and Testing", Ketholieke Universiteit Leuven, Celestijnenlaan 300B, B-3001 Leuven, Belgium
- Hong, S., Choi, Y. R., Park, J. B., Park, Y. K. and Kim, Y. H. (2002), "Experimental Study on Vortex-induced Vibration of Towed Pipes", Journal of Sound and Vibration, 249(4), pp. 649-661
- Jauvtis, N. and Williamson, C. H. K. (2003), "Vortex-induced Vibration of A Cylinder with Two Degrees of Freedom", Journal of Fuilds and Structures 17 (2003) 1035-1042
- Khalak, A. and Williamson, C. H. K. (1997), "Investigation of the Relative Effects of Mass and Damping in Vortex-induced Vibration of A Circular Cylinder", J. Wind Eng. Ind. Aerodyn. 69-71:341-50
- Khalak, A. and Williamson, C. H. K., (1999), "Motions, Forces and Mode Transitions in Vortex-induced Vibrations at Low Mass-damping", Journal of Fluids and Structures, 13, pp.813-851
- Lie, H., Mo, K. and Vandiver, J. K. (1998), "VIV Model Test of a Bare- and a Staggered Buoyancy Riser in a Rotating Rig", Proceedings of Offshore Technology Conference, Vol. 2, Houston, U.S.A, pp.177-187
- Liagre, P. F. and Niedzwecki, J. M. (2003), "Estimating nonlinear coupled frequency-dependent parameters in offshore engineering", Applied Ocean Research 25, 1-19
- Morgan, N. (1990), "Marine Technology Reference Book", Butterworth & Co. Ltd
- Niedzwecki, J. M. and Liagre, P. F. (2003), "System identification of distributed-parameter marine riser models", Ocean Engineering 30, 1387-1415
- Patel, M. H. and Witz, J. A. (1991), "Compliant Offshore Structures", Butterworth-Heinemann Ltd
- Olson, J. R. (1985), "Design and Analysis of Deep Water Marine Riser Systems for Floating Production Facilities, Case Histories in Offshore Engineering", Springer Verlag Wien-New York
- Raman-Nair, W. and Baddour, R. E. (2001), "Three-Dimensional Marine Riser Dynamics", Report of IMD, St. John's, Canada

- Robinson, N. J. (2002), "Faroes Gap to Offshore West Africa: Challenges for drilling risers in two radically different deepwater exploration areas", EnergyWise Workshop: Signposting deepwater technology requirements for Atlantic Canada, St. John's, Canada
- Sampaio, P. A. B. and Coutinho, A. L. G. A., (2000), "Simulating vortex shedding at high Reynolds numbers", Proceedings of the Tenth International And Polar Engineering Conference, Vol. III, Seattle, USA, pp. 461-466
- Sarpkaya, T. (1976), "In-line and Transverse Forces on Cylinder in Oscillating Flow at High Reynolds Number", Proceedings of Offshore Technology Conference, Houston, U.S.A, OTC 2533, 1976, pp. 95-108
- Sarpkaya, T. (1977), "Transverse Oscillations of A Circular Cylinder in Uniform Flow", Part I. Naval Postgraduate School Report No. NPS-69SL77071
- Sarpkaya, T. and Dalton, C. (1992), "Analysis of Wave Plus Current-Induced Forces on Cylinders", Proceedings of Offshore Technology Conference, Vol. 1, Houston, U.S.A, pp. 87-93
- Serta, O. B., Longo, C. E. V. and Roveri, F. E. (2001), "Riser Systems for Deep and Ultra-deepwaters", Proceedings of Offshore Technology Conference, OTC 13185, Houston, U.S.A, pp.101-108
- Sharp, J. J., Deb, A. and Deb, M. K. (1992), "Applications of Matrix Manipulation in Dimensional Analysis Involving Large Numbers of Variables", Marine Structures 5, Elsevier Science Publishers Ltd, England, pp. 333-348
- Sumer, B. M. and Fredsoe, J. (1997), "Hydrodynamics around cylindrical structures", World Scientific
- Thomas, D. O. and Hearn, G. E. (1994), "Deepwater Mooring Line Dynamics with Emphasis on Seabed Interference Effects", Proceedings of Offshore Technology Conference, Vol. 3, Houston, U.S.A, pp. 203-214
- Triantafyllou, M. S., Triantafyllou, G., Tein, Y., D. and Ambrose, B. D.(1999), "Pragmatic Riser VIV Analysis", Proceedings of Offshore Technology Conference, Vol. 3, Houston, U.S.A, pp. 419-426
- Vandiver, J. K. and Chung, T. Y. (1987), "Hydrodynamic Damping on Flexible Cylinders in Shear Flow", Proceedings of Offshore Technology Conference, Huston, U.S.A, OTC 5524
- Vandiver, J. K. and Chung, T. Y. (1988), "Predicted and Measured Response of Flexible Cylinders in Sheared Flow", Proceedings of ASME Winter Annual Meeting Symposium on Flow-induced Vibration, Chicago, USA

Vandiver, J. K. (1993), "Dimensionless Parameters Important to the Prediction of Vortex-induced Vibration of Long, Flexible Cylinders in Ocean Currents", *Journal of Fluids and Structures*, 7, 423-455

Vandiver, J. K., Allen, D. and Li, L. (1996), "The Occurrence of Lock-in under Highly Shear Conditions", *Journal of Fluids and Structures*, 10, 555-561

Vandiver, J. K. and Marcollo, H. (2003), "High Mode Number VIV Experiments", IUTAM Symposium on Integrated Modeling of Fully Coupled Fluid-Structure Interaction Using Analysis, Computations, and Experiments, 1-6 June, 2003, Kluwer Academic Publishers, Dordrecht

Ward, E. G., Haring, R. E. and Devlin, P. V. (1999), "Deepwater Mooring and Riser Analysis for Depth to 10,000feet", *Proceedings of Offshore Technology Conference*, Vol. 2-part1, Houston, U.S.A, pp. 297-303

Williamson, C. H. K. and Govardhan, R. (2004), "Vortex-Induced Vibrations", *Annual Review, Fluid Mech.* 2004. 36:413-55

Wilson, J. F. (1984), "Dynamics of Offshore Structures", John Wiley & Sons, Inc.

Appendix A

Governing equation for model riser motions

Patel and Witz (1991) presented a method to analyze the structure of a vertical marine riser. In the case of this research, the model riser was horizontally placed on a supporting frame, and the governing equations for the horizontal riser may be derived through a modification of the model presented by Patel and Witz.

The model riser may be regarded as a hollow beam column subjected to external hydrostatic and hydrodynamic pressure as well as axial and lateral loadings. Similar to the analysis presented by Patel and Witz, the analysis presented in this Appendix is restricted to two dimensions for simplicity. Firstly, consider a differential element of the riser on the x - z plane (x denotes the axial direction of riser, and z denotes the cross-flow direction), as shown in Figure A-1. The static forces acting on the element include:

- a) an axial tension at the ends of the element T_s ;
- b) a shear force at the ends of the element Q ;
- c) a bending moment at the ends of the element M ;
- d) a horizontal force due to the resultant external hydrostatic pressure dF_{xo} ;
- e) a vertical force due to the resultant external hydrostatic pressure dF_{zo} ;
- f) the weight of the element dW .

The dynamic forces acting on the element include:

- a) the horizontal component of the inertial force dF_{xa} ;
- b) the vertical component of the inertial force dF_{za} ;

- c) the horizontal component of the damping force dF_{xb} ;
- d) the vertical component of the damping force dF_{zb} ;
- e) the horizontal component of the vortex-shedding force dF_{xv} ;
- d) the vertical component of the vortex-shedding force dF_{zv} ;
- e) a vertical shaker-excitation force dF_s .

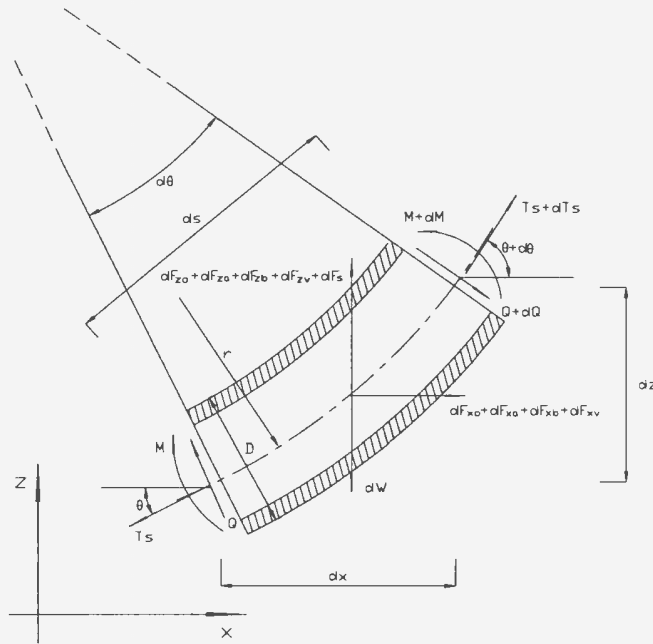


Figure A-1 Forces acting on a differential riser element

For a horizontal model riser, only the vertical motions are considered; thus summing components of force in the z direction and summing components of moment around the mid-point of the element yield the equations as follows:

$$(T_s + dT_s) \sin(\theta + d\theta) - T_s \sin \theta - (Q + dQ) \cos(\theta + d\theta) + Q \cos \theta + (dF_{zo} + dF_{zo} + dF_{zb} + dF_{zv} + dF_s) - dW = 0$$

$$(M + dM) - M - (Q + dQ) \frac{ds}{2} - Q \frac{ds}{2} = 0$$

where θ is the angle between the x -axis and the centre line of the element, and ds is the length of the element on its centre line. The differentials ds and dW may be written as

$$ds = \sqrt{(dx)^2 + (dz)^2}$$

$$dW = \rho_s g A ds$$

where ρ_s is the structural mass density of the riser, g is the gravitational acceleration, and A is the area of cross-section of the riser.

For a small $d\theta$, the trigonometric functions of $d\theta$ can be approximated by their first series term, and the equations above can be simplified to

$$\left. \begin{aligned} & (T_s \cos \theta + Q \sin \theta) \frac{\partial \theta}{\partial s} - \frac{\partial Q}{\partial s} \cos \theta + \frac{\partial T_s}{\partial s} \sin \theta \\ & + \frac{\partial F_{zo}}{\partial s} + \frac{\partial F_{za}}{\partial s} + \frac{\partial F_{zb}}{\partial s} + \frac{\partial F_{zv}}{\partial s} + \frac{\partial F_s}{\partial s} - \rho_s g A = 0 \\ & \frac{\partial M}{\partial s} - Q = 0 \end{aligned} \right\} \quad (A-1)$$

The force acting on a cylindrical element due to external hydrostatic pressure, F_{zo} , can be determined by finding the force on an arbitrary section of the element and resolving it into components before integrating to obtain the total force on the element. Figure A-2 shows an element of the cylinder to conduct this analysis. In the analysis, the hydrostatic pressure is assumed to vary linearly along the centre line.

As shown in Figure A-2, the length of any strip on the cylinder circumference parallel to its centre line is given by

$$ds' = \left(r + \frac{1}{2} D \sin \varphi \right) d\theta \quad (A-2)$$

where r is the radius of curvature of the element; D is the diameter of the element; φ and θ are defined in Figure A-2. The pressure at the lower end of the strip can be written as

$$p_l = p + \frac{1}{2} \rho g D \cos \theta \sin \varphi \quad (A-3)$$

where ρ is the water density, g is the acceleration of the gravity and p is the fluid pressure at the lower end of the center line of the element. The pressure at the higher end of the strip can be written as

$$p_h = p_l - \rho g \sin \theta ds' \quad (A-4)$$

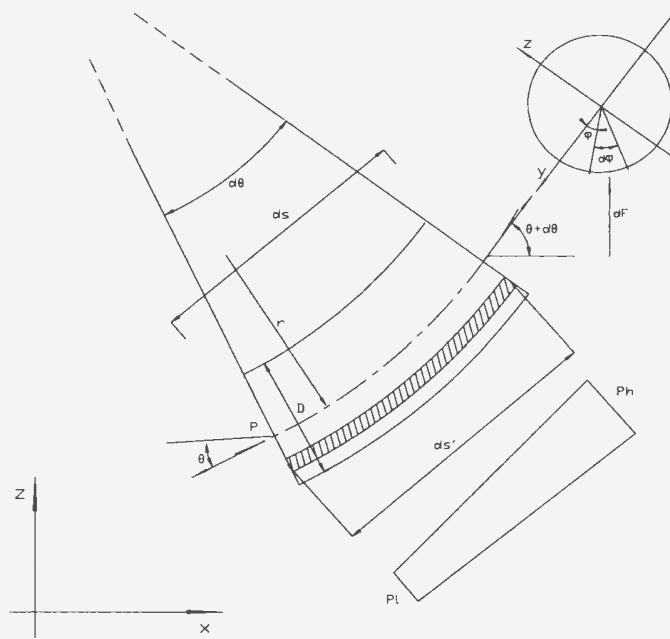


Figure A-2 Pressure integration variables

The area of the strip can be calculated by the following equation:

$$dA = \frac{1}{2} D d\varphi ds' \quad (A-5)$$

and the force acting on the strip is then

$$dF = \frac{1}{2} (p_l + p_h) dA \quad (A-6)$$

Substituting equations (A-2), (A-3), (A-4) and (A-5) into equation (A-6) leads to

$$dF = \frac{1}{2} \left[p + \frac{1}{2} \rho g D \cos \theta \sin \varphi - \frac{1}{2} \rho g \sin \theta \left(r + \frac{1}{2} D \sin \varphi \right) \right] d\theta \left[D \left(r + \frac{1}{2} D \sin \varphi \right) \right] d\theta d\varphi$$

Expanding the individual terms gives

$$\begin{aligned} dF &= \frac{1}{2} r D \left[p - \frac{1}{2} \rho g r \sin \theta d\theta \right] d\theta d\varphi + \frac{1}{4} D^2 \left[p + \rho g r \cos \theta - \rho g r \sin \theta d\theta \right] d\theta \sin \varphi d\varphi \\ &+ \frac{1}{8} \rho g D^3 \left[\cos \theta - \frac{1}{2} \sin \theta d\theta \right] d\theta \sin^2 \varphi d\varphi \end{aligned} \quad (A-7)$$

The forces, F_{zo} , in the z direction can be obtained the following equations:

$$dF_{zo} = \int_{\varphi=0}^{\varphi=2\pi} dF \cos \theta \sin \varphi \quad (A-8)$$

Substituting equation (A-7) into equation (A-8) yields

$$dF_{zo} = A \left(p + \rho g r \cos \theta - \rho g r \sin \theta d\theta \right) \cos \theta d\theta \quad (A-9)$$

where A is the area of cross-section of the element, namely

$$A = \frac{\pi}{4} D^2$$

Substituting equation (A-9) into equation (A-1) and applying the relation $ds=r d\theta$ gives

$$\left. \begin{aligned} &\left(\frac{\partial T_s}{\partial s} + Q \frac{\partial \theta}{\partial s} \right) \sin \theta + \left(-\frac{\partial Q}{\partial s} + T_s \frac{\partial \theta}{\partial s} + p A \frac{\partial \theta}{\partial s} \right) \cos \theta + A \rho g \cos^2 \theta \\ &+ \frac{\partial F_{za}}{\partial s} + \frac{\partial F_{zb}}{\partial s} + \frac{\partial F_{zv}}{\partial s} + \frac{\partial F_s}{\partial s} - \rho_s g A = 0 \\ &\frac{\partial M}{\partial s} - Q = 0 \end{aligned} \right\} \quad (A-10)$$

The inertial force dF_{za} and damping force dF_{zb} can respectively be represented by the structural mass, added mass, structural damping and hydrodynamic damping of the element, namely

$$\left. \begin{aligned} dF_{za} &= -(m_s + m_a) \frac{\partial^2}{\partial t^2} z(t, x) ds \\ dF_{zb} &= -(c_s + c_a) \frac{\partial}{\partial t} z(t, x) ds \end{aligned} \right\} \quad (A-11)$$

where $z(t, x)$ denotes the vibration displacement of the element in the vertical direction; m_s and m_a are respectively the structural and added mass per unit length; c_s and c_a are respectively the structural and hydrodynamic damping per unit length. It is a linear damping model if c_a is independent of $z(t, x)$; otherwise, it is a nonlinear damping model.

For a horizontal riser, we have:

$$\left. \begin{aligned} \sin \theta &\approx \theta \approx \frac{\partial z}{\partial x} \\ \cos \theta &\approx 1 \\ ds &\approx dx \end{aligned} \right\} \quad (A-12)$$

Beam theory is applied to the element, and the following equation is obtained:

$$M = EI \frac{\partial \theta}{\partial s} \quad (A-13)$$

where E is the modulus and I is the second moment of the cross-section of the element.

Substituting equations (A-11), (A-12) and (A-13) into equation (A-10) leads to

$$\left. \begin{aligned} \left(\frac{\partial T_s}{\partial x} + Q \frac{\partial^2 z}{\partial x^2} \right) \frac{\partial z}{\partial x} - \frac{\partial Q}{\partial x} + (T_s + pA) \frac{\partial^2 z}{\partial x^2} - m_T \frac{\partial^2 z}{\partial t^2} - c_T \frac{\partial z}{\partial t} \\ + f_v + f_s - (\rho_s - \rho) g A = 0 \\ EI \frac{\partial^3 z}{\partial x^3} - Q = 0 \end{aligned} \right\} \quad (A-14)$$

where m_T , c_T , f_v and f_s are respectively the total mass per unit length, the total damping coefficient, the vortex-shedding force per unit length and the shaker-excitation force per unit length. They have the forms as follows:

$$\begin{aligned} m_T &= m_s + m_a \\ c_T &= c_s + c_a \\ f_v &= \frac{\partial F_{zv}}{\partial s} \\ f_s &= \frac{\partial F_s}{\partial s} \end{aligned}$$

Since a horizontal riser has almost identical water depths over its length, the static fluid pressure p is almost a constant over the riser length; thus we have the relation as follows:

$$\frac{\partial T_s}{\partial x} \approx \frac{\partial(T_s + pA)}{\partial x} \quad (A-15)$$

Substitute equations (A-15) into equation (A-14), and equation (A-14) can be rewritten as

$$\left. \begin{aligned} &\frac{\partial}{\partial x} (T_s + pA) \frac{\partial z}{\partial x} - \frac{\partial Q}{\partial x} + (T_s + pA) \frac{\partial^2 z}{\partial x^2} - m_T \frac{\partial^2 z}{\partial t^2} - c_T \frac{\partial z}{\partial t} + f_v + f_s \\ &+ Q \frac{\partial^2 z}{\partial x^2} \frac{\partial z}{\partial x} - (\rho_s - \rho)gA = 0 \\ &EI \frac{\partial^3 z}{\partial x^3} - Q = 0 \end{aligned} \right\} \quad (A-16)$$

For a small $z(t,x)$, equation (A-16) can be simplified to

$$\frac{\partial}{\partial x} \left[(T_s + pA) \frac{\partial z}{\partial x} \right] - EI \frac{\partial^4 z}{\partial x^4} - m_T \frac{\partial^2 z}{\partial t^2} - c_T \frac{\partial z}{\partial t} + f_v + f_s - (\rho_s - \rho)gA = 0 \quad (A-17)$$

It is noted that the last term of the left side of equation (A-17) is independent of the time t , which represents the weight of the element in water. This means that this term only has the static effects, not the dynamic effects; thus it can be removed when only the dynamic responses are analyzed, namely equation (A-17) is further simplified to

$$m_T \frac{\partial^2 z(t,x)}{\partial t^2} + c_T \frac{\partial z(t,x)}{\partial t} - \frac{\partial}{\partial x} \left[T(t,x) \frac{\partial z(t,x)}{\partial x} \right] + EI \frac{\partial^4 z(t,x)}{\partial x^4} = f_v(t,x) + f_s(t,x) \quad (A-18)$$

where T is the equivalent tension, and it has the forms as follows:

$$T(t,x) = T_s(t,x) + Ap(x)$$

Similarly, the governing equation of the riser motion in the x - y plane can be derived as follows:

$$m_r \frac{\partial^2 y(t, x)}{\partial t^2} + c_r \frac{\partial y(t, x)}{\partial t} - \frac{\partial}{\partial x} \left[T(t, x) \frac{\partial y(t, x)}{\partial x} \right] + EI \frac{\partial^4 y(t, x)}{\partial x^4} = f_v(t, x) \quad (A-19)$$

The boundary conditions for equations (A-18) and (A-19) depend on the end connections of the riser. In this research, the end connections for the model riser were close to a pinned connection; that is, the displacement motions at the ends of the riser were strictly constrained, while the rotation motions were almost free. Thus, the corresponding boundary conditions for equation (A-18) can be written as

$$\left. \begin{aligned} z(t, 0) &= 0 \\ z(t, L) &= 0 \\ M_y(t, 0) &= 0 \\ M_y(t, L) &= 0 \end{aligned} \right\} \quad (A-20)$$

where L is the riser length, and M_y is the bending moment of the riser.

Substituting equations (A-12) and (A-13) into equation (A-20) gives the boundary conditions as follows

$$\left. \begin{aligned} z(t, 0) &= 0 \\ z(t, L) &= 0 \\ \frac{\partial^2}{\partial x^2} z(t, 0) &= 0 \\ \frac{\partial^2}{\partial x^2} z(t, L) &= 0 \end{aligned} \right\} \quad (A-21)$$

Similarly, the boundary conditions for equation (A-19) can be written as

$$\left. \begin{aligned} y(t,0) &= 0 \\ y(t,L) &= 0 \\ \frac{\partial^2}{\partial x^2} y(t,0) &= 0 \\ \frac{\partial^2}{\partial x^2} y(t,L) &= 0 \end{aligned} \right\} \quad (A - 22)$$

The initial conditions for equations (A-18) and (A-19) is not important when the steady vibration responses are analyzed. According to the basic theory of linear vibration (Chakrabarti, 2002), for a damped vibration system, the initial conditions only affect the unsteady vibration responses during the initial period of the vibration process, and the steady vibration responses are independent of the initial conditions. This research only focuses on the steady vibration responses of the riser, so that the initial conditions may not be considered.

Appendix B

Validation of the program to estimate the spectral density functions

Method of Estimation

Spectral analysis is an important tool for the data analysis in this research, and it is crucial to develop a reliable program for the data analysis. A method for the validation of this program is to apply the program to some typical examples with known spectral density functions and then to compare the estimated spectral density functions with the known spectral density functions. If the estimated spectral density functions match the known spectral density functions pretty well, the program is validated.

The cross-spectral density function of any two time series, $x_1(t)$ and $x_2(t)$ in the frequency-domain is normally a complex function, i.e. it can be written in the form as (Bendat and Piersol, 1971)

$$S_{x_1x_2}(f) = \frac{1}{2} [C_{x_1x_2}(f) - iQ_{x_1x_2}(f)]$$

If $x_1(t) = x_2(t)$, the cross-spectral density function becomes the auto-spectral density function of $x_1(t)$ or $x_2(t)$, and the imaginary part of the function will become zero. The standard method to estimate the spectral density functions is based on the Fourier transform relation between spectral density functions and autocorrelation functions.

In theory, Fourier transform is used to handle the time series with infinite sampling time period, but in practice, the time series always have finite sampling time period, as it is impossible for one to acquire a time series with infinite sampling time period. It is well known that a finite sampling time period will result in the so-called leakage errors for the

estimate of spectral density function, but an appropriate window function can reduce the leakage errors.

For the digital data of $x_1(t)$ and $x_2(t)$ with sample size N , at an arbitrary value of the frequency f in the range $0 \leq f \leq f_c$, estimates of the cross-spectral density functions are

(Bendat and Piersol,1971)

$$\tilde{C}_{x_1x_2}(f) = 2h \left[D_0 \tilde{A}_0 + 2 \sum_{r=1}^{m-1} D_r \tilde{A}_r \cos\left(\frac{\pi r f}{f_c}\right) + D_m \tilde{A}_m \cos\left(\frac{\pi m f}{f_c}\right) \right] \quad (B-1)$$

$$\tilde{Q}_{x_1x_2}(f) = 2h \left[2 \sum_{r=1}^{m-1} D_r \tilde{B}_r \sin\left(\frac{\pi r f}{f_c}\right) + D_m \tilde{B}_m \sin\left(\frac{\pi m f}{f_c}\right) \right] \quad (B-2)$$

where h is the sampling interval, $f_c=1/2h$ is the cutoff frequency, m is the number of correlation lag value, $D_r, r=0, 1, 2, 3, \dots, m$, are the window functions, and

$$\begin{aligned} \tilde{A}_r &= \frac{1}{2} [\tilde{R}_{x_1x_2}(rh) + \tilde{R}_{x_2x_1}(rh)] \\ \tilde{B}_r &= \frac{1}{2} [\tilde{R}_{x_1x_2}(rh) - \tilde{R}_{x_2x_1}(rh)] \\ \tilde{R}_{x_1x_2}(rh) &= \frac{1}{N-r} \sum_{n=1}^{N-r} x_{1,n} x_{2,n+r} \\ \tilde{R}_{x_2x_1}(rh) &= \frac{1}{N-r} \sum_{n=1}^{N-r} x_{2,n} x_{1,n+r} \\ r &= 0,1,2, \dots, m \end{aligned}$$

Several window functions have been developed, and in this research three window functions are used to investigate their effects on the estimated values of spectral density function. These window functions are

1. Boxcar window function in the form as

$$\begin{aligned} D_r &= 1 \\ r &= 0,1,2, \dots, m \end{aligned}$$

2. Hanning window function in the form as

$$D_r = \frac{1}{2} \left[1 + \cos\left(\frac{\pi r}{m}\right) \right]$$

$$r = 0, 1, 2, \dots, m$$

3. Parzen window function in the form as

$$D_r = \begin{cases} 1 - 6\left(\frac{r}{m}\right)^2 + 6\left(\frac{r}{m}\right)^3 & \text{when } r = 0, 1, 2, \dots, \frac{m}{2} \\ 2\left(1 - \frac{r}{m}\right)^3 & \text{when } r = \frac{m}{2} + 1, \dots, m \end{cases}$$

Case Studies

A program has been developed based on equations (B-1) and (B-2). In the case studies, this program was used to analyze some typical samples, and the numerical results of these case studies demonstrate the validation of this program.

Case study 1 Auto-spectral density function of single sine wave

In this case study, the simplest case of a single sine wave is selected. The amplitude, frequency and phase of this sine wave are respectively 0.9m, 0.02Hz and $\pi/4$, namely

$$x(t) = a \sin(2\pi ft + \alpha)$$

$$a = 0.9(m)$$

$$f = 0.02(\text{Hz})$$

$$\alpha = \frac{\pi}{4}$$

Assuming the sampling interval $h=0.5s$, the correlation lag value $m=500$ and the sample size $N=1000, 2000, 3000$ and 4000 and using Parzen window function, the estimated auto-spectral density function of this single sine wave is shown in Figure B-1.

As seen in Figure B-1, a spectral function with single peak and very narrow bandwidth is obtained. The peak appears at a frequency of $0.02Hz$, which matches the frequency of the sine wave.

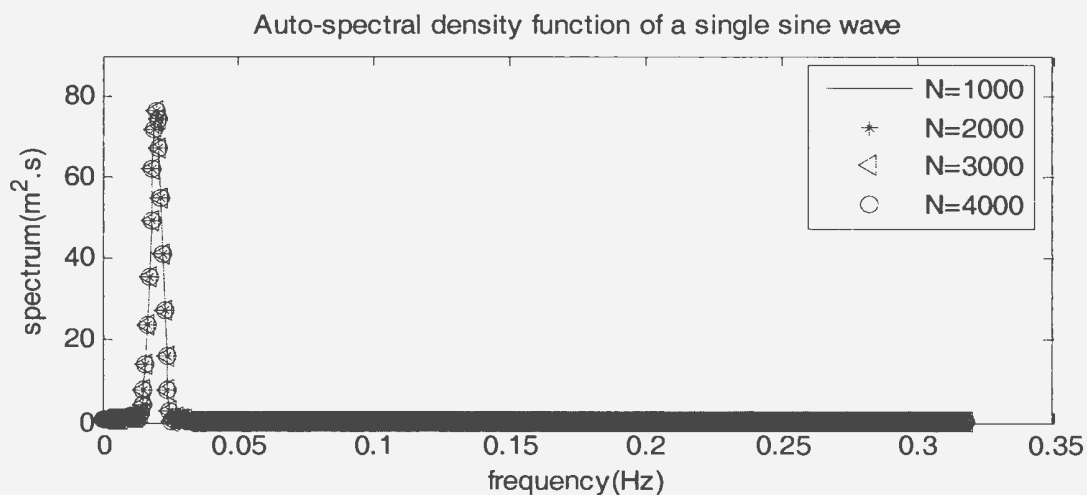


Figure B-1 Estimated auto-spectral density function of a single sine wave using Parzen window function

The estimated auto-spectral function exhibits a bandwidth ranging from 0.015 to $0.025Hz$ near the peak frequency and this is not true, as in principle the spectral density function of a single sine wave is a Delta function and does not have such a bandwidth. However, the bandwidth of the estimated spectral density function is very narrow so that the estimated spectral density function can be regarded as an approximation of the Delta function.

Figure B-1 shows that the sampling size does not produce a significant effect on the estimated results if the sampling size is greater than 1000 , and this means that the effects

of sample size on the estimates of spectral density function can be ignored when the sample sizes are large enough.

Now examine the effects of window function on the estimated spectral functions. Assuming that $h=0.5s$, $m=500$ and the sample size $N=1000$ and using the different window functions, the estimated spectral density functions are shown in Figure B-2.

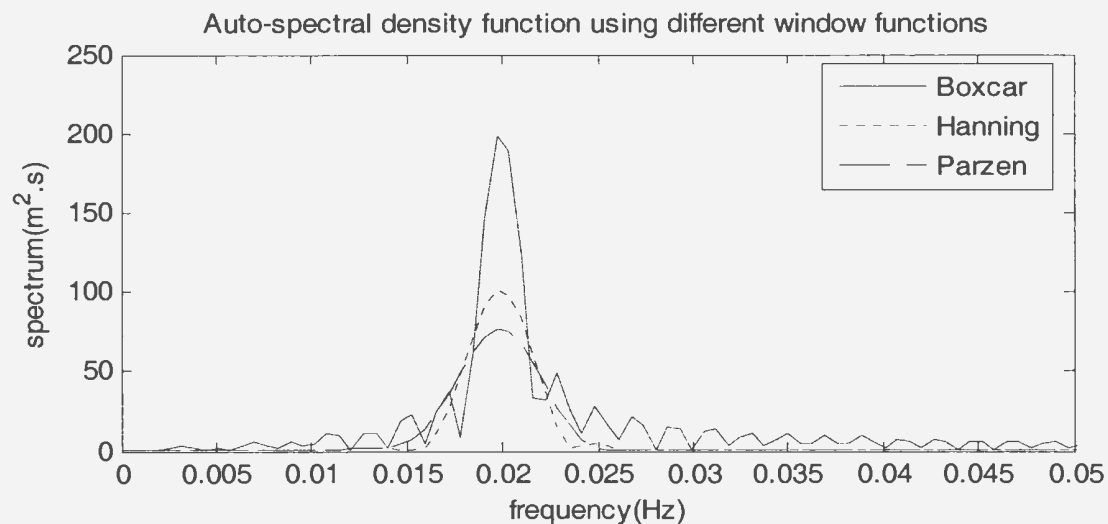


Figure B-2 Estimated auto-spectral density functions using different window functions

As seen in Figure B-2, Boxcar window function can not reduce the leakage errors, as the spectral density function estimated based on this window function contains an infinite number of peaks. This will cause a misunderstanding of having the infinite number of frequency components in the estimated spectral function. Both Hanning and Parzen window functions can reduce the leakage errors, as the estimated spectral density functions contain only one peak.

It is noted that all window functions do not change the dominant-peak frequency, and this means that the spectral analysis does not skew the frequency components. However, the window functions influence the dominant-peak height and the bandwidth, and this

means that the peak magnitude values of the estimated spectral function lose their direct physical meaning. For the case of estimating frequency response functions, the peak magnitude values is not important, as these frequency response functions are estimated from a ratio between two spectral functions. In other words, the ratio between two spectral functions is independent of window functions used. In fact, the important thing is the smoothness of estimated spectral functions. As Parzen window function can produce the smoothest results, this window function was, therefore, chosen for this research.

The relationship between the amplitude of the sine wave and the peak magnitude values of the estimated spectral functions can be represented by a coefficient, λ , defined as the ratio of the square of sine wave amplitude to the spectral peak value. For Parzen window function, from Figure B-1 we have

$$\lambda = \frac{0.9^2}{75.95} \approx 0.0107 \quad (B-3)$$

Case study 2 Auto-spectral density functions of sum of two sine waves

As discussed earlier, there is a bandwidth in the estimated spectral function, and this means that the program presented may cause two very close frequencies to be merged to a frequency. Now examine the minimum frequency interval which can be separated by the program. Consider the sum of two sine waves in the form as

$$x(t) = a_1 \sin(2\pi f_1 t + \alpha_1) + a_2 \sin(2\pi f_2 t + \alpha_2)$$

where a_1 and a_2 are the amplitudes of the two sine waves, f_1 and f_2 are the frequencies, and α_1 and α_2 are the phases.

Let $a_1=0.9m$, $a_2=1.8m$, $f_1=0.02Hz$, $f_2=0.04Hz$, $\alpha_1=\pi/4$, $\alpha_2= \pi/3$, $h=0.5s$, $m=500$ and the sample size $N=1000$, 2000 , 3000 and 4000 , and the estimated spectral density functions

are shown in Figure B-3. As seen in Figure B-3, as the frequencies of the two sine waves are far away, the dominant frequencies are clearly exhibited. The peak frequencies are 0.02Hz and 0.0399Hz, which are equal to the frequencies of the two sine waves. The spectral values at two peaks are respectively $75.7m^2$ and $303.4m^2$, and the values of λ corresponding to the two peaks are 0.0107. This means that the ratio λ is independent of the frequency and amplitude of sine waves.

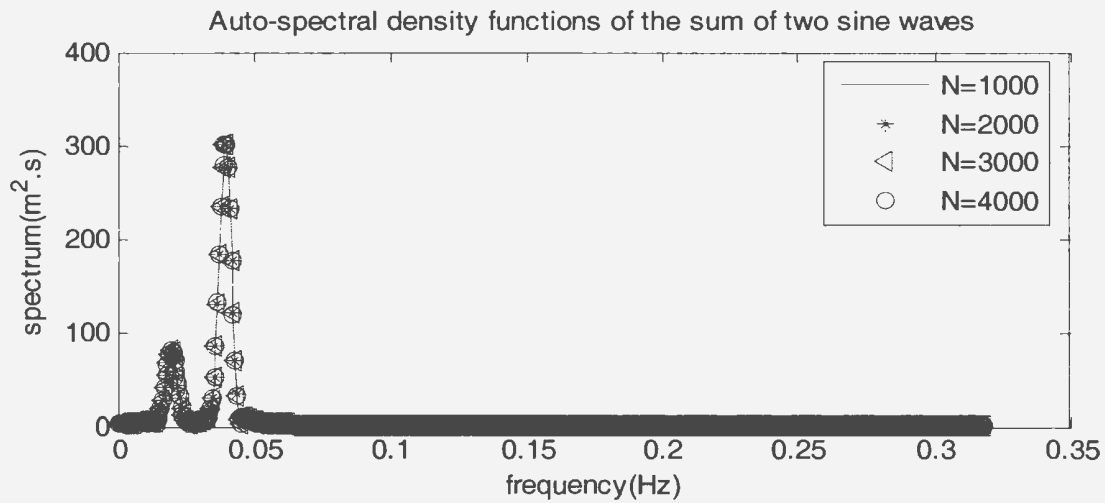


Figure B-3 Estimated auto-spectral density function of the sum of two sine waves with far frequencies

Consider two sine waves with relatively close frequencies. Let $a_1=0.9m$, $a_2=1.8m$, $f_1=0.02Hz$, $f_2=0.0271Hz$, $\alpha_1=\pi/4$, $\alpha_2= \pi/3$, $h=0.5s$, $m=500$ and the sample size $N=1000$, 2000, 3000 and 4000 respectively, and the estimated spectral density function is shown in Figure B-4. As seen in Figure B-4, the values of the estimated spectral density functions at two peaks are $74.5(m^2)$ and $302.5(m^2)$, and the corresponding peak frequencies are $0.02(1/s)$ and $0.0269(1/s)$. The results demonstrate that the two close frequencies can still be separated clearly in the frequency- domain, but the peak widths almost overlap together. This implies that the minimum frequency interval which can be separated is about 0.007Hz.

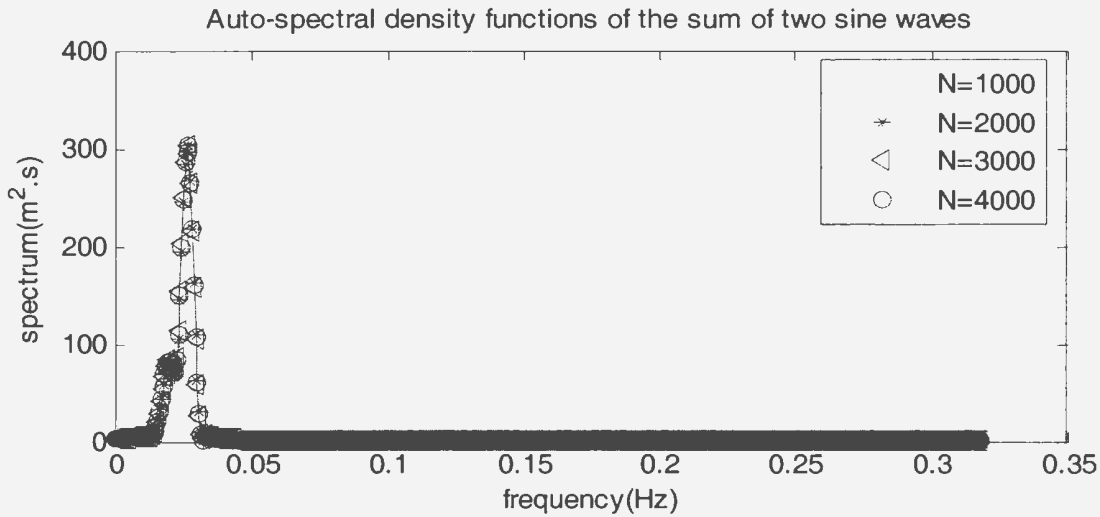


Figure B-4 Estimated auto-spectral density functions of sum of two sine waves with close frequencies

Case study 3 Cross-spectral density function of two sine waves

In theory, the cross-spectral density function of two sine waves with different frequencies is equal to zero, and this provides a way to check the accuracy of the applied program. In other words, the smaller the values of estimated cross-spectral density function are, the better the accuracy of the estimated results is. Consider two sine waves as

$$x(t) = a_1 \sin(2\pi f_1 t + \alpha_1)$$

$$y(t) = a_2 \sin(2\pi f_2 t + \alpha_2)$$

where a_1 and a_2 are the amplitudes of the two sine waves, f_1 and f_2 are the frequencies, and α_1 and α_2 are the phases.

Let $a_1=0.9m$, $a_2=1.8m$, $f_1=0.02Hz$, $f_2=0.027Hz$, $\alpha_1=\pi/4$, $\alpha_2=\pi/3$, $h=0.5s$, $m=500$ and $N=1000, 2000, 3000$ and 4000 , and the estimated cross-spectral density functions are shown in Figure B-5. The results exhibit that the estimate error is a function of frequency. The errors at the frequencies of the sine waves are obviously larger than those at other

frequencies. The results also show that the sample sizes can improve the accuracy, namely the larger the sample sizes are, the more accurate the estimate is.

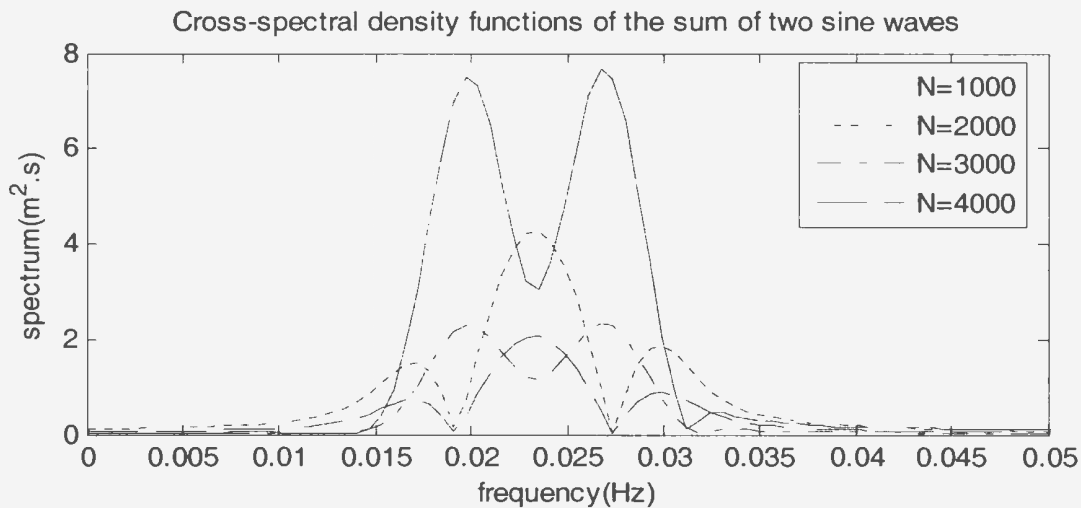


Figure B-5 Estimated cross-spectral density functions of the sum of two sine waves

Figure B-6 presents the estimated cross-spectral density functions using the different window functions. As seen in Figure B-6, the window functions have an apparent effect on the accuracy of the estimated results. Boxcar window function generates the largest errors, while Parzen window function has the smallest errors. This means that the estimate accuracy can be improved by selecting a proper window function.

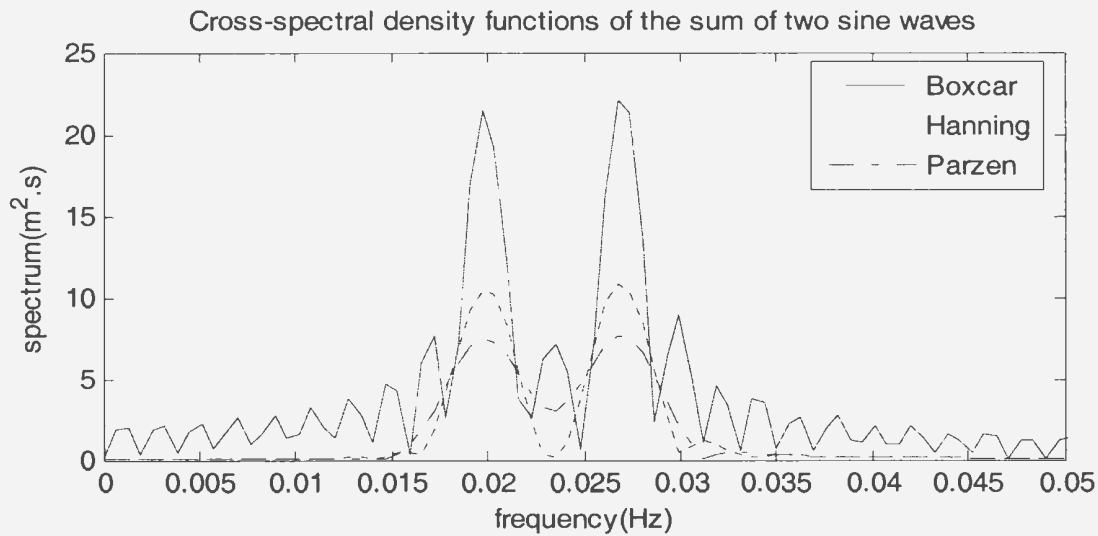


Figure B-6 Estimated cross-spectral density function for the sum of two sine waves using different window functions

Case study 4 Auto-spectral density function of single random wave

In the shaker-excitation tests, the random excitations were used, and the random riser responses were obtained. It is important for this program to obtain a reliable result for random waves. In order to validate the program, a random wave was first designed by composition of a large amount of harmonic component waves, namely

$$x(t) = \sum_{j=1}^n a_j \sin(\omega_j t + \alpha_j) \quad (B-4)$$

where n is the amount of the component sine waves, and a_j , ω_j and α_j are respectively the amplitudes, frequencies and random phases of the component sine waves.

The values of auto-spectral density function of the random wave generated by equation (B-4) are proportional to the square of the amplitudes a_j , i.e. if the values of the estimated auto-spectral density function are proportional to the square of the amplitude a_j , the program is validated.

Now let $n=1401$, $\omega_1=1\text{rad/s}$, $\omega_j = \omega_1 + j\Delta\omega$, where: $\Delta\omega = 0.0457\text{rad/s}$, and α_j take the random values shown in Table B-1, which is generated by Matlab rand function with a

seed of 123, ranging $[0, 2\pi]$ with a uniform distribution, and the amplitude distribution over the frequency range is assumed as

$$a_j = \sqrt{0.00105 \left(\frac{n-j}{n} \right)^3 + 0.000112} \quad (B-5)$$

$$j = 1, 2, \dots, n$$

This equation was designed based on the capacity of an existing shaker provided by Oceanic Consulting Corporation. The generated random wave is shown in Figure B-7.

Let $h=0.01s$, $m=500$ and the sample size $N=12001$, and the estimated auto-spectral density function, using Parzen window function, is shown in Figure B-8. The line in Figure B-8 was calculated by

$$s(\omega_j) = \frac{a_j^2}{\lambda} \quad (B-6)$$

where $\omega_j = \omega_1 + j\Delta\omega$, λ takes the value of 0.0107 from equation (B-3), and a_j take the values from equation (B-5).

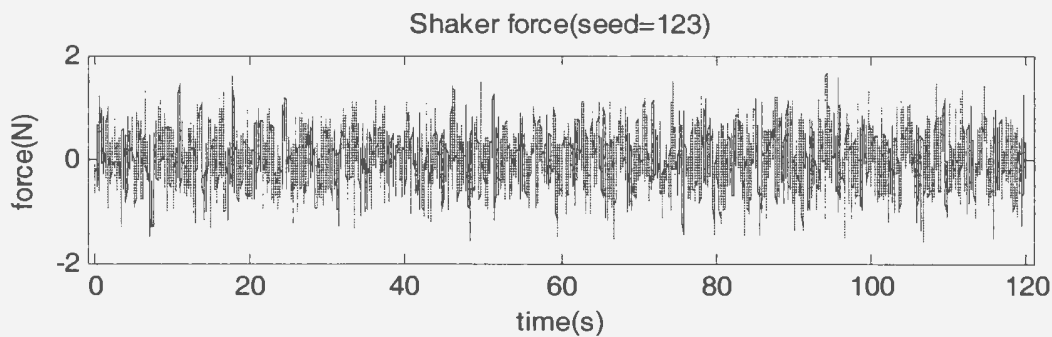


Figure B-7 A random wave generated by Matlab rand function using a seed of 123

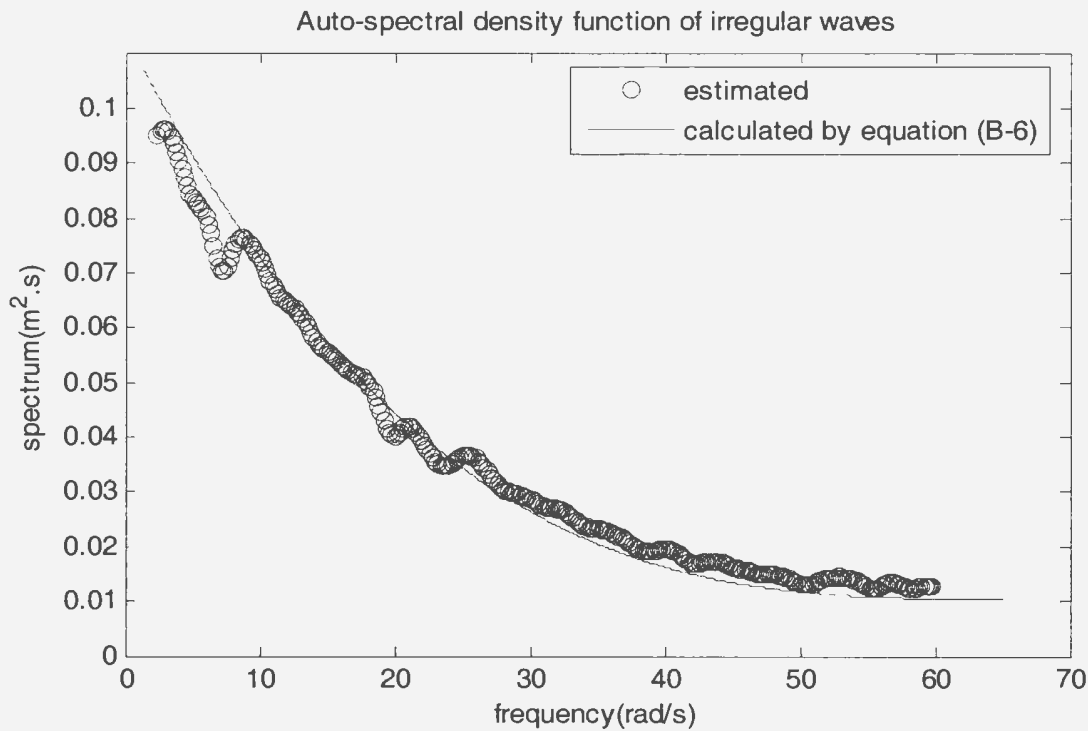


Figure B-8 Estimated auto-spectral density function of random waves

As seen in Figure B-8, at the majority of the frequencies, the estimated spectral function can match the line pretty well, while at some frequencies, for example from $\omega=4$ to 8rad/s, there are considerable errors.

Case study 5 Cross-spectral density function of two random waves

In addition to the random wave shown in Figure B-7, another random wave was designed. The new random wave was assumed to be a response of a SDOF (single degree of freedom) linear mass-damping-spring system to the old random wave. Assume M , C and K are respectively the mass, damping and stiffness of this system, and the new random wave can be obtained by

$$y(t) = \sum_{j=1}^n b_j \sin(\omega_j t + \beta_j)$$

where

$$b_j = \frac{1}{\sqrt{(-M\omega_j^2 + K)^2 + \omega_j^2 C^2}} a_j$$

$$\beta_j = \alpha_j + \tan^{-1} \left(\frac{-\omega_j C}{-M\omega_j^2 + K} \right)$$

The natural frequency for the mass-damping-stiffness system is

$$\omega_n = \sqrt{\frac{K}{M}}$$

and a peak is expected at the natural frequency for the cross-spectral density function.

Let $M=1\text{kg}$, $C=5\text{N.s/m}$ and $K=900\text{N/m}$, and the natural frequency is 30rad/s . The new random wave is shown in Figure B-9. Let $h=0.01\text{s}$, $m=500$ and $N=12001$, and the estimated cross-spectral density function is shown in Figure B-10. As seen in Figure B-10, a peak is found at the frequency of 30rad/s , which is equal to the natural frequency of the assumed system. This result validates the program for the estimate of cross-spectral density functions for random waves.

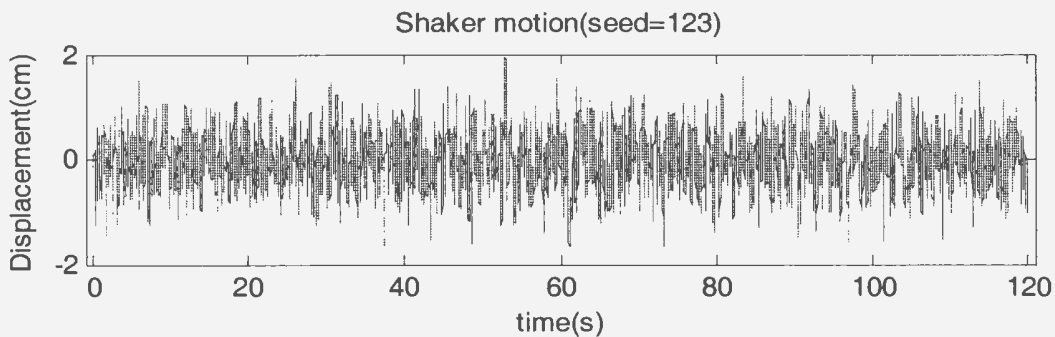


Figure B-9 Another random wave generated by an assumed mass-damping-spring system

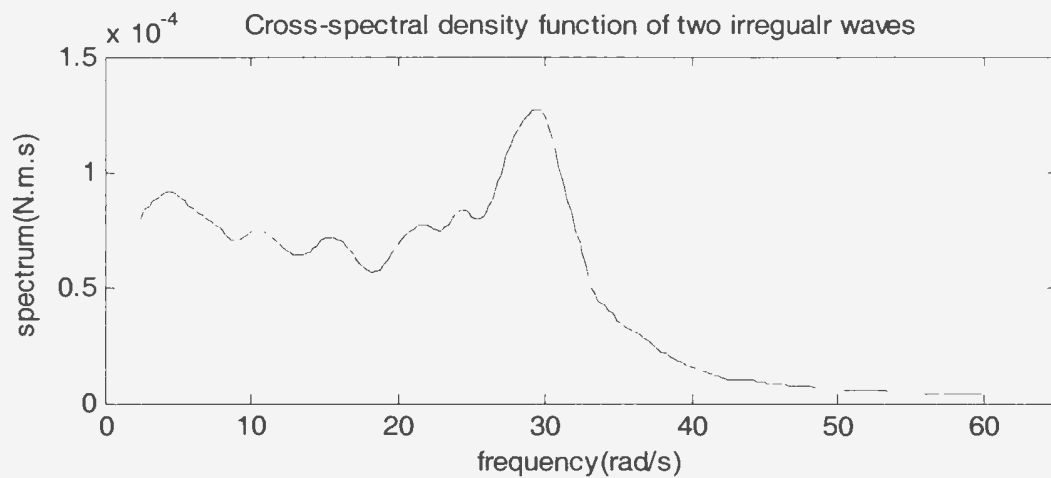


Figure B-10 Estimated cross-spectral density function of two random waves

Conclusions

- i). the program can produce the spectral density functions with enough accuracy for sine waves and random waves;
- ii). if the sample sizes are large enough, the sample size effects on the estimates of spectral density functions can be ignored;
- iii). window functions are important in estimating spectral density functions. Hanning and Parzen window functions can reduce the leakage errors of the estimated spectral density functions.

Table B-1

| | | | | | | | | | | |
|--------|--------|--------|--------|--------|--------|--------|--------|--------|--------|--------|
| 0.5517 | 4.0181 | 0.6197 | 4.3393 | 2.1459 | 1.4824 | 1.6593 | 3.7977 | 2.6270 | 0.8563 | 3.9867 |
| 6.1403 | 5.1868 | 1.8458 | 2.4558 | 0.7544 | 5.4179 | 3.2973 | 5.9992 | 2.9154 | 2.3946 | 2.4297 |
| 1.9588 | 3.7232 | 2.3900 | 5.8889 | 2.2803 | 4.2281 | 5.4263 | 5.6303 | 4.2190 | 3.2650 | 4.3059 |
| 0.1731 | 0.4634 | 2.9152 | 5.9424 | 2.9261 | 0.0634 | 4.5260 | 4.2099 | 0.7135 | 2.8846 | 0.9059 |
| 2.0216 | 4.2039 | 6.1884 | 2.9187 | 2.5571 | 5.7763 | 1.3624 | 2.2683 | 3.7079 | 1.5481 | 0.8238 |
| 3.4811 | 3.7398 | 4.3646 | 0.2788 | 4.2960 | 2.7791 | 4.5797 | 2.1734 | 3.5710 | 0.1680 | 3.0871 |
| 4.4631 | 2.0914 | 2.3870 | 6.1912 | 5.2791 | 1.2376 | 2.7786 | 3.8011 | 3.7621 | 2.2295 | 4.1296 |
| 2.4295 | 4.0115 | 2.4923 | 4.1124 | 1.6738 | 2.4975 | 3.8587 | 3.8660 | 1.0336 | 5.0371 | 5.5908 |
| 0.0100 | 4.0028 | 0.7855 | 1.4156 | 4.0294 | 2.2498 | 0.1796 | 2.7984 | 2.6489 | 4.2465 | 0.8842 |
| 0.5513 | 4.1542 | 1.3661 | 1.5540 | 4.9122 | 4.1935 | 1.7028 | 4.9773 | 5.8696 | 4.3296 | 2.1931 |
| 1.8854 | 1.1430 | 2.9574 | 4.4245 | 0.9322 | 4.3330 | 3.1166 | 4.0403 | 3.7107 | 4.8205 | 3.4712 |
| 1.8148 | 3.5647 | 1.0452 | 5.3099 | 3.9652 | 3.7809 | 4.5474 | 5.6328 | 2.1439 | 5.4301 | 0.7500 |
| 0.5723 | 4.8519 | 3.4431 | 0.1654 | 3.0255 | 5.7636 | 0.5778 | 3.2012 | 0.1109 | 4.7788 | 6.1625 |
| 0.4750 | 3.7047 | 5.5676 | 6.0733 | 3.7219 | 5.0890 | 3.8269 | 4.2808 | 4.5920 | 1.5916 | 2.5229 |
| 3.9917 | 2.2784 | 3.7020 | 3.2689 | 0.7853 | 3.7607 | 3.5756 | 2.8993 | 3.0877 | 1.9725 | 1.8480 |
| 0.9727 | 5.8982 | 1.9753 | 4.4943 | 5.2593 | 1.9263 | 4.7314 | 6.2487 | 5.3371 | 1.7711 | 3.8133 |
| 1.1783 | 5.5924 | 1.9246 | 1.4774 | 6.0619 | 0.6202 | 0.4532 | 1.6359 | 5.8547 | 4.5662 | 0.9073 |
| 5.4960 | 2.5441 | 0.9767 | 4.3952 | 5.5343 | 4.3793 | 1.5673 | 1.8346 | 3.1207 | 3.2618 | 0.6486 |
| 0.5160 | 1.6163 | 3.3550 | 1.4871 | 5.0221 | 5.1069 | 3.1747 | 0.5186 | 1.2960 | 5.0549 | 2.8064 |
| 4.9812 | 1.9485 | 0.9290 | 5.9705 | 3.2014 | 2.5381 | 2.1002 | 5.6793 | 3.6911 | 2.8130 | 3.0951 |
| 0.2627 | 4.2469 | 1.2644 | 0.7271 | 6.0341 | 3.7922 | 5.4779 | 5.3177 | 2.8157 | 5.2431 | 5.3510 |
| 3.1104 | 0.8676 | 5.4320 | 1.6292 | 5.5025 | 4.9608 | 4.5797 | 1.5435 | 5.2298 | 1.4689 | 0.6311 |
| 0.1731 | 5.6775 | 5.2305 | 0.5407 | 2.5876 | 4.0863 | 3.4408 | 5.7810 | 3.7360 | 3.4887 | 5.7845 |
| 6.1989 | 3.5006 | 5.0158 | 5.4466 | 0.9489 | 1.4899 | 2.6969 | 0.0154 | 0.8412 | 0.6041 | 6.1954 |
| 0.7242 | 1.5268 | 0.0330 | 2.3635 | 1.5840 | 0.7890 | 3.3341 | 3.2665 | 4.3028 | 4.0959 | 1.9223 |
| 6.1716 | 2.8547 | 6.0302 | 1.0887 | 1.7450 | 5.2339 | 1.8188 | 0.8938 | 6.1160 | 4.4712 | 0.1265 |
| 2.7069 | 3.9247 | 1.2916 | 5.7537 | 4.6082 | 4.2902 | 0.1895 | 0.1182 | 1.7337 | 3.6788 | 2.6081 |
| 3.6501 | 4.8414 | 1.4898 | 1.1161 | 2.8725 | 4.3328 | 5.4686 | 0.7392 | 1.4722 | 5.6531 | 3.4005 |
| 0.2175 | 4.2699 | 4.2995 | 5.3566 | 2.9965 | 1.8546 | 0.1301 | 0.2125 | 3.4117 | 6.1622 | 1.8649 |
| 2.4873 | 2.2375 | 0.9464 | 2.8735 | 2.5149 | 1.5479 | 3.3439 | 3.9257 | 5.6419 | 3.0995 | 0.1981 |
| 5.2276 | 2.2182 | 3.8103 | 1.1840 | 1.2219 | 3.3317 | 0.9642 | 0.5479 | 4.4114 | 1.4343 | 4.2604 |
| 0.8393 | 0.5860 | 3.5158 | 3.1588 | 3.0446 | 0.4588 | 1.3801 | 4.6113 | 4.5060 | 1.0804 | 0.2591 |
| 0.7402 | 0.2935 | 0.0244 | 1.9713 | 6.0288 | 3.6841 | 4.1965 | 2.1072 | 3.2227 | 2.8816 | 5.7357 |
| 3.1754 | 5.1289 | 2.3742 | 4.9306 | 5.2428 | 0.7577 | 4.2838 | 5.0300 | 5.1168 | 0.0277 | 0.7359 |
| 2.5069 | 4.1126 | 5.3262 | 0.6511 | 4.3242 | 5.8844 | 2.4223 | 3.5018 | 0.2173 | 2.0150 | 0.1195 |
| 3.5844 | 0.4719 | 1.5928 | 4.0666 | 5.0451 | 1.2654 | 5.3033 | 5.9945 | 5.7058 | 3.2570 | 1.4745 |
| 0.9626 | 5.7616 | 5.3030 | 6.1399 | 3.9236 | 2.3453 | 2.7804 | 1.3331 | 5.4618 | 5.2093 | 2.7706 |
| 1.2923 | 5.5002 | 3.0172 | 4.3947 | 2.7439 | 3.8164 | 2.9317 | 0.5463 | 2.2089 | 3.8201 | 3.2970 |
| 2.0251 | 5.2969 | 5.4675 | 1.2588 | 0.8115 | 4.7064 | 2.0645 | 2.8184 | 6.1952 | 4.1624 | 6.2375 |
| 4.4217 | 4.4870 | 2.9582 | 0.1438 | 4.5071 | 0.7717 | 1.9601 | 0.3751 | 2.5745 | 3.9497 | 0.7745 |
| 4.7482 | 0.6090 | 5.9272 | 5.1160 | 5.6750 | 1.5480 | 4.7054 | 4.0405 | 0.6163 | 3.7584 | 1.8271 |
| 2.3496 | 5.8080 | 0.0798 | 3.4390 | 6.1033 | 5.8797 | 4.7373 | 5.3766 | 5.8729 | 2.9784 | 0.1069 |
| 5.7662 | 1.5120 | 3.5946 | 1.4490 | 5.2542 | 2.7387 | 5.0576 | 4.1442 | 2.4254 | 4.8754 | 2.2942 |
| 5.1902 | 1.4885 | 3.5755 | 1.7398 | 4.3909 | 2.4180 | 5.4372 | 6.0984 | 4.1605 | 6.0022 | 2.5535 |
| 2.1897 | 1.9692 | 2.4538 | 4.0027 | 5.3759 | 0.2321 | 5.8313 | 2.0563 | 3.2449 | 4.8719 | 5.7220 |
| 4.7625 | 2.2742 | 1.7894 | 3.7834 | 1.9403 | 1.6668 | 4.0017 | 1.5748 | 2.1479 | 2.9821 | 5.8064 |
| 3.8032 | 1.9165 | 2.1702 | 0.1966 | 5.9674 | 2.6883 | 5.3606 | 1.0459 | 3.7992 | 3.0333 | 5.1064 |
| 1.7656 | 4.7619 | 3.9039 | 3.9146 | 1.2596 | 1.4214 | 1.0546 | 0.1197 | 1.8395 | 2.7300 | 3.5027 |
| 3.4595 | 5.1884 | 3.1842 | 3.1265 | 0.1323 | 5.1196 | 2.8673 | 5.4940 | 0.3226 | 0.2944 | 2.7327 |
| 5.3066 | 3.7442 | 2.5612 | 5.6091 | 5.5025 | 3.8056 | 4.8676 | 2.0171 | 4.2857 | 6.2744 | 3.3313 |
| 5.6703 | 4.3513 | 3.0196 | 1.3524 | 3.5470 | 0.2536 | 2.1405 | 4.9425 | 4.5700 | 2.3122 | 5.9718 |
| 0.9330 | 4.6501 | 3.8157 | 4.4223 | 1.0885 | 3.6870 | 3.4277 | 4.3732 | 0.3139 | 4.7055 | 4.8737 |
| 5.4938 | 3.6112 | 4.1383 | 3.6569 | 6.0873 | 0.8588 | 1.4520 | 6.0927 | 2.3387 | 5.1093 | 5.3201 |

| | | | | | | | | | | |
|--------|--------|--------|--------|--------|--------|--------|--------|--------|--------|--------|
| 5.0989 | 1.6579 | 5.4724 | 0.9915 | 1.2303 | 0.0639 | 5.1861 | 2.5830 | 1.9995 | 3.0271 | 1.7581 |
| 4.4107 | 1.4309 | 4.0611 | 0.4973 | 1.5067 | 1.6472 | 1.5728 | 1.0995 | 0.4299 | 5.4593 | 1.3151 |
| 5.2378 | 3.4935 | 5.2420 | 6.0807 | 2.8329 | 4.3289 | 2.9149 | 1.1790 | 4.9937 | 4.9597 | 4.1344 |
| 0.6663 | 1.2192 | 2.4395 | 3.4913 | 5.7605 | 4.8526 | 1.8169 | 0.9979 | 1.8019 | 0.1426 | 3.4472 |
| 5.6070 | 2.2792 | 3.4318 | 5.0722 | 4.6936 | 6.1658 | 0.5173 | 4.0458 | 0.5768 | 4.9896 | 4.5175 |
| 6.1753 | 2.5146 | 2.6204 | 1.6463 | 4.1622 | 3.1124 | 2.1725 | 1.5099 | 5.0032 | 0.8305 | 4.0343 |
| 2.4531 | 4.9030 | 0.5895 | 4.6591 | 4.3234 | 4.3568 | 0.4838 | 0.0297 | 2.5320 | 5.2606 | 4.3272 |
| 0.1190 | 1.8904 | 4.7252 | 2.8081 | 3.1763 | 1.4839 | 1.2835 | 1.0827 | 1.0176 | 0.5439 | 4.8217 |
| 4.7794 | 2.4536 | 0.3557 | 3.0604 | 2.0347 | 3.7680 | 1.1177 | 3.9417 | 4.7656 | 3.6934 | 2.6348 |
| 5.0141 | 1.4874 | 3.8097 | 3.7378 | 1.6291 | 4.4497 | 3.5531 | 1.3756 | 3.4327 | 1.7957 | 1.9955 |
| 5.4991 | 3.3549 | 1.0528 | 0.3616 | 1.9263 | 4.4441 | 4.2870 | 2.2540 | 1.9256 | 4.4828 | 1.5515 |
| 0.6438 | 0.3613 | 2.9206 | 2.6614 | 0.3963 | 1.0122 | 3.7182 | 6.2587 | 2.8734 | 1.0403 | 4.3427 |
| 2.7633 | 3.9247 | 1.7217 | 2.1691 | 1.6184 | 0.2316 | 3.8480 | 0.2253 | 4.5751 | 5.8830 | 3.4021 |
| 2.5447 | 5.5273 | 0.3312 | 5.0300 | 5.1827 | 1.6653 | 3.9474 | 6.2213 | 3.5352 | 1.5896 | 0.9011 |
| 2.3056 | 1.2172 | 5.4916 | 2.8281 | 0.3300 | 5.1162 | 2.1717 | 1.3136 | 5.4875 | 3.7302 | 6.0494 |
| 3.6438 | 4.8380 | 1.7295 | 1.4420 | 0.8596 | 1.9055 | 0.6177 | 1.4939 | 0.9421 | 0.5994 | 2.6159 |
| 1.3814 | 1.2766 | 4.9504 | 5.6497 | 2.9639 | 1.1235 | 1.7268 | 5.9147 | 2.9244 | 2.9550 | 1.5913 |
| 2.9456 | 1.4123 | 5.2247 | 3.6679 | 2.4281 | 0.0445 | 5.7508 | 5.2141 | 1.7240 | 4.1561 | 1.9060 |
| 1.8204 | 2.3046 | 4.4218 | 5.4264 | 0.6638 | 3.7432 | 5.3542 | 0.2676 | 5.4685 | 4.4357 | 0.5251 |
| 3.4467 | 3.9393 | 2.5911 | 6.2107 | 0.2726 | 1.3238 | 0.8002 | 3.6409 | 0.2791 | 4.3594 | 0.6525 |
| 2.6300 | 0.6778 | 0.6679 | 3.4948 | 1.3234 | 0.1714 | 2.2927 | 4.0786 | 5.7427 | 1.7305 | 0.4865 |
| 2.6549 | 3.2922 | 1.8524 | 5.7038 | 1.3085 | 1.0103 | 3.1300 | 2.4440 | 3.7767 | 2.2548 | 2.0283 |
| 2.8370 | 3.9214 | 2.6967 | 3.4225 | 0.0930 | 4.7958 | 2.3525 | 4.3393 | 1.2316 | 3.4798 | 1.8494 |
| 5.7963 | 4.2529 | 0.1768 | 5.8682 | 5.3129 | 4.1936 | 3.4479 | 5.8856 | 3.8419 | 4.5466 | 4.5586 |
| 5.9227 | 4.7017 | 4.4021 | 1.5980 | 2.9189 | 4.9942 | 0.3999 | 4.8519 | 3.2685 | 0.4221 | 0.5192 |
| 4.4569 | 4.8271 | 1.2842 | 0.0582 | 4.9689 | 3.0068 | 5.7543 | 0.9881 | 6.0193 | 0.2489 | 5.4121 |
| 0.1328 | 1.0894 | 0.6346 | 2.5276 | 0.8027 | 0.7012 | 3.5191 | 2.0074 | 4.5371 | 2.9576 | 1.4610 |
| 0.0086 | 0.5888 | 0.3087 | 4.3587 | 0.5487 | 4.1165 | 2.2102 | 1.4489 | 5.1230 | 3.9245 | 3.8048 |
| 2.7625 | 3.1152 | 5.1007 | 5.6369 | 1.8462 | 3.4770 | 4.6691 | 2.9961 | 2.6099 | 1.2582 | 4.1565 |
| 2.4404 | 5.9800 | 6.2824 | 5.4999 | 4.8944 | 0.2837 | 6.0032 | 0.0894 | 0.3449 | 3.5363 | 1.2628 |
| 0.0517 | 1.5461 | 4.8601 | 2.7671 | 4.2893 | 3.3696 | 3.1581 | 4.0213 | 4.5299 | 0.8476 | 1.4842 |
| 0.0224 | 6.2523 | 2.3745 | 3.5555 | 4.7287 | 5.2992 | 0.0635 | 5.2231 | 2.1973 | 3.6103 | 1.7805 |
| 4.1000 | 1.8044 | 3.6037 | 3.5886 | 1.0705 | 3.8545 | 2.7947 | 2.9112 | 0.7902 | 4.3000 | 0.7448 |
| 1.0119 | 4.8236 | 4.5534 | 6.2513 | 3.7694 | 6.0627 | 0.8311 | 0.3881 | 1.3424 | 5.2162 | 4.8324 |
| 1.1663 | 4.1816 | 3.3913 | 2.8762 | 4.3571 | 4.7728 | 4.5905 | 1.8798 | 1.8960 | 4.0662 | 4.0160 |
| 3.3445 | 2.0900 | 4.2691 | 2.6383 | 1.8056 | 4.3998 | 6.0935 | 3.4020 | 0.0651 | 1.3714 | 2.5757 |
| 5.1918 | 3.5794 | 2.9345 | 2.8307 | 5.7533 | 4.5281 | 1.8750 | 2.7310 | 1.9842 | 3.7517 | 3.8322 |
| 4.4022 | 2.8273 | 4.8866 | 1.0826 | 5.3928 | 2.6413 | 1.7650 | 0.8516 | 0.1362 | 2.7658 | 0.9800 |
| 2.3425 | 5.6496 | 0.5876 | 4.6919 | 2.5336 | 0.8318 | 0.1348 | 3.0572 | 5.4615 | 0.0643 | 5.6879 |
| 4.5995 | 1.4412 | 0.6892 | 2.7501 | 1.5871 | 2.1978 | 0.2654 | 0.2427 | 1.8610 | 0.7026 | 1.7750 |
| 0.7007 | 1.6279 | 2.5029 | 1.1472 | 4.2935 | 4.6266 | 4.7686 | 4.5618 | 2.0775 | 1.3463 | 1.7791 |
| 5.9962 | 1.3194 | 2.3136 | 4.9618 | 3.3717 | 5.9898 | 1.6594 | 5.0467 | 3.0029 | 3.2137 | 2.1856 |
| 1.6656 | 2.4432 | 1.4264 | 3.4851 | 1.5631 | 0.3886 | 3.0005 | 0.8210 | 6.1813 | 3.2215 | 1.9618 |
| 4.3773 | 4.9444 | 5.7447 | 4.3654 | 0.9787 | 5.1313 | 5.5953 | 5.6726 | 4.7654 | 0.9969 | 4.2491 |
| 5.8797 | 3.8666 | 5.3258 | 1.1741 | 3.8629 | 5.2798 | 0.1657 | 1.6881 | 3.7286 | 3.8230 | 1.0292 |
| 0.9305 | 0.1172 | 3.6892 | 1.5848 | 1.1576 | 3.1008 | 2.8591 | 5.8610 | 5.0991 | 4.8270 | 4.3491 |
| 2.4328 | 2.7955 | 4.1595 | 2.7093 | 0.9698 | 0.4778 | 0.3730 | 3.9508 | 0.6903 | 3.1191 | 2.3694 |
| 0.2780 | 3.2761 | 1.6426 | 5.0343 | 1.7398 | 5.6964 | 2.8276 | 4.2439 | 1.3464 | 3.5612 | 5.5528 |
| 2.1795 | 5.3345 | 1.7240 | 3.8801 | 5.3420 | 2.0197 | 3.1727 | 4.7028 | 3.9381 | 6.2654 | 2.8226 |
| 1.7726 | 4.2517 | 5.5900 | 4.4136 | 0.2772 | 2.8949 | 3.0998 | 4.2443 | 0.9790 | 5.1885 | 4.4939 |
| 5.4980 | 5.1095 | 3.1568 | 1.1244 | 3.9796 | 0.2366 | 5.8416 | 5.1233 | 2.8598 | 4.9652 | 3.4135 |
| 5.1757 | 4.2056 | 3.1597 | 5.0872 | 4.4845 | 4.4962 | 5.5986 | 5.0664 | 1.4068 | 1.2375 | 1.7875 |
| 2.8956 | 2.3467 | 1.6426 | 4.6092 | 1.6604 | 2.8539 | 5.5185 | 2.7360 | 3.3369 | 5.7373 | 4.8830 |
| 3.1965 | 2.2847 | 1.7746 | 4.9160 | 6.1936 | 3.0167 | 2.4038 | 0.1257 | 1.3288 | 2.8529 | 1.2840 |
| 3.1279 | 5.8302 | 2.6788 | 3.6967 | 2.2057 | 1.2197 | 4.5301 | 4.5929 | 4.2745 | 5.8266 | 3.9190 |
| 0.3882 | 2.3458 | 5.3956 | 5.6278 | 5.9160 | 4.9072 | 2.5255 | 2.5331 | 5.8308 | 5.0439 | 0.8743 |

Appendix B

| | | | | | | | | | | |
|--------|--------|--------|--------|--------|--------|--------|--------|--------|--------|--------|
| 4.1411 | 6.2381 | 3.1104 | 0.5220 | 2.6198 | 5.4355 | 3.0324 | 3.1503 | 5.5526 | 3.8711 | 4.8451 |
| 0.8711 | 0.4949 | 4.8691 | 2.7981 | 5.0768 | 0.7117 | 4.2943 | 5.7642 | 4.4595 | 5.1347 | 5.9653 |
| 4.9511 | 5.2100 | 2.1863 | 1.4407 | 4.3392 | 0.0373 | 5.6271 | 5.7044 | 4.3150 | 2.2555 | 1.0454 |
| 2.2704 | 1.6223 | 3.7424 | 4.1619 | 5.1634 | 3.4308 | 0.4288 | 0.4567 | 3.2666 | 5.7787 | 3.1135 |
| 1.8126 | 2.8189 | 2.4971 | 3.6555 | 0.7750 | 0.2795 | 3.4937 | 1.4285 | 1.1945 | 1.3632 | 2.9816 |
| 3.9766 | 6.1252 | 3.2455 | 2.5889 | 6.0406 | 1.1772 | 5.1452 | 0.2307 | 0.8057 | 1.4572 | 4.8758 |
| 2.6514 | 1.8494 | 5.7352 | 1.9285 | 3.5583 | 1.8252 | 0.9341 | 4.5247 | 0.7499 | 4.9433 | 5.8140 |
| 5.2467 | 2.6135 | 5.1993 | 4.3313 | 4.7881 | 5.3720 | 3.6249 | 1.4283 | 3.1573 | 3.5812 | 3.1551 |
| 3.4532 | 0.6969 | 1.2588 | 1.0439 | 1.6657 | 3.5420 | 3.5842 | 1.9553 | 1.5370 | 1.7501 | 2.1333 |
| 2.4483 | 5.6219 | 0.4411 | 6.0299 | 2.7274 | 4.1794 | 4.1841 | 1.5278 | 5.0860 | 3.1240 | 2.4797 |
| 5.8213 | 3.5473 | 5.1227 | 5.1387 | 3.5111 | 5.5760 | 2.3973 | 3.9722 | 2.2950 | 5.5779 | 3.1385 |
| 1.1957 | 2.5035 | 4.0069 | 1.5155 | 5.7974 | 4.1512 | 0.4583 | 6.1214 | 0.7896 | 1.5220 | 1.1087 |
| 4.9684 | 0.8953 | 5.2586 | 1.6430 | 5.5083 | 1.7529 | 5.6596 | 5.9100 | 5.1512 | 0.3328 | 0.6825 |
| 4.5308 | 3.1660 | 5.0512 | 2.7983 | 1.1276 | 1.8303 | 6.1504 | 5.2063 | 2.7718 | 1.7409 | 5.2027 |
| 4.6750 | 1.7248 | 4.2530 | 2.4404 | 4.7116 | 0.7173 | 4.9741 | 2.2460 | 5.3221 | 0.7677 | 3.4268 |
| 2.6288 | 4.9720 | 4.6020 | 6.0045 | 2.6400 | 5.3619 | 4.3189 | 4.3558 | 2.8243 | 5.5004 | 0.4587 |
| 5.6402 | 0.0391 | 3.7887 | 2.4393 | 5.8532 | 4.3917 | 3.3747 | 0.9532 | 4.4046 | 5.1798 | 3.4172 |
| 5.2748 | 4.7695 | 0.9245 | 5.9063 | 6.2047 | 0.4864 | 0.6127 | 5.5993 | 4.7839 | 3.9362 | 5.7658 |
| 0.0298 | 4.9152 | 5.1280 | 0.6324 | | | | | | | |

Appendix C

Validation of the program to estimate system parameters for a linear system

Method of Estimation

Physical and engineering systems can be classified into linear and nonlinear systems.

A system is a linear system if the following equality exists (Bendat, 1998):

$$p[c_1x_1 + c_2x_2] = c_1p[x_1] + c_2p[x_2] \quad (C-1)$$

where x_1 and x_2 represent any inputs to the system, p represents the corresponding outputs from the system, and c_1 and c_2 represents any constants.

The dynamic characteristics of a single-degree-of-freedom (SDOF) linear system can be described by weighting function $h(\tau)$ and the time-domain relationship between the system input $x(t)$ and the system output $p(t)$ is established by

$$p(t) = \int_{-\infty}^{\infty} h(\tau)x(t-\tau)d\tau \quad (C-2)$$

From equation (C-2), two expressions can be obtained. Fourier transform of both sides of equation (C-2) gives the first expression as follows:

$$P(\omega) = H(\omega)X(\omega) \quad (C-3)$$

where $P(\omega)$, $X(\omega)$ and $H(\omega)$ are respectively Fourier transforms of $p(t)$, $x(t)$ and $h(\tau)$. $H(\omega)$ are called Dynamic Stiffness (DS), which are generally complex functions, and the inverse of DS is known as Frequency Response Function (FRF).

According to equation (C-2), the product $z(t)q(t+\tau)$ is given by

$$x(t)p(t+\tau) = \int_{-\infty}^{+\infty} h(\xi)x(t)x(t+\tau-\xi)d\xi \quad (C-4)$$

Fourier transform of both sides of equation (C-4) yields the second expression for the DS as follows:

$$S_{xx}(\omega)H(\omega) = S_{xp}(\omega) \quad (C-5)$$

where the symbols $S_{xx}(\omega)$ and $S_{xp}(\omega)$ respectively denote Fourier transforms of the auto-correlation function of $x(t)$ and the cross-correlation function of $x(t)$ and $p(t)$, i.e. the auto-spectral density function of $x(t)$ and the cross-spectral density function of $x(t)$ and $p(t)$.

On other hand, for a mass-damping-stiffness system, the input $x(t)$ and output $p(t)$ follow a linear differential equation, namely we have

$$M\ddot{x}(t) + C\dot{x}(t) + Kx(t) = p(t) \quad (C-6)$$

where M , C and K are the mass, damping and stiffness, which are called the system parameters. Fourier transform of both sides of equation (C-6) gives

$$[(-\omega^2 M + K) + i\omega C]X(f) = P(f) \quad (C-7)$$

where $X(\omega)$ is Fourier transform of $x(t)$, and $F(\omega)$ is Fourier transform of $f(t)$.

Combination of equations (C-3), (C-5) and (C-7) gives

$$H(\omega) = (-\omega^2 M + K) + i\omega C = \frac{S_{xp}(\omega)}{S_{xx}(\omega)} \quad (C-8)$$

$$i = \sqrt{-1}$$

Note that there is a linear relationship in equation (C-8) between the real part of $H(\omega)$ and ω^2 , namely

$$\text{Re}[H(\omega)] = \text{Re}\left(\frac{S_{xp}(\omega)}{S_{xx}(\omega)}\right) = -\omega^2 M + K$$

and obviously the slope is related to the mass M , and the intercept is related to the stiffness K . This linear relationship provides a way to estimate the system parameters M and K using a linear fit based on the DS. Specifically, if the input and output are known,

the DS can be estimated based on the auto-spectral density function of the input and the cross-spectral density function between the input and output, and then the system parameters M and K can be obtained by the linear fit of $Re[H(\omega)]$ versus ω^2 . The modal natural frequency ω_n and modal damping can then be estimated using the following formulae:

$$\omega_n = \sqrt{\frac{K}{M}}$$

$$C = \frac{1}{\omega_n} I_m \left[\frac{S_{xp}(\omega_n)}{S_{xx}(\omega_n)} \right]$$

Case Studies

Case study C-1 System parameters of large-damping system

For the system defined by equation (C-6), the major system characteristics depend on two dimensionless parameters, or undamped natural frequency f_n and damping ratio ζ , which are defined as

$$f_n = \frac{1}{2\pi} \sqrt{\frac{K}{M}}$$

$$\zeta = \frac{C}{2\sqrt{KM}}$$

A system is a large-damping system if ζ is greater than 0.5 (He and Fu, 2001). It is well-known that no peak exists in the FRF amplitude plot for a large-damping system.

Case C-1-1 Assume $M=1\text{kg}$, $C=50\text{N.s/m}$, $K=900\text{N/m}$, and this system is a large-damping system, because $\zeta=0.833$. The random input $x(t)$ is obtained by composition of a large amount of harmonic component waves, namely

$$x(t) = \sum_{j=1}^n a_j \sin(\omega_j t + \alpha_j) \quad (C-9)$$

where n is the amount of the harmonic components, and a_j , ω_j and α_j are respectively the amplitudes, frequencies and random phases of the harmonic components. Let $n=1401$, $\omega_1=1\text{rad/s}$, $\omega_j= \omega_1+ j\Delta\omega$, where: $\Delta\omega =0.0457\text{rad/s}$, and α_j take the random values shown in Table B-1, and the amplitude distribution over the frequency range is assumed as

$$a_j = \sqrt{0.00105 \left(\frac{n-j}{n} \right)^3 + 0.000112}$$

$$j = 0,1,2,\dots,n$$

The resultant random input $x(t)$ is shown in Figure B-7.

The output $p(t)$ can be calculated based on equations (C-6) and (C-9), namely we have

$$p(t) = \sum_{j=1}^n \left[(-\omega_j^2 M + K) a_j \sin(\omega_j t + \alpha_j) + \omega_j \cos(\omega_j t + \alpha_j) \right] \quad (C-10)$$

The generated output contains the information of the system parameters M , C and K . Now apply the present technique to the input and output. If the estimated values of M , C and K are close to the actual values of 1kg , 50N.s/m and 900N/m , the present technique is validated.

The estimated FRF is shown in Figure C-1. From equation (C-8), the actual FRF can be calculated by

$$\Theta(f) = \frac{1}{\sqrt{(-\omega^2 M + K)^2 + \omega^2 C^2}} \quad (C-11)$$

and the actual FRF is also plotted in Figure C-1. As seen in Figure C-1, there is a good agreement between the two groups of values.

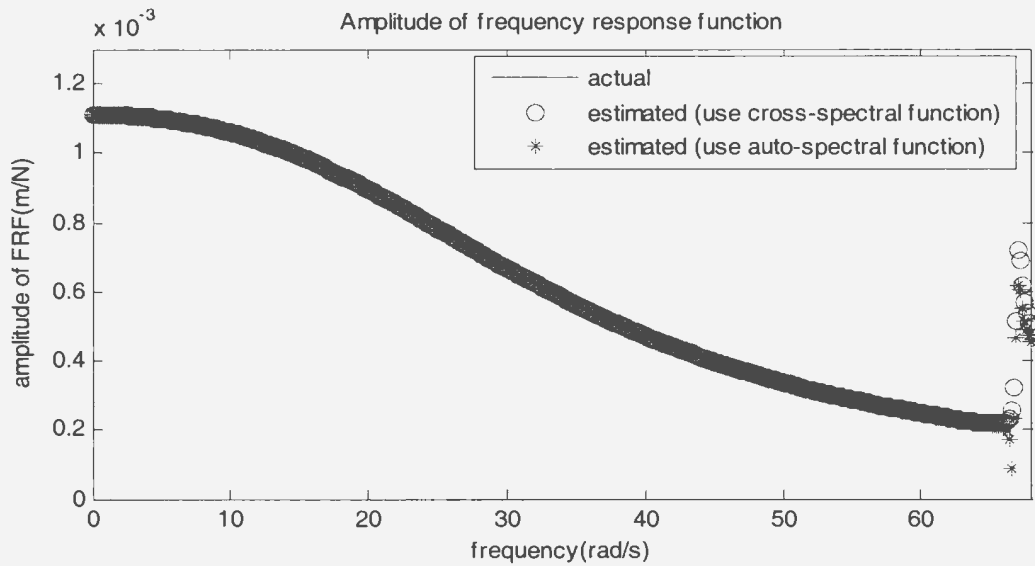


Figure C-1 The actual and estimated FRF amplitude for a large-damping system ($\zeta=0.833$)

It is noted that the values at the frequencies beyond 65(rad/s) are useless, because the input does not contain these frequency components.

The Matlab fit function was used to fit the real part of the DS function, and the fitting plot is shown in Figure C-2.

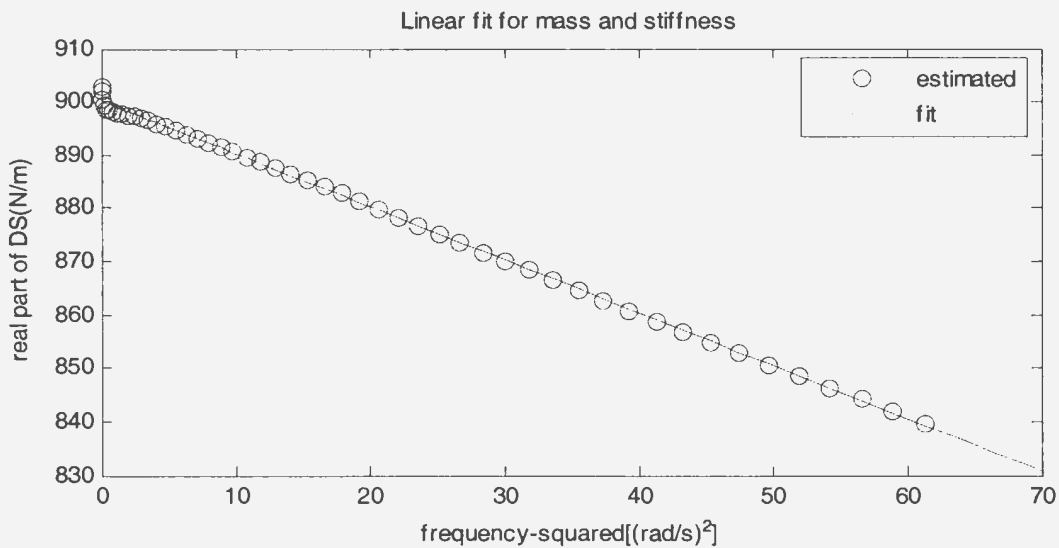


Figure C-2 Linear fit for mass and stiffness for a large-damping system ($\zeta=0.833$)

The slope and intercept of the fitting line in Figure C-2 are respectively 0.992 and 900.09. These values represent respectively the estimates of M and K , which are close to the actual values of M and K .

The imaginary part of the dynamic stiffness function is shown in Figure C-3. As seen in Figure C-3, as the damping used is independent of frequency, the imaginary part of the dynamic stiffness function is a linear function of frequency. The estimated damping is 47.03 N.s/m, which is close to the actual value of 50 N.s/m.

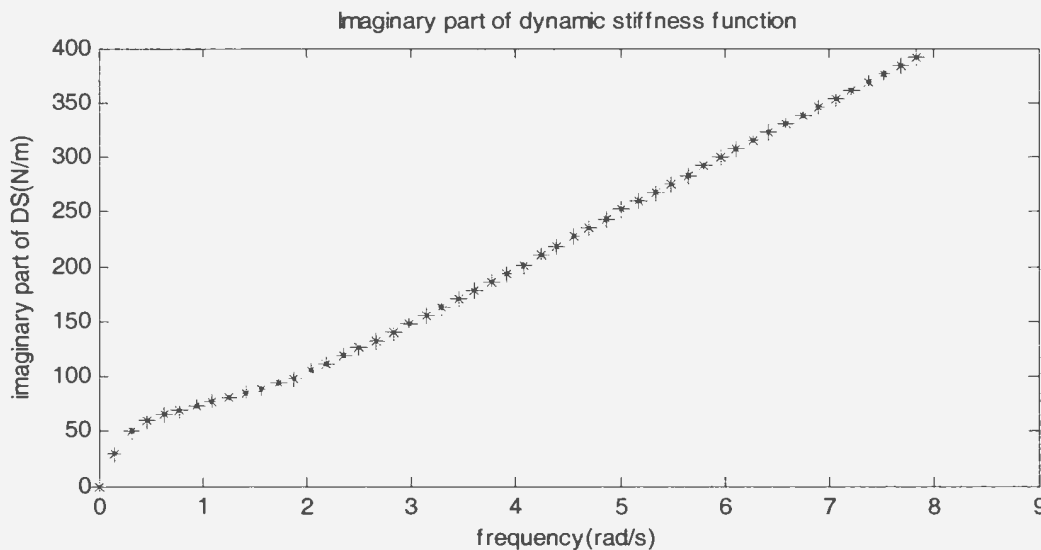


Figure C-3 Imaginary part of dynamic stiffness function for a large-damping system ($\zeta=0.833$)

Case study C-2 System parameters of moderate-damping SDOF linear system

A system is a moderate-damping system if ζ is greater than 0.05 and smaller than 0.5. It is well-known that an obtuse peak exists in the FRF amplitude plot for a moderate-damping system (He and Fu, 2001).

Case C-2-1 Assume $M=1\text{kg}$, $C=5\text{N.s/m}$, $K=900\text{N/m}$, and this system is obviously a moderate-damping system, because $\zeta =0.0833$. The input $x(t)$ still takes the same time

series as in Case C-1-1, and the output can be calculated using equation (C-10). The estimated and actual FRFs are shown in Figure C-4. As seen in Figure C-4, the estimated FRF matches the actual FRF well for the moderate-damping system.

Figure C-5 shows the real part of the estimated dynamic stiffness function and the linear fit for estimate of the mass and stiffness. The estimated mass and stiffness are 0.983kg and 898.89N/m, which are close to the actual values.

Figure C-6 shows the imaginary part of the estimated dynamic stiffness function, and the estimated damping is 4.766N.s/m, which is close to the actual value of the damping.

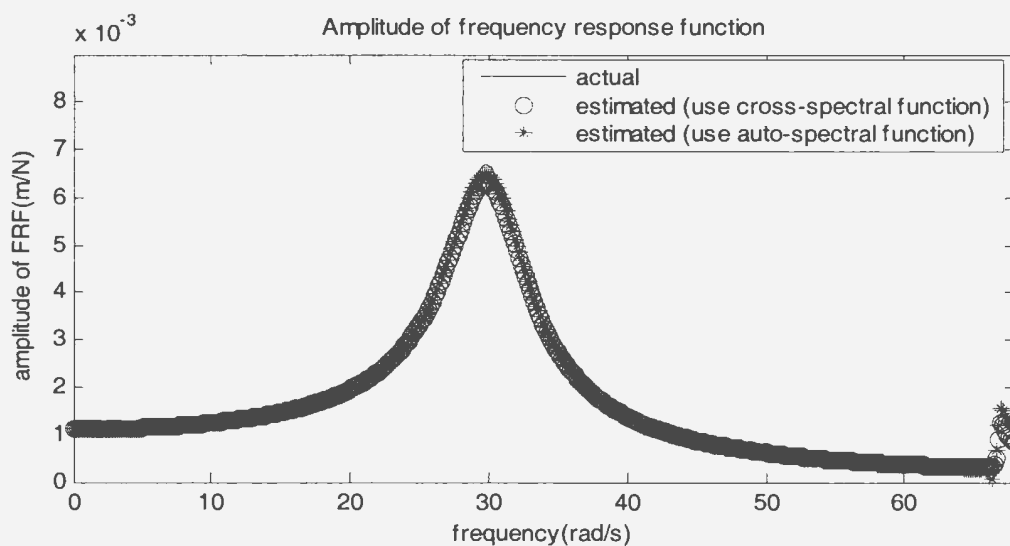


Figure C-4 The actual and estimated FRFs for a moderate-damping system ($\zeta = 0.0833$)

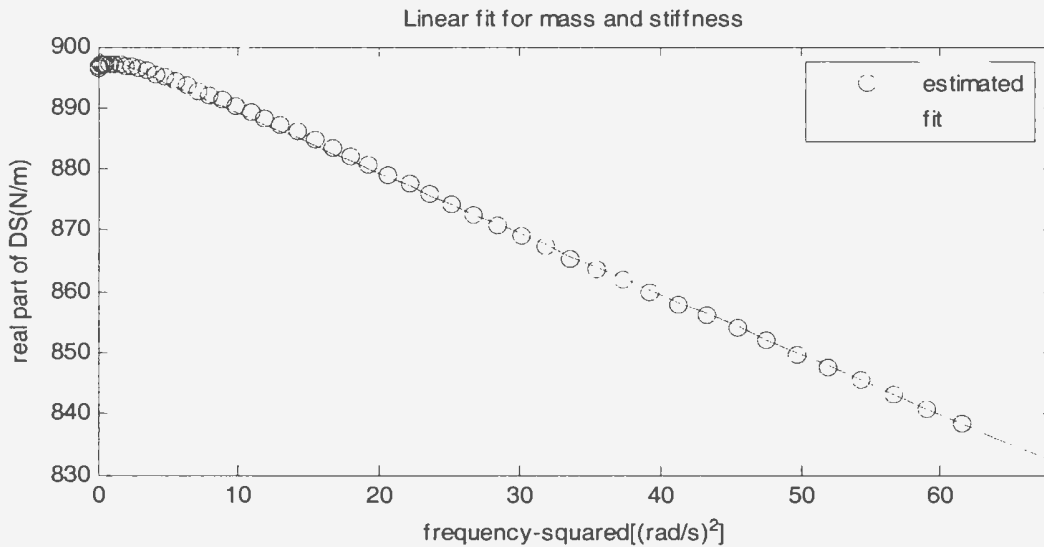


Figure C-5 Linear fit for mass and stiffness for a moderate-damping system ($\zeta=0.0833$)

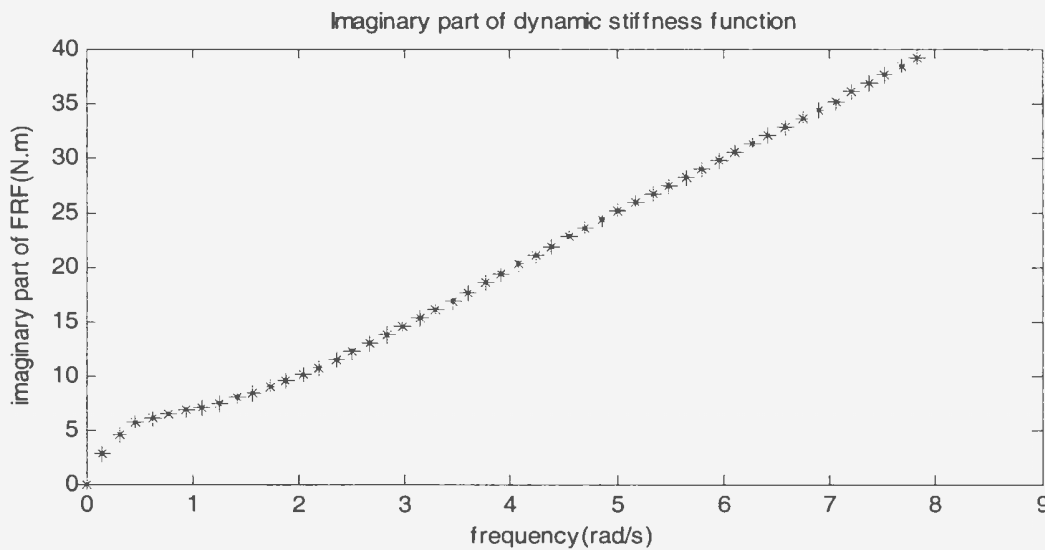


Figure C-6 Imaginary part of dynamic stiffness function for a moderate-damping system ($\zeta=0.0833$)

Case C-2-2 Assume $M=0.25\text{kg}$, $C=5\text{N.s/m}$, $K=900\text{N/m}$, and this system is also a moderate-damping system, because $\zeta=0.167$. The input $x(t)$ still takes the same time series as in Case C-1-1, and the output can be calculated using equation (C-10). The estimated and actual FRFs are shown in Figure C-7. As seen in Figure C-7, the estimated FRF matches the actual FRF well for this moderate-damping system.

Figure C-8 shows the real part of the estimated dynamic stiffness function and the linear fit for estimate of the mass and stiffness. The estimated mass and stiffness are 0.261kg and 900.35N/m, which are close to the actual values.

Figure C-9 shows the imaginary part of the estimated dynamic stiffness function, and the estimated damping is 4.495N.s/m, which is close to the actual value of the damping.

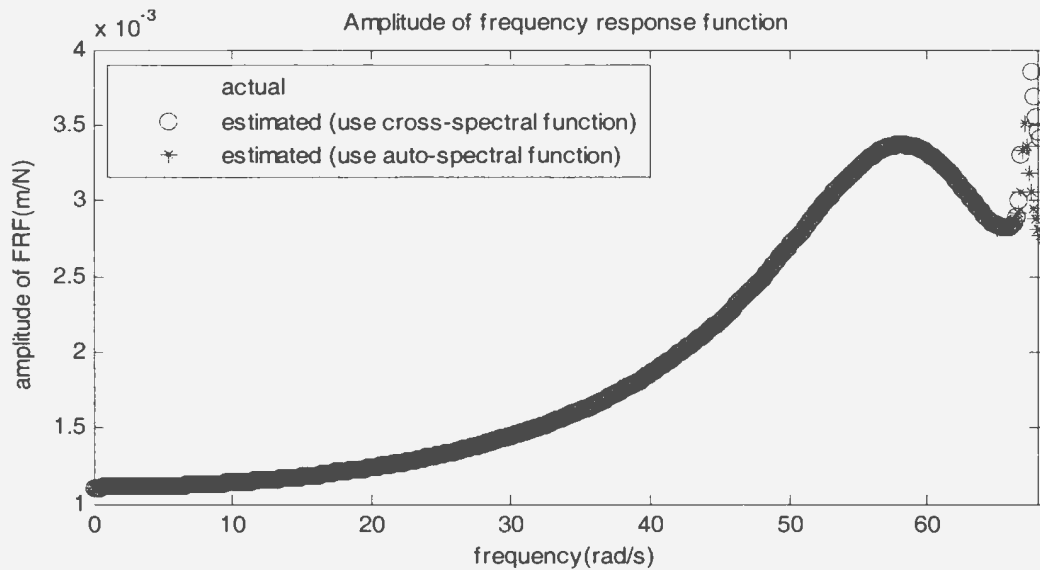


Figure C-7 The actual and estimated FRFs for a moderate-damping system ($\zeta=0.167$)

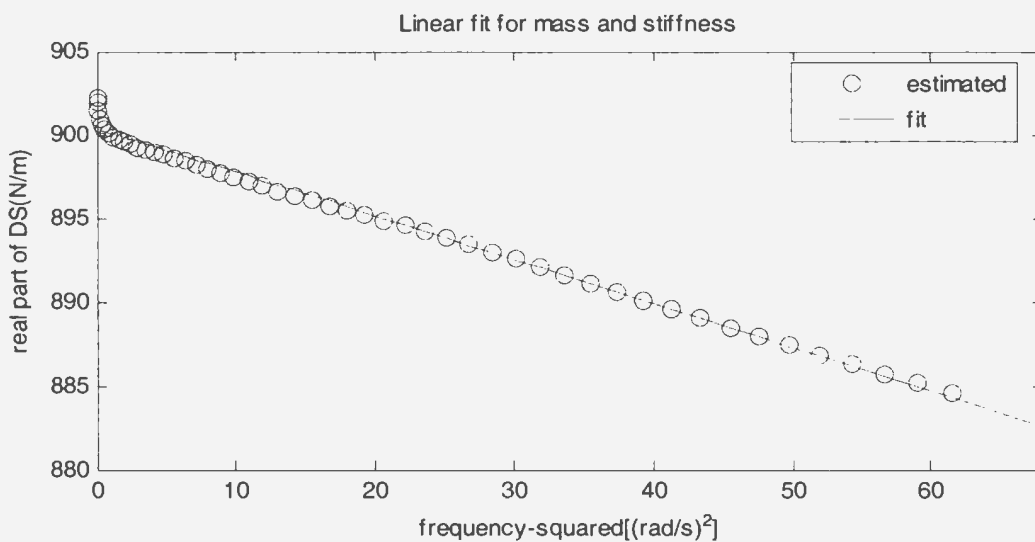


Figure C-8 Linear fit for mass and stiffness for a moderate-damping system ($\zeta=0.167$)

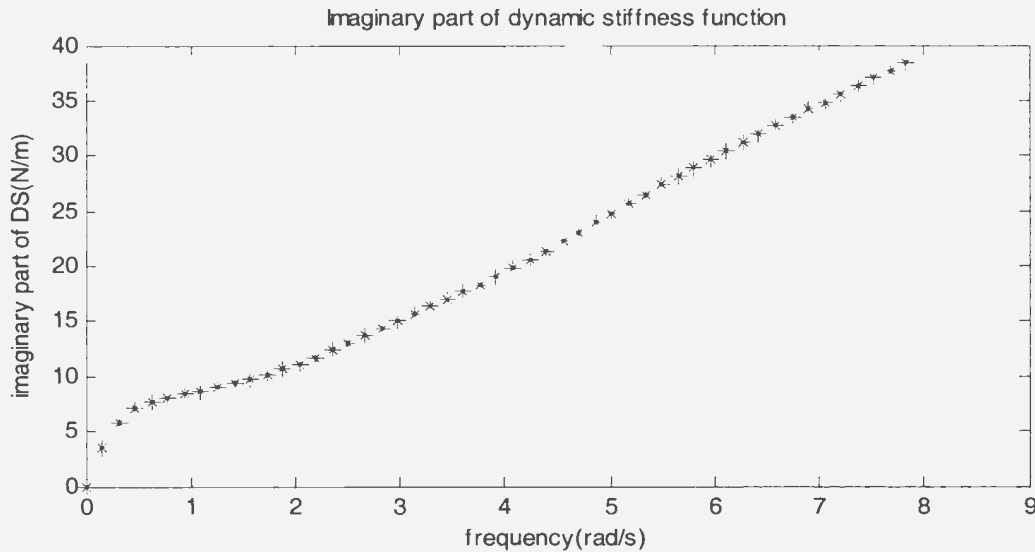


Figure C-9 Imaginary part of dynamic stiffness function for a moderate-damping system ($\zeta = 0.167$)

Case C-2-3 Assume $M=1\text{kg}$, $C=5\text{N.s/m}$, $K=225\text{N/m}$, and this system is obviously a moderate-damping system, because $\zeta = 0.167$. The input $x(t)$ takes the same time series as in Case C-1-1, and the output can be calculated using equation (C-10). The estimated and actual FRFs are shown in Figure C-10. As seen in Figure C-10, the estimated FRF matches the actual FRF well for this moderate-damping system.

Figure C-8 shows the real part of the estimated dynamic stiffness function and the linear fit to estimate the mass and stiffness. The estimated mass and stiffness are 0.997 kg and 223.61N/m , which are close to the actual values.

Figure C-9 shows the imaginary part of the estimated dynamic stiffness function, and the estimated damping is 5.065N.s/m , which is close to the actual value of the damping.

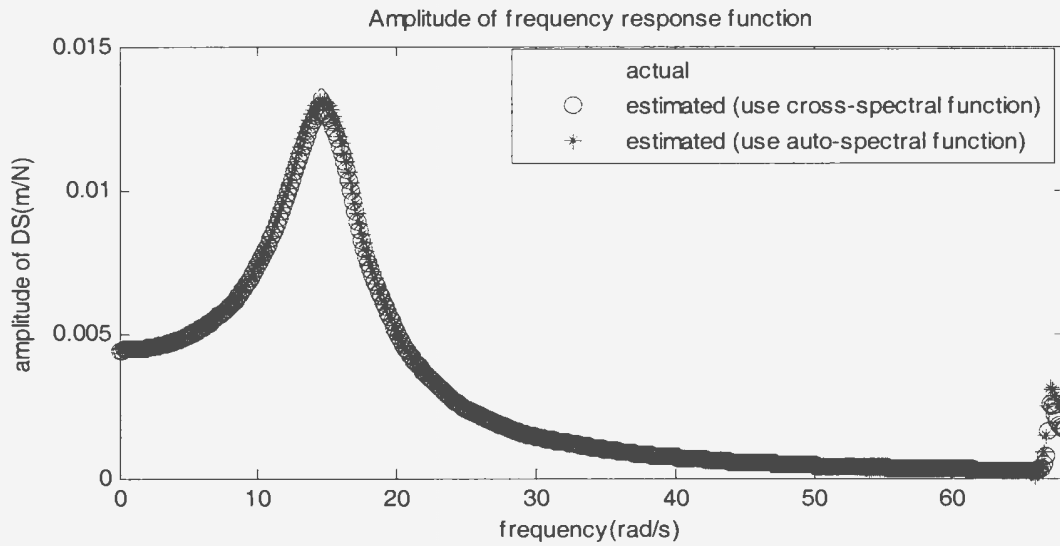


Figure C-10 The actual and estimated FRFs for a moderate-damping system ($\zeta=0.167$)

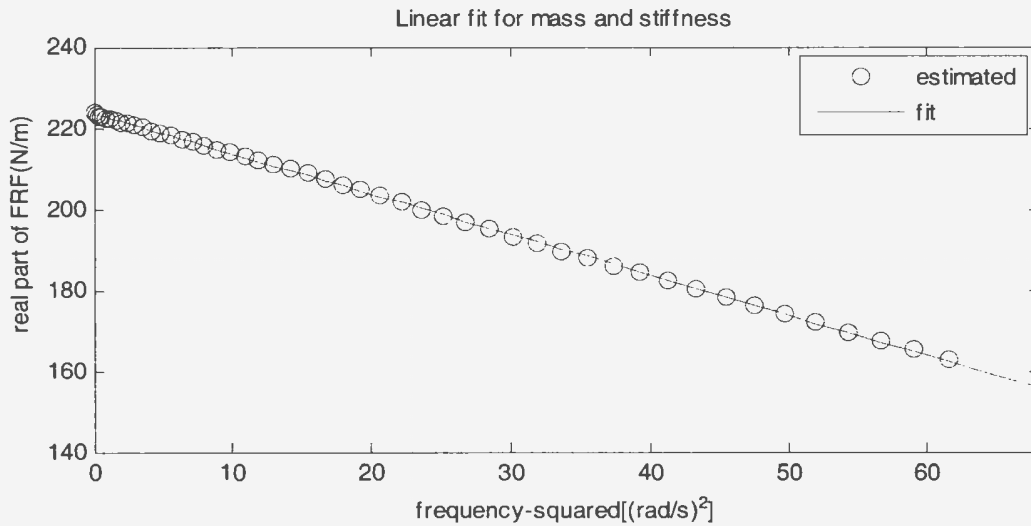


Figure C-11 Linear fit for mass and stiffness for a moderate-damping system ($\zeta=0.167$)

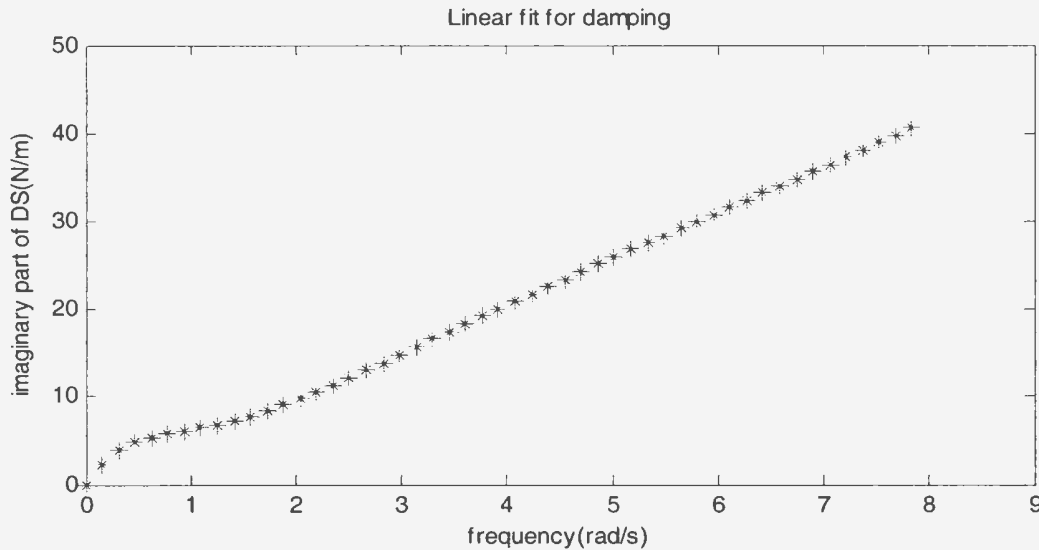


Figure C-12 Imaginary part of dynamic stiffness function for a moderate-damping system ($\zeta=0.167$)

Case study C-3 System parameters of small-damping SDOF linear system

A system is a small-damping system if ζ is smaller than 0.05 (He and Fu, 2001). It is well-known that a sharp peak exists in the FRF amplitude plot of a small-damping system.

Case C-3-1 Assume $M=1\text{kg}$, $C=2.5\text{N.s/m}$, $K=900\text{N/m}$, and this system is a small-damping system, because $\zeta=0.0417$. The input $x(t)$ takes the same time series as in Case C-1-1, and the output can be calculated using equation (C-10). The estimated and actual FRFs are shown in Figure C-13. As seen in Figure C-13, the estimated FRF matches the actual FRF well for this small -damping system.

Figure C-14 shows the real part of the estimated dynamic stiffness function and the linear fit to estimate the mass and stiffness. The estimated mass and stiffness are 0.946kg and 897.81N/m, which are close to the actual values.

Figure C-15 shows the imaginary part of the estimated dynamic stiffness function, and the estimated damping is 2.71N.s/m, which is close to the actual value of the damping.

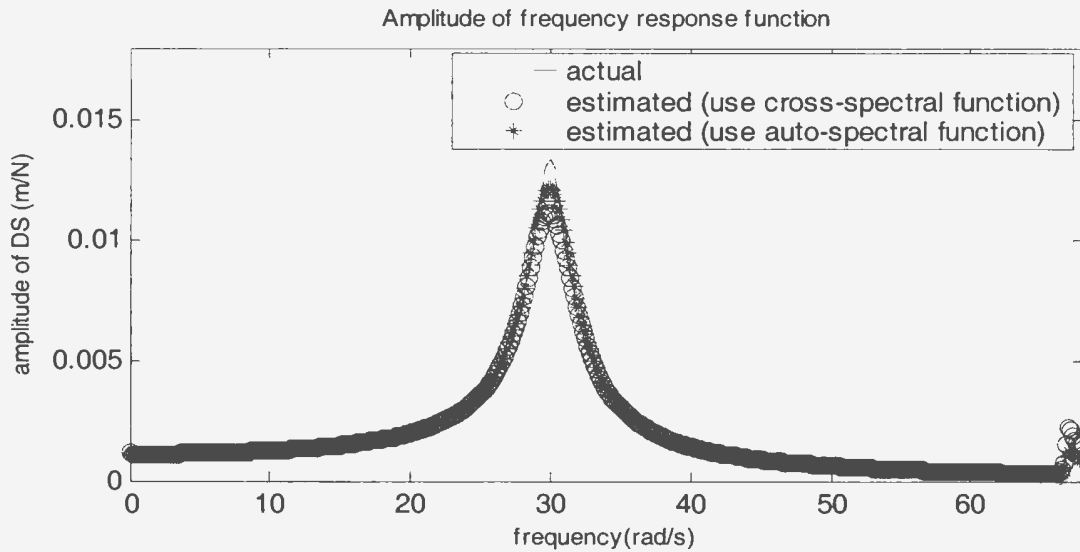


Figure C-13 The actual and estimated FRFs for a small-damping system ($\zeta=0.0417$)

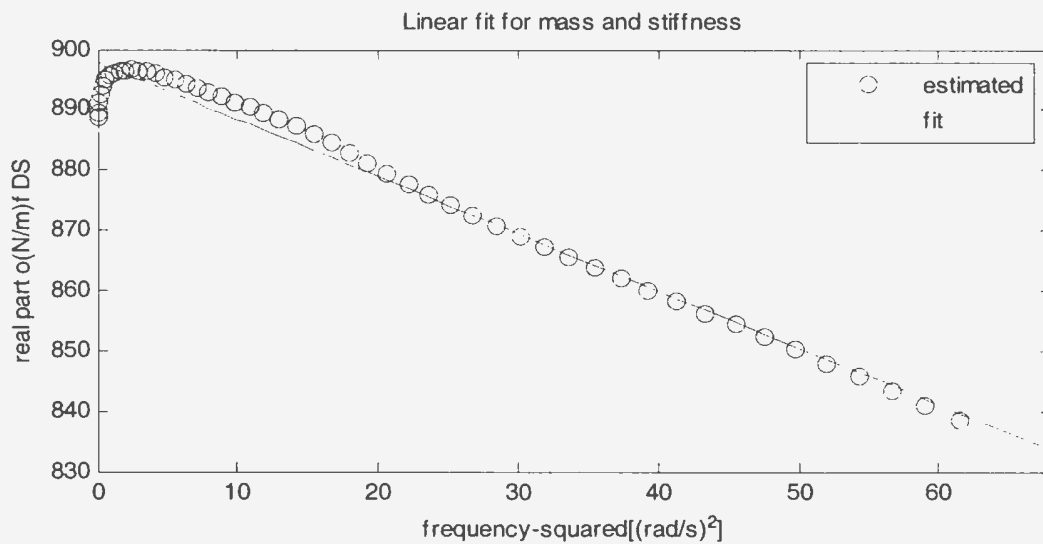


Figure C-14 Linear fit for mass and stiffness for a small-damping system ($\zeta=0.0417$)

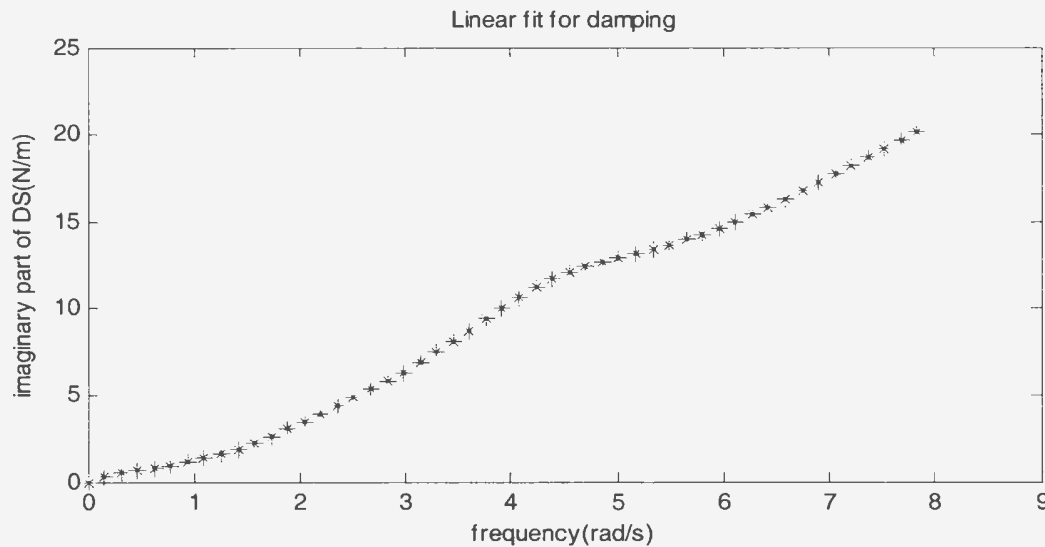


Figure C-15 Imaginary part of dynamic stiffness function for a small-damping system ($\zeta=0.0417$)

Case C-3-2 Assume $M=1\text{kg}$, $C=1.5\text{N.s/m}$, $K=900\text{N/m}$, and this system is a small-damping system, because $\zeta=0.025$. The input $x(t)$ takes the same time series as in Case C-1-1, and the output can be calculated using equation (C-10). The estimated and actual FRFs are shown in Figure C-16. As seen in Figure C-16, the estimated FRF matches the actual FRF well for this small-damping system.

Figure C-17 shows the real part of the estimated dynamic stiffness function and the linear fit to estimate the mass and stiffness. The estimated mass and stiffness are 0.916kg and 896.88N/m , which are close to the actual values.

Figure C-18 shows the imaginary part of the estimated dynamic stiffness function, and the estimated damping is 2.067N.s/m , which is close to the actual value of the damping.

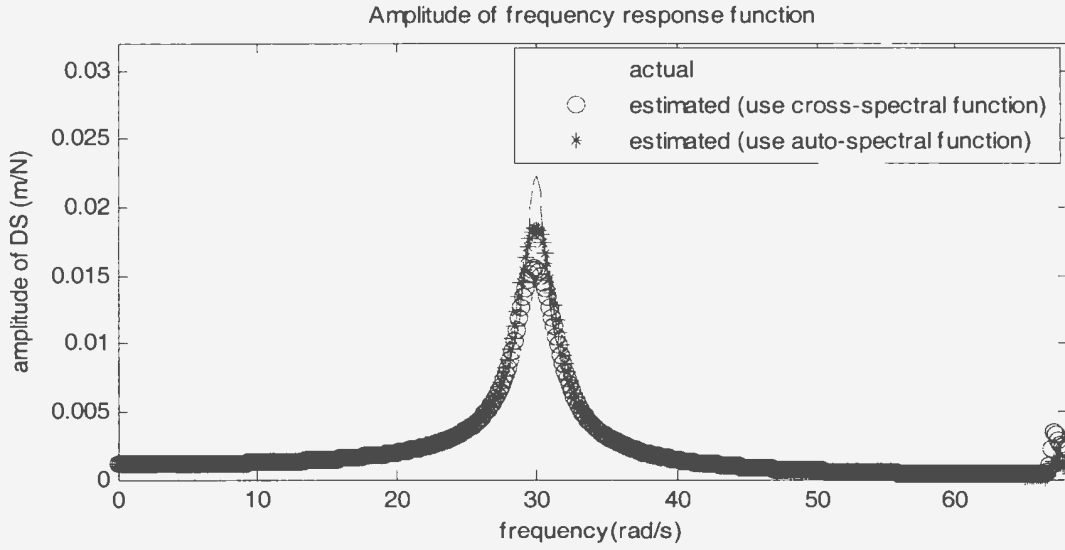


Figure C-16 The actual and estimated FRFs for a small-damping system ($\zeta=0.025$)

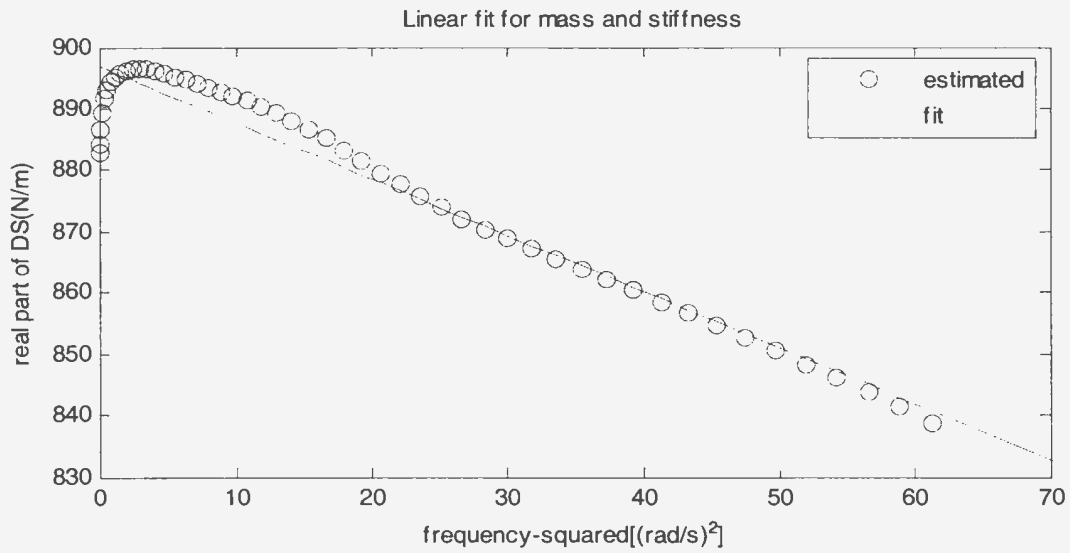


Figure C-17 Linear fit for mass and stiffness for a small-damping system ($\zeta=0.025$)

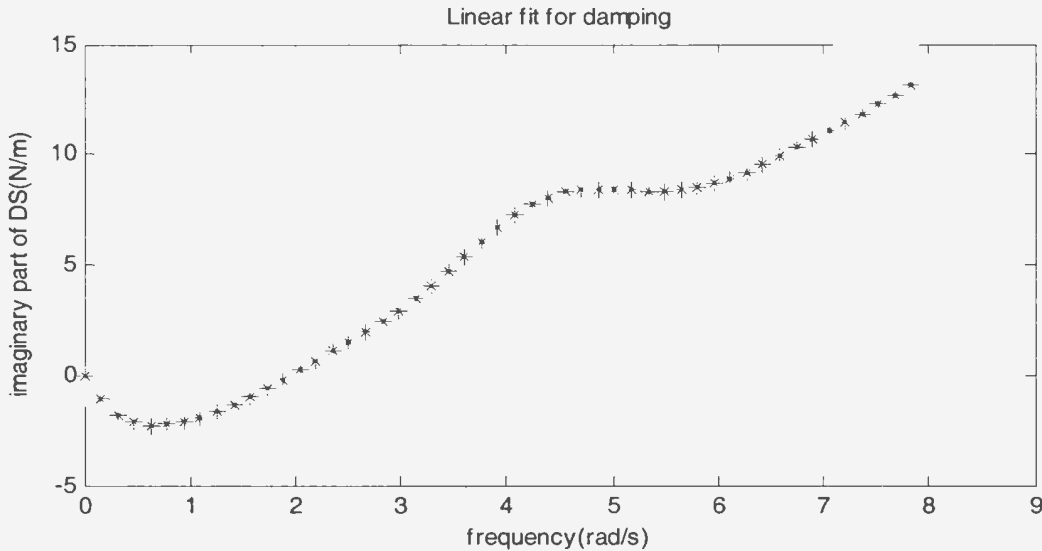


Figure C-18 Imaginary part of dynamic stiffness function for a small-damping system ($\zeta = 0.025$)

Case C-3-3 Assume $M=4\text{kg}$, $C=5\text{N.s/m}$, $K=900\text{N/m}$, and this system is obviously a small-damping system, because $\zeta = 0.0417$. The input $x(t)$ takes the same time series as in Case C-1-1, and the output can be calculated using equation (C-10). The estimated and actual FRFs are shown in Figure C-19. As seen in Figure C-19, the estimated FRF matches the actual FRF well for this small-damping system.

Figure C-20 shows the real part of the estimated dynamic stiffness function and the linear fit to estimate the mass and stiffness. The estimated mass and stiffness are 3.967kg and 893.29N/m , which are close to the actual values.

Figure C-20 shows the imaginary part of the estimated dynamic stiffness function, and the estimated damping is 6.444N.s/m , which is close to the actual value of the damping.

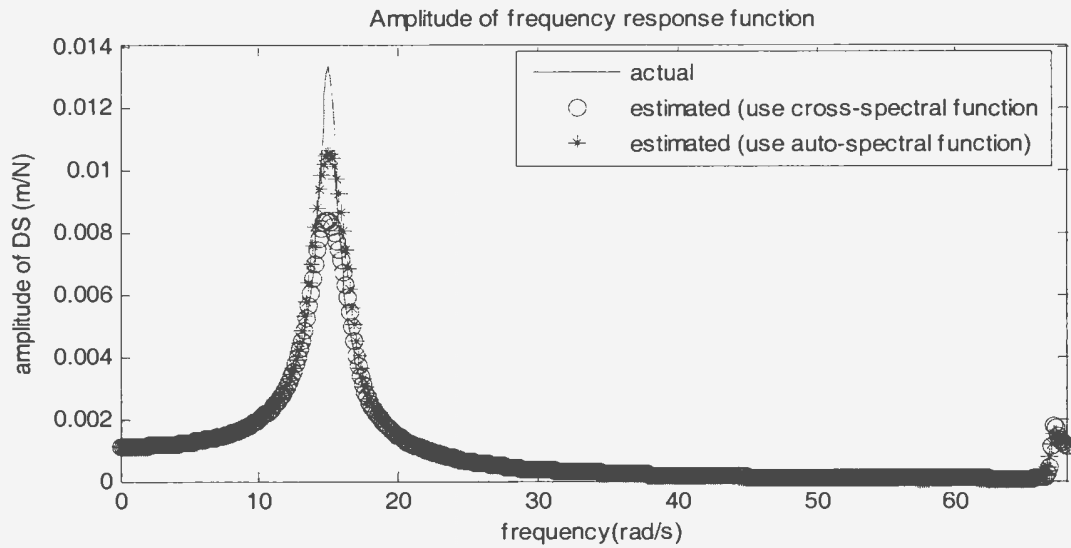


Figure C-19 The actual and estimated FRFs for a small-damping system ($\zeta = 0.0417$)

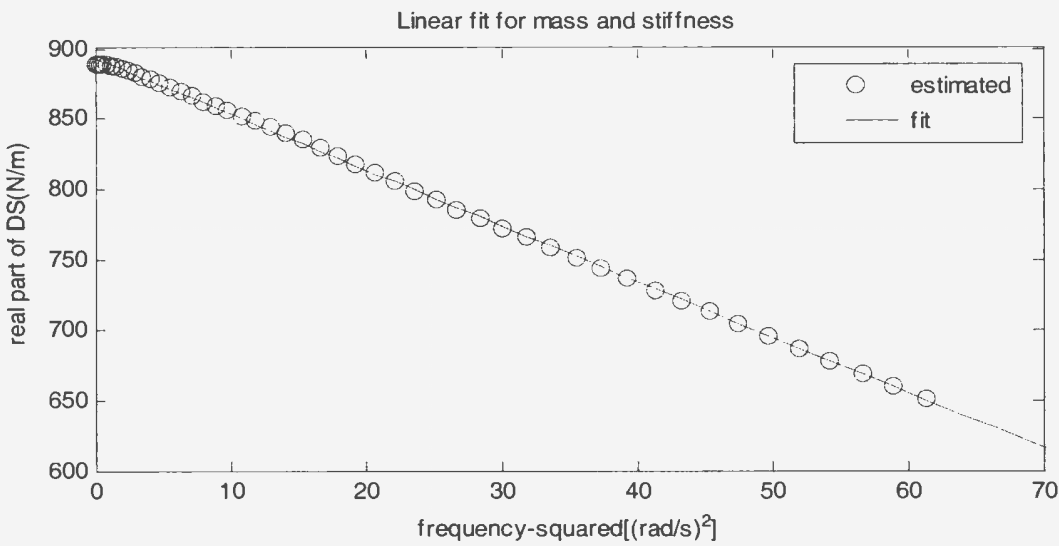


Figure C-20 Linear fit for mass and stiffness for a small-damping system ($\zeta = 0.0417$)

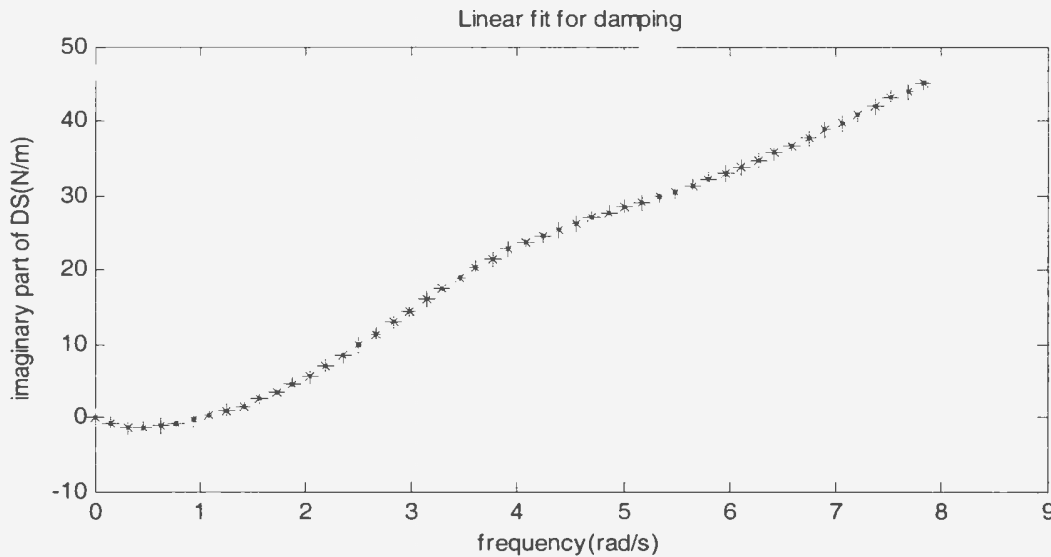


Figure C-21 Imaginary part of dynamic stiffness function for a small-damping system ($\zeta=0.0417$)

Case C-3-3 Assume $M=1\text{kg}$, $C=5\text{N.s/m}$, $K=3600\text{N/m}$, and this system is obviously a small-damping system, because $\zeta=0.0417$. The input $x(t)$ takes the same time series as in Case C-1-1, and the output can be calculated using equation (C-10). The estimated and actual FRFs are shown in Figure C-22. As seen in Figure C-22, the estimated FRF matches the actual FRF well for this small-damping system.

Figure C-23 shows the real part of the estimated dynamic stiffness function and the linear fit to estimate the mass and stiffness. The estimated mass and stiffness are 1.1kg and 3604.8N/m , which are close to the actual values.

Figure C-24 shows the imaginary part of the estimated dynamic stiffness function, and the estimated damping is 2.700N.s/m , which is close to the actual value of the damping.

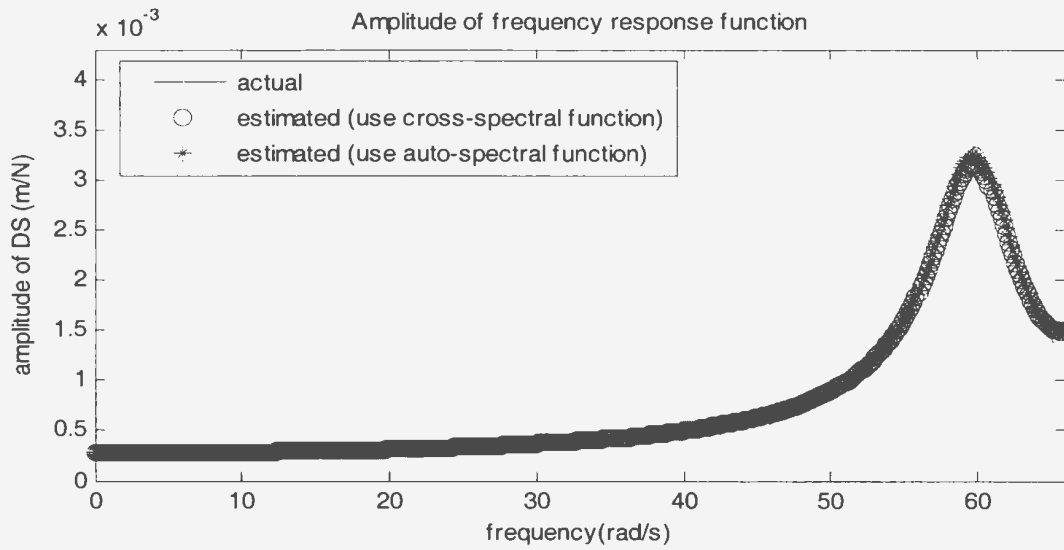


Figure C-22 The actual and estimated FRFs for a small-damping system ($\zeta=0.0417$)

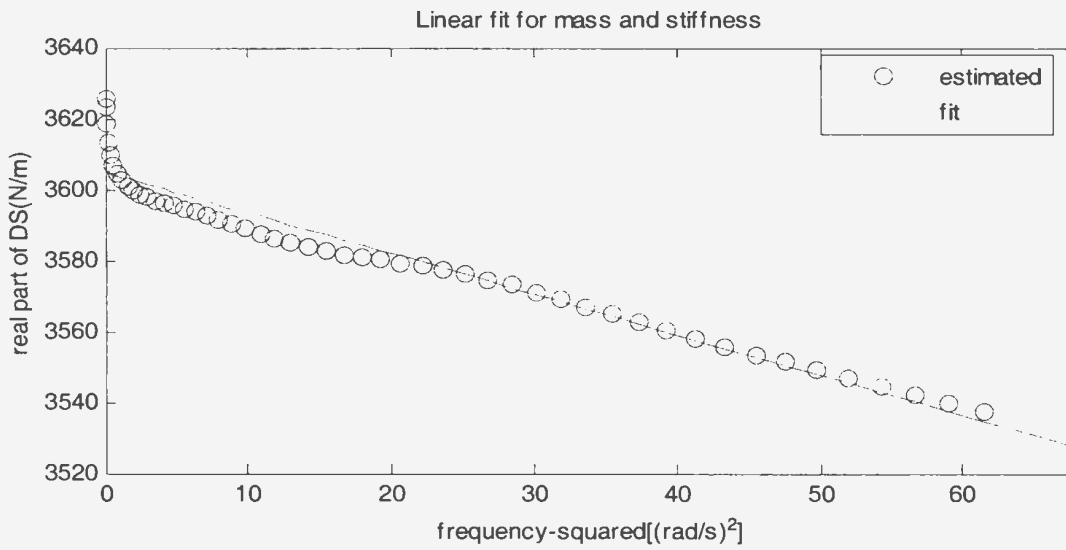


Figure C-23 Linear fit for mass and stiffness for a small-damping system ($\zeta=0.0417$)

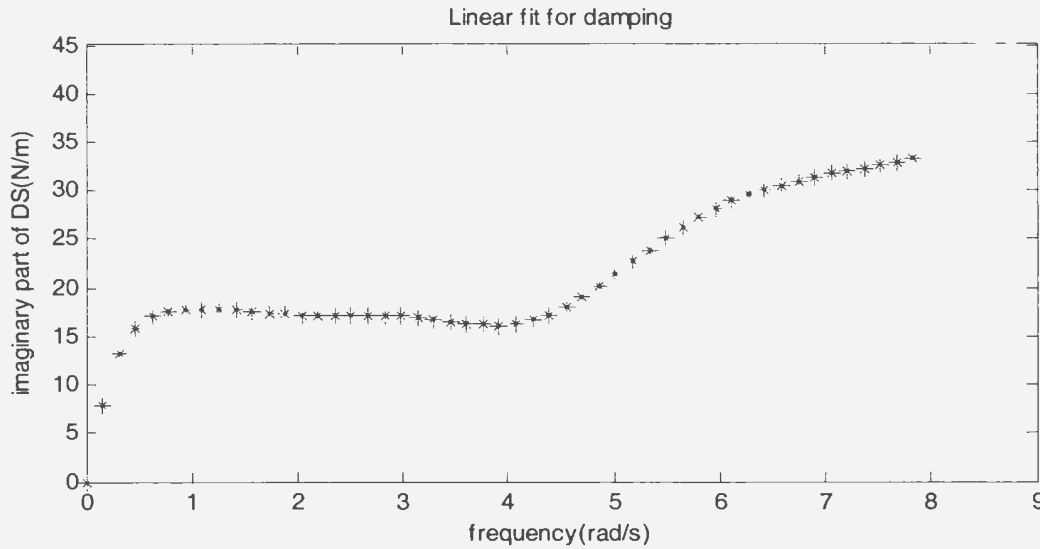


Figure C-24 Imaginary part of dynamic stiffness function for a small-damping system($\zeta=0.0417$)

Conclusions

Table C-1 summarizes the estimated results.

Table C-1 The comparison of the actual and estimated values

| case | actual | | | | estimated | | | |
|-------|--------|-----------|---------|------------|-----------|-----------|---------|------------|
| | M (kg) | C (N.s/m) | K (N/m) | fn (rad/s) | M (kg) | C (N.s/m) | K (N/m) | fn (rad/s) |
| C-1-1 | 1 | 50 | 900 | 30 | 0.992 | 47.03 | 900.09 | 30.13 |
| C-2-1 | 1 | 5 | 900 | 30 | 0.983 | 4.766 | 898.89 | 30.25 |
| C-3-1 | 1 | 2.5 | 900 | 30 | 0.946 | 2.710 | 897.81 | 30.81 |
| C-3-2 | 1 | 1.5 | 900 | 30 | 0.916 | 2.067 | 896.88 | 31.29 |
| C-3-3 | 4 | 5 | 900 | 15 | 3.967 | 6.444 | 893.29 | 15.01 |
| C-2-2 | 0.25 | 5 | 900 | 60 | 0.261 | 4.495 | 900.35 | 58.68 |
| C-3-4 | 1 | 5 | 3600 | 60 | 1.100 | 2.700 | 3604.8 | 56.20 |
| C-2-3 | 1 | 5 | 225 | 15 | 0.997 | 5.065 | 223.61 | 14.97 |

The following conclusions can be obtained:

- a. The frequency response functions can be estimated using the methods presented in this appendix, and the estimated frequency response functions match the actual frequency response functions;

b. The estimated values of mass and stiffness match the actual values of mass and stiffness, while the accuracy of the estimated damping depends on damping ratio ζ . If damping ratio ζ is too small, the accuracy of the estimated damping values becomes poor.

Appendix D

Validation of the program to estimate system parameters for a nonlinear system

Method of Estimation

A system is a linear system if equation (C-1) is not satisfied. A single-input/single-output nonlinear system can usually be regarded as sum of two subsystems (Bendat, 1998). The first is a linear subsystem and another is a nonlinear subsystem, namely we have

$$p(t) = p_1(t) + p_2(t) \quad (D-1)$$

where $p(t)$ is the output of the nonlinear system, $p_1(t)$ is the output of the linear subsystem, and $p_2(t)$ is the output of the nonlinear subsystem. The linear subsystem can be described by a weighting function $h_1(\tau)$, namely

$$p_1(t) = \int_{-\infty}^{\infty} h_1(\tau)x(t-\tau)d\tau \quad (D-2)$$

where $x(t)$ is the input of the nonlinear system. The nonlinear subsystem can be described by a nonlinear operation of the input $x(t)$, which is followed by a linear system defined by another weighting function $h_2(\tau)$, namely

$$p_2(t) = \int_{-\infty}^{\infty} h_2(\tau)q[x(t-\tau)]d\tau \quad (D-3)$$

where $q[\]$ denotes a nonlinear operation. Substitution of equations (D-2) and (D-3) into equation (D-1) yields

$$p(t) = \int_{-\infty}^{\infty} h_1(\tau)x(t-\tau)d\tau + \int_{-\infty}^{\infty} h_2(\tau)q[x(t-\tau)]d\tau \quad (D-4)$$

From equation (D-2), the products $x(t)p(t+\tau)$ and $q(t)p(t+\tau)$ are respectively given by

$$\left. \begin{aligned} x(t)p(t+\tau) &= \int_{-\infty}^{+\infty} h_1(\xi)x(t)x(t+\tau-\xi)d\xi + \int_{-\infty}^{+\infty} h_2(\xi)x(t)q[x(t+\tau-\xi)]d\xi \\ q[x(t)]p(t+\tau) &= \int_{-\infty}^{+\infty} h(\xi)q[x(t)]x(t+\tau-\xi)d\xi + \int_{-\infty}^{+\infty} h_2(\xi)q[x(t)]q[x(t+\tau-\xi)]d\xi \end{aligned} \right\} (D-5)$$

Fourier transforms of both sides of equation (D-5) yields the expressions as follows:

$$\left. \begin{aligned} S_{xx}(\omega)H_1(\omega) + S_{xq}(\omega)H_2(\omega) &= S_{xp}(\omega) \\ S_{qx}(\omega)H_1(\omega) + S_{qq}(\omega)H_2(\omega) &= S_{qp}(\omega) \end{aligned} \right\} (D-6)$$

where the symbols $S_{xx}(\omega)$, $S_{qq}(\omega)$, $S_{xq}(\omega)$, $S_{qx}(\omega)$, $S_{xp}(\omega)$ and $S_{qp}(\omega)$ respectively denote Fourier transforms of the auto- and cross-correlation functions of $x(t)$, $q[x(t)]$ and $p(t)$, i.e. the auto- and cross-spectral density functions of $x(t)$, $q[x(t)]$ and $p(t)$.

Solving equation (D-6) gives the DS function for the nonlinear subsystem as

$$H_2(\omega) = \frac{S_{qp}(\omega)}{S_{qq}(\omega)}\psi(\omega) \quad (D-7)$$

where

$$\psi(\omega) = \frac{1 - \frac{S_{xp}(\omega)S_{xq}(\omega)}{S_{qp}(\omega)S_{xx}(\omega)}}{1 - \frac{S_{qx}(\omega)S_{xq}(\omega)}{S_{xx}(\omega)S_{qq}(\omega)}}$$

For a given nonlinear operation $q[\]$, the nonlinear system parameters can be estimated based on the DS function for the nonlinear subsystem using equation (D-7).

Case Study

Assume a nonlinear mass-damping-spring system defined by the following governing equation:

$$M\ddot{x}(t) + C\dot{x}(t) + Kx(t) + K_n x^3(t) = p(t) \quad (D-8)$$

where M , C , K and K_n are respectively the mass, damping, linear stiffness and nonlinear stiffness. This nonlinear system can be regarded as sum of a linear subsystem and a nonlinear subsystem, namely

$$\begin{aligned} p(t) &= p_1(t) + p_2(t) \\ p_1(t) &= M\ddot{x}(t) + C\dot{x}(t) + Kx(t) \\ p_2(t) &= K_n q[x(t)] \\ q[x(t)] &= x^3(t) \end{aligned} \tag{D-9}$$

The random input $x(t)$ can be obtained by composition of a large amount of harmonic components, namely

$$x(t) = \sum_{j=1}^n a_j \sin(\omega_j t + \alpha_j) \tag{D-10}$$

where n is the amount of the harmonic components, and a_j , ω_j and α_j are respectively the amplitudes, frequencies and random phases of the harmonic components. Let $n=1401$, $\omega_1=1\text{rad/s}$, $\omega_j = \omega_1 + j\Delta\omega$, where: $\Delta\omega = 0.0457\text{rad/s}$, and α_j take the random values shown in Table B-1, and the amplitude distribution over the frequency range is assumed as

$$\begin{aligned} a_j &= \sqrt{0.00105 \left(\frac{n-j}{n} \right)^3 + 0.000112} \\ j &= 0, 1, 2, \dots, n \end{aligned}$$

The input for the nonlinear subsystem $q[x(t)]$ can be calculated by equations (D-9) and (D-10), and the time series of $x(t)$ and $q[x(t)]$ are show in Figures D-1 and D-2.

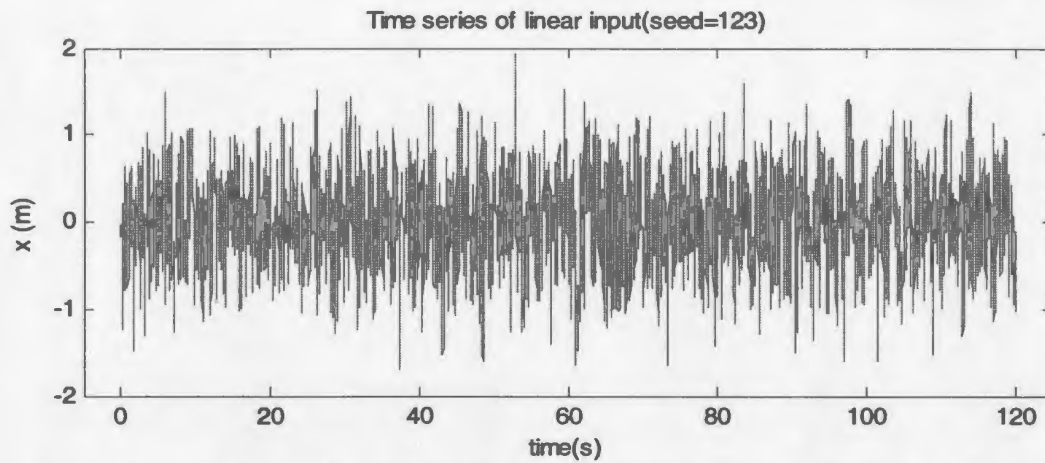


Figure D-1 The linear input generated by equation (D-9)

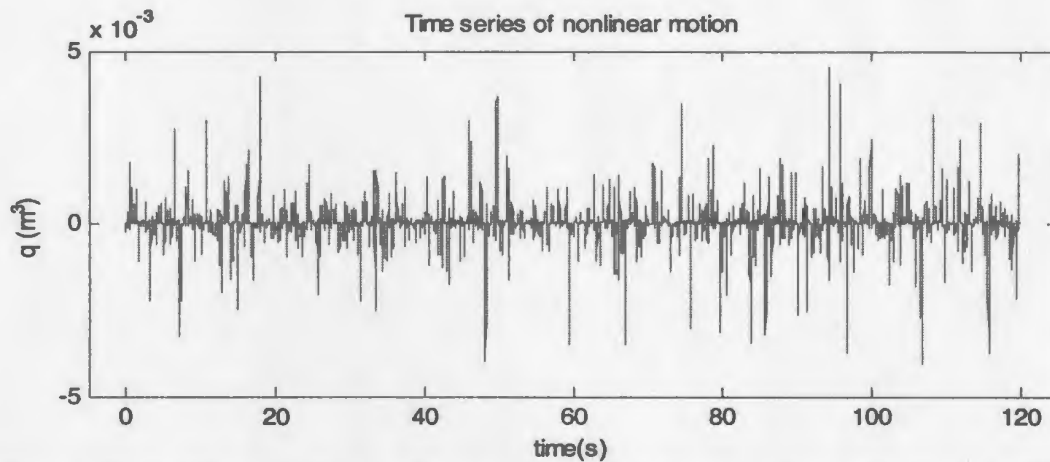


Figure D-2 The nonlinear input generated by equations (D-9) and (D-10)

The output $p(t)$ can be calculated based on equations (D-8) and (D-10), namely we have

$$p(t) = \sum_{j=1}^n [(-\omega_j^2 M + K) a_j \sin(\omega_j t + \alpha_j) + \omega_j \cos(\omega_j t + \alpha_j)] + K_n \left[\sum_{j=1}^n a_j \sin(\omega_j t + \alpha_j) \right]^3 \quad (D-11)$$

Assume that $M=1\text{kg}$, $C=50\text{N.s/m}$, $K=900\text{N/m}$ and $K_n=500\text{N/m}^3$, and a time series of the output $p(t)$ can be generated from equation (D-11), and the result is shown in Figure D-3.

The generated output contains the information of the system parameters M , C , K and K_n .

Now apply the present technique to the inputs and output. If the estimated values of M , C ,

K and K_n are close to the actual values of 1kg, 50N.s/m, 900N/m and 500N/m³, the present technique is then validated.

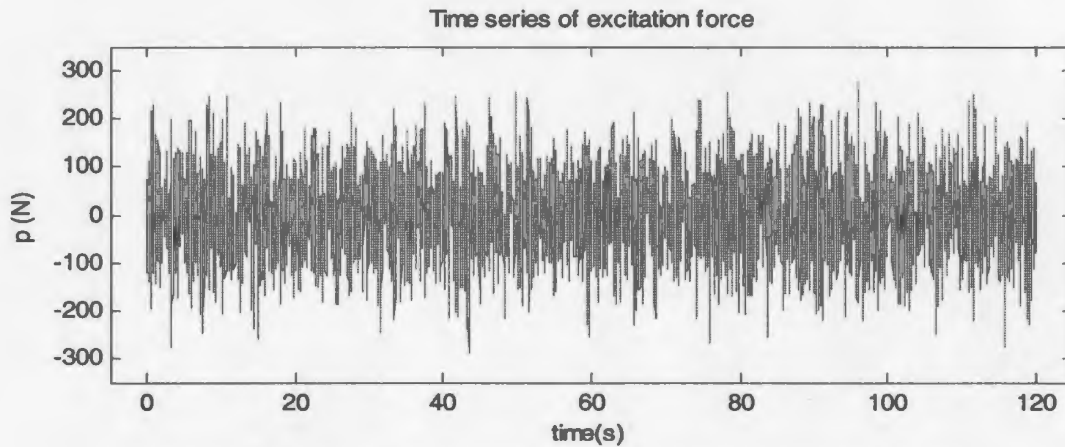


Figure D-3 The output generated by equation (D-11)

The auto- and cross-spectral density functions between $x(t)$, $q(t)$ and $p(t)$ are shown in Figures D-4, D-5, D-6, D-7 and D-8. Figure D-9 gives the linear fit plot for estimation of the mass and linear stiffness. Figure D-10 presents the imaginary part of the estimated linear dynamic stiffness function, which was used to estimate the linear damping. Figure D-10 shows the linear fit plot for the estimation of the nonlinear stiffness. The estimated mass M , damping C , linear stiffness K and the nonlinear stiffness K_n are respectively 1.003 kg, 50.0750N.s/m, 899.4 N/m and 556.4 N/m³. The estimated values of the linear system parameters demonstrate a good agreement with their actual values, while the estimated value of the nonlinear stiffness contains a 10% error. This error contains two types of errors: random error and bias error. The random error results from the performance over a finite number of sampling records for an infinite time series, and the bias error results from windowing operations in Δt . In theory, $\Delta t \rightarrow 0$, but in practice Δt must be finite.

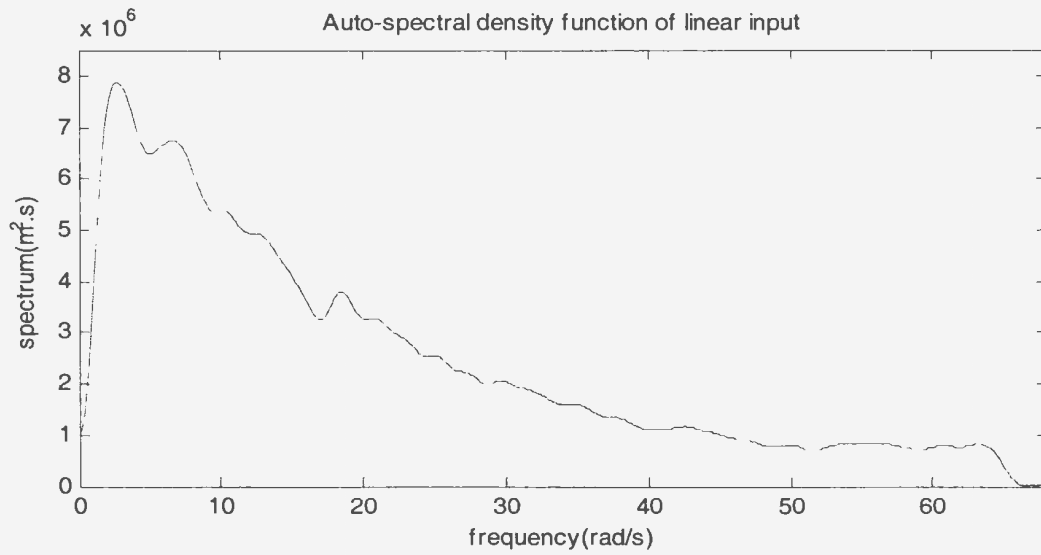


Figure D-4 The auto-spectral density function $S_{xx}(\omega)$ of linear input $x(t)$

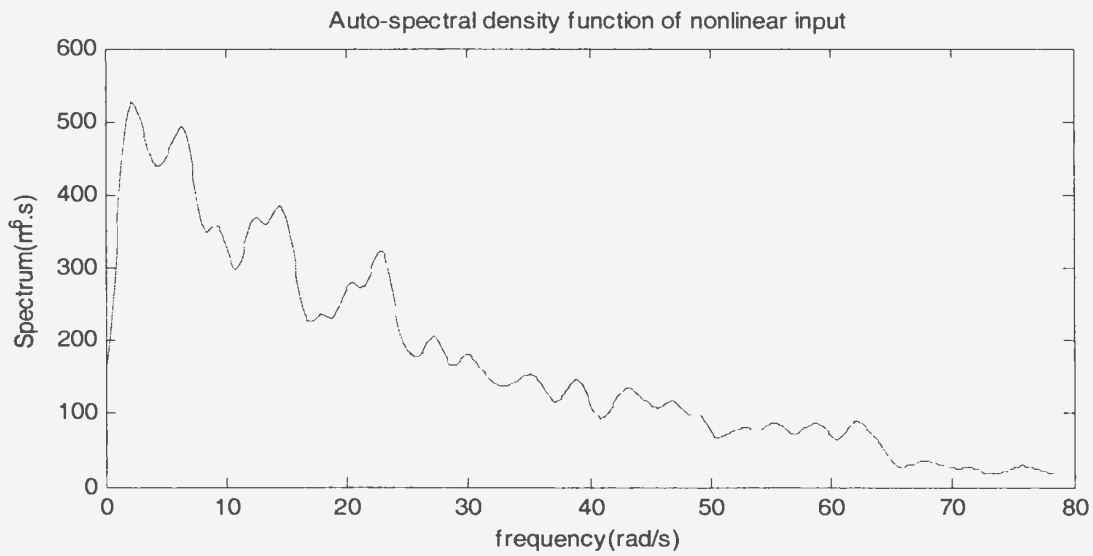


Figure D-5 The auto-spectral density function $S_{qq}(\omega)$ of nonlinear input $q(t)$

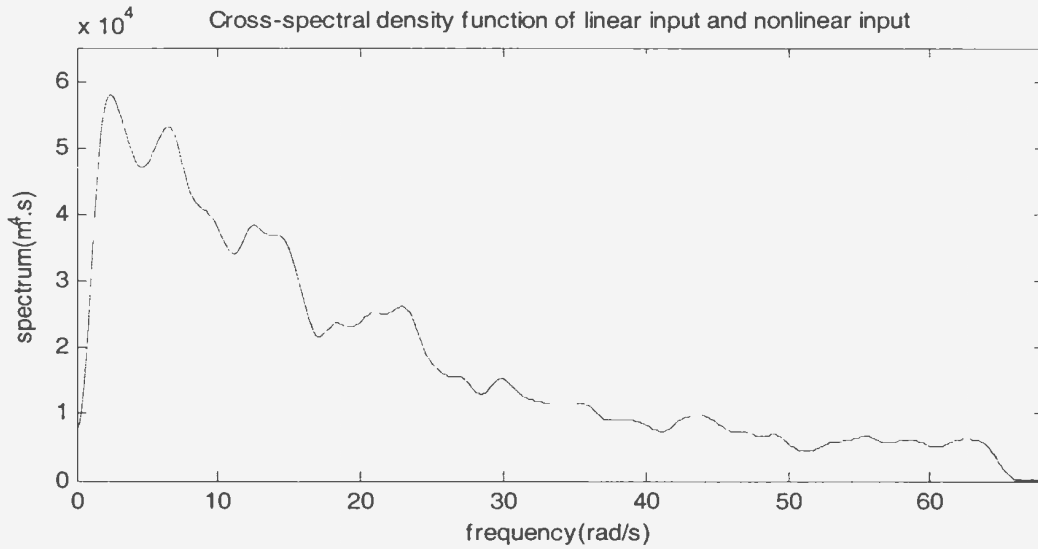


Figure D-6 The cross-spectral density function $S_{xq}(\omega)$ of linear input $x(t)$ and nonlinear input $q(t)$

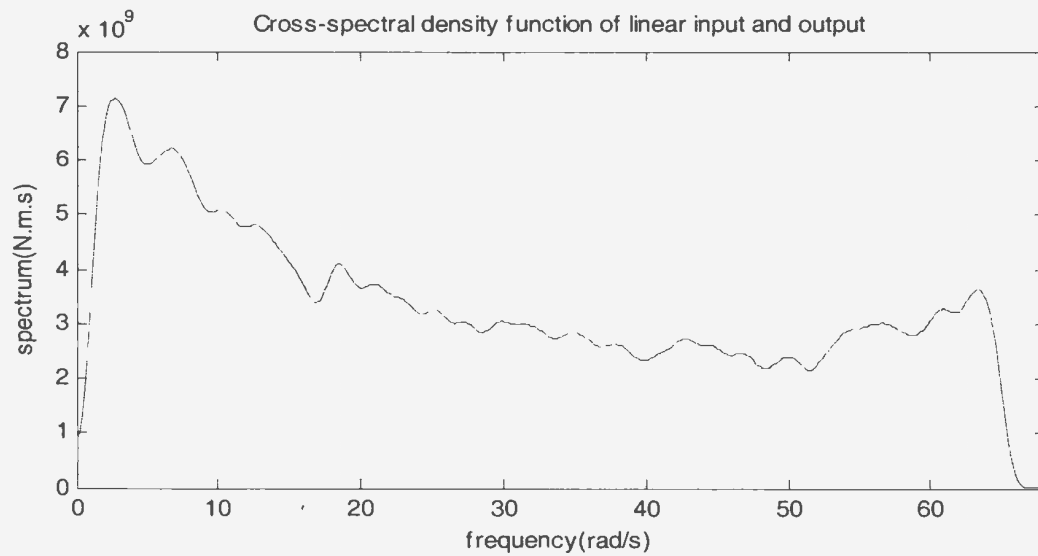


Figure D-7 The cross-spectral density function $S_{xp}(\omega)$ of linear input $x(t)$ and output $p(t)$

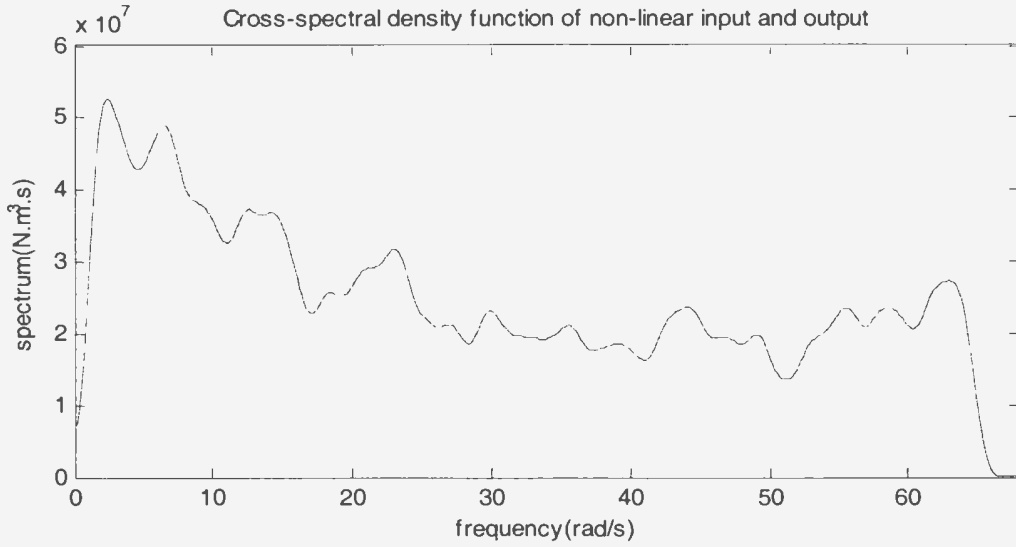


Figure D-8 The cross-spectral density function $S_{qp}(\omega)$ of nonlinear input $q(t)$ and output $p(t)$

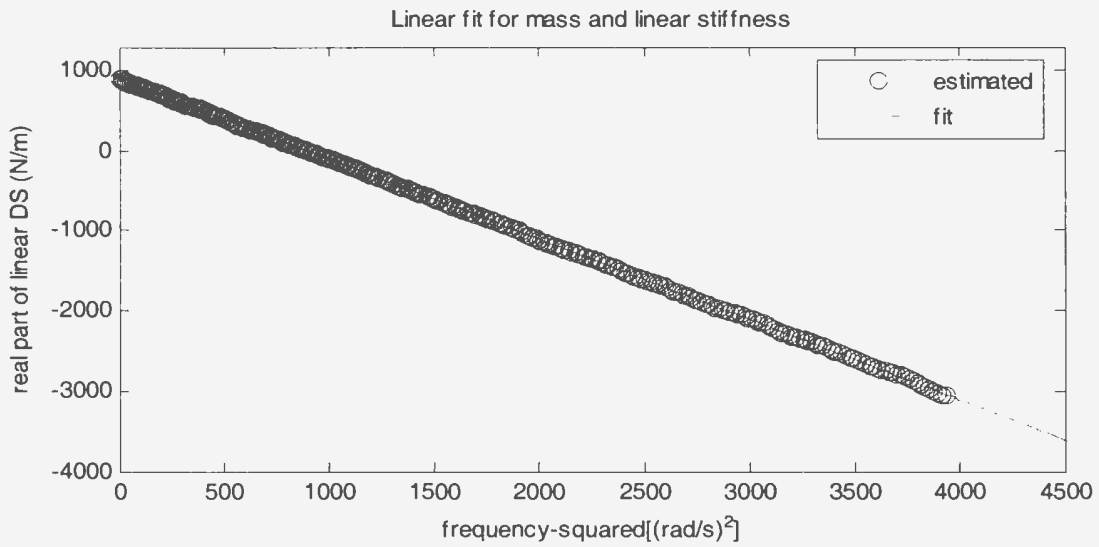


Figure D-9 Linear fit for mass and linear stiffness

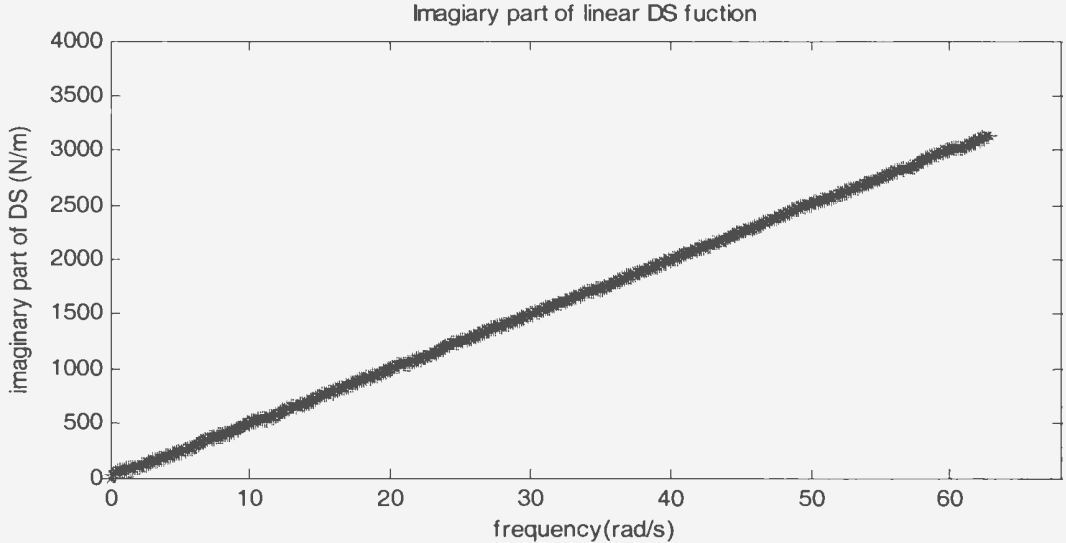


Figure D-10 Linear fit for mass and linear stiffness

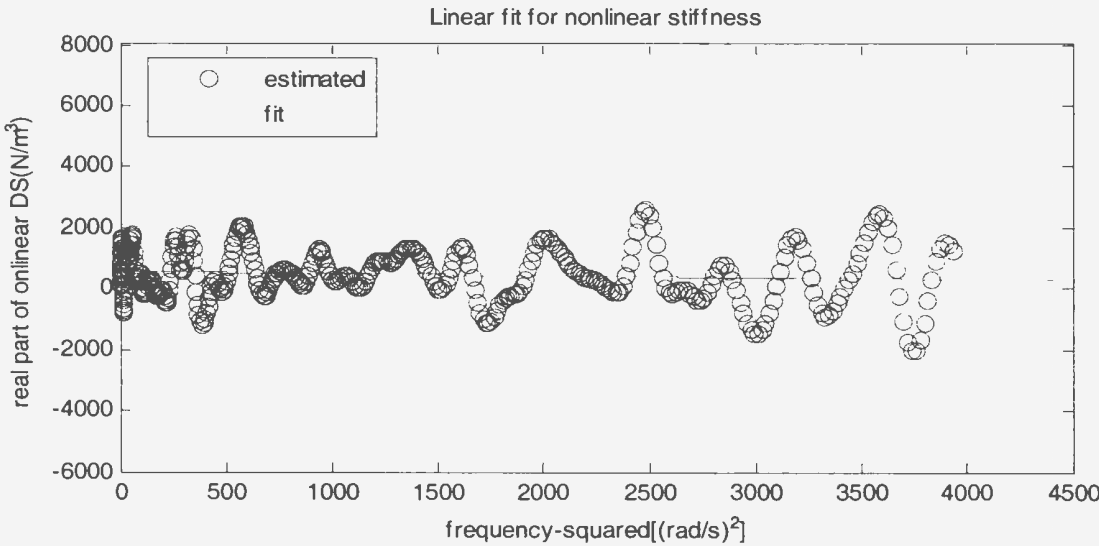


Figure D-11 Linear fit for nonlinear stiffness

100

100

100

100

100

100

100

100

100

100

100

100

100

100

100

100

100

100

100

